

MOSAIC VARIEGATED ANEUPLOIDY

Elucidating the molecular causes of constitutional aneuploidy in humans



Bas de Wolf

MOSAIC VARIEGATED ANEUPLOIDY

Elucidating the molecular causes of constitutional aneuploidy in
humans

Bas de Wolf

Mosaic Variegated Aneuploidy

Elucidating the molecular causes of constitutional aneuploidy in humans

ISBN 978-94-6416-192-2

Layout by Publiss | www.publiss.nl

Print by Ridderprint | www.ridderprint.nl

Copyright © 2020 B. de Wolf, Utrecht, the Netherlands

No part of this thesis may be reproduced, stored, or transmitted in any form or by any means, without prior permission of the author.

MOSAIC VARIEGATED ANEUPLOIDY

Elucidating the molecular causes of constitutional
aneuploidy in humans

Mozaïek gevarieerde aneuploïdie

Opheldering van de moleculaire oorzaken van
constitutionele aneuploïdie bij mensen

(met een samenvatting in het Nederlands)

Proefschrift

ter verkrijging van de graad van doctor aan de
Universiteit Utrecht
op gezag van de
rector magnificus, prof.dr. H.R.B.M. Kummeling,
ingevolge het besluit van het college voor promoties
in het openbaar te verdedigen op

donderdag 15 oktober 2020 des middags te 2.30 uur

door

Bas de Wolf

geboren op 6 juni 1989
te Amsterdam

PROMOTOR:

Prof. dr. G.J.P.L. Kops

Dedicated to the patients

CONTENTS

	Preface	7
Chapter 1	General introduction	9
	Scope of this thesis	12
Chapter 2	Kinetochore malfunction in human pathologies	19
Chapter 3	Biallelic <i>TRIP13</i> mutations predispose to Wilms tumor and chromosome missegregation	43
Chapter 4	Constitutional aneuploidy caused by defects in splicing of a minor intron subtype	71
Chapter 5	Mutations in KNL1 complex members in patients with Mosaic Variegated Aneuploidy syndrome	113
Chapter 6	General discussion	137
	Summary	138
Addendum	Table 1. Overview of clinical and cytogenetic findings in MVA patients	152
	Nederlandse samenvatting	166
	Greek summary Ελληνική σύνοψη	168
	List of publications	170
	Curriculum vitae	171
	Acknowledgements Dankwoord Ευχαριστίες	172

PREFACE

Once upon a time, you started out as one tiny cell (well, actually two cells but never mind that for now), which grew into the big assembly of cells that is now reading this thesis. The process that is responsible for this transition lies at the heart of this thesis: cell division. After the DNA of a cell has been replicated, it is divided (in the form of chromosomes) over two new daughter cells. This distribution of DNA, however, does not always happen equally. When a mistake occurs, this can lead to a condition called aneuploidy: having a set of chromosomes that is different from the normal two copies of all 23 chromosomes (see **Figure 1**). For some reason, patients with the disorder called Mosaic Variegated Aneuploidy (MVA) have many of these so-called aneuploid cells. This means that during their transition from a single cell to a human being, many cell division mistakes have occurred. The goals of this thesis are: A) to investigate what is causing these mistakes to happen at the molecular level, and B) to investigate how these mistakes can lead to the severe symptoms that are associated with this disorder.



Figure 1. Aneuploid karyotypes of two cultured, immortalized lymphoblastoid cells from a MVA patient with mutations in *BUB1B* (1). Red rectangles indicate the anomalies.

CONTENTS

1.1 ANEUPLOIDY & CHROMOSOMAL INSTABILITY (CIN)	10
1.2 CAUSES OF ANEUPLOIDY & CIN	10
1.3 CONSEQUENCES OF ANEUPLOIDY & CIN	10
1.4 SCOPE OF THIS THESIS	12

CHAPTER 1

GENERAL INTRODUCTION

1.1 Aneuploidy & Chromosomal Instability (CIN)

Aneuploidy is defined as the state of having an amount of chromosomes that deviates from an exact multiple of the haploid number (23 in humans) (see also **chapter 2.2**). Aneuploidy usually refers to whole-chromosome or numerical aneuploidy: having gained or lost one or more whole chromosomes. Structural aneuploidy instead refers to gains, losses, or translocations of parts of a chromosome. Both whole-chromosome and structural aneuploidy are the result of chromosome segregation errors in mitosis, but can also be caused by defects preceding mitosis (discussed below). When cells are predisposed to missegregate chromosomes, for instance because of a mutation in a mitotic regulator, they are called chromosomally unstable (CIN) (see also **chapter 2.2**). Aneuploidy is therefore a *state*, whereas CIN is a *phenotype* that can lead to aneuploidy (2).

1.2 Causes of Aneuploidy & CIN

Chromosome segregation errors can be the result of defects that have either occurred before mitosis, for instance DNA damage or replication stress (3, 4), or in mitosis, such as defects in the spindle assembly checkpoint (SAC, **chapter 2.1.2**), erroneous kinetochore-microtubule attachments (**chapters 2.1 and 2.4.2**), unstable kinetochore-microtubule attachments (**chapters 2.1 and 2.4.2**), sister chromatid cohesion loss (**chapter 2.4.1**), supernumerary spindle poles (**chapter 2.4.2**), and increased microtubule assembly rates (**chapter 2.4.2**). These defect can lead to one or more of the following types of chromosome segregation errors (see also **Figure 1**): lagging chromosomes (which are separated later than the other chromosomes and can break during cytokinesis (5) or can be taken up into micronuclei, in which they can undergo chromothripsis (**chapter 2.2**), misaligned chromosomes (which fail to align at the metaphase plate and don't separate), anaphase bridges or ultrafine anaphase bridges (which occur when a chromosome is stretched between the two packs of segregating chromosomes, potentially leading to chromosome breakage (6, 7)), and multipolar mitoses (when a cell divides into more than two daughter cells). Furthermore, persistent mitotic defects can also lead to mitotic arrest and apoptosis (cell death).

1.3 Consequences of Aneuploidy & CIN

Aneuploid cells are rare in healthy tissues (8), with recent estimates, based on single-cell sequencing data, ranging from close to 0% of cells in the skin up to approximately 5% of cells in liver and brain tissues (8, 9). However, when it occurs, aneuploidy can have diverse negative effects on a cell (see also **chapter 2.2**). In most cases, aneuploidy leads to the activation of the transcription factor p53, which in turn induces apoptosis or cell-cycle arrest and cellular senescence, both of which prevent the cell from further proliferation (8, 10). Although it is debated exactly how aneuploidy leads to p53 activation (8), it happens more effectively in response to structural aneuploidies than whole-chromosome aneuploidies (11, 12). In addition, aneuploidy is thought to confer a fitness disadvantage, for instance by inducing proteotoxic or metabolic stress (13, 14), and it can evoke an immune response aimed at the removal of the affected cells (11). Although it is therefore detrimental for proliferation in general, aneuploidy is also able to drive tumorigenesis under specific circumstances (13).

On the organismal level, aneuploidy is intimately associated with disease. It is a hallmark of cancer (see also **chapter 2.4**) (13), the most common cause of human miscarriages and congenital disorders (15), and associated with ageing (10). When part of a disease phenotype,

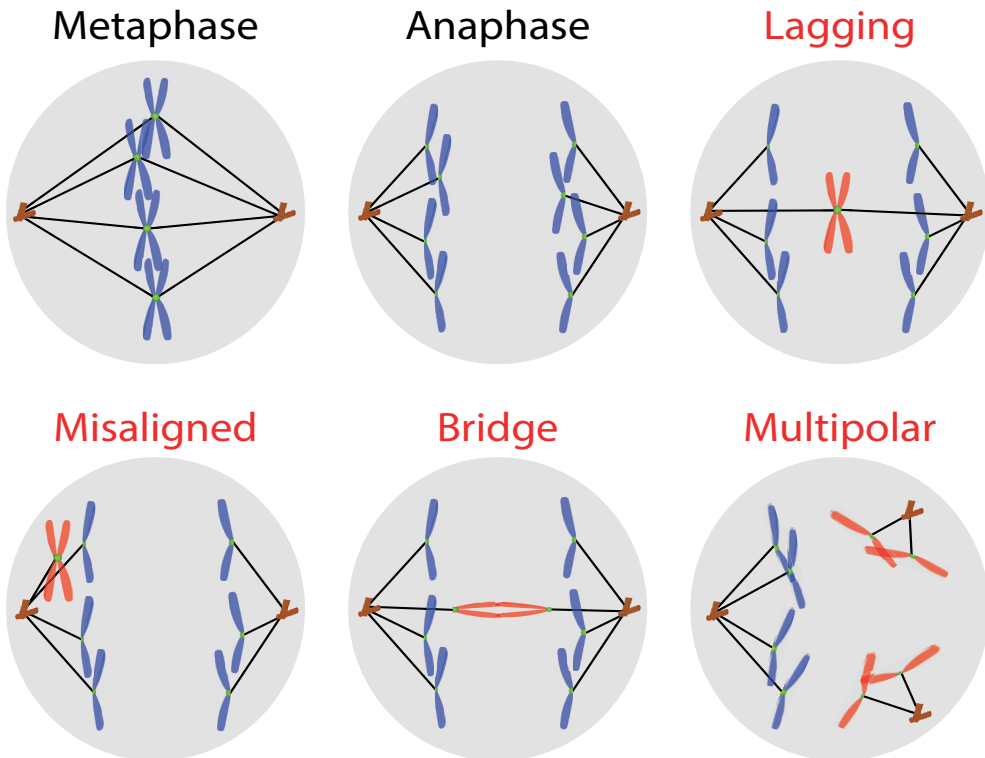


Figure 1. Schematic representations of chromosomes (blue or red) and the mitotic spindle (brown centrosomes and black microtubules) during a normal metaphase and anaphase (top left) and anaphases with one of four different chromosome missegregation types: a lagging chromosome, a misaligned chromosome, a chromosome bridge, and a multipolar spindle. Missegregating chromosomes are depicted in red, kinetochores are depicted in green.

aneuploidy is referred to as either *constitutional* (when acquired in a gamete or embryonal cell) or *somatic* (when acquired in a somatic cell) (16). Examples of *constitutional* aneuploidy disorders are Down Syndrome (MIM 190685), in which all cells of the affected patient have an extra copy of chromosome 21 (also referred to as trisomy 21), and Turner Syndrome (MIM 300082), which is defined by the loss of one X chromosome (or monosomy X) (Turner Syndrome only affects females). *Somatic* aneuploidy, on the other hand, has been implicated in several neurodegenerative disorders, such as Alzheimer disease (MIM 104300) and Lewy body disease (MIM 127750) (17, 18). When aneuploidy is not present in every cell of a patient (as is the case for the *somatic* aneuploidies in the above neurodegenerative disorders), it is often referred to as *mosaic*: one or more aneuploid cells (mosaic aneuploidies) in a diploid population. Examples of disorders with *constitutional*, *mosaic* aneuploidies are Mosaic Variegated Aneuploidy syndrome (MVA, see **chapter 2.3.5** for a detailed description and **Table 1** for a list of all known patients and their phenotypes) and the so-called chromosome instability syndromes, which are caused by defects in DNA repair mechanisms (see also **chapter 2.2**) (19, 20). Whereas mosaic aneuploidies are always present in multiple tissue samples of all MVA patients, they are detected in only a small subset of patients with one of the chromosome instability syndromes (18–20).

1.4 Scope of this Thesis

The work presented in this thesis aims to further our understanding of both cause and consequence of aneuploidy in human pathologies. Mosaic Variegated Aneuploidy (MVA) is a rare developmental disorder that is characterized by the presence of mosaic aneuploidies and is therefore uniquely equipped for studying this phenomenon. These aneuploid cells are most likely the result of chromosome segregation errors in mitosis, as disease-causing mutations were found in the mitotic genes *BUB1B* and *CEP57* (1, 21). Although mosaic aneuploidies are the defining feature of MVA, it is currently unclear what is the mechanism of pathogenicity underlying this disorder and whether the presence of aneuploid cells contributes to it. With this thesis, I set out to uncover the molecular defects responsible for causing aneuploidy in MVA patients and to reveal how these defects can lead to the pathogenic mechanism underlying MVA. In **chapter 2**, I first provide a summary of the current knowledge about the processes governing mitosis and about the disorders that are currently associated with mutations in kinetochore genes. The following chapters (**3, 4, and 5**) contain the experiments that led to the identification of disease-causing mutations in the mitotic regulators *TRIP13*, *CENATAC*, *KNL1*, and *ZWINT*. In addition, these chapters include case reports of the affected patients, and the results of our investigation into how the malfunction of these genes can lead to chromosome segregation errors and aneuploidy. In **chapter 3**, we show that patient mutations in both *BUB1B* and *TRIP13* led to a severe impairment of the spindle assembly checkpoint (SAC), and we uncover a striking correlation between the mutations in these genes and the occurrence of specific childhood cancers in MVA patients. In **chapter 4**, we identify disease-causing mutations in *CCDC84* (which we re-name *CENATAC*), a gene of which the function was hitherto unknown. Driven by the knowledge that its malfunction caused aneuploidy, and that its function must therefore be of significant importance, we set out to uncover its role in mitosis and discovered that it is a novel component of the minor spliceosome. In addition, we reveal a previously unknown aspect of pre-mRNA splicing and link the minor spliceosome to the regulation of mitosis. In **chapter 5**, we show that *KNL1* patient mutations weakened the SAC and reduced the kinetochore localization of several key mitotic regulators. In addition, we uncover an intriguing inconsistency between MVA and MCPH4: both of these disorders are the result of mutations in *KNL1* and are associated with the same symptoms, yet mosaic aneuploidies were only detected in the tissues of MVA patients. Finally, in **chapter 6**, I discuss the different theories regarding the molecular mechanism of pathogenicity underlying MVA and why the presence of mosaic aneuploidies may not actually be required for it. In addition, I discuss the contributions of CIN and aneuploidy to the development of cancer, the striking similarities between MVA and various other developmental disorders, and why it may be necessary to re-define MVA.

REFERENCES

1. S. Hanks, K. Coleman, S. Reid, A. Plaja, H. Firth, D. Fitzpatrick, A. Kidd, K. Méhes, R. Nash, N. Robin, N. Shannon, J. Tolmie, J. Swansbury, A. Irrthum, J. Douglas, N. Rahman, Constitutional aneuploidy and cancer predisposition caused by biallelic mutations in BUB1B. *Nat. Genet.* 36, 1159–61 (2004).
2. R. H. van Jaarsveld, G. J. P. L. Kops, Difference Makers: Chromosomal Instability versus Aneuploidy in Cancer. *Trends in Cancer.* 2, 561–571 (2016).
3. R. A. Burrell, S. E. McClelland, D. Endesfelder, P. Groth, M.-C. Weller, N. Shaikh, E. Domingo, N. Kanu, S. M. Dewhurst, E. Gronroos, S. K. Chew, A. J. Rowan, A. Schenk, M. Sheffer, M. Howell, M. Kschischo, A. Behrens, T. Helleday, J. Bartek, I. P. Tomlinson, C. Swanton, Replication stress links structural and numerical cancer chromosomal instability. *Nature.* 494, 492–496 (2013).
4. M. Löbrich, P. A. Jeggo, The impact of a negligent G₂/M checkpoint on genomic instability and cancer induction. *Nat. Rev. Cancer.* 7, 861–869 (2007).
5. A. Janssen, M. Van Der Burg, K. Szuhai, G. J. P. L. Kops, R. H. Medema, Chromosome segregation errors as a cause of DNA damage and structural chromosome aberrations. *Science (80-.)* 333, 1895–1898 (2011).
6. Y. W. Chan, K. Fugger, S. C. West, Unresolved recombination intermediates lead to ultra-fine anaphase bridges, chromosome breaks and aberrations. *Nat. Cell Biol.* 20, 92–103 (2018).
7. M. Fernández-Casañas, K. L. Chan, The unresolved problem of DNA bridging. *Genes (Basel).* 9 (2018), doi:10.3390/genes9120623.
8. S. Santaguida, A. Amon, Short- and long-term effects of chromosome mis-segregation and aneuploidy. *Nat. Rev. Mol. Cell Biol.* 16, 473–85 (2015).
9. K. A. Knouse, J. Wu, C. A. Whittaker, A. Amon, Single cell sequencing reveals low levels of aneuploidy across mammalian tissues. *Proc Natl Acad Sci U S A.* 111, 13409–13414 (2014).
10. R. M. Naylor, J. M. van Deursen, Aneuploidy in Cancer and Aging. *Annu. Rev. Genet.* 50, 45–66 (2016).
11. S. Santaguida, A. Richardson, D. R. Iyer, O. M'Saad, L. Zasadil, K. A. Knouse, Y. L. Wong, N. Rhind, A. Desai, A. Amon, Chromosome Mis-segregation Generates Cell-Cycle-Arrested Cells with Complex Karyotypes that Are Eliminated by the Immune System. *Dev. Cell.* 41, 638–651.e5 (2017).
12. M. Soto, J. A. Raaijmakers, B. Bakker, D. C. J. Spierings, P. M. Lansdorp, F. Foijer, R. H. Medema, p53 Prohibits Propagation of Chromosome Segregation Errors that Produce Structural Aneuploidies. *Cell Rep.* 19, 2423–2431 (2017).
13. U. Ben-David, A. Amon, Context is everything: aneuploidy in cancer. *Nat. Rev. Genet.* 21, 44–62 (2020).
14. N. K. Chunduri, Z. Storchová, The diverse consequences of aneuploidy. *Nat. Cell Biol.* 21, 54–62 (2019).
15. S. I. Nagaoka, T. J. Hassold, P. A. Hunt, Human aneuploidy: Mechanisms and new insights into an age-old problem. *Nat. Rev. Genet.* 13, 493–504 (2012).
16. H. H. Heng, Distinguishing constitutional and acquired nonclonal aneuploidy. *Proc. Natl. Acad. Sci. U. S. A.* 111 (2014), doi:10.1073/pnas.1323636111.
17. C. E. Shepherd, Y. Yang, G. M. Halliday, Region- and Cell-specific Aneuploidy in Brain Aging and Neurodegeneration. *Neuroscience.* 374, 326–334 (2018).
18. H. Potter, H. J. Chial, J. Caneus, M. Elos, N. Elder, S. Borysov, A. Granic, Chromosome Instability and Mosaic Aneuploidy in Neurodegenerative and Neurodevelopmental Disorders. *Front. Genet.* 10 (2019), doi:10.3389/fgene.2019.01092.

19. Z. H. Wu, Phenotypes and genotypes of the chromosomal instability syndromes. *Transl. Pediatr.* 5, 79–83 (2016).
20. A. M. R. Taylor, C. Rothblum-Oviatt, N. A. Ellis, I. D. Hickson, S. Meyer, T. O. Crawford, A. Smogorzewska, B. Pietrucha, C. Weemaes, G. S. Stewart, Chromosome instability syndromes. *Nat. Rev. Dis. Prim.* 5 (2019), doi:10.1038/s41572-019-0113-0.
21. K. Snape, S. Hanks, E. Ruark, P. Barros-Núñez, A. Elliott, A. Murray, A. H. Lane, N. Shannon, P. Callier, D. Chitayat, J. Clayton-Smith, D. R. Fitzpatrick, D. Gisselsson, S. Jacquemont, K. Asakura-Hay, M. a Micale, J. Tolmie, P. D. Turnpenny, M. Wright, J. Douglas, N. Rahman, Mutations in CEP57 cause mosaic variegated aneuploidy syndrome. *Nat. Genet.* 43, 527–529 (2011).
22. A. Plaja, T. Vendrell, D. Smeets, E. Sarret, T. Gili, V. Catal, C. Mediano, J. M. J. C. Scheres, Variegated aneuploidy related to premature centromere division (PCD) is expressed in vivo and is a cancer-prone disease (2001), vol. 98.
23. P. Callier, L. Faivre, V. Cusin, N. Marle, C. Thauvin-Robinet, D. Sandre, T. Rousseau, P. Sagot, E. Lacombe, V. Faber, F. Mugneret, Microcephaly is not mandatory for the diagnosis of mosaic variegated aneuploidy syndrome. *Am. J. Med. Genet. A.* 137, 204–7 (2005).
24. J. L. Tolmie, E. Boyd, P. Batstone, M. E. Ferguson-Smith, L. al Roomi, J. M. Connor, Siblings with chromosome mosaicism, microcephaly, and growth retardation: the phenotypic expression of a human mitotic mutant? *Hum. Genet.* 80, 197–200 (1988).
25. H. García-Castillo, A. I. Vázquez-Velásquez, H. Rivera, P. Barros-Núñez, Clinical and genetic heterogeneity in patients with mosaic variegated aneuploidy: delineation of clinical subtypes. *Am. J. Med. Genet. A.* 146A, 1687–95 (2008).
26. L. PAPI, E. MONTALI, G. MARCONI, R. GUZZELLI, U. BIGOZZI, P. MARASCHIO, O. ZUFFARDI, Evidence for a human mitotic mutant with pleiotropic effect. *Ann. Hum. Genet.* 53, 243–248 (1989).
27. K. Miller, W. Müller, L. Winkler, M. R. Hadam, J. H. H. Ehrich, S. D. Flatz, Mitotic disturbance associated with mosaic aneuploidies. *Hum. Genet.* 84, 361–364 (1990).
28. D. Warburton, K. Anyane-Yeboah, P. Taterka, C. Y. Yu, D. Olsen, Mosaic variegated aneuploidy with microcephaly: a new human mitotic mutant? *Ann. Genet.* 34, 287–292 (1991).
29. T. Kajii, T. Kawai, T. Takumi, H. Misu, O. Mabuchi, Y. Takahashi, M. Tachino, F. Nihei, T. Ikeuchi, Mosaic variegated aneuploidy with multiple congenital abnormalities: homozygosity for total premature chromatid separation trait. *Am. J. Med. Genet.* 78, 245–249 (1998).
30. S. Matsuura, Y. Matsumoto, K. I. Morishima, H. Izumi, H. Matsumoto, E. Ito, K. Tsutsui, J. Kobayashi, H. Tauchi, Y. Kajiwara, S. Hama, K. Kurisu, H. Tahara, M. Oshimura, K. Komatsu, T. Ikeuchi, T. Kajii, Monoallelic BUB1B mutations and defective mitotic-spindle checkpoint in seven families with premature chromatid separation (PCS) syndrome. *Am. J. Med. Genet.* 140 A, 358–367 (2006).
31. H. Ochiai, T. Miyamoto, A. Kanai, K. Hosoba, T. Sakuma, Y. Kudo, K. Asami, A. Ogawa, A. Watanabe, T. Kajii, T. Yamamoto, S. Matsuura, TALEN-mediated single-base-pair editing identification of an intergenic mutation upstream of BUB1B as causative of PCS (MVA) syndrome. *Proc. Natl. Acad. Sci. U. S. A.* 111, 1461–6 (2014).
32. W. L. Flejter, B. Issa, B. a Sullivan, J. C. Carey, a R. Brothman, Variegated aneuploidy in two siblings: phenotype, genotype, CENP-E analysis, and literature review. *Am. J. Med. Genet.* 75, 45–51 (1998).
33. C. Limwongse, S. Schwartz, M. Bocian, N. H. Robin, Child with mosaic variegated aneuploidy and embryonal rhabdomyosarcoma. *Am. J. Med. Genet.* 82, 20–24 (1999).
34. H. Kawame, Y. Sugio, Y. Fuyama, Y. Hayashi, H. Suzuki, K. Kurosawa, K. Maekawa, Syndrome of microcephaly, Dandy-Walker

- malformation, and Wilms tumor caused by mosaic variegated aneuploidy with premature centromere division (PCD): report of a new case and review of the literature. *J. Hum. Genet.* 44, 219–24 (1999).
35. T. Kajii, T. Ikeuchi, Z. Q. Yang, Y. Nakamura, Y. Tsuji, K. Yokomori, M. Kawamura, S. Fukuda, S. Horita, A. Asamoto, Cancer-prone syndrome of mosaic variegated aneuploidy and total premature chromatid separation: report of five infants. *Am. J. Med. Genet.* 104, 57–64 (2001).
 36. S. Matsuura, E. Ito, H. Tauchi, K. Komatsu, T. Ikeuchi, T. Kajii, Chromosomal instability syndrome of total premature chromatid separation with mosaic variegated aneuploidy is defective in mitotic-spindle checkpoint. *Am. J. Hum. Genet.* 67, 483–6 (2000).
 37. S. Jacquemont, M. Bocéno, J. M. Rival, F. Méchinaud, A. David, High risk of malignancy in mosaic variegated aneuploidy syndrome. *Am. J. Med. Genet.* 109, 17–21 (2002).
 38. A. H. Lane, N. Aijaz, P. Galvin-Parton, J. Lanman, R. Mangano, T. a Wilson, Mosaic variegated aneuploidy with growth hormone deficiency and congenital heart defects. *Am. J. Med. Genet.* 110, 273–7 (2002).
 39. C.-P. Chen, C.-C. Lee, W.-L. Chen, W. Wang, C.-Y. Tzen, Prenatal diagnosis of premature centromere division-related mosaic variegated aneuploidy. *Prenat. Diagn.* 24, 19–25 (2004).
 40. M. A. Micale, D. Schran, S. Emch, T. W. Kurczynski, N. Rahman, D. L. Van Dyke, Mosaic variegated aneuploidy without microcephaly: Implications for cytogenetic diagnosis. *Am. J. Med. Genet. Part A.* 143, 1890–1893 (2007).
 41. T. R. Frio, J. Lavoie, N. Hamel, T. Rio Frio, J. Lavoie, N. Hamel, F. Geyer, Y. Kushner, D. Novak, L. Wark, C. Capelli, J. Reis-Filho, S. Mai, T. Pastinen, M. Tischkowitz, V. Marcus, W. D. Foulkes, Homozygous BUB1B mutation and susceptibility to gastrointestinal neoplasia. *N. Engl. J. Med.* 363, 2628–2637 (2010).
 42. L. Pinson, L. Mannini, M. Willems, F. Cucco, N. Sirvent, T. Frebourg, V. Quarantotti, C. Collet, A. Schneider, P. Sarda, D. Geneviève, J. Puechberty, G. Lefort, A. Musio, CEP57 mutation in a girl with mosaic variegated aneuploidy syndrome. *Am. J. Med. Genet. Part A.* 164, 177–181 (2014).
 43. N. Akasaka, J. Tohyama, A. Ogawa, T. Takachi, A. Watanabe, K. Asami, Refractory infantile spasms associated with mosaic variegated aneuploidy syndrome. *Pediatr. Neurol.* 49, 364–7 (2013).
 44. C. H. Cho, M. J. Oh, C. S. Lim, C. K. Lee, Y. Cho, S. Y. Yoon, A case report of a fetus with mosaic autosomal variegated aneuploidies and literature review. *Ann. Clin. Lab. Sci.* 45, 106–109 (2015).
 45. F. Chaker, M. Chihaoui, M. Yazidi, O. Rejeb, H. Slimane, S. Neji, H. Kraoua, Polycystic ovary syndrome: A new phenotype in mosaic variegated aneuploidy syndrome? *Ann. Endocrinol. (Paris).* 78, 58–61 (2017).
 46. M. Kato, T. Kato, E. Hosoba, M. Ohashi, M. Fujisaki, M. Ozaki, M. Yamaguchi, H. Sameshima, H. Kurahashi, PCS/MVA syndrome caused by an Alu insertion in the BUB1B gene. *Hum. Genome Var.* 4, 17021 (2017).
 47. K. Ochiai, A. Yamada, Y. Kimoto, H. Imamura, T. Ikeda, M. Matsukubo, S. Ieiri, H. Moritake, Long-term remission of bilateral Wilms tumors that developed from premature separation of chromatids/mosaic variegated aneuploidy syndrome due to bilateral nephrectomy and peritoneal dialysis. *Pediatr. Blood Cancer.* 66 (2019), doi:10.1002/pbc.27804.
 48. S. Yost, B. de Wolf, S. Hanks, A. Zachariou, C. Marcozzi, M. Clarke, R. M. De Voer, B. Etemad, E. Ujttewaal, E. Ramsay, H. Wylie, A. Elliott, S. Picton, A. Smith, S. Smithson, S. Seal, E. Ruark, G. Houge, J. Pines, G. J. P. L. P. L. Kops, N. Rahman, Biallelic TRIP13 mutations predispose to Wilms tumor and chromosome missegregation. *Nat. Genet.* 49, 1148–1151 (2017).
 49. T. Yamaguchi, M. Yamaguchi, K. Akeno, M. Fujisaki, K. Sumiyoshi, M. Ohashi, H.

- Sameshima, M. Ozaki, M. Kato, T. Kato, E. Hosoba, H. Kurahashi, Prenatal diagnosis of premature chromatid separation/ mosaic variegated aneuploidy (PCS/MVA) syndrome. *J. Obstet. Gynaecol. Res.* 44, 1313–1317 (2018).
50. O. De la Torre-García, R. Mar-Aldama, R. Salgado-Sangri, N. Díaz-Gómez, L. Bonilla-Arcaute, J. Díaz-Ponce-Medrano, R. Guevara-Yañez, E. J. Córdova, T. Monge-Cazares, L. Orozco, A. Martínez-Hernández, A homozygous CEP57 c.915_925dupCAATGTTTCAGC mutation in a patient with mosaic variegated aneuploidy syndrome with rhizomelic shortening in the upper and lower limbs and a narrow thorax. *Eur. J. Med. Genet.* 62, 195–197 (2019).
51. D. S. Brightman, S. Ejaz, A. Dauber, Mosaic variegated aneuploidy syndrome caused by a CEP57 mutation diagnosed by whole exome sequencing. *Clin. Case Reports.* 6, 1531–1534 (2018).
52. H. Tingyan, C. Dong, H. Yanyan, L. Xianze, Y. Jun, Clinical features and genetic analysis of a child with mosaic variegated aneuploidy syndrome. *Chinese J. Med. Genet.* 35, 844–847 (2018).
53. M. Nishitani-Isa, Y. Hiraumi, Y. Nishida, I. Usami, T. Maihara, Rhabdomyosarcoma with premature chromatid separation–mosaic variegated aneuploidy syndrome: Reduced-intensity chemotherapy. *Pediatr. Int.* 61, 613–616 (2019).
54. A. Laberko, D. Balashov, E. Deripapa, O. Soldatkina, E. Raikina, A. Maschan, G. Novichkova, A. Shcherbina, Hematopoietic stem cell transplantation in a patient with type 1 mosaic variegated aneuploidy syndrome. *Orphanet J. Rare Dis.* 14 (2019), doi:10.1186/s13023-019-1073-x.
55. L. Pezzani, L. Pezzoli, A. Pansa, B. Facchinetti, D. Marchetti, A. Scatigno, A. R. Lincesso, L. Perego, M. Pingue, I. Pelliccioli, L. Migliazza, G. Mangili, L. Galletti, U. Giussani, E. Bonanomi, A. Cereda, M. Iascone, Double homozygosity in CEP57 and DYNC2H1 genes detected by WES: Composite or expanded phenotype? *Mol. Genet. Genomic Med.* 8 (2020), doi:10.1002/mgg3.1064.
56. A. Saadi, F. Verny, K. Siquier-Pernet, C. Bole-Feysot, P. Nitschke, A. Munnich, M. Abada-Dendib, M. Chaouch, M. Abramowicz, L. Colleaux, Refining the phenotype associated with CASC5 mutation. *Neurogenetics.* 17, 71–78 (2016).
57. R. M. De Voer, A. Geurts van Kessel, R. D. A. Weren, M. J. L. Ligtenberg, D. Smeets, L. Fu, L. Vreede, E. J. Kamping, E. T. P. Verwiel, M.-M. M. Hahn, M. Ariaans, L. Spruijt, T. van Essen, G. Houge, H. K. Schackert, J. Q. Sheng, H. Venselaar, C. M. a Van Ravenswaaij-Arts, J. H. J. M. Van Krieken, N. Hoogerbrugge, R. P. Kuiper, Germline mutations in the spindle assembly checkpoint genes BUB1 and BUB3 are risk factors for colorectal cancer. *Gastroenterology.* 145, 544–547 (2013).



CONTENTS

2.1 MITOSIS AND MITOTIC SURVEILLANCE MECHANISMS	21
2.2 ANEUPLOIDY AND CHROMOSOMAL INSTABILITY	23
2.3 CONGENITAL KINETOCHORE SYNDROMES	24
2.4 KINETOCHORE PROTEINS AND CANCER	30
2.5 CONCLUSIONS AND FUTURE PERSPECTIVES	32

CHAPTER 2

KINETOCHORE

MALFUNCTION IN HUMAN

PATHOLOGIES

Bas de Wolf and Geert J.P.L. Kops

Cell Division Machinery and Disease, Advances in Experimental Medicine and Biology
2017;1002:69-91

ABSTRACT

The cell cycle culminates in mitosis with the purpose of dividing the cell's DNA content equally over two daughter cells. Error-free segregation relies on correct connections between chromosomes and spindle microtubules. Kinetochores are complex multi-protein assemblies that mediate these connections and are the platforms for attachment-error-correction and spindle assembly checkpoint signaling. Proper kinetochore function is therefore key in preventing aneuploidization. Mutations in genes encoding kinetochore proteins are associated with several severe developmental disorders associated with microcephaly, and kinetochore defects contribute to chromosomal instability in certain cancers. This chapter gives an overview of the processes necessary for faithful chromosome segregation and how kinetochore malfunction causes various human pathologies.

2.1 Mitosis and Mitotic Surveillance Mechanisms

During cell division, accurate chromosome segregation ensures that each daughter cell receives a complete and identical copy of the genetic code, a process that is essential for cell and organismal viability. Chromosome segregation errors result in apoptosis or an abnormal DNA content referred to as aneuploidy (**chapters 1.1 and 2.2**). Aneuploidy, in turn, leads to abnormal gene dosage, causing human conditions such as Down syndrome and Turner syndrome, exposes detrimental recessive mutations, and is associated with cancer (1, 2).

Chromosome segregation is mediated by microtubules that emanate from the spindle poles and attach to chromosomes through large protein complexes, known as kinetochores, that are assembled on centromeric DNA (3). Vital for correct segregation is the stable attachment of each of the sister chromatids to the opposing spindle poles (*amphitelic* attachments), a state called bi-orientation. The initial capture of microtubules by kinetochores is stochastic and individual kinetochores typically bind multiple microtubules (a fully attached HeLa cell kinetochore is bound by approximately 20 microtubules, also known as k-fibers) (4). This frequently results in erroneous attachments configurations such as *merotelly* (one kinetochore bound to microtubules from both spindle poles) or *syntely* (both kinetochores bound to microtubules from the same spindle pole). Such attachments are corrected by the error-correction machinery, orchestrated by the Aurora B kinase (5).

Until proper bi-orientation has been achieved, the lack of stable attachments needs to be communicated to the cell cycle machinery, which cannot be permitted to prematurely initiate chromosome segregation (anaphase) and exit from mitosis. Anaphase and mitotic exit are initiated by the E3 ubiquitin ligase anaphase-promoting complex (APC/C) (6). The surveillance mechanism responsible for this *wait-anaphase* signal is the spindle assembly checkpoint (SAC, also known as the mitotic checkpoint). The SAC is a feedback-control system that monitors kinetochore-microtubule attachments and if needed delays anaphase onset by generating an inhibitor of the APC/C, known as the mitotic checkpoint complex (MCC) (7, 8). Once the last kinetochores achieve stable attachments, inhibitor production is shut down, the APC/C is liberated, and anaphase can ensue.

2.1.1 Kinetochores

Kinetochores are complex, multi-subunit structures that consist of more than a 100 different proteins in human cells, each at up to hundreds of copies per kinetochore. Metazoan and fungal kinetochores are built on specialized centromeric nucleosomes that contain the histone H3 variant CENP-A/ CenH3 (9) (**Figure 1**). These nucleosomes direct assembly of an inner-kinetochore network known as the CCAN (constitutive centromere-associated network) that is composed of 16 'CENP' subunits (CENP-C, CENP-S-X-T-W, CENP-H-I-K-M, CENP-L-N, and CENP-O-P-Q-R- U) (3, 9). CCAN complexes in turn recruit outer kinetochore protein subcomplexes including the KMN network that contains direct microtubule-binding proteins. The KMN network consist of the subcomplexes KNL1-C (KNL1-Zwint1), Mis12-C (Mis12, Dsn1, Nsl1, Pmf1), and NDC80-C (NDC80/HEC1, Nuf2, Spc24, Spc25). The NDC80-C is the main interface of kinetochore-microtubule interactions responsible for load-bearing attachments, with some contributions from the KNL1 protein (10). The MIS12-C is required to properly target NDC80-C and KNL1-C to the kinetochore by connecting them to the CCAN, and enhances their microtubule-binding affinities (11).

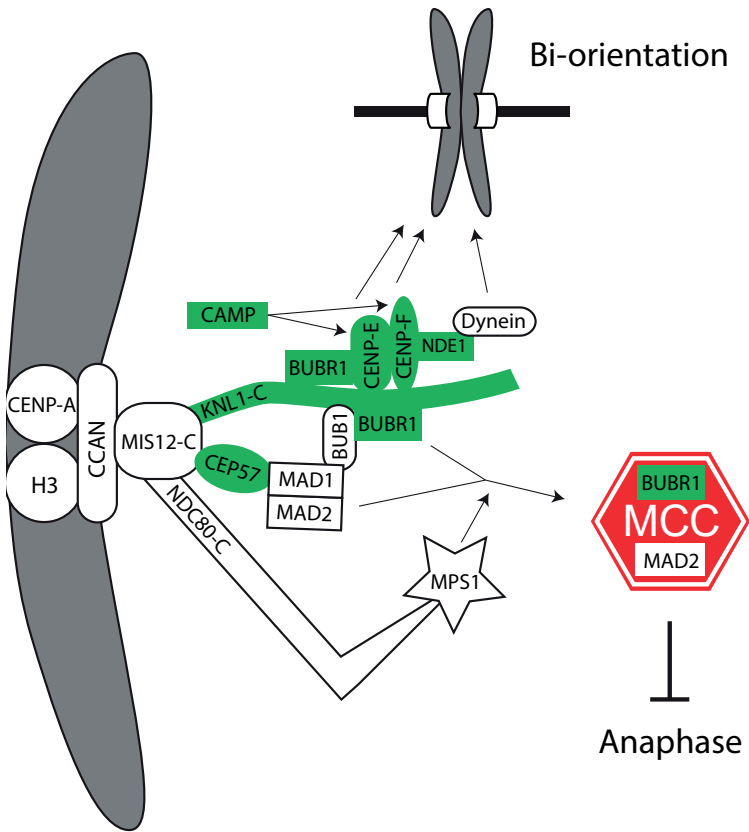


Figure 1. SAC signaling and contributions to chromosome bi-orientation at the kinetochore. At an unattached kinetochore, MPS1 phosphorylation recruits BUB1, BUBR1, MAD1 and MAD2 to the kinetochore and triggers MCC formation. In parallel CAMP, CENP-E, CENP-F and NDE1-Dynein are also recruited to the kinetochore, where they (and BUBR1) contribute to chromosome bi-orientation (*Note*: the interactions that contribute to localization of CAMP, CENP-E and CENP-F are not known). The kinetochore proteins that are associated with disease (as discussed in **chapter 2.3**) are depicted in green.

2.1.2 Error-Correction and the SAC

Kinetochore not only connect to microtubules, but are also the central hubs for integrating error-correction and SAC signaling (7). Aurora B kinase localizes to the inner centromere as a member of the chromosomal passenger complex (CPC) during early mitosis. Its activity weakens the affinity of the kinetochore for microtubules by phosphorylating various members of the KMN network, eventually resulting in release of the kinetochore-microtubule connection (5). When it is unbound by a microtubule, the NDC80-C directly binds MPS1, the master kinase of the SAC (12, 13), which then phosphorylates KNL1 on multiple repeat motifs, forming docking sites for the BUB3-BUB1 heterodimeric kinase complex (8). This MPS1-BUB1 axis is responsible for recruiting a host of other proteins to the kinetochore, including those essential for forming the anaphase inhibitor (BUBR1, MAD1, MAD2, CDC20, RZZ complex), those contributing to stabilization of attachments (e.g. CENP-F,

BUBR1-bound B56-PP2A, and the kinesin motor CENP-E), as well as those responsible for attachment-error- correction (14–19). While forming the anaphase inhibitor does not seem to require BUB1 kinase activity, attachment-error-correction does: BUB1 phosphorylates the C-terminal tail of Histone H2B, allowing binding of adaptor proteins of the Aurora B kinase (20, 21). Once a kinetochore achieves stable attachment to spindle microtubules, the surveillance mechanisms at kinetochores have to be quenched. This occurs by various mechanisms including displacement of MPS1, removal of proteins by the Dynein motor complex, mechanical alteration within kinetochores, and dephosphorylation of kinetochore substrates of MPS1 and Aurora B. These events have been amply covered in various recent reviews and we refer the reader to those for more details (22–25).

2.1.3 Microtubule Motors at Kinetochores

Chromosome movements and stability of kinetochore-microtubule attachments involve kinetochore-localized motor proteins. The plus-end directed kinesin CENP-E, for example, promotes chromosome congression to the spindle equator and contributes to full stability of attachment (26). It is unclear how it localizes to kinetochores, but one of its binding partners there is BUBR1 (27). Kinetochores also bind the minus-end directed motor complex Dynein, where it promotes microtubule attachment, chromosome movement during anaphase, and spindle checkpoint silencing (26, 28). Dynein binds to kinetochores via several receptors, most notably the RZZ-Spindly and the CENPF-NdeL1-Nde1 pathways (28). How these pathways cooperate in ensuring proper Dynein localization and function is currently unclear.

2.2 Aneuploidy and Chromosomal Instability

Defects in any of the kinetochore-related processes can cause whole-chromosome segregation errors in mitosis or meiosis and lead to aneuploid progeny (29). Aneuploidy (a chromosome number that is not an exact multiple of the haploid set) is a hallmark of human cancers, and is a common cause for spontaneous abortions and developmental disorders (2) (see also **chapter 1**). Specific aneuploidies (for instance trisomy or monosomy of a certain chromosome) present throughout the body are referred to as *constitutional* aneuploidies. Such aneuploidies are caused by chromosome segregation errors during germ cell formation in one of the parents (30). A *somatic* aneuploidy, on the other hand, is the result of a mitotic error and is present in only a subset of an individual's cells. Most constitutional aneuploidies cause embryonic lethality, with trisomy 21 (also known as Down Syndrome, MIM 190685) being the most notable exception. The consequences of somatic aneuploidies can also be severe. Losing chromosome X during early embryonic development (monosomy X), for instance, can cause Mosaic Turner Syndrome in women, a milder version of Turner Syndrome which is characterized by short stature and an early loss of ovarian function (31). Another example is Mosaic Variegated Aneuploidy (MVA), which will be more extensively discussed in **chapter 2.3.5**. Other disorders characterized by increased aneuploidy include those with defects in DNA repair mechanisms, such as Ataxia Telangiectasia (MIM 208900) and Nijmegen Breakage Syndrome (MIM 251260) (32), and cohesinopathies, such as Cornelia de Lange Syndrome (MIM 122470), Roberts Syndrome (MIM 268300) and Warsaw Breakage Syndrome (MIM 613398) (33, 34).

Aneuploidy is a result of chromosome segregation errors (see also **chapter 1.2**), and cells prone to missegregate chromosomes (either as a whole or in parts) are referred to as displaying a chromosomal instability (CIN) phenotype. It is important to emphasize that

aneuploidy represents a karyotype state, while CIN refers to the elevated chance of making segregation errors. Down syndrome patient cells are aneuploid but not CIN. While this seems intuitive, CIN is often erroneously inferred from aneuploid karyotypes, most notably in cancer studies.

On a cellular level, CIN and aneuploidy can have numerous effects (see also **chapter 1.3**). Errors in chromosome segregation lead to p53 activation and G1 arrest (35), likely through DNA damage (36) or elevated ROS levels (37). Gains or losses of chromosomes in most cases result in a corresponding change in the expression of both genes located on that chromosome (38), as well as genes on chromosomes other than the aneuploid ones, the latter likely through alteration of transcriptional networks (38, 39). In addition to these chromosome-specific changes, studies of aneuploid yeast, plant, mice and human cells have revealed conserved gene expression responses to the aneuploid state, most notably those related to cell growth, proliferation, nucleic acid metabolism, and stress responses (40). Strikingly, complex aneuploidies elicit the same transcriptional changes as a trisomy (41). This all ties in with an aneuploidy-induced proteotoxic stress response that is caused by limitations in protein folding and protein turnover, leading to an accumulation of unfolded and misfolded proteins (42). All in all, aneuploidy usually results in reduced proliferation.

On top of whole-chromosome aneuploidy, chromosome segregation errors can cause additional genomic insults, depending on the type of error made. For example, chromosomes that lag behind in anaphase or that end up in micronuclei can acquire extensive DNA damage by various mechanisms, including cytokinesis-induced double-strand breaks and incomplete replication (36, 43). The results can be devastating: unbalanced translocations and even chromosome shattering, also known as chromothripsis (36, 44, 45). Errors in cell division can therefore lead to whole-chromosomal aneuploidy as well as structural aneuploidy, and may thus be at the root of complex genomic alterations in some cancers and congenital diseases (46, 47).

Given these various far-reaching adverse effects, it is not surprising that aneuploid cells are rare in healthy tissues. Recent single-cell sequencing efforts have shown that the prevalence of aneuploid cells in healthy skin, liver and brain tissue is less than 5% (48, 49). It is unknown if this is due to very high fidelity of the chromosome segregation process throughout all phases of development and in our adult stem cell populations, or whether aneuploid cells are cleared efficiently, as recently shown in a CIN mouse model (50).

2.3 Congenital Kinetochore Syndromes

Mutations in the kinetochore genes *KNL1*, *CENP-E*, *CENP-F*, *NDE1*, *CHAMP1*, *BUB1B*, and *CEP57* (**Figure 1, Table 1**) are associated with various congenital diseases. Each of these syndromes is described in more detail below. Strikingly, a common characteristic of patients carrying these mutations is microcephaly: a condition in which the brain does not develop properly resulting in a smaller than normal head circumference. This seems to be a common outcome of mutations in components of mitotic structures (centrosomes, spindle, kinetochores). The molecular details behind this causal relationship are unknown, but a leading hypothesis is related to the neural stem cells, the cells that generate the various differentiated lineages in the brain, including neurons. Asymmetric divisions of these stem cells by spindle mispositioning, or aneuploidy by chromosome segregation errors can cause neural stem cell death and depletion of the stem cell pool (51, 52). In support of

this, *Drosophila* brains developed to a smaller size when aneuploidy was introduced in the neural stem cells (53). A plausible scenario therefore is that kinetochore gene mutations cause microcephaly by aneuploidy-induced clearance of a fraction of the brain stem cells.

Of note: mutations in *SGO1* (a centromere and kinetochore protein important for sister-chromatid cohesion) are known to cause CAID syndrome (MIM 616201), a disorder characterized by chronic atrial and intestinal dysrhythmia (54). However, since the patient mutations do not seem to affect kinetochore function, we have not included this disorder in the following discussion.

2.3.1 Primary Microcephaly (MCPH): *CASC5/KNL1* and *CENP-E*

Autosomal recessive primary microcephaly (MCPH, MIM 251200) is a disorder characterized by an unusually small head circumference, intellectual disability, and in some cases mild facial dysmorphism and/or short stature. 16 loci are associated with MCPH; these include many genes that are important for proper cell division, such as those implicated in centrosome biogenesis and mitotic spindle assembly, as well as proteins that affect neuronal migration, DNA replication and the DNA damage response. Two of the 16 loci are genes encoding the kinetochore proteins CENP-E and *CASC5/KNL1* (see below).

Mutations in *CASC5/KNL1* (hereafter named *KNL1*) are associated with the microcephaly variant syndrome MCPH4 (MIM 604321) (Table 1). MCPH4 patients exhibit mild to severe cognitive impairment, normal to short stature, and in some cases some dysmorphic features. *KNL1* (kinetochore null 1) is a large, multifunctional kinetochore scaffold protein (11) that, together with *Zwint1*, forms the *KNL1-C*, a part of the *KMN* network. *KNL1* is involved in the formation of kinetochore-microtubule attachments and SAC signaling among others by providing docking sites for the *BUB1* and *BUBR1* proteins (11). In experimental systems, penetrant depletion of *KNL1* induces chromosome misalignment and premature mitotic exit, causing chromosome segregation errors and thus aneuploidy (72–74).

Table 1. Kinetochore gene mutations and associated disorders

Gene	Mutations	Disorder	Refs
<i>CASC5/KNL1</i>	c.6125G>A; p.M2041I c.6673-19T>A; p.M2225Ifs*7	MCPH4	(55–58)
<i>CENP-E</i>	c.2797G>A;p.D933N c.4063A>G;p.K1355E	MCPH13	(59)
<i>CENP-F</i>	c.165_193del; p.N57Kfs*11 c.574-2A>C c.1744G>T; p.E582* c.2734G>T; p.E912X c.8692C>T; p.R2898* c.9280C>T; p.R3094*	Strømme syndrome	(60–62)
<i>NDE1</i>	c.-43-3548_83+622del c.83+1G>T; p.A29Qfs*114 c.684_685delAC; p.P229Wfs*85 c.733dup; p.L245Pfs*70	Microhydranencephaly Microlissencephaly	(63) (64, 65)

Gene	Mutations	Disorder	Refs
<i>CHAMP1</i>	c.635delC; p.P212Lfs*7 c.1192C>T; R398* c.1768C>T; p.Q590* c.1866_1867delCA; p.D622Efs*8	Mental retardation-40	(66, 67)
<i>BUB1B</i>	c.107G>A; p.R36Q c.580C>T; p.R194* c.670C>T; p.R224X c.IVS10-1G>T; p.Q467fs*483 c.IVS10-5A>G; W468fs*480 c.1649G>A; p.R550Q c.1833delT; p.F611fs*625 c.2211-2insGTTA; p.S738fs*753 c.2441G>A; p.R814H c.2530C>T; p.L844F c.2726T>C; p.I909T c.2763G>C; Q921H c.3035T>C; p.L1012P 6G3 haplotype	MVA	(68, 69)
<i>CEP57</i>	c.241C>T; p.R81* c.520_521delGA; p.E174Tfs*4 c.915_925dup11; p.L309Pfs*9	MVA	(70, 71)

c coding DNA sequence, p protein sequence

All MCPH4 patients carry homozygous *KNL1* mutations that lead to incidental skipping of exon 18 or 25, resulting in a frameshift and subsequent truncation of the protein (**Table 1**). The mutation that causes incidental skipping of exon 18 also causes a M2041I substitution (in both full length and truncated protein), located in the Zwint1 interaction motif. Nevertheless, the mutation had no significant effect on total *KNL1* levels, and, though conclusive live cell imaging data is lacking, quantification of micronuclei suggested that chromosome segregation fidelity was not substantially affected, at least in the lymphoblastoid cell lines analyzed (58). Possibly therefore, the effect of this mutation reveals itself only in brain tissue. On the other hand, skipping of exon 25 resulted in a reduction of total *KNL1* levels to about 50% of the controls. In fibroblast and lymphoblastoid cells derived from these patients, mitotic delays, increased micronuclei and an abnormal DNA damage response were observed (56, 55). The latter could be a novel function of *KNL1* or could be related to damage caused by mitotic segregation errors (36, 43).

Mutations in *CENPE* caused MCPH13 (MIM 616051) in two siblings. Both exhibited profound short stature and microcephaly (also known as microcephalic primordial dwarfism) associated with developmental delay, simplified gyri and other isolated abnormalities. In both patients compound heterozygous point mutations were identified (D993N and K1355E, in the central coiled-coil region; **Table 1**) which did not adversely affect CENP-E (centromere protein E) protein expression or stability (59).

CENP-E is a microtubule plus-end-directed motor protein required for proper kinetochore-microtubule attachments and the congression of chromosomes to the spindle equator (75, 76). Experimental depletion of CENP-E impairs kinetochore-microtubule attachment,

slows chromosome congression, and consequently prolongs mitosis. CENP-E also affects centrosome stability as their fragmentation increases upon CENP-E knockdown (27). Patient mitotic lymphocytes displayed reduced kinetochore levels of mutant CENP-E, which correlated with substantial spindle multipolarity, chromosome segregation errors and micronuclei (59).

2.3.2 Strømme Syndrome: *CENP-F*

Strømme syndrome (MIM 243605) is characterized by microcephaly, and affects multiple systems with features of a ciliopathy (a disorder characterized by defects in the microtubule/membrane-based protrusions known as cilia that mediate cell motility and transduce sensory information (77)). Affected individuals suffer from microcephaly, intestinal atresia (absence of part of the intestine), variable ocular abnormalities, and occasionally defects in other systems, such as the kidneys and heart. The causative mutations were found to reside in the *CENP-F* gene (Table 1), which severely affected protein expression (62, 61).

CENP-F (centromere protein F) is a large coiled-coil protein with two unusual microtubule-binding domains that it uses for multiple processes in mitosis. CENP-F couples mitochondria to polymerizing microtubules to allow for their segregation during mitosis (78), and it enables kinetochores to remain bound to shortening microtubules during anaphase (79). Besides binding microtubules, CENP-F plays a role in the recruitment of the two kinetochore motors Dynein (via NDE1) and CENP-E (80) that mediate correct kinetochore-microtubule attachment and chromosome alignment. Depletion of CENP-F also results in premature chromatid separation, suggesting a role in the protection of sister-chromatid cohesion (17). Finally, CENP-F is required for ciliogenesis, possibly by targeting IFT88 to the ciliary axoneme (62). No cell biological analyses were performed on cells derived from the patients, so it is unknown which processes are affected in the patients. Nevertheless, they may suffer from a combination of cellular defects that together cause the wide array of symptoms observed in these patients.

2.3.3 Microhydranencephaly and Microlissencephaly: *NDE1*

Eleven patients in five families were diagnosed with microhydranencephaly or microlissencephaly. Microhydranencephaly (MIM 605013) is a disorder in which microcephaly is associated with severe hydranencephaly (where missing parts of brain hemispheres are filled with fluid, causing enlarged head size, also known as hydrocephalus). In microlissencephaly (MIM 614019), microcephaly is associated with lissencephaly (where brain folds and grooves are underdeveloped). All patients have homozygous truncating mutations in the *NDE1* gene that result in the expression of an unstable protein.

NDE1 (NudE neurodevelopment protein 1) is an adaptor protein of the Dynein microtubule motor complex. NDE1 is found on centrosomes and the nuclear envelope (NE) in interphase, where it ensures NE-centrosome anchoring, which is necessary for proper spindle formation. In mitosis, it is found on kinetochores, where it interacts with CENP-F, the protein mutated in Strømme syndrome (chapter 2.3.2), to enable Dynein recruitment. Depletion of NDE1 leads to an increase in chromosomes that are incorrectly attached to the mitotic spindle, causing a significant increase in chromosome segregation errors (80). Interestingly, NDE1 was reported to be a negative regulator of ciliogenesis (81). The unstable, truncated NDE1 proteins expressed in the 11 patients lack the domains responsible for the interactions with both CENP-F and Dynein (Table 1) (64, 82, 65). NDE1 malfunction in patient cells may thus

lead to mitotic defects as well as impairment of (interphasic) Dynein function. The latter inhibits neuronal migration, a likely cause for lissencephaly (83).

2.3.4 Mental Retardation-40: *CHAMP1*

Autosomal dominant mental retardation-40 (MRD40, MIM 616579) disorder is characterized by intellectual disability, global developmental delay and dysmorphic facial features, as well as microcephaly (84, 85, 67). All patients carried heterozygous truncating mutations in the *CHAMP1* gene, which encodes the CAMP protein (Table 1).

Relatively little is known about the function of CAMP (chromosome alignment maintaining phosphoprotein). It localizes to chromosomes, the mitotic spindle and kinetochores. CAMP binds MAD2L2 (MAD2B/hRev7), a protein involved in regulating mitotic entry and DNA repair at telomeres (86). CAMP is also required for the kinetochore localization of CENP-E and CENP-F, though direct interactions have not been observed (86). Knockdown of CAMP results in abnormal spindle formation and chromosome alignment defects, possibly by misregulation of CENP-E and CENP-F (86). This role of CAMP may further involve Aurora B activation, as CAMP interacts with HP1 (Heterochromatin protein 1) and POGZ (POGO transposable element with ZNF domain), both of which impact Aurora B localization and sister chromatid cohesion (87, 88). The *CHAMP1* mutations in MRD40 patients affected transcript level, and the resulting protein lacks the domains necessary for its localization to chromosomes and the mitotic spindle as well as its interaction with POGZ and HP1 (84). Intriguingly, loss-of-function mutations in *POGZ* have been identified in individuals affected by neurodevelopmental disorders with a similar phenotype (intellectual disability, microcephaly) (89). Loss of the POGZ-CAMP interaction and misregulation of CENP-E and CENP-F function (both associated with microcephaly syndromes, see chapters 2.3.1 and chapter 2.3.2) may thus be key molecular causes of MRD40.

2.3.5 Mosaic Variegated Aneuploidy: *BUB1B* and *CEP57*

Mosaic Variegated Aneuploidy syndrome (MVA, MIM 257300) is a rare autosomal recessive disorder characterized by aneuploidies (predominantly trisomies and monosomies) of mostly random chromosomes in different tissues. Although the proportion of aneuploid cells usually is more than 25%, there does not seem to be a correlation between the clinical phenotype and the observed karyotypes (90). MVA patients usually suffer from intrauterine growth retardation and microcephaly. Eye anomalies, mild dysmorphism, variable developmental delay, and a broad spectrum of additional congenital abnormalities and medical conditions are also frequently part of the MVA phenotype (see also Addendum Table 1). Furthermore, a subset of MVA patients has developed childhood cancers such as Wilms tumor, rhabdomyosarcoma, and leukemia (68). To date, pathogenic mutations in two genes have been identified in MVA patients: *BUB1B* and *CEP57* (Table 1), both of which are associated with the kinetochore (91, 71). The phenotypes associated with *BUB1B* and *CEP57* mutations are broadly similar, although only *BUB1B* mutations are strongly associated with cancer. Aneuploidy seems the most likely culprit causing the symptoms, but MVA has also been suggested to be a ciliopathy (92) or a progeria (premature ageing) syndrome (93).

BUB1B (BUB1 mitotic checkpoint serine/threonine kinase B) encodes BUBR1, a multi-domain pseudokinase implicated in various, mostly mitotic processes. BUBR1 localizes to mitotic kinetochores via KNL1 and binds CENP-E, the genes mutated in MCPH4/13 (chapter 2.3.1).

BUBR1 is required for SAC signaling by directly inhibiting APC/C. It also promotes stable kinetochore-microtubule attachments through direct binding of the B56-PP2A phosphatase (18). In interphase, BUBR1 is thought to prevent inappropriate centrosome amplification (94) and to positively regulate ciliogenesis through the suppression of disheveled (DVL), canonical Wnt-activation and cell cycle progression (92). *BUB1B* mutations in MVA result in low protein expression, which is the primary molecular cause of BUBR1 malfunction (95). The low expression is due to either biallelic combinations of a truncating mutation that leads to RNA decay with a missense mutation that destabilizes the protein, to a combination of two missense mutations that destabilize the protein, or to one truncating mutation together with a haplotype that is associated with low BUBR1 expression. All mutations analyzed impair SAC function and chromosome alignment (95). Furthermore, cells derived from patients with *BUB1B* mutations displayed centrosome amplification and multipolar mitoses as well as impaired ciliogenesis (92, 94).

CEP57 (centrosomal protein 57) was initially identified as an intracellular transporter of fibroblast growth factor 2 (96), but has recently acquired more attention for its roles at centrosomes and kinetochores. CEP57 binds and stabilizes microtubules and thereby promotes spindle assembly, spindle pole integrity and central spindle organization (97). At kinetochores, CEP57 promotes SAC signaling, although it is not absolutely required for it. It does so by binding the KMN network member MIS12 and functioning as a scaffold for MAD1- MAD2 (98). The MVA-associated mutations in *CEP57* are homozygous truncating mutations (71). It is unknown whether they affect protein expression, though it is very likely that its microtubule-binding capacity is impaired. Unfortunately, functional assays on cells derived from these patients have not been performed so it is currently unknown if the cellular defects of *CEP57* mutant cells are similar to those of *BUB1B* patient cells.

2.3.6 Kinetochore Mutations in Microcephaly Syndromes: One Common Pathway?

Strikingly, all proteins mutated in the congenital syndromes discussed above have been functionally linked in various studies (Figure 2). CENP-E depends on KNL1, CAMP and CENP-F for its kinetochore recruitment and is known to interact with BUBR1. CENP-F likewise depends on KNL1 and CAMP for its localization and, in turn, recruits NDE1 to the kinetochore. A common molecular defect in almost all kinetochore syndromes (with the exception of CEP57) may therefore be malfunction of the kinetochore motor proteins CENP-E and Dynein (via CENP-F and NDE1), both of which promote kinetochore-microtubule attachments and chromosome bi-orientation. With the caveat of relatively low number of patients, this begs the question if there is a particular reason why this pathway as opposed to others involved in similar kinetochore functions is found more frequently mutated. Mutation in components of this pathway may simply result in a 'just right' level of aneuploidy that causes disease without early embryonic death, while mutations in components of other pathways do not. Alternatively, there is a functional difference between this pathway and others, for example impacting spindle assembly or cilia function, in addition to aneuploidization. Organismal studies of these and other mutations will be required to answer this question.

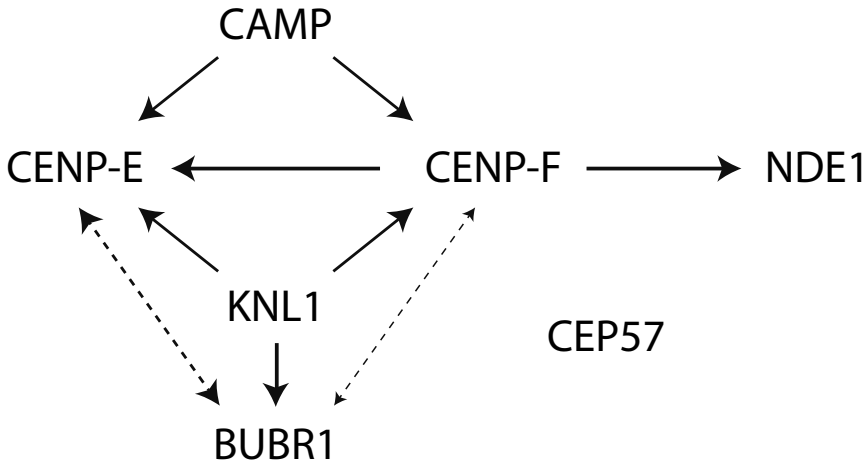


Figure 2. Model showing dependencies of kinetochore localization of disease-associated kinetochore proteins. *Dotted arrows* connecting CENP-E and BUBR1 signify a direct interaction (exact contributions to localization are unknown) (27). Thin *dotted arrows* connecting CENP-F and BUBR1 signify interaction found in a yeast two-hybrid screen (direct interaction has not been observed) (99).

2.4 Kinetochore Proteins and Cancer

One of the hallmarks of cancer is the presence of highly abnormal karyotypes that are characterized by structural and numerical aneuploidies. Over 90% of solid tumors and 50% of blood tumors is aneuploid, with a quarter of the genome of a typical cancer cell affected by either whole-arm or whole-chromosome copy number alterations (100, 101). Aneuploidy may signal ongoing CIN, which is thought to contribute to tumorigenesis, tumor progression, and the development of therapy resistance (102). Several mechanisms contribute to CIN in laboratory cancer cell lines, including replication stress (103), centrosome amplification (104), chromatid cohesion loss (88), increased spindle microtubule dynamics (105), impaired SAC signaling (106), and erroneous kinetochore-microtubule attachments (107–109). Those related to kinetochore functions are discussed below.

2.4.1 Premature Sister Chromatid Separation (PSCS)

Impaired SAC signaling and cohesion loss have in common that both defects lead to premature separation of the sister chromatids. Experimental reduction of SAC protein expression in mice has not lead to conclusive insight into a potential role of SAC defects in cancer. Whereas some models develop benign tumors late in life in specific tissues, others suffer from earlier and more widespread tumor formation, and yet others do not develop tumors at all or only with carcinogen challenges (110). The actual levels of CIN and the sensitivity of particular tissues to those levels may explain the differences between animal models. Although SAC defects can cause cancer, they may not be a common cause of tumor formation in humans. SAC defects do not appear to be a common characteristic of laboratory CIN cancer cells (111) and with the possible exception of MAD2 in gastric tumors (112), mutations in kinetochore genes are a rare occurrence (29, 113). Moreover, though numerous studies have reported the deregulation of SAC gene expression in different types of cancer, there is no consistency between reports, and some reported overexpressions

may reflect a general activation of the cell division machinery (114).

Sister chromatids are held together by ring-shaped cohesin protein complexes. The majority of cohesin complexes are removed from the DNA, but centromeric cohesin is protected from removal by members of the inner centromere–shugoshin (ICS) network until anaphase is initiated (115). Premature cohesin removal in cancer cells has been reported to occur at two levels. First, STAG2, a component of the cohesin ring, is mutated frequently in cancers (116). Targeted correction of the mutant alleles of *STAG2* led to reduced cohesion defects and enhanced chromosomal stability (117). Second, a recent study found that ICS network impairment is a cause for CIN in various laboratory cancer cell lines derived from lung, colon, skin and bone tissues (88). Mutations in components of the ICS network (*BUB1*, *SGO1*, *CPC*) are rare in human cancers (118), but misregulation of the network at other levels may occur.

2.4.2 Persistence of Erroneous Kinetochore-Microtubule Attachments

The type of segregation error most frequently seen in laboratory cancer cell lines is lagging of chromosomes, most likely the result of a merotelic attachment state (119). Merotelically can be caused by various means, including altered microtubule dynamics. Measurements of kinetochore-microtubule attachment turnover rates revealed that attachments were generally more stable in CIN cancer cell lines than in those that are non-cancerous and genetically stable. Reducing k-fiber stability in the CIN cells was sufficient to restore chromosomal stability (105). K-fiber stability is regulated by various processes, including Aurora B-dependent regulation of the microtubule-binding protein NDC80/HEC1 and the microtubule depolymerase MCAK (5). Genes such as *AURKB* and *MCAK* are rarely mutated or inactivated in human cancer (118), but deregulated genes may indirectly promote attachment stability. HEC1, for instance, is frequently overexpressed in human cancer, as is *MAD2*, which, instead of mediating hyper-activity of the SAC, was found to hyperstabilize kinetochore-microtubule attachments (120). However, as mentioned in **chapter 2.4.1** it is worth to keep in mind that some reported overexpressions may reflect a general activation of the cell division machinery rather than a specific selection for over-expression of the gene in question (114). Finally, the deregulation of the ICS network deregulates Aurora B localization to inner centromeres, possibly affecting k-fiber stability. Another means to achieve merotelicity is the presence of supernumerary centrosomes that cause transient multipolar spindles which are enriched for merotelic attachments (121, 122). Late centrosome clustering then bipolarizes the spindle but does not resolve some of the merotelic attachments. Centrosome amplification has been shown to occur frequently in tumors and has a strong correlation with CIN (108).

In colorectal cancer cell lines, attachment errors and lagging chromosomes appear to be caused by an increase in microtubule plus end assembly rates (123). This mechanism has similarities to merotelicity caused by centrosome amplification as it also triggers transient spindle geometry abnormalities that facilitate the generation of erroneous kinetochore attachments. It seems likely that increased assembly rates involve altered kinetochore function, but it is unclear if this is the case and what the mechanism is.

2.4.3 Tumor-Suppressor Loss and Kinetochore Function

Altered expression of kinetochore proteins rather than mutations may be a more common

mechanism for CIN in tumor cells. Recent studies have implied various transcriptional and post-transcriptional alterations due to loss of tumor suppressor genes as a potential cause for this. Mutations in *BRCA2* predispose to breast cancer (124) as well as cancers in the ovary and pancreas (125). One of its many functions is the recruitment of P/CAF acetyltransferase to BUBR1 at the kinetochore, which facilitates BUBR1 acetylation and protects it from proteasomal degradation. *BRCA2*-deficient cells exhibit lower BUBR1 levels and impaired SAC signaling (126). Inhibition of the *BRCA2*-BUBR1 interaction in mice led to spontaneous tumorigenesis (126, 127). In another example, mutations in *TP53* or *RB1* increase *MAD2* expression, leading to hyperstabilization of kinetochore-microtubule attachments (128). This is mediated by the transcription factor E2F, which is inhibited by Rb, as well as indirectly by p53. *MAD2* upregulation is required for CIN in mutant *TP53* and *RB1* cancer mouse models (129, 130). Conversely, *MAD2* expression is also downregulated in certain types of cancer, for instance in neuro- and medulloblastomas. In these tumors, the *repressor-element-1-silencing transcription factor (REST)* is frequently overexpressed, which negatively regulates *MAD2* levels (131).

Finally, the tumor suppressor APC, inactivated in most colorectal tumors, localizes to kinetochores in mouse embryonic stem cells, where it ensures proper spindle assembly and k-fiber stability (132). Whether there is a role for APC mutations in CIN in human cancers is debatable, as APC loss in human intestinal organoid cultures did not cause substantial CIN (133).

2.5 Conclusions and Future Perspectives

Recent next generation sequencing approaches have significantly contributed to the rapid discovery of mutations in many new genes associated with a wide variety of diseases. This has resulted in an increasingly longer list of mutated kinetochore genes, especially in congenital neurodevelopmental disorders. Although the mechanistic relation between the mutations and the disorders is unknown in all cases, most affected genes control chromosome bi-orientation, spindle assembly, or both. Consistent with this idea, many of the MCPH-associated genes encode centrosome-associated proteins (134), raising the possibility that spindle assembly defects are the common denominator of the microcephaly-causing gene mutations. Mosaic Variegated Aneuploidy and Strømme Syndrome are characterized by a much wider variety of symptoms than the other mentioned disorders. Both have been suggested to be ciliopathies, and it will be of interest to further investigate whether ciliary defects are common in these patients and whether this contributes to their symptoms. Aneuploidy-induced senescence may also contribute to the different disease phenotypes, and may explain some of the progeroid-like symptoms of MVA patients (135). We expect that the discovery of disease-associated mutations will continue to expand rapidly over the coming years. It will be interesting to see whether mutations in kinetochore genes continue to converge in certain functional pathways and whether they contribute to diseases other than neurodevelopmental disorders.

A major unanswered question is how kinetochore defects contribute to cancer. CIN seems the most parsimonious explanation, but there is currently a discrepancy between levels of CIN/aneuploidy in models of kinetochore malfunction and the extent of tumor development/progression. An animal model in which CIN can be conditionally induced to various levels and monitoring CIN in the relevant tissues will be crucial in addressing this conundrum. Finally, it is not understood why, given the widespread occurrence of

aneuploidy in human cancers, mutations in kinetochore components are rarely found in cancer genomes. We speculate that such mutations do occur but are either neutral or purged as a result of causing too much aneuploidy. Loss of a single allele of kinetochore proteins in mice is generally well tolerated while loss of both causes early embryonic death (136). A level of aneuploidy that eventually is beneficial to tumor cells may thus be more easily attainable by other mechanisms, including altered expression levels, for example by mutating transcriptional regulators. Whether this is true awaits identification of the molecular causes of CIN in human cancers.

REFERENCES

1. J. J. Siegel, A. Amon, New insights into the troubles of aneuploidy. *Annu. Rev. Cell Dev. Biol.* 28, 189–214 (2012).
2. R. M. Ricke, J. M. van Deursen, Aneuploidy in health, disease, and aging. *J. Cell Biol.* 201, 11–21 (2013).
3. I. M. Cheeseman, The Kinetochore. *Cold Spring Harb. Perspect. Biol.* 6, 1063–1072 (2014).
4. K. L. Wendell, L. Wilson, M. a. Jordan, Mitotic block in HeLa cells by vinblastine: ultrastructural changes in kinetochore-microtubule attachment and in centrosomes. *J. Cell Sci.* 104, 261–274 (1993).
5. M. Carmena, M. Wheelock, H. Funabiki, W. C. Earnshaw, The chromosomal passenger complex (CPC): from easy rider to the godfather of mitosis. *Nat. Rev. Mol. Cell Biol.* 13, 789–803 (2012).
6. I. Primorac, A. Musacchio, Panta rhei: The APC/C at steady state. *J. Cell Biol.* 201 (2013), pp. 177–189.
7. C. Sacristan, G. J. P. L. Kops, Joined at the hip: Kinetochores, microtubules, and spindle assembly checkpoint signaling. *Trends Cell Biol.* 25, 21–28 (2015).
8. N. London, S. Biggins, Signalling dynamics in the spindle checkpoint response. *Nat. Rev. Mol. Cell Biol.* 15, 736–47 (2014).
9. K. L. McKinley, I. M. Cheeseman, The molecular basis for centromere identity and function. *Nat Rev Mol Cell Biol.* 17, 16–29 (2016).
10. D. Varma, E. D. Salmon, The KMN protein network—chief conductors of the kinetochore orchestra. *J. Cell Sci.* 125, 5927–36 (2012).
11. G. V. Caldas, J. G. DeLuca, KNL1: Bringing order to the kinetochore. *Chromosoma.* 123, 169–181 (2014).
12. Y. Hiruma, C. Sacristan, S. T. Pachis, A. Adamopoulos, T. Kuijt, M. Ubbink, E. von Castelmur, A. Perrakis, G. J. P. L. Kops, CELL DIVISION CYCLE. Competition between MPS1 and microtubules at kinetochores regulates spindle checkpoint signaling. *Science.* 348, 1264–7 (2015).
13. Z. Ji, H. Gao, H. Yu, Kinetochore attachment sensed by competitive Mps1 and microtubule binding to NDC80C. *Science (80-)*. 348, 1260–1264 (2015).
14. M. Vleugel, T. A. Hoek, E. Tromer, T. Sliedrecht, V. Groenewold, M. Omerzu, G. J. Kops, Dissecting the roles of human BUB1 in the spindle assembly checkpoint. *J Cell Sci.* 128, 2975–2982 (2015).
15. G. Zhang, T. Lischetti, D. G. Hayward, J. Nilsson, Distinct domains in Bub1 localize RZZ and BubR1 to kinetochores to regulate the checkpoint. *Nat. Commun.* 6, 7162 (2015).
16. V. L. Johnson, M. I. F. Scott, S. V Holt, D. Hussein, S. S. Taylor, Bub1 is required for kinetochore localization of BubR1, Cenp-E, Cenp-F and Mad2, and chromosome congression. *J. Cell Sci.* 117, 1577–1589 (2004).
17. S. V Holt, M. a S. Vergnolle, D. Hussein, M. J. Wozniak, V. J. Allan, S. S. Taylor, Silencing Cenp-F weakens centromeric cohesion, prevents chromosome alignment and activates the spindle checkpoint. *J. Cell Sci.* 118, 4889–900 (2005).
18. S. J. E. Suijkerbuijk, M. Vleugel, A. Teixeira, G. J. P. L. Kops, Integration of Kinase and Phosphatase Activities by BUBR1 Ensures Formation of Stable Kinetochore-Microtubule Attachments. *Dev. Cell.* 23, 745–755 (2012).
19. T. Akera, Y. Goto, M. Sato, M. Yamamoto, Y. Watanabe, Mad1 promotes chromosome congression by anchoring a kinesin motor to the kinetochore. *Nat. Cell Biol.* 17, 1124–33 (2015).
20. S. A. Kawashima, Y. Yamagishi, T. Honda, K. Ishiguro, Y. Watanabe, Phosphorylation of H2A by Bub1 prevents chromosomal instability through localizing shugoshin. *Sci.*

- (New York, NY). 327, 172–177 (2010).
21. Y. Yamagishi, T. Honda, Y. Tanno, Y. Watanabe, Two histone marks establish the inner centromere and chromosome bi-orientation. *Science* (80-.). 330, 239–243 (2010).
 22. G. J. P. L. Kops, J. V. Shah, Connecting up and clearing out: how kinetochore attachment silences the spindle assembly checkpoint. *Chromosoma*. 121 (2012), pp. 509–525.
 23. H. Funabiki, D. J. Wynne, Making an effective switch at the kinetochore by phosphorylation and dephosphorylation. *Chromosoma*. 122 (2013), pp. 135–158.
 24. E. a Foley, T. M. Kapoor, Microtubule attachment and spindle assembly checkpoint signalling at the kinetochore. *Nat. Rev. Mol. Cell Biol.* 14, 25–37 (2013).
 25. B. Etemad, G. J. P. L. Kops, Attachment issues: Kinetochore transformations and spindle checkpoint silencing. *Curr. Opin. Cell Biol.* 39, 101–108 (2016).
 26. G. J. P. L. Kops, A. T. Saurin, P. Meraldi, Finding the middle ground: How kinetochores power chromosome congression. *Cell. Mol. Life Sci.* 67 (2010), pp. 2145–2161.
 27. X. Yao, a Abrieu, Y. Zheng, K. F. Sullivan, D. W. Cleveland, CENP-E forms a link between attachment of spindle microtubules to kinetochores and the mitotic checkpoint. *Nat. Cell Biol.* 2, 484–491 (2000).
 28. J. R. Bader, K. T. Vaughan, Dynein at the kinetochore: Timing, Interactions and Functions. *Semin. Cell Dev. Biol.* 21 (2010), pp. 269–275.
 29. S. L. Thompson, S. F. Bakhoum, D. A. Compton, Mechanisms of Chromosomal Instability. *Curr. Biol.* 20 (2010).
 30. T. Hassold, P. Hunt, To err (meiotically) is human: the genesis of human aneuploidy. *Nat. Rev. Genet.* 2, 280–291 (2001).
 31. Al Alwan I, M K, Amir, et al., Turner Syndrome Genotype and phenotype and their effect on presenting features and timing of Diagnosis. *Int. J. Health Sci. (Qassim)*. 8, 195–202 (2014).
 32. J. Knoch, Y. Kamenisch, C. Kubisch, M. Berneburg, Rare hereditary diseases with defects in DNA-repair. *Eur. J. Dermatology*. 22, 443–455 (2012).
 33. F. Cucco, A. Musio, Genome stability: What we have learned from cohesinopathies. *Am. J. Med. Genet. Part C Semin. Med. Genet.* 172 (2016), pp. 171–178.
 34. M. Zakari, K. Yuen, J. L. Gerton, Etiology and pathogenesis of the cohesinopathies. *Wiley Interdiscip. Rev. Dev. Biol.* 4, 489–504 (2015).
 35. S. L. Thompson, D. A. Compton, Proliferation of aneuploid human cells is limited by a p53-dependent mechanism. *J. Cell Biol.* 188, 369–381 (2010).
 36. A. Janssen, M. Van Der Burg, K. Szuhai, G. J. P. L. Kops, R. H. Medema, Chromosome segregation errors as a cause of DNA damage and structural chromosome aberrations. *Science* (80-.). 333, 1895–1898 (2011).
 37. M. Li, X. Fang, D. J. Baker, L. Guo, X. Gao, Z. Wei, S. Han, J. M. van Deursen, P. Zhang, The ATM-p53 pathway suppresses aneuploidy-induced tumorigenesis. *Proc. Natl. Acad. Sci. U. S. A.* 107, 14188–93 (2010).
 38. S. Stingele et al., Global analysis of genome, transcriptome and proteome reveals the response to aneuploidy in human cells. *Mol. Syst. Biol.* 8, 608 (2012).
 39. M. B. Upender, J. K. Habermann, L. M. McShane, E. L. Korn, J. C. Barrett, M. J. Diflippantonio, T. Ried, Chromosome transfer induced aneuploidy results in complex dysregulation of the cellular transcriptome in immortalized and cancer cells. *Cancer Res.* 64, 6941–6949 (2004).
 40. M. Dürrbaum, Z. Storchová, *FEBS J.*, in press, doi:10.1111/febs.13591.
 41. M. Dürrbaum, A. Y. Kuznetsova, V. Passerini, S. Stingele, G. Stoehr, Z. Storchová, Unique features of the transcriptional response to model aneuploidy in human cells. *BMC*

- Genomics*. 15, 139 (2014).
42. S. Santaguida, A. Amon, Short- and long-term effects of chromosome mis-segregation and aneuploidy. *Nat. Rev. Mol. Cell Biol.* 16, 473–85 (2015).
 43. K. Crasta, N. J. Ganem, R. Dagher, A. B. Lantermann, E. V Ivanova, Y. Pan, L. Nezi, A. Protopopov, D. Chowdhury, D. Pellman, DNA breaks and chromosome pulverization from errors in mitosis. *Nature*. 482, 53–8 (2012).
 44. Z. Storchov, W. P. Kloosterman, The genomic characteristics and cellular origin of chromothripsis. *Curr. Opin. Cell Biol.* 40 (2016), pp. 106–113.
 45. C.-Z. Zhang, A. Spektor, H. Cornils, J. M. Francis, E. K. Jackson, S. Liu, M. Meyerson, D. Pellman, Chromothripsis from DNA damage in micronuclei. *Nature*. 522, 179–184 (2015).
 46. M. S. De Pagter, M. J. Van Roosmalen, A. F. Baas, I. Renkens, K. J. Duran, E. Van Binsbergen, M. Tavakoli-Yaraki, R. Hochstenbach, L. T. Van Der Veken, E. Cuppen, W. P. Kloosterman, Chromothripsis in healthy individuals affects multiple protein-coding genes and can result in severe congenital abnormalities in offspring. *Am. J. Hum. Genet.* 96, 651–656 (2015).
 47. W. P. Kloosterman, V. Guryev, M. van Roosmalen, K. J. Duran, E. de Bruijn, S. C. M. Bakker, T. Letteboer, B. van Nesselrooij, R. Hochstenbach, M. Poot, E. Cuppen, Chromothripsis as a mechanism driving complex de novo structural rearrangements in the germline. *Hum. Mol. Genet.* 20, 1916–1924 (2011).
 48. K. A. Knouse, J. Wu, C. A. Whittaker, A. Amon, Single cell sequencing reveals low levels of aneuploidy across mammalian tissues. *Proc Natl Acad Sci U S A*. 111, 13409–13414 (2014).
 49. M. J. McConnell, M. Lindberg, K. J. Brennand, J. C. Piper, T. Voet, C. Cowing-Zitron, S. Shumilina, R. S. Lasken, J. R. Vermeesch, I. M. Hall, F. H. Gage, Mosaic Copy Number Variation in Human Neurons. *Science (80-)*. 342, 632–638 (2013).
 50. S. J. Pfau, R. E. Silberman, K. A. Knouse, A. Amon, Aneuploidy impairs hematopoietic stem cell fitness and is selected against in regenerating tissues in vivo. *Genes Dev.* 30, 1395–1408 (2016).
 51. V. Marthiens, M. a Rujano, C. Pannetier, S. Tessier, P. Paul-Gilloteaux, R. Basto, Centrosome amplification causes microcephaly. *Nat. Cell Biol.* 15, 731–40 (2013).
 52. C. G. Woods, R. Basto, Microcephaly. *Curr. Biol.* 24, R1109–R1111 (2014).
 53. D. Gogondeau, K. Siudeja, D. Gambarotto, C. Pannetier, A. J. Bardin, R. Basto, Aneuploidy causes premature differentiation of neural and intestinal stem cells. *Nat. Commun.* 6, 8894 (2015).
 54. P. Chetaille, C. Preuss, S. Burkhard, J.-M. Côté, C. Houde, J. Castilloux, J. Piché, N. Gosset, S. Leclerc, F. Wünnemann, M. Thibeault, C. Gagnon, A. Galli, E. Tuck, G. R. Hickson, N. El Amine, I. Boufaied, E. Lemyre, P. de Santa Barbara, S. Faure, A. Jonzon, M. Cameron, H. C. Dietz, E. Gallo-McFarlane, D. W. Benson, C. Moreau, D. Labuda, S. H. Zhan, Y. Shen, M. Jomphe, S. J. M. Jones, J. Bakkers, G. Andelfinger, Mutations in SGOL1 cause a novel cohesinopathy affecting heart and gut rhythm. *Nat. Genet.* 46, 1245–1249 (2014).
 55. A. Saadi, F. Verny, K. Siquier-Pernet, C. Bole-Feysot, P. Nitschke, A. Munnich, M. Abada-Dendib, M. Chaouch, M. Abramowicz, L. Colleaux, Refining the phenotype associated with CASC5 mutation. *Neurogenetics*. 17, 71–78 (2016).
 56. S. Szczepanski et al., A novel homozygous splicing mutation of CASC5 causes primary microcephaly in a large Pakistani family. *Hum. Genet.* 135, 1–14 (2016).
 57. C. R. Jamieson, C. Govaerts, M. J. Abramowicz, Primary autosomal recessive microcephaly: homozygosity mapping of MCPH4 to chromosome 15. *Am. J. Hum. Genet.* 65, 1465–9 (1999).
 58. A. Genin, J. Desir, N. Lambert, M. Biervliet, N. Van der Aa, G. Pierquin, A. Killian,

- M. Tosi, M. Urbina, A. Lefort, F. Libert, I. Pirson, M. Abramowicz, Kinetochores KMN network gene *CASC5* mutated in primary microcephaly. *Hum. Mol. Genet.* 21, 5306–5317 (2012).
59. G. M. Mirzaa, B. Vitre, G. Carpenter, I. Abramowicz, J. G. Gleeson, A. R. Paciorkowski, D. W. Cleveland, W. B. Dobyns, M. O'Driscoll, Mutations in *CENPE* define a novel kinetochores-centromeric mechanism for microcephalic primordial dwarfism. *Hum. Genet.* 133, 1023–1039 (2014).
 60. P. Stromme, E. Dahl, T. Flage, H. Stene-Johansen, Apple peel intestinal atresia in siblings with ocular anomalies and microcephaly. *Clin Genet.* 44, 208–210 (1993).
 61. I. Filges, E. Bruder, K. Brandal, S. Meier, D. E. Undlien, T. R. Waage, I. Hoesli, M. Schubach, T. de Beer, Y. Sheng, S. Hoeller, S. Schulzke, O. Røsby, P. Miny, S. Tercanli, T. Oppedal, P. Meyer, K. K. Selmer, P. Strømme, Strømme Syndrome Is a Ciliary Disorder Caused by Mutations in *CENPF*. *Hum. Mutat.* 37, 359–363 (2016).
 62. A. M. Waters et al., The kinetochores protein, *CENPF*, is mutated in human ciliopathy and microcephaly phenotypes. *J. Med. Genet.* 52, 147–56 (2015).
 63. G. N. Kavaslar, S. Onengut, O. Derman, A. Kaya, A. Tolun, The novel genetic disorder microhydranencephaly maps to chromosome 16p13.3-12.1. *Am. J. Hum. Genet.* 66, 1705–1709 (2000).
 64. M. Bakircioglu, O. P. Carvalho, M. Khurshid, J. J. Cox, B. Tuysuz, T. Barak, S. Yilmaz, O. Caglayan, A. Dincer, A. K. Nicholas, O. Quarrell, K. Springell, G. Karbani, S. Malik, C. Gannon, E. Sheridan, M. Crosier, S. N. Lisgo, S. Lindsay, K. Bilguvar, F. Gergely, M. Gunel, C. G. Woods, The essential role of centrosomal *NDE1* in human cerebral cortex neurogenesis. *Am. J. Hum. Genet.* 88, 523–535 (2011).
 65. F. S. Alkuraya, X. Cai, C. Emery, G. H. Mochida, M. S. Al-Dosari, J. M. Felie, R. S. Hill, B. J. Barry, J. N. Partlow, G. G. Gascon, A. Kentab, M. Jan, R. Shaheen, Y. Feng, C. A. Walsh, Human mutations in *NDE1* cause extreme microcephaly with lissencephaly. *Am. J. Hum. Genet.* 88, 536–547 (2011).
 66. A. Rauch, D. Wiczorek, E. Graf, T. Wieland, S. Endele, T. Schwarzmayr, B. Albrecht, D. Bartholdi, J. Beygo, N. Di Donato, A. Dufke, K. Cremer, M. Hempel, D. Horn, J. Hoyer, P. Joset, A. Röpke, U. Moog, A. Riess, C. T. Thiel, A. Tzschach, A. Wiesener, E. Wohlleber, C. Zweier, A. B. Ekici, A. M. Zink, A. Rump, C. Meisinger, H. Grallert, H. Sticht, A. Schenck, H. Engels, G. Rappold, E. Schröck, P. Wieacker, O. Riess, T. Meitinger, A. Reis, T. M. Strom, Range of genetic mutations associated with severe non-syndromic sporadic intellectual disability: An exome sequencing study. *Lancet.* 380, 1674–1682 (2012).
 67. M. Hempel, K. Cremer, C. W. Ockeloen, K. D. Lichtenbelt, J. C. Herkert, J. Denecke, T. B. Haack, A. M. Zink, J. Becker, E. Wohlleber, J. Johannsen, B. Alhaddad, R. Pfundt, S. Fuchs, D. Wiczorek, T. M. Strom, K. L. I. Van Gassen, T. Kleefstra, C. Kubisch, H. Engels, D. Lessel, De Novo Mutations in *CHAMP1* Cause Intellectual Disability with Severe Speech Impairment. *Am. J. Hum. Genet.* 97, 493–500 (2015).
 68. H. García-Castillo, A. I. Vásquez-Velásquez, H. Rivera, P. Barros-Núñez, Clinical and genetic heterogeneity in patients with mosaic variegated aneuploidy: delineation of clinical subtypes. *Am. J. Med. Genet. A.* 146A, 1687–95 (2008).
 69. H. Ochiai, T. Miyamoto, A. Kanai, K. Hosoba, T. Sakuma, Y. Kudo, K. Asami, A. Ogawa, A. Watanabe, T. Kajii, T. Yamamoto, S. Matsuura, TALEN-mediated single-base-pair editing identification of an intergenic mutation upstream of *BUB1B* as causative of PCS (MVA) syndrome. *Proc. Natl. Acad. Sci. U. S. A.* 111, 1461–6 (2014).
 70. L. Pinson, L. Mannini, M. Willems, F. Cucco, N. Sirvent, T. Frebourg, V. Quarantotti, C. Collet, A. Schneider, P. Sarda, D. Geneviève, J. Puechberty, G. Lefort, A. Musio, CEP57 mutation in a girl with mosaic variegated aneuploidy syndrome. *Am. J. Med. Genet.*

- Part A*. 164, 177–181 (2014).
71. K. Snape, S. Hanks, E. Ruark, P. Barros-Núñez, A. Elliott, A. Murray, A. H. Lane, N. Shannon, P. Callier, D. Chitayat, J. Clayton-Smith, D. R. Fitzpatrick, D. Gisselsson, S. Jacquemont, K. Asakura-Hay, M. a Micale, J. Tolmie, P. D. Turnpenny, M. Wright, J. Douglas, N. Rahman, Mutations in CEP57 cause mosaic variegated aneuploidy syndrome. *Nat. Genet.* 43, 527–529 (2011).
 72. V. Silió, A. D. McAinsh, J. B. Millar, KNL1-Bubs and RZZ Provide Two Separable Pathways for Checkpoint Activation at Human Kinetochores. *Dev. Cell.* 35, 600–613 (2015).
 73. T. Kiyomitsu, C. Obuse, M. Yanagida, Human Blinkin/AF15q14 Is Required for Chromosome Alignment and the Mitotic Checkpoint through Direct Interaction with Bub1 and BubR1. *Dev. Cell.* 13, 663–676 (2007).
 74. M. Vleugel, E. Tromer, M. Omerzu, V. Groenewold, W. Nijenhuis, B. Snel, G. J. P. L. Kops, Arrayed BUB recruitment modules in the kinetochore scaffold KNL1 promote accurate chromosome segregation. *J. Cell Biol.* 203, 943–955 (2013).
 75. T. M. Kapoor, M. a Lampson, P. Hergert, L. Cameron, D. Cimini, E. D. Salmon, B. F. McEwen, A. Khodjakov, Chromosomes Can Congress to the Metaphase Plate Before Biorientation. *Science.* 311, 388–391 (2006).
 76. T. J. Yen, G. Li, B. T. Schaar, I. Szilak, D. W. Cleveland, CENP-E is a putative kinetochore motor that accumulates just before mitosis. *Nature.* 359, 536–539 (1992).
 77. N. Powles-Glover, Cilia and ciliopathies: Classic examples linking phenotype and genotype-An overview. *Reprod. Toxicol.* 48, 98–105 (2014).
 78. G. Kanfer, T. Courthéoux, M. Peterka, S. Meier, M. Soste, A. Melnik, K. Reis, P. Aspenström, M. Peter, P. Picotti, B. Kornmann, Mitotic redistribution of the mitochondrial network by Miro and Cenp-F. *Nat. Commun.* 6, 8015 (2015).
 79. V. A. Volkov, P. M. Grissom, V. K. Arzhanik, A. V. Zaytsev, K. Renganathan, T. McClure-Begley, W. M. Old, N. Ahn, J. Richard McIntosh, Centromere protein F includes two sites that couple efficiently to depolymerizing microtubules. *J. Cell Biol.* 209, 813–828 (2015).
 80. M. A. S. Vergnolle, S. S. Taylor, Cenp-F Links Kinetochores to Nde1/Nde1/Lis1/Dynein Microtubule Motor Complexes. *Curr. Biol.* 17, 1173–1179 (2007).
 81. S. Kim, N. a Zaghloul, E. Bubenshchikova, E. C. Oh, S. Rankin, N. Katsanis, T. Obara, L. Tsiokas, Nde1-mediated inhibition of ciliogenesis affects cell cycle re-entry. *Nat. Cell Biol.* 13, 351–360 (2011).
 82. A. Guven, A. Gunduz, T. M. Bozoglu, C. Yalcinkaya, A. Tolun, Novel NDE1 homozygous mutation resulting in microhydranencephaly and not microlyssencephaly. *Neurogenetics.* 13, 189–194 (2012).
 83. T. J. Dantas, A. Carabalona, D. Jun-Kit Hu, R. B. Vallee, *Cytoskeleton*, in press, doi:10.1002/cm.21293.
 84. B. Isidor, S. K??ry, J. A. Rosenfeld, T. Besnard, S. Schmitt, S. Joss, S. J. Davies, R. Roger Lebel, A. Henderson, C. P. Schaaf, H. E. Streff, Y. Yang, V. Jain, N. Chida, X. Latypova, C. Le Caignec, B. Cogn??, S. Mercier, M. Vincent, E. Colin, D. Bonneau, A. S. Denomm??, P. Parent, B. Gilbert-Dussardier, S. Odent, A. Toutain, A. Piton, C. Dina, A. Donnart, P. Lindenbaum, E. Charpentier, R. Redon, K. lemura, M. Ikeda, K. Tanaka, S. B??zieau, De Novo Truncating Mutations in the Kinetochore-Microtubules Attachment Gene CHAMP1 Cause Syndromic Intellectual Disability. *Hum. Mutat.* 37, 354–358 (2016).
 85. A. J. Tanaka, M. T. Cho, K. Retterer, J. R. Jones, C. Nowak, J. Douglas, Y.-H. Jiang, A. McConkie-Rosell, G. B. Schaefer, J. Kaylor, O. A. Rahman, A. Telegrafi, B. Friedman, G. Douglas, K. G. Monaghan, W. K. Chung, De novo pathogenic variants in CHAMP1 are

- associated with global developmental delay, intellectual disability, and dysmorphic facial features. *Mol. Case Stud.* 2, a000661 (2016).
86. G. Itoh, S. Kanno, K. S. K. Uchida, S. Chiba, S. Sugino, K. Watanabe, K. Mizuno, A. Yasui, T. Hirota, K. Tanaka, CAMP (C13orf8, ZNF828) is a novel regulator of kinetochore-microtubule attachment. *EMBO J.* 30, 130–144 (2011).
 87. R.-S. Nozawa, K. Nagao, H.-T. Masuda, O. Iwasaki, T. Hirota, N. Nozaki, H. Kimura, C. Obuse, Human POGZ modulates dissociation of HP1alpha from mitotic chromosome arms through Aurora B activation. *Nat. Cell Biol.* 12, 719–727 (2010).
 88. Y. Tanno, H. Susumu, M. Kawamura, H. Sugimura, T. Honda, Y. Watanabe, The inner centromere – shugoshin network prevents chromosomal instability. *Science (80-.)*. 349, 1237–1241 (2015).
 89. Y. Ye, M. T. Cho, K. Retterer, N. Alexander, T. Ben-Omran, M. Al-Mureikhi, I. Cristian, P. G. Wheeler, C. Crain, D. Zand, V. Weinstein, H. J. Vernon, R. McClellan, V. Krishnamurthy, P. Vitazka, F. Millan, W. K. Chung, De novo POGZ mutations are associated with neurodevelopmental disorders and microcephaly. *Mol. Case Stud.* 1, a000455 (2015).
 90. S. Jacquemont, M. Bocéno, J. M. Rival, F. Méchinaud, A. David, High risk of malignancy in mosaic variegated aneuploidy syndrome. *Am. J. Med. Genet.* 109, 17–21 (2002).
 91. S. Hanks, K. Coleman, S. Reid, A. Plaja, H. Firth, D. Fitzpatrick, A. Kidd, K. Méhes, R. Nash, N. Robin, N. Shannon, J. Tolmie, J. Swansbury, A. Irrthum, J. Douglas, N. Rahman, Constitutional aneuploidy and cancer predisposition caused by biallelic mutations in BUB1B. *Nat. Genet.* 36, 1159–61 (2004).
 92. T. Miyamoto, S. Porazinski, H. Wang, A. Borovina, B. Ciruna, A. Shimizu, T. Kajii, A. Kikuchi, M. Furutani-Seiki, S. Matsuura, Insufficiency of BUBR1, a mitotic spindle checkpoint regulator, causes impaired ciliogenesis in vertebrates. *Hum. Mol. Genet.* 20, 2058–2070 (2011).
 93. D. J. Baker, K. B. Jeganathan, J. D. Cameron, M. Thompson, S. Juneja, A. Kopecka, R. Kumar, R. B. Jenkins, P. C. de Groen, P. Roche, J. M. van Deursen, BubR1 insufficiency causes early onset of aging-associated phenotypes and infertility in mice. *Nat. Genet.* 36, 744–9 (2004).
 94. H. Izumi, Y. Matsumoto, T. Ikeuchi, H. Saya, T. Kajii, S. Matsuura, BubR1 localizes to centrosomes and suppresses centrosome amplification via regulating Plk1 activity in interphase cells. *Oncogene.* 28, 2806–20 (2009).
 95. S. J. E. Suijkerbuijk, M. H. J. Van Osch, F. L. Bos, S. Hanks, N. Rahman, G. J. P. L. Kops, Molecular causes for BUBR1 dysfunction in the human cancer predisposition syndrome mosaic variegated aneuploidy. *Cancer Res.* 70, 4891–4900 (2010).
 96. C. Bossard, H. Laurell, L. Van den Berghe, S. Meunier, C. Zanibellato, H. Prats, Translokoin is an intracellular mediator of FGF-2 trafficking. *Nat. Cell Biol.* 5, 433–439 (2003).
 97. K. Momotani, A. S. Khromov, T. Miyake, P. T. Stukenberg, A. V Somlyo, Cep57, a multidomain protein with unique microtubule and centrosomal localization domains. *Biochem. J.* 412, 265–73 (2008).
 98. H. Zhou, T. Wang, T. Zheng, J. Teng, J. Chen, Cep57 is a Mis12-interacting kinetochore protein involved in kinetochore targeting of Mad1-Mad2. *Nat. Commun.* 7, 10151 (2016).
 99. G. K. T. Chan, B. T. Schaar, T. J. Yen, Characterization of the kinetochore binding domain of CENP-E reveals interactions with the kinetochore proteins CENP-F and hBUBR1. *J. Cell Biol.* 143, 49–63 (1998)
 100. R. Beroukhim, C. Mermel, D. Porter, The landscape of somatic copy-number alteration across human cancers. *Nature.* 463, 899–905 (2010).
 101. M. Griffith, O. L. Griffith, Mitelman Database (Chromosome Aberrations and Gene Fusions in Cancer). *Dict. Bioinforma. Comput. Biol.* (2004), p. Retrieved on 10.04.2012, , doi:10.1002/9780471650126.dob0996.

102. P. H. G. G. Duijf, R. Benezra, The cancer biology of whole-chromosome instability. *Oncogene*. 32, 4727–36 (2013).
103. R. A. Burrell, S. E. McClelland, D. Endesfelder, P. Groth, M.-C. Weller, N. Shaikh, E. Domingo, N. Kanu, S. M. Dewhurst, E. Gronroos, S. K. Chew, A. J. Rowan, A. Schenk, M. Sheffer, M. Howell, M. Kschischo, A. Behrens, T. Helleday, J. Bartek, I. P. Tomlinson, C. Swanton, Replication stress links structural and numerical cancer chromosomal instability. *Nature*. 494, 492–496 (2013).
104. K. Fukasawa, Centrosome amplification, chromosome instability and cancer development. *Cancer Lett.* 230 (2005), pp. 6–19.
105. S. F. Bakhroum, S. L. Thompson, A. L. Manning, D. a Compton, Genome stability is ensured by temporal control of kinetochore-microtubule dynamics. *Nat. Cell Biol.* 11, 27–35 (2009).
106. G. J. P. L. Kops, B. a a Weaver, D. W. Cleveland, On the road to cancer: aneuploidy and the mitotic checkpoint. *Nat. Rev. Cancer*. 5, 773–785 (2005).
107. S. F. Bakhroum, G. Genovese, D. A. Compton, Deviant Kinetochore Microtubule Dynamics Underlie Chromosomal Instability. *Curr. Biol.* 19, 1937–1942 (2009).
108. D. J. Gordon, B. Resio, D. Pellman, Causes and consequences of aneuploidy in cancer. *Nat. Rev. Genet.* 13, 189–203 (2012).
109. H. Bastians, in *Chromosomal Instability in Cancer Cells*, B. Ghadimi, T. Ried, Eds. (2015), vol. 200, pp. 95–113.
110. J. E. Simon, B. Bakker, F. Foijer, in *Chromosomal Instability in Cancer Cells* (2015), pp. 39–60.
111. A. Tighe, V. L. Johnson, M. Albertella, S. S. Taylor, Aneuploid colon cancer cells have a robust spindle checkpoint. *EMBO Rep.* 2, 609–614 (2001).
112. H. S. Kim, H. P. Kyung, S. A. Kim, J. Wen, W. P. Seung, B. Park, C. W. Gham, J. H. Woo, H. N. Sung, K. K. Ho, S. Y. Song, Frequent mutations of human Mad2, but not Bub1, in gastric cancers cause defective mitotic spindle checkpoint. *Mutat. Res. - Fundam. Mol. Mech. Mutagen.* 578, 187–201 (2005).
113. S. J. E. Suijkerbuijk, G. J. P. L. Kops, Preventing aneuploidy: The contribution of mitotic checkpoint proteins. *Biochim. Biophys. Acta - Rev. Cancer.* 1786 (2008), pp. 24–31.
114. P. Thiru, D. M. Kern, K. L. McKinley, J. K. Monda, F. Rago, K.-C. Su, T. Tsinman, D. Yazar, G. W. Bell, I. M. Cheeseman, Kinetochore genes are coordinately up-regulated in human tumors as part of a FoxM1-related cell division program. *Mol. Biol. Cell.* 25, 1983–94 (2014).
115. P. Trivedi, P. T. Stukenberg, A Centromere-Signaling Network Underlies the Coordination among Mitotic Events. *Trends Biochem. Sci.* 41 (2016), pp. 160–174.
116. V. K. Hill, J.-S. Kim, T. Waldman, Cohesin mutations in human cancer. *Biochim. Biophys. Acta - Rev. Cancer.* 1866, 1–11 (2016).
117. D. A. Solomon, T. Kim, L. A. Diaz-Martinez, J. Fair, A. G. Elkahloun, B. T. Harris, J. A. Toretsky, S. A. Rosenberg, N. Shukla, M. Ladanyi, Y. Samuels, C. D. James, H. Yu, J. S. Kim, T. Waldman, Mutational inactivation of STAG2 causes aneuploidy in human cancer. *Science (80-.)*. 333, 1039–1043 (2012).
118. M. S. Lawrence, P. Stojanov, C. H. Mermel, J. T. Robinson, L. a Garraway, T. R. Golub, M. Meyerson, S. B. Gabriel, E. S. Lander, G. Getz, Discovery and saturation analysis of cancer genes across 21 tumour types. *Nature*. 505, 495–501 (2014).
119. S. F. Bakhroum, W. T. Silkworth, I. K. Nardi, J. M. Nicholson, D. A. Compton, D. Cimini, The mitotic origin of chromosomal instability. *Curr. Biol.* 24 (2014), . doi:10.1016/j.cub.2014.01.019.
120. L. Kabeche, D. A. Compton, Checkpoint-independent stabilization of kinetochore-microtubule attachments by Mad2 in human cells. *Curr. Biol.* 22, 638–644 (2012).

121. W. T. Silkworth, I. K. Nardi, L. M. Scholl, D. Cimini, Multipolar spindle pole coalescence is a major source of kinetochore mis-attachment and chromosome mis-segregation in cancer cells. *PLoS One*. 4 (2009), doi:10.1371/journal.pone.0006564.
122. N. J. Ganem, S. a Godinho, D. Pellman, A mechanism linking extra centrosomes to chromosomal instability. *Nature*. 460, 278–82 (2009).
123. N. Ertych, A. Stolz, A. Stenzinger, W. Weichert, S. Kaulfuß, P. Burfeind, A. Aigner, L. Wordeman, H. Bastians, Increased microtubule assembly rates influence chromosomal instability in colorectal cancer cells. *Nat. Cell Biol*. 16, 779–91 (2014).
124. R. Wooster, Identification of the breast cancer susceptibility gene BRCA2. *Nature*. 378, 789–792 (1995).
125. C. The Breast Cancer Linkage, Cancer risks in BRCA2 mutation carriers. *J. Natl. Cancer Inst*. 91, 1310–6 (1999).
126. E. Choi, P.-G. G. Park, H. O. Lee, Y.-K. K. Lee, G. H. Kang, J. W. Lee, W. Han, H. C. Lee, D.-Y. Y. Noh, S. Lekomtsev, H. Lee, BRCA2 Fine-Tunes the Spindle Assembly Checkpoint through Reinforcement of BubR1 Acetylation. *Dev. Cell*. 22, 295–308 (2012).
127. I. Park, H. H. ock H. H. ock H. H. ock Lee, E. Choi, Y.-K. K. Lee, M.-S. S. Kwon, J. Min, P.-G. G. Park, S. Lee, Y.-Y. Y. Kong, G. Gong, H. H. ock H. H. ock H. H. ock Lee, Loss of BubR1 acetylation causes defects in spindle assembly checkpoint signaling and promotes tumor formation. *J. Cell Biol*. 202, 295–309 (2013).
128. E. Hernando, Z. Nahlé, G. Juan, E. Diaz-Rodriguez, M. Alaminos, M. Hemann, L. Michel, V. Mittal, W. Gerald, R. Benezra, S. W. Lowe, C. Cordon-Cardo, Rb inactivation promotes genomic instability by uncoupling cell cycle progression from mitotic control. *Nature*. 430, 797–802 (2004).
129. R. Sotillo, J.-M. Schwartzman, N. D. Socci, R. Benezra, Mad2-induced chromosome instability leads to lung tumour relapse after oncogene withdrawal. *Nature*. 464, 436–40 (2010).
130. J. M. Schwartzman, P. H. G. Duijf, R. Sotillo, C. Coker, R. Benezra, Mad2 is a critical mediator of the chromosome instability observed upon Rb and p53 pathway inhibition. *Cancer Cell*. 19, 701–714 (2011).
131. D. Guardavaccaro, D. Frescas, N. V Dorrello, A. Peschiaroli, A. S. Multani, T. Cardozo, A. Lasorella, A. Iavarone, S. Chang, E. Hernando, M. Pagano, Control of chromosome stability by the beta-TrCP-REST-Mad2 axis. *Nature*. 452, 365–369 (2008).
132. C. M. Caldwell, K. B. Kaplan, The role of APC in mitosis and in chromosome instability. *Adv. Exp. Med. Biol*. 656, 51–64 (2009).
133. J. Drost, R. H. van Jaarsveld, B. Ponsioen, C. Zimmerlin, R. van Boxtel, A. Buijs, N. Sachs, R. M. Overmeer, G. J. Offerhaus, H. Begthel, J. Korving, M. van de Wetering, G. Schwank, M. Logtenberg, E. Cuppen, H. J. Snippert, J. P. Medema, G. J. P. L. Kops, H. Clevers, Sequential cancer mutations in cultured human intestinal stem cells. *Nature*. 521, 43–47 (2015).
134. D. J. Morris-Rosendahl, A. M. Kaindl, What next-generation sequencing (NGS) technology has enabled us to learn about primary autosomal recessive microcephaly (MCPH). *Mol. Cell. Probes*. 29 (2015), pp. 271–281.
135. B. G. Childs, M. Durik, D. J. Baker, J. M. van Deursen, Cellular senescence in aging and age-related disease: from mechanisms to therapy. *Nat. Med*. 21, 1424–1435 (2015).
136. F. Fojter, V. M. Draviam, P. K. Sorger, Studying chromosome instability in the mouse. *Biochim. Biophys. Acta - Rev. Cancer*. 1786 (2008), pp. 73–82.



CHAPTER 3

BIALLELIC TRIP¹³

MUTATIONS PREDISPOSE
TO WILMS TUMOR
AND CHROMOSOME
MISSEGREGATION

Shawn Yost*, Bas de Wolf*, Sandra Hanks*, Anna Zachariou, Chiara Marcozzi, Matthew Clarke, Richarda de Voer, Banafsheh Etemad, Esther Ujttewaal, Emma Ramsay, Harriet Wylie, Anna Elliott, Susan Picton, Audrey Smith, Sarah Smithson, Sheila Seal, Elise Ruark, Gunnar Houge, Jonathan Pines, Geert J.P.L. Kops*, Nazneen Rahman*

* Co-first authors

+ Joint senior authors

Nature Genetics 2017;49(7):1148-1151

Through exome sequencing, we identified six individuals with biallelic loss-of-function mutations in *TRIP13*. All six developed Wilms tumor. Constitutional mosaic aneuploidies, microcephaly, developmental delay and seizures, which are features of mosaic variegated aneuploidy (MVA) syndrome^{1,2}, were more variably present. Through functional studies, we show that *TRIP13*-mutant patient cells have no detectable *TRIP13* and have substantial impairment of the spindle assembly checkpoint (SAC), leading to a high rate of chromosome missegregation. Accurate segregation, as well as SAC proficiency, is rescued by restoring *TRIP13* function. Individuals with biallelic *TRIP13* or *BUB1B* mutations have a high risk of embryonal tumors³, and here we show that their cells display severe SAC impairment. MVA due to biallelic *CEP57* mutations⁴, or of unknown cause, is not associated with embryonal tumors and cells from these individuals show minimal SAC deficiency. These data provide insights into the complex relationships between aneuploidy and carcinogenesis.

Accurate chromosome segregation during cell division is required to maintain the correct number of chromosomes in cells. Errors of chromosome segregation can lead to aneuploidy, a term that describes cells with loss or gain of one or more chromosomes (**chapter 1.1**). Aneuploidy is an important cause of human disease and is implicated in diverse pathologies, including recurrent miscarriage, infertility, developmental disorders and cancer⁵⁻⁷ (**chapter 1.3**). Many biological processes, including spindle assembly, chromatid-spindle attachment, attachment error correction and the SAC, are involved in ensuring that chromosome segregation proceeds flawlessly and that aneuploidy is prevented^{6,8} (**chapter 2.1**).

Rare individuals with constitutional mosaic aneuploidies involving varying chromosomes are well documented^{1,2}. Affected individuals often have other clinical features such as microcephaly, developmental delay and various congenital abnormalities, and the term MVA is used to describe this condition¹⁻³ (**chapter 2.3.5, Addendum Table 1**). Cancer predisposition is one of the most important associations of MVA, with affected individuals having substantially increased risk of childhood malignancies, particularly Wilms tumor and rhabdomyosarcoma^{3,9,10}.

We have been studying this rare condition for over a decade. We previously reported biallelic mutations in the (SAC) gene *BUB1B* as a cause of MVA and childhood cancer³. Thus far, we have identified 14 individuals with biallelic *BUB1B* mutations. More recently, we identified biallelic mutations in *CEP57*, which encodes a centrosomal protein, in four individuals with MVA, none of whom have developed cancer⁴. Together, these two genes only account for a proportion of MVA cases. See also **chapter 2.3.5**.

To identify additional MVA-related genes, we undertook exome sequencing in 43 individuals from 20 families, including 21 probands with MVA (**Table S1**). We generated exome data using Illumina exome capture assays and called variants using the OpEx pipeline as previously described^{11,12}. We performed two analyses to prioritize variants for further evaluation. We first undertook an individual proband analysis to identify genes with two rare variants, as MVA is a recessively inherited condition. We also identified genes with protein-truncating variants (PTVs) present in more than one proband, using the PTV prioritization method^{4,12}.

We identified a homozygous stop-gain mutation in the *TRIP13* gene (NM_004237), called *TRIP13* c.1060C>T_p.Arg354X, in three probands (ID_0319, ID_0644 and ID_7054) (**Table 1, Figure S1, Addendum Table 1**, patients 39-41). The mutation leads to nonsense-mediated

mRNA decay (**Figure S2**) and the absence of detectable TRIP13 protein (**Figure S3**). Protein expressed from exogenous cDNA was present at a substantially lower level than wild-type TRIP13 (**Figure S4**). This shows that, in addition to altering mRNA stability, the mutation also directly affects the TRIP13 protein. Therefore, the *TRIP13* c.1060C>T_p.Arg354X allele is highly unlikely to produce any functional TRIP13 protein.

The three individuals had been independently recruited and there was no known relationship between them, but they were all from families of Asian origin. Interestingly, all three had Wilms tumor. To further explore the association of *TRIP13* with Wilms tumor, we performed exome sequencing in 11 UK individuals of reported Asian origin with Wilms tumor. Two, ID_0649 and ID_6112, were also homozygous for *TRIP13* c.1060C>T_p.Arg354X (**Table 1, Figure S1**). ID_0649 had been noted to have premature chromatid separation but no mosaic aneuploidies in lymphocytes (**Addendum Table 1, patient 54**). No constitutional karyotype has been performed in ID_6112, but the tumor karyotype was reported to be normal. Of note, the sister of ID_6112 died at 4 years of age after developing a Sertoli–Leydig cell tumor of the left ovary and acute myeloid leukemia (AML). No sample was available for mutation testing, but this observation suggests that biallelic *TRIP13* mutations may also predispose to cancers other than Wilms tumor.

The four available parental samples were all heterozygous for the mutation, consistent with recessive inheritance. The mutation was not present in the Exome Aggregation Consortium (ExAC) or ICR1000 series^{33,34}, nor was it present in 11,677 other exomes we have analyzed with the same pipeline. Multidimensional scaling analysis strongly suggested that the families originated from Pakistan (**Figure S5**). Exploration of the available family history suggests that the families come from the Azad Kashmir region of Pakistan. Many Azad Kashmir families were given work permits for the UK in the 1960s because of the construction of the Mangla Dam, which led to large-scale local displacement. Further evaluation of the contribution of the *TRIP13* mutation to Wilms tumor in this population would therefore be of interest.

We subsequently became aware of a Norwegian girl, ID_7679, who developed Wilms tumor at 15 months, who was homozygous for a different truncating *TRIP13* mutation (**Table 1, Addendum Table 1, patient 55**). The mutation, c.673-1G>C, is predicted to disrupt the canonical 3' splice site in intron 7 of *TRIP13*, and a new splice site 2 bp upstream is predicted to be used, resulting in a 2-bp frameshift and premature protein truncation. No constitutional mosaic aneuploidies were observed in her lymphocytes.

These data provide compelling genetic evidence that *TRIP13* is a cancer predisposition gene. Biallelic loss-of-function *TRIP13* mutations confer a high risk of Wilms tumor and also predispose to chromosome segregation dysfunction, which can manifest as mosaic aneuploidies and/or premature chromatid separation. There were no consistent phenotypic features among the six probands, although developmental delay, microcephaly, seizures and growth retardation were each noted in more than one individual (**Table 1, Figure S1**).

TRIP13 encodes a highly conserved AAA+ATPase that contributes to homolog pairing, synapsis and recombination during meiosis¹⁵. In mitosis, TRIP13 remodels the crucial SAC effector MAD2 from a 'closed' (active) to an 'open' (inactive) form^{16,17}. This has a dual impact on SAC function: in prometaphase, MAD2 remodeling is thought to enable continuous replenishment of the MAD2 pools that can be activated by unattached kinetochores for the generation of the initial SAC inhibitor. TRIP13 thus ensures robust and long-lasting SAC signaling. In metaphase, however, when no new active MAD2 is generated by kinetochores,

Table 1. Summary of molecular and clinical findings in individuals with biallelic *TRIP13* mutations

ID	TRIP13 mutations	Aneuploidy	Premature chromatid separation	Wilms tumor age at diagnosis	Current status	Other clinical features
ID_0319	c.1060C>T_p.Arg354X c.1060C>T_p.Arg354X	Yes	U	2 years	Alive, 6 years	Microcephaly, developmental delay, arthrogryposis
ID_0644	c.1060C>T_p.Arg354X c.1060C>T_p.Arg354X	Yes	Yes	4 years, relapse 5 years	Alive, 43 years	Growth retardation
ID_7054	c.1060C>T_p.Arg354X c.1060C>T_p.Arg354X	Yes	Yes	2 years	Alive, 5 years	Café-au-lait patches
ID_0649	c.1060C>T_p.Arg354X c.1060C>T_p.Arg354X	No	Yes	2 years, relapse 10 years	Died, 10 years	Microcephaly, growth retardation, seizures, abnormal skin pigmentation
ID_6112	c.1060C>T_p.Arg354X c.1060C>T_p.Arg354X	U	U	5 years	Alive, 6 years	
ID_7679	c.673-1G>C c.673-1G>C	No	U	1.3 years	Alive, 2.5 years	Microcephaly, seizures, developmental delay

Fuller details are provided in Figure S1. U, unknown.

MAD2 inactivation by *TRIP13* promotes disassembly of the inhibitor and causes SAC silencing and mitotic exit^{18–20}. See also **chapter 2.1**.

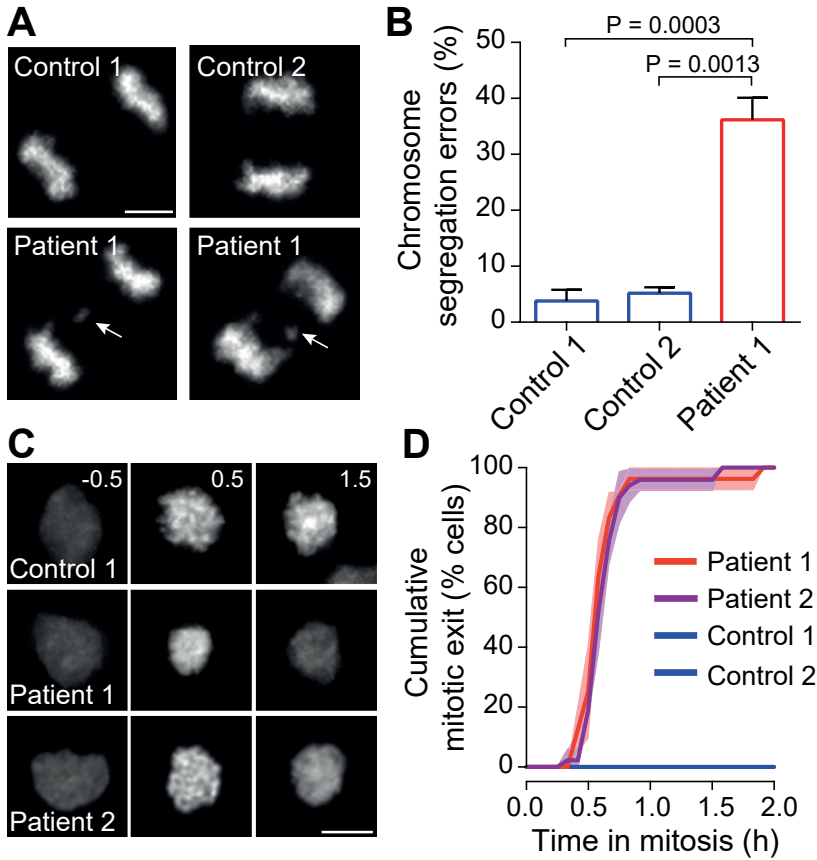


Figure 1. *TRIP13* loss-of-function mutations cause chromosome segregation errors and SAC deficiency. (A) Representative anaphases of immortalized control (top) and *TRIP13*-mutant patient (bottom) lymphoblasts expressing H2B-mNeon, showing a lagging chromosome in the bottom panels (white arrows). Scale bar, 5 μ m. (B) Quantification of the chromosome segregation errors of lymphoblasts as visualized in A. Each bar depicts the mean of three (control 2) or four (control 1 and patient 1) independent experiments \pm s.e.m., with 160 (control 1), 93 (control 2) and 64 (patient 1) cells in total. *P* values \leq 0.05 from two-sided unpaired Student's *t* tests are shown. Cells from patient 1 show increased levels of chromosome segregation errors. (C) Representative images of H2B-mNeon-expressing control (top) and patient (middle, bottom) lymphoblasts going through mitosis (time in hours with mitotic entry at *t* = 0.0) in the presence of nocodazole. Unlike control cell lines, both patient cell lines had exited from mitosis by 1.5 h (third column of the second and third rows). Scale bar, 10 μ m. (D) Analysis of the mitotic delay of cells as visualized in C, indicating the cumulative percentage of cells that exited from mitosis as a function of time (mean of three independent experiments \pm s.e.m. (shaded regions)), with 30 (controls 1 and 2) or 90 (patients 1 and 2) cells in total. Both patient cell lines escaped mitotic arrest within 1 h. Patient 1, ID_0644; patient 2, ID_7054.

We sought to examine which defective molecular processes underlie aneuploidy and chromosome missegregation in *TRIP13*-mutant patients. We first infected immortalized *TRIP13*-mutant patient lymphoblasts with virus encoding histone H2B (H2B)-mNeon to visualize chromatin. Live-cell imaging showed that patient lymphoblasts had high levels of chromosome segregation errors, such as lagging chromosomes and chromosome bridges (**Figure 1A-B**). To understand how *TRIP13* mutations cause chromosomal instability (CIN) in patient cells, we examined the fidelity of the SAC, the main chromosome segregation surveillance mechanism in which *TRIP13* has been implicated. To this end, we analyzed cells for their ability to maintain mitotic arrest after exposure to the spindle poison nocodazole (**Figures 1C, S6**). Control cells maintained the arrest for >2 h, whereas all cells from two different *TRIP13*-mutant patients escaped the arrest within 1 h (**Figure 1C-D**). Mitotic exit despite unattached chromosomes is indicative of a compromised SAC.

To gain insight into the molecular defect causing SAC impairment, we analyzed SAC protein expression and subcellular localization. Immunofluorescence imaging of the SAC effector *MAD2* in nocodazole-treated cells showed that *TRIP13*-mutant patient cells recruited ~50% fewer molecules of *MAD2* to their unattached kinetochores (**Figure 2A-B**). Kinetochores levels of the *MAD2* receptor *MAD1* were unaffected (**Figure 2C**). Absence of *TRIP13* caused increased overall p31^{comet} expression in one patient and reduced overall *MAD2* expression in both patients (**Figure S7**), consistent with data reported in *TRIP13*-knockout HeLa cells²⁰.

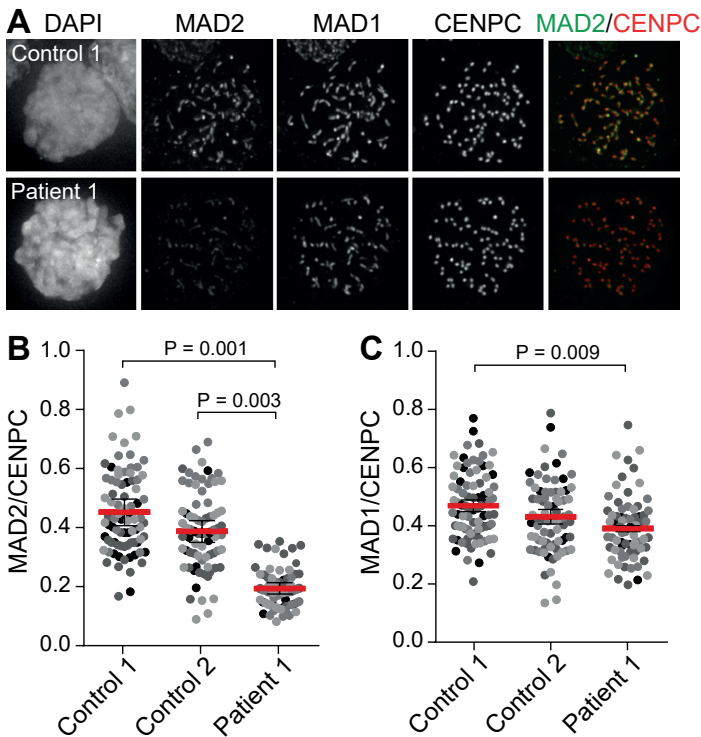


Figure 2. *TRIP13* loss-of-function mutations cause reduced levels of *MAD2* on unattached kinetochores. (A–C) Immunofluorescence labeling (A) and quantification (B,C) of the indicated proteins

in nocodazole-arrested control or patient lymphoblasts. In the plots, each dot represents one cell, with dots from separate independent experiments in different shades of gray. The red bar depicts the mean of four experiments \pm s.e.m., with 82 (control 1), 75 (control 2) and 71 (patient 1) cells in total. *P* values ≤ 0.05 from two-sided unpaired Student's *t* tests are shown. Cells from patient 1 had reduced kinetochore levels of MAD2, but not MAD1, in comparison to the controls. Patient 1, ID_0644; CENPC, kinetochore marker; DAPI, DNA stain. Scale bar, 3 μ m.

We next restored TRIP13 function by expressing GFP-TRIP13 in patient lymphoblasts using lentiviral delivery. Notably, GFP-TRIP13 expression rescued the CIN as well as the SAC defect (**Figure 3A-B**). Moreover, GFP-tagged Arg354X TRIP13 was unable to rescue an impaired SAC caused by CRISPR-Cas9-mediated knockout of the *TRIP13* gene in HCT116 chromosomally stable colorectal carcinoma cells (**Figures 3C, S8 and S9**). These observations provide an explanation for the chromosome segregation defects observed in individuals with biallelic *TRIP13* loss-of-function mutations. They also show that the SAC defects and resulting CIN are directly due to the loss of TRIP13 function caused by the homozygous *TRIP13* c.1060C>T_p.Arg354X mutations.

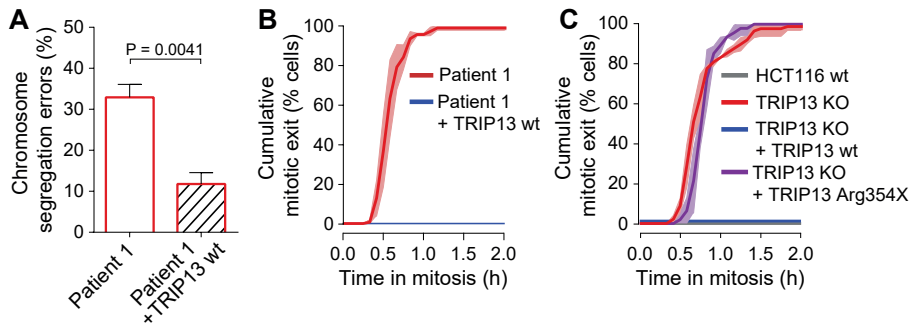


Figure 3. SAC deficiency and CIN caused by *TRIP13* loss of function is rescued with wild-type but not mutant TRIP13. (A) Quantification of the chromosome segregation errors of *TRIP13*-mutated patient lymphoblasts expressing H2B-mNeon or coexpressing GFP-tagged wild-type TRIP13 (GFP-TRIP13 wt). Each bar depicts the mean of three (patient 1) or four (patient 1 + TRIP13 wt) independent experiments \pm s.e.m., with 88 (patient 1) and 92 (patient 1 + TRIP13 wt) cells in total. *P* values ≤ 0.05 from two-sided unpaired Student's *t* tests are shown. Addition of GFP-TRIP13 wt to cells from patient 1 significantly reduced the rate of chromosome missegregation. (B) Analysis of mitotic delay as in **Figure 1D** in nocodazole-treated patient lymphoblasts expressing H2B-mNeon or coexpressing GFP-TRIP13 wt. The mean of three independent experiments \pm s.e.m. (shaded regions) is shown, with 100 (patient 1) and 35 (patient 1 + TRIP13 wt) cells in total. Cells from patient 1 expressing GFP-TRIP13 wt now maintained mitotic arrest. (C) Analysis of mitotic delay as in B in nocodazole-treated wild-type or *TRIP13*-knockout (KO) HCT116 cells expressing H2B-mNeon, coexpressing GFP-TRIP13 wt or coexpressing TRIP13 Arg354X. The mean of three independent experiments \pm s.e.m. (shaded regions) is shown, with 85 (HCT116 wt), 90 (*TRIP13* KO and *TRIP13* KO + TRIP13 wt) and 48 (*TRIP13* KO + TRIP13 Arg354X) cells in total. HCT116 wt and *TRIP13* KO + TRIP13 wt cells both maintained mitotic arrest, unlike *TRIP13* KO and *TRIP13* KO + TRIP13 Arg354X cells. Patient 1, ID_0644.

TRIP13 and BUBR1 (the protein encoded by *BUB1B*) are close functional partners in the SAC¹⁵. BUBR1 is part of the anaphase inhibitory complex MCC, which also includes MAD2, the main target of TRIP13's remodeling activity in mitosis²¹. Notably, severe SAC impairment was observed in *TRIP13*-mutant and *BUB1B*-mutant patient cells but not in cells from patients with *CEP57* mutations or in whom the cause of MVA remains unclear after exome sequencing (**Figure 4**).

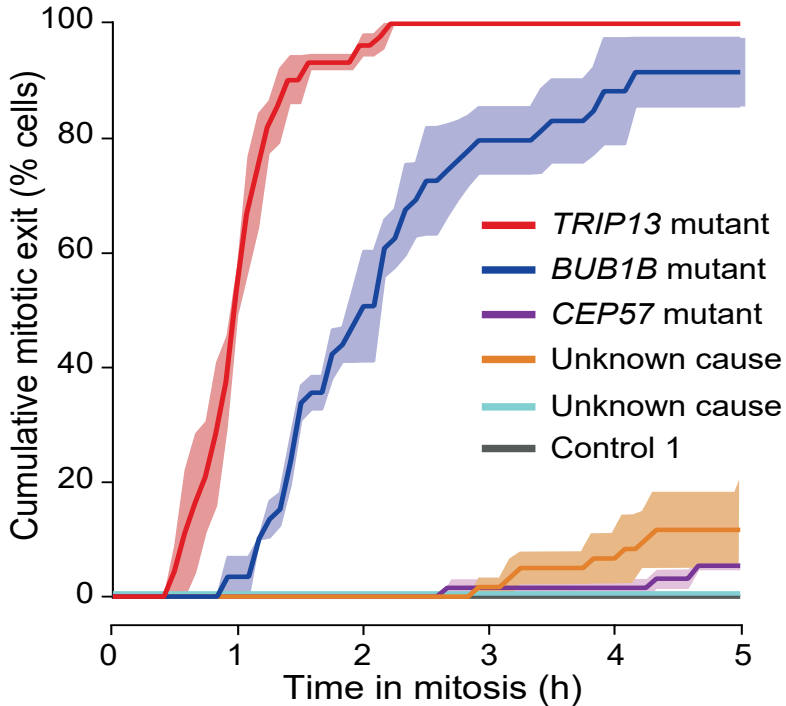


Figure 4. Patient cells with *TRIP13* or *BUB1B* mutations have a severely compromised SAC. Analysis of mitotic delay as in **Figure 1D** in nocodazole-treated patient lymphoblasts from patients with MVA treated with far-red DNA dye to visualize the DNA, showing the cumulative percentage of cells that exited from mitosis as a function of time (mean of three independent experiments \pm s.e.m. (shaded regions), with 60 cells in total per cell line. Only *TRIP13*-mutant and *BUB1B*-mutant patient cells rapidly escaped from mitotic arrest.

All six children with biallelic *TRIP13* mutations developed Wilms tumor in childhood, five of whom were successfully treated (**Table 1**). Limited information is available, but there were no obvious distinctive histopathological features in the tumors. Individuals with biallelic *BUB1B* mutations are also at high risk of childhood embryonal tumors. In fact, all MVA cases with childhood solid tumors in our series had either *BUB1B* or *TRIP13* mutations. By contrast, only one individual with MVA in our series without mutations in *BUB1B* or *TRIP13* had developed cancer, an acute lymphoblastic leukemia (ALL), at 3 years; the cause of MVA remains unknown in this child¹⁰. It is therefore tempting to speculate that the high cancer risk may be causally related to severe impairment of the SAC (see also **chapter 6.4**). Irrespective of the mechanism, our findings have clinical utility, indicating that individuals positive for mutations in *BUB1B* and *TRIP13* are at high risk of cancer and require close surveillance, whereas other individuals with MVA may be at lower cancer risk.

The data also suggest that the mechanism generating aneuploidy in affected individuals determines the cancer risk, not the aneuploidy per se. If confirmed, this is an important distinction, as there has long been a debate regarding whether aneuploidy is a cause or consequence of cancer⁵. Further studies into the biological sequelae of these rare human mutations may therefore provide insights into the complex relationships between aneuploidy and carcinogenesis.

ACKNOWLEDGEMENTS

We thank the families for their participation and the researchers who recruited them, including K. Asakura-Hay, S. Bernardo de Sousa, P. Callier, D. Chitayat, J. Clayton-Smith, S. Fernandes, D. FitzPatrick, L. Florentin, J. Hurst, B. Isidor, S. Jacquemont, R. Marin Iglesias, M. Micalé and J. Tolmie. We thank H.J. Snippert (UMC Utrecht) for providing the lentiviral H2B plasmid. We thank A. Renwick, S. Mahamdallie, C. Loveday and members of the Kops laboratory for helpful discussions and A. Strydom and B. Rex for assistance in preparing the manuscript. We acknowledge NHS funding to the Royal Marsden/ICR NIHR Biomedical Research Centre. This research was supported by the Wellcome Trust (100210/Z/12/Z), by the Netherlands Organisation for Scientific Research (NWO-ALW 823.02.004 to G.J.P.L.K.) and by the Dutch Cancer Society (KWF Kankerbestrijding to R.M.d.V., KUN2014-6666).

Author Contributions

N.R. designed and oversaw the study. G.K. designed and oversaw the functional experiments. E. Ra. undertook the exome sequencing. S.H., H.W. and S.Se. performed the molecular analyses. S.Y., M.C., and E.Ru. performed bioinformatic analyses. B.dW., E.U., R.dV., B.E. and C.M. undertook functional analyses under the supervision of G.K., and J.P. S.P., A.S., S.Sm., G.H. provided samples and data, coordinated by A.Z. and A.E. S.Y., S.H., B.dW., A.Z., G.K. and N.R. wrote the paper with input from the other authors.

Competing Financial Interests

The authors declare that they have no competing financial interests.

URLs

OpEx variant calling pipeline: www.icr.ac.uk/opex

ICR1000 UK exome series: www.icr.ac.uk/icr1000exomes

Exome Aggregation Consortium (ExAC): <http://exac.broadinstitute.org>.

1000 Genomes Project: <ftp://ftp.1000genomes.ebi.ac.uk/vol1/ftp/release/20110521/>

PLINK: <http://pngu.mgh.harvard.edu/~purcell/plink/>

Exon-Primer from UCSC: <http://genome.ucsc.edu/>

METHODS

Data availability statement

The authors declare that the data supporting the findings of this study are available within the paper and its supplementary information. The ICR1000 UK exome series data is available at the European Genome-phenome archive (EGA), reference number EGAD00001001021.

Samples

The study was approved by the London Multicentre Research Ethics Committee (05/MRE02/17). For mutational analyses DNA was obtained through our ongoing research of cancer predisposition syndromes. Appropriate consent was obtained from patients and/or parents as applicable. DNA was extracted from whole blood or an EBV-transformed lymphoblastoid cell line (ID_0644, ECACC ID:96061307) using standard protocols.

For the functional experiments the following patient LCLs were used: ID_0644 (patient 1, biallelic *TRIP13* mutations, ECACC ID:96061307), ID_7054 (patient 2, biallelic *TRIP13* mutations), ID_0675 (patient with biallelic *BUB1B* mutations, Coriell ID:GM22006), ID_0663 (patient with biallelic *CEP57* mutations, Coriell ID:GM21654), ID_0639 (Coriell ID:GM09703) and ID_5728_01 (ECACC ID:FACT5728DLB).

Two control LCLs were also used: ID_5728_03, an unaffected sibling of ID_5728_01 (control 1, ECACC ID:FACT5728KC) and C0106 (control 2, ECACC ID:91071212). Cells were cultured in RPMI supplemented with 15% fetal bovine serum (FBS), 100 µg/ml penicillin/streptomycin and 2 mM alanine-glutamine. Cells expressing H2B-mNeon were created by lentiviral transduction, using standard procedures.

Exome sequencing

We performed exome sequencing using the TruSeq Exome Enrichment Kit (Illumina) or the Nextera Rapid Capture Exome Kit (Illumina). For TruSeq exome sequencing we prepared libraries from 1.5 µg genomic DNA using the TruSeq Paired-End DNA Sample Preparation Kit (Illumina). DNA was fragmented using Covaris technology and libraries were prepared without gel size selection. For Nextera exome sequencing we prepared libraries from 50 ng genomic DNA using the Nextera DNA Sample Preparation Kit (Illumina). Captured DNA libraries were PCR amplified using the supplied paired-end PCR primers. Paired-end sequencing was performed on an Illumina HiSeq 2000 or HiSeq 2500 (high output mode) using v3 chemistry.

Alignment and variant calling

We used OpEx v1.0 pipeline to perform variant calling (www.icr.ac.uk/opex)²¹. Raw data was converted to FASTQs using CASAVA version 1.8.2 with default settings. The OpEx v1.0 pipeline uses Stampy²² to map to the human reference genome, Picard (<http://picard.sourceforge.net>) to flag duplicates, Platypus²³ to call variants, and CAVA²⁴ to provide consistent annotation of variants with the HGVS-compliant CSN (Clinical Sequencing Notation) standard v1.0²⁴. Only high quality calls, as defined by OpEx, were used in the analyses.

Reference datasets

We used the following datasets as control samples: the Exome Aggregation Consortium (ExAC) data¹³ version 3 accessed on 13/11/2015 (excluding the TCGA samples), the 1000 Genomes Project data²⁵ and the ICR1000 UK exome series²⁴. The ICR1000 UK exome series was generated using the same sequencing and analysis pipelines as the cases.

PTV prioritization method

The protein truncating variant (PTV) prioritization method is a gene-based strategy that aims to prioritize potential disease-associated genes for follow-up by leveraging two properties of protein truncating variants: (1) the strong association of rare truncating variants with disease, and (2) collapsibility; different PTVs within a gene typically result in the same functional effect and can be combined equally. We output all the predicted protein truncating variants: stop gains, coding frameshifts and essential splice site variants (-2, -1, +1, +2). For this experiment we defined 'rare' as PTVs that had an alternate allele frequency <1% in the control datasets. We next stratified the genes according to the number of different rare PTVs called in each affected individual.

Recessive analysis

We prioritized variants for evaluation in each affected individual assuming a recessive inheritance model. We removed all intronic, 3'/5' UTR, and non-essential splice site variants and any variant that had an allele frequency >1% in control datasets. We also removed any heterozygous variant combination pair or homozygous alternate variant in which both alleles were from a single parent.

Sanger sequencing

We used Sanger sequencing to confirm the *TRIP13* mutations identified in patients through exome sequencing and to confirm the presence of mutation following CRISPR-Cas9-mediated knockout of *TRIP13* in HCT116 cells. For patient samples, primers were designed using Exon-Primer from the UCSC genome browser. PCRs were prepared using the QIAGEN Multiplex PCR Kit (QIAGEN) according to the manufacturer's instructions. Amplicons were bidirectionally sequenced using the BigDyeTerminator Cycle sequencing kit and an ABI 3730 automated sequencer (Life Technologies). We analyzed sequencing traces using Mutation Surveyor software (SoftGenetics) and by visual inspection. For samples derived from HCT116 cells, primers were designed manually and PCRs were prepared using the Phusion® High-Fidelity DNA Polymerase PCR protocol (New England BioLabs) according to the manufacturer's instructions. Amplicons were sent to Macrogen for sequencing and sequencing traces were analyzed using ApE version V2.0.49.10 software and by visual inspection. Primer sequences are available on request.

Multidimensional scaling analysis

We used the multidimensional scaling (MDS) analysis tool provided by PLINK to identify which population in the 1000 Genomes Project was most similar to the individuals with the *TRIP13* c.1060C>T_p.Arg354X mutation. To identify the set of variants to use in the MDS analysis, we took the union of all coding and splice-site base substitutions in the 45 individuals with exome sequencing data and the 1000 Genomes Project individuals. We then removed variants for which 20 or more individuals had less than 15x coverage. We selected a subset of the individuals to use in the MDS analysis (**Figure S5**). We then used PLINK to remove variants with a minor allele frequency <0.01 or a Hardy-Weinberg equilibrium p-value <1x10⁻¹⁰. We removed non-independent variants using default settings for the --indep-pairwise method in PLINK (--indep-pairwise 50 5 0.5). We then used the MDS algorithm (--mDS-plot) to extract the first four dimensions from the variant data.

HCT116 cell culture and *TRIP13* knockout

HCT116 cells were cultured in McCoy's-5A medium supplemented with 10% Tet-approved FBS, 100 µg/ml penicillin/streptomycin and 2 mM alanyl-glutamine. HCT116 *TRIP13* knockout cells were generated by transient expression of pSpCas9(BB)-2A-GFP (Addgene 48138) with sgRNA against exon 11 (sgTRIP13 in **Table S2**), followed by single-cell FACS sorting of GFP⁺ cells. Knockouts were verified by immunoblotting for protein expression and Sanger sequencing (**Figures S8 and S9**).

HeLa cell culture and stable Trex Flp-In cell line creation

HeLa Trex Flp-In cells were grown in DMEM high glucose supplemented with 10% Tet-approved FBS, 100 µg/ml penicillin/streptomycin, 2 mM alanyl-glutamine, 4 µg/ml blasticidin and 200 µg/ml hygromycin. To generate stably integrated HeLa Flp-In cell lines, pCDNA5-constructs were co-transfected with pOG44 recombinase in a 1:9 ratio using Eugene HD (Roche) according to the manufacturer's instructions. Constructs were expressed by addition of 1 µg/ml doxycycline for 24 hours.

Plasmids, cloning and virus production

For the HeLa Trex Flp-In cell lines stably expressing *TRIP13*, pcDNA5-LAP-TRIP13-WT was created by cloning *TRIP13* cDNA derived from HeLa cells into empty pCDNA5-LAP using the cDNA PCR primers in **Table S2** and digestion with BamHI and SpeI. pcDNA5-LAP-TRIP13-p.Arg354X was created by PCR mutagenesis of pcDNA5-LAP-TRIP13-WT using the Gibson Assembly strategy²⁶ with two fragments generated using the Mutagenesis 1 and 2 PCR primers in **Table S2**.

Lentiviral *TRIP13* constructs were derived from a lentiviral construct encoding fluorescently tagged histone 2B (H2B) and a puromycin-resistance cassette (pLV-H2B-mNeon-ires-Puro)²⁷. The fluorescently tagged H2B was substituted by LAP-TRIP13-WT derived from pcDNA5-LAP-TRIP13-WT (see above) with LAP-TRIP13-WT PCR primers in **Table S2** and digestion with AscI and NheI. For the subsequent steps the Gibson Assembly strategy was used²⁶. The puromycin resistance cassette was substituted by fluorescently tagged H2B (H2B-mNeon 1 and 2 primers in **Table S2**). The CMV promoter was substituted by the ubiquitin promoter from pUB6/V5-His vector (Invitrogen) (pUB 1 and 2 primers in **Table S2**). Finally, the *TRIP13* c.1060C>T_p.Arg354X mutation was inserted by assembling two PCR fragments generated with the Mutagenesis 1 and 2 primers in **Table S2**.

Virions were generated by transient transfection of HEK 293T cells with the transfer vector and separate plasmids that express Gag-Pol, Rev, Tat and VSV-G. Supernatants were clarified by filtration.

Live cell imaging analysis of chromosome segregation errors

Lymphoblasts stably expressing H2B-mNeon were arrested in early S-phase for 24 hours by addition of 2 mM thymidine. Cells were then released from thymidine for 4 hours and mitotic progression was assayed. Cells were plated in 8-well Ibidi µ-slides in a thin layer of 0.15% UltraPure agarose with a layer of 0.3% agar on top. Cells were imaged in a heated chamber (37°C and 5% CO₂). Images were acquired every 3 minutes at 1 x 1 binning in 15 x 15 µm z layers and projected to a single layer by maximum intensity projection using NIS-

Elements software 4.45.

Imaging was performed with a Nikon Ti-Eclipse microscope equipped with CSUW spinning disk (yokogawa), Borealis, Andor iXon Ultra 888 EMCCD camera, 40x water objective NA 1.15 WD 0.6 mm, and 488 nm laser. Analysis of these experiments was carried out with ImageJ software. Chromosome segregation errors include one or more lagging chromosomes, misaligned chromosomes, chromosome bridges, and multipolar mitoses. Percentage of chromosome segregation errors is the amount of divisions with one or more mitotic errors divided by the total amount of divisions. Three or four independent experiments were performed. Quantifications were subjected to two-sided unpaired Student's t-tests; $P < 0.05$.

Live cell imaging analysis of mitotic delay

Lymphoblasts or HCT116 cells were synchronized and plated as described above (HCT116 cells were plated in 24-well plates without agarose). After release from thymidine, mitotic progression was assayed in the presence of $0.83 \mu\text{M}$ nocodazole. For experiments in **Figure 4**, lymphoblasts were incubated with 100 nM SiR-DNA dye (Spirochrome) for 4 hours prior to imaging, to facilitate visualization of mitotic arrest. For experiments in **Figure 3**, cells were infected with a lentivirus expressing LAP-TRIP13 (wt or p.Arg354X)-IRES-H2B-mNeon, ensuring that H2B-mNeon-positive cells co-express LAP-TRIP13.

Images (far-red for **Figure 4**; mNeon for **Figure 1D**, **Figure 3B-C**) were acquired every 5 minutes on a Nikon Ti-Eclipse widefield microscope equipped with an Andor Zyla 4.2 sCMOS camera, 40x oil objective NA 1.3 WD 0.2 mm, and Lumencor SpectraX light engine. Analysis of these experiments was carried out with ImageJ software. Time in mitosis was defined as the time between chromosome condensation and anaphase onset. Three independent experiments were performed. Quantifications were subjected to two-sided unpaired Student's t-tests; $P < 0.05$.

Immunofluorescence imaging

Cells were plated on round 12 mm coverslips (coated with poly-L-lysine (Santa Cruz) according to manufacturer's instructions for LCLs) and treated for 2.5 hours with $3.3 \mu\text{M}$ nocodazole and $5 \mu\text{M}$ MG132 before being pre-extracted with 0.1% Triton X-100 in PEM (100 mM PIPES pH 6.8, 1 mM MgCl_2 and 5 mM EGTA) for ± 60 seconds before fixation with zinc formalin fixative, 1:1 in PEM with 0.1% Triton X-100 for 5-10 minutes. Coverslips were washed twice with cold PBS and blocked with 3% BSA in PBS for 16 hours at 4°C , incubated with primary antibodies for 16 hours at 4°C , washed 4 times with PBS containing 0.1% Triton X-100, and incubated with secondary antibodies for 1 hour at room temperature. Coverslips were then washed 4 times with PBS/0.1% Triton X-100 and mounted using ProLong Gold Antifade with DAPI (Molecular Probes). All images were acquired on a deconvolution system (DeltaVision Elite; Applied Precision/GE Healthcare) equipped with a 100x/1.40 NA UPlanSApo objective (Olympus) using SoftWorx 6.0 software (Applied Precision/GE Healthcare). Images are maximum intensity projections of deconvolved stacks. A CellProfiler40²⁸ pipeline was used to threshold and select all kinetochores and all chromosome areas (excluding kinetochores) using the DAPI and CENP-C. This was used to calculate the relative average kinetochore intensity of various proteins ((kinetochores- chromosome arm intensity (kinetochore localized protein of interest))/(kinetochores- chromosome arm intensity (CENP-C))). Quantifications were subjected to two-sided unpaired Student's t-tests; $P < 0.05$. Primary

antibodies used were guinea pig anti-CENP-C (MBL International, PD030), rabbit anti-MAD2 (custom raised against full-length 6 x His-tagged MAD2 as antigen) and mouse anti-MAD1 (Millipore, MABE867). Secondary antibodies used were goat anti-guinea pig Alexa Fluor 647 (A21450), goat anti-rabbit Alexa Fluor 488 (A11034) and anti-mouse Alexa Fluor 568 (A11031), all obtained from Invitrogen Molecular Probes.

Quantitative real-time PCR

Lymphoblasts were seeded at 500,000 cells/ml in 20 ml medium and split in two the following day. 50% of cells were treated with 100 µg/ml cycloheximide (Sigma) for 4.5 hours, and the remaining cells were left untreated. Total mRNA was extracted using the RNeasy Mini Kit (Qiagen). Equal amounts of RNA (0.5 µg) were reverse-transcribed using the iScript cDNA Synthesis Kit (Bio-Rad) with an optimum blend of oligo(dT) and random hexamers. Real-time quantification was performed with IQ SYBR green Supermix (Bio-Rad) on a CFX connect Real-Time system (Bio-Rad) using probes generated against *TRIP13* and *GAPDH* (qPCR 1 and 2 primer pairs in **Table S2**). The data were normalized to *GAPDH* expression and patient sample data were compared to the average expression of two control samples to quantify relative expression levels of *TRIP13*, using the $2^{-\Delta\Delta Ct}$ method. Three independent independent experiments were performed.

Immunoblotting analysis of TRIP13 expression

For the data in **Figures S3, S4 and S7** cells were treated as indicated and lysed in Laemmli lysis buffer (4% SDS, 120 mM Tris pH 6.8 and 20% glycerol). Lysates were processed for SDS-polyacrylamide gel electrophoresis and transferred to nitrocellulose membranes. Immunoblotting was performed using standard protocols. Visualization of signals was performed on an Amersham Imager 600 scanner using enhanced chemiluminescence. For quantification of immunostainings, all images of similarly stained independent experiments were acquired with identical illumination settings. Primary antibodies used were mouse anti-Tubulin (Sigma, T5168), mouse anti-GFP (Roche, 11-814-460-001), rabbit anti-Histone H3 (Abcam, ab1791) and rabbit anti-TRIP13 (Abcam, ab128171). Secondary antibodies used and obtained from Bio-Rad were goat anti-mouse HRP (170-6516) and goat anti-rabbit HRP (170-6515), both obtained from Bio-Rad.

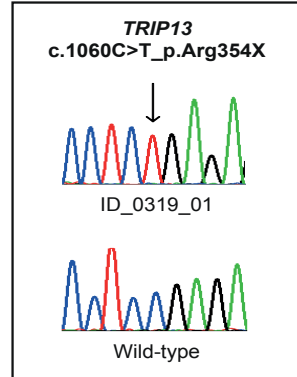
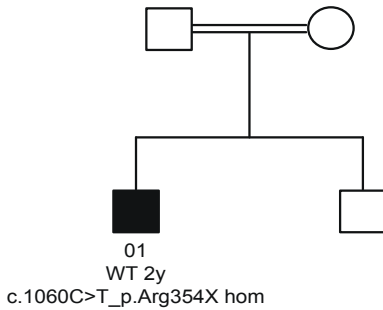
Immunoblotting analysis of TRIP13 p31^{comet} and MAD2 expression

For the data in **Figure S7** cell pellets were resuspended in lysis buffer (50 mM Tris pH 7.5, 150 mM NaCl, 0.5% NP-40 supplemented with 1 tablet per 10 ml of protease inhibitor cocktail (Roche) and 10 µM microcystin), vortexed and incubated for 20 minutes on ice. They were clarified by centrifugation for 10 minutes at 4°C at 14000 rpm. Protein concentration was measured by Bradford assay using Coomassie Plus Protein Assay reagent (Thermo Scientific). Absorbance at 595 nm was measured on a spectrophotometer (Amersham). Primary antibodies used were Mad2 (Bethyl, A300-301A), p31^{comet} (Clone E29.19.14; a kind gift of Andrea Musacchio), beta tubulin (Sigma, T4026) and TRIP13 (Bethyl lab, A303-605A). Secondary antibodies used were IRDye 800CW donkey anti-rabbit (926-32213) and IRDye 680CW donkey anti-mouse (926-68072). The molecular marker used was Odyssey® One-Color Protein Molecular Weight Marker (928-40000). Quantitative immunoblotting was performed using an Odyssey infrared imager (LICOR Biosciences) running Odyssey

v1.2 software. Images were opened in ImageStudio Lite and the mean intensity values were extracted by drawing rectangles around the band of interest. The background was measured close to each individual band and automatically subtracted by the software. Protein levels were normalized to tubulin as a loading control.

SUPPLEMENTARY DATA

ID_0319. The proband was the first child of consanguineous parents of Asian origin. He had microcephaly and severe global developmental delay. An MRI scan showed multiple cerebral cysts and neuronal migration defects. Dysmorphic features included large low-set ears, a beaked nose and cleft palate. He also had arthrogryposis, severe cone-rod dystrophy and nystagmus. He had a horseshoe kidney and developed Wilms tumor (WT) at 2 years. Chromosome analysis confirmed a diagnosis of MVA, although karyotypic details were not provided. Parental samples were not available. The proband was alive at 6 years of age.



ID_0644. The proband, of Asian origin, had short stature and developed WT at 4 years and relapsed at 5 years. Tumor histology is unknown. Chromosome analysis of cells from an EBV-transformed lymphoblastoid cell line showed gains and losses of various chromosomes. Cells from two different passages were analyzed. Aneuploidy was present in 13/28 (46%) cells from the initial passage and in 19/25 (76%) cells following four subsequent passages. Premature chromatid separation (PCS) was also observed. Parental samples were not available. The proband was alive at 43 years of age.

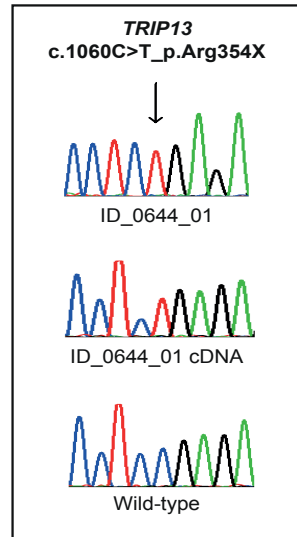
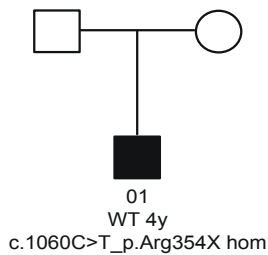


Figure S1. Case reports, pedigrees and chromatograms of individuals with mutations in *TRIP13*.

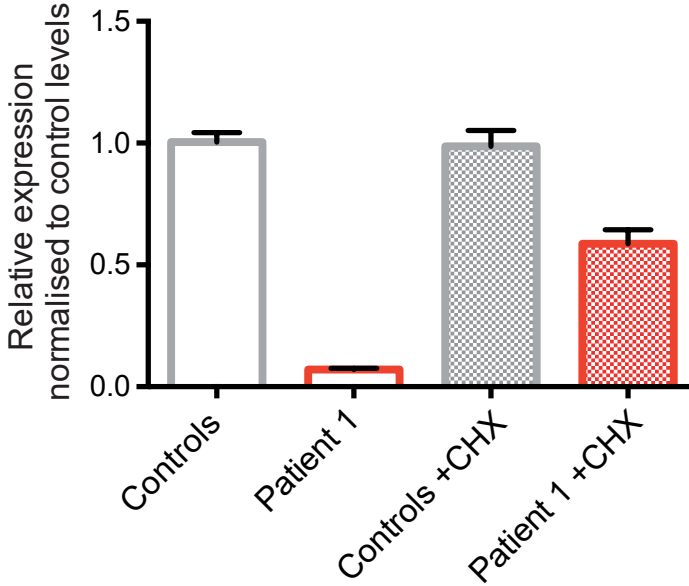


Figure S2. *TRIP13* p.Arg354X mRNA is degraded by nonsense-mediated mRNA decay. q-PCR analysis of *TRIP13* mRNA in controls and patient 1 lymphoblasts, untreated or treated with the inhibitor of nonsense-mediated mRNA decay cycloheximide for 4.5 hrs. *TRIP13* p.Arg354X mRNA is degraded by nonsense-mediated mRNA decay. Key: controls, average data from control 1 and control 2; CHX, cycloheximide.

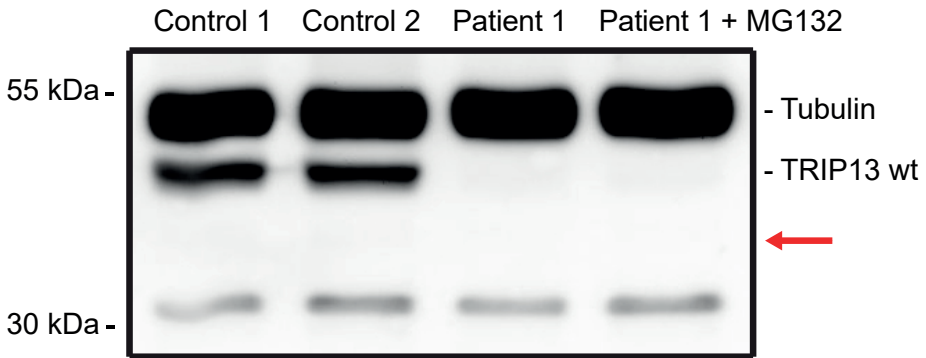


Figure S3. *TRIP13* p.Arg354X leads to absence of TRIP13 protein. Control 1, control 2 and patient 1 lymphoblast whole cell lysates were immunoblotted for TRIP13 and tubulin. Right-most lane of patient 1 lymphoblasts were treated with the proteasome inhibitor MG132 for 8 hours. The red arrow indicates the expected position of the truncated TRIP13 protein resulting from the p.Arg354X patient mutation. No TRIP13 protein can be detected in patient lymphoblasts. Key: wt, wild-type.

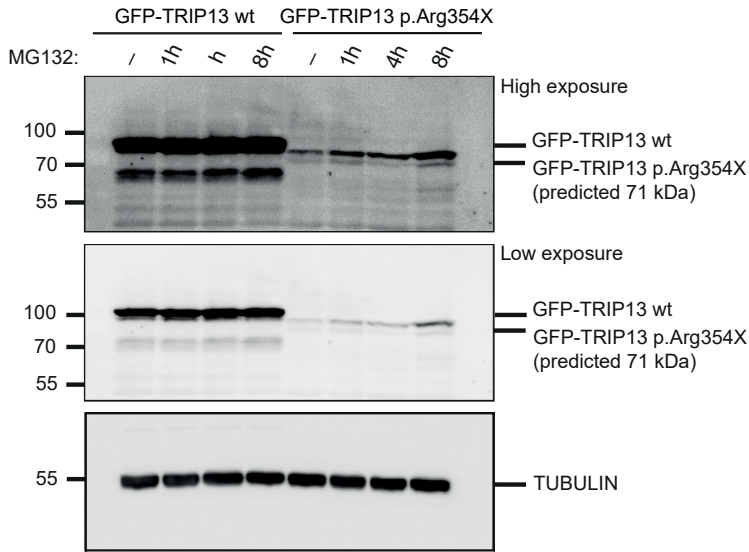


Figure S4. *TRIP13* p.Arg354X expressed from cDNA in HeLa cells is present at a much lower level compared to wild-type *TRIP13*. Whole cell lysates of HeLa T-REx Flp-In cells ectopically expressing GFP-*TRIP13* wt or p.Arg354X from the same genomic locus were immunoblotted for *TRIP13* and tubulin after treatment without (-) or with the proteasome inhibitor MG132 for indicated amount of hours. GFP-*TRIP13* p.Arg354X was expressed at significantly lower levels compared to wild type, even after being treated with MG132 for 8 hours. Key: wt, wild-type; GFP, green fluorescent protein.

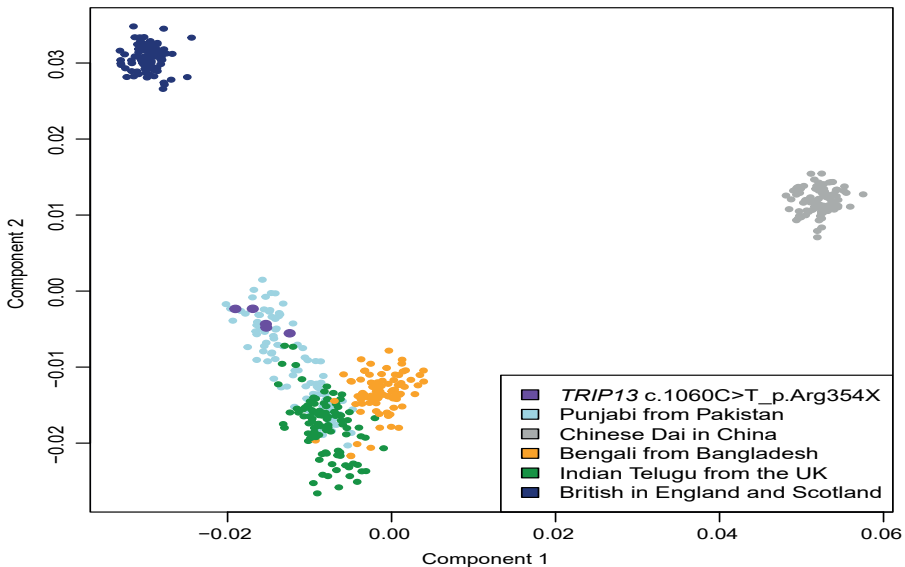


Figure S5. MDS analysis strongly suggests the families with the *TRIP13* c.1060C>T_p.Arg354X mutation are from Pakistan. Multidimensional scaling analysis (MDS) of individuals with *TRIP13* c.1060C>T_p.Arg354X mutation and select individuals from 1000 Genomes project. Individuals with the *TRIP13* c.1060C>T_p.Arg354X mutation are closely related to the Pakistan group from the 1000 Genomes project.

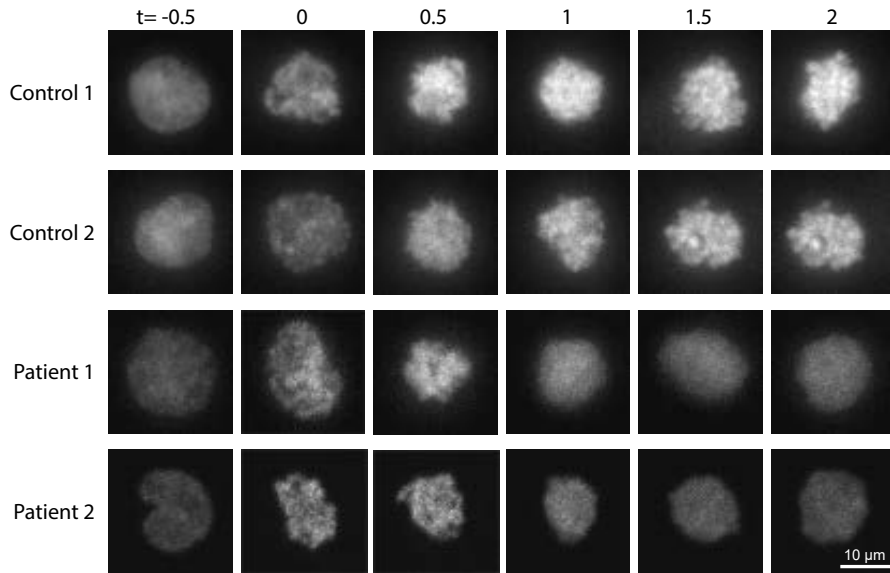


Figure S6. *TRIP13* p.Arg354X mutant patient cell lines exit mitosis within 1 hour. Representative images of H2B-mNeon expressing control (row one and two) and patient (row three and four) lymphoblasts going through mitosis (time in hours with mitotic entry at t=0.0) in the presence of nocodazole. Both patient 1 and patient 2 cells exit from mitosis after 1 hour.

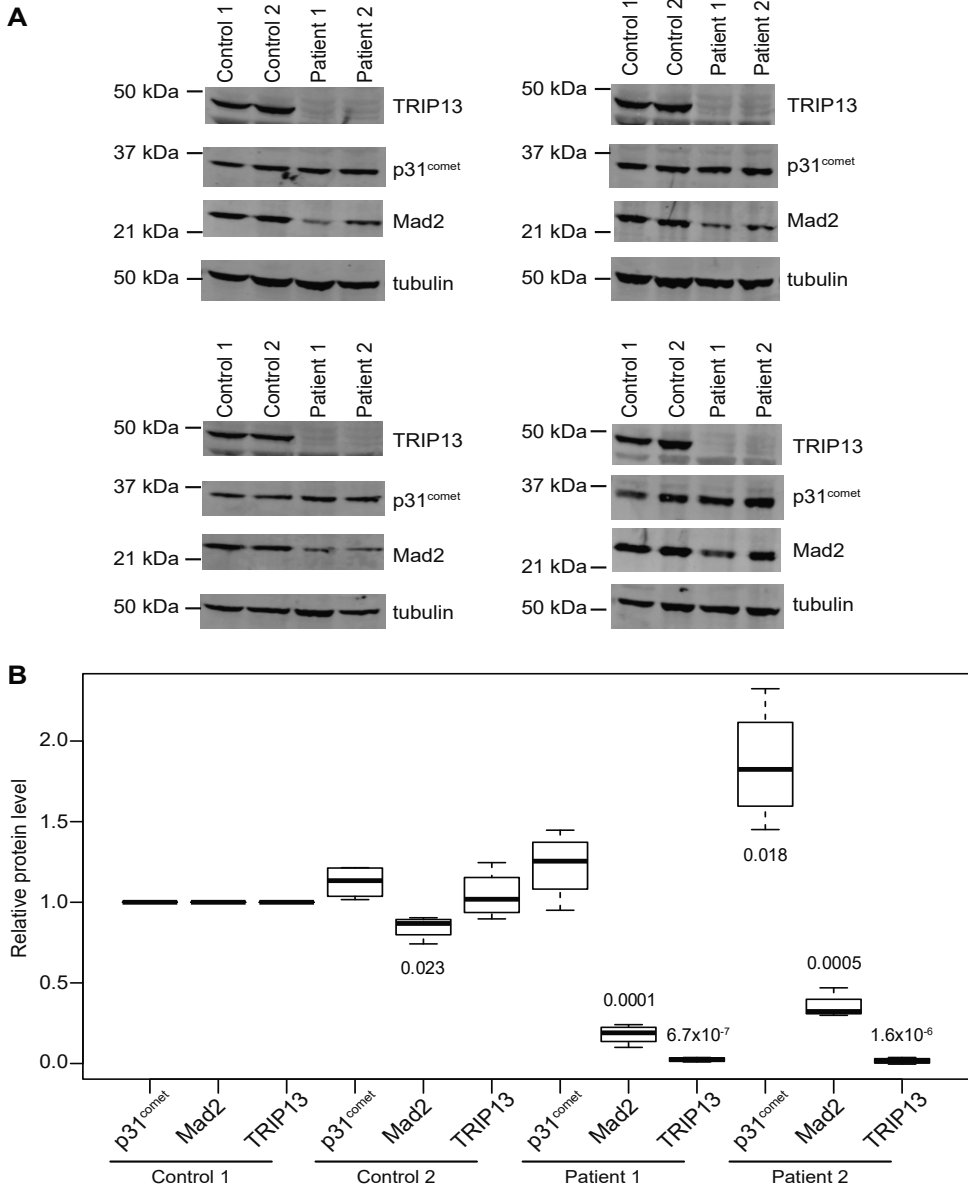


Figure 57. *TRIP13* p.Arg354X cells have increased p31^{comet} and reduced MAD2 expression. (A) Immunoblots of cell lysates that were probed with anti-MAD2, anti-p31^{comet} and anti-TRIP13 antibodies. Tubulin was used as loading control. **(B)** MAD2, p31^{comet} and TRIP13 levels were first normalized against tubulin and subsequently against the control cell line (control 1). Bars are the average of 4 independent experiments with SEM shown. Unpaired Student t-test against control 1 was applied for statistical analyses, shown are P-values ≤ 0.005 . Both patient 1 and patient 2 cells show statistically significantly decreased levels of MAD2 and TRIP13; one patient has significantly increased levels of p31^{comet}. Key: SEM, standard error of the mean.

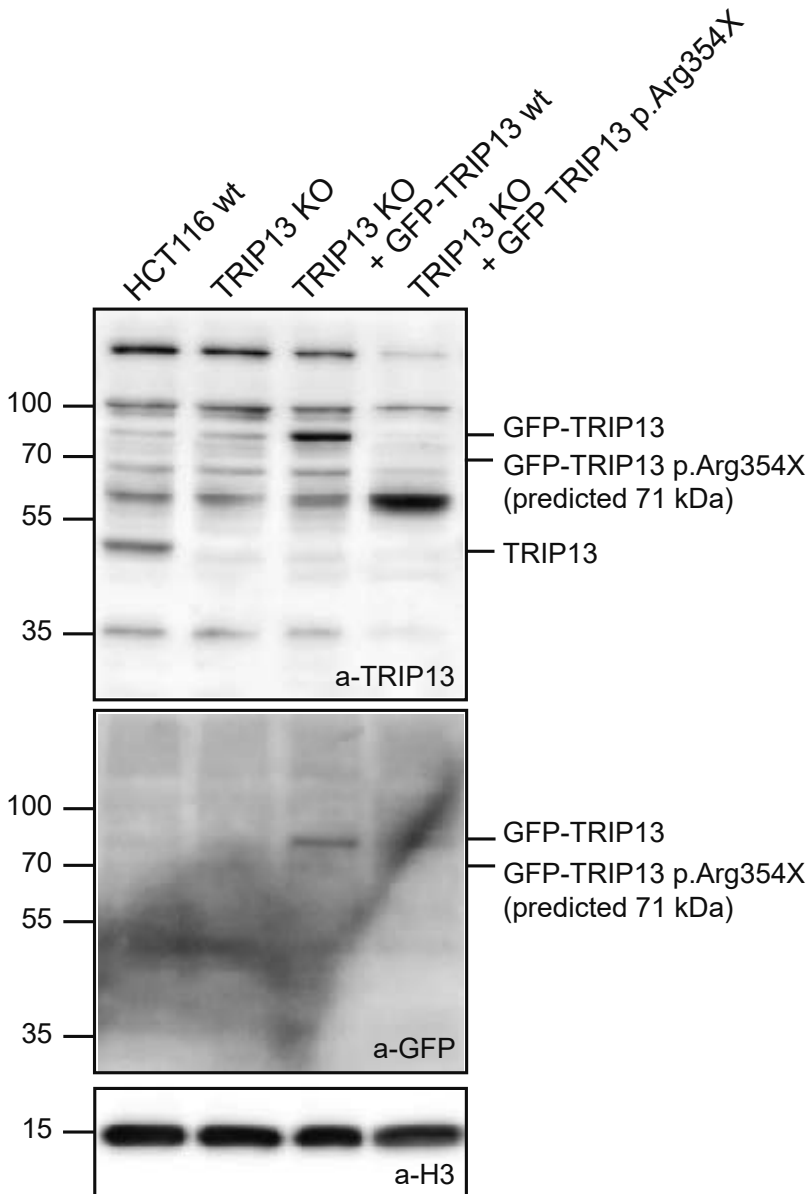


Figure S8. TRIP13 protein levels of HCT116 wt and TRIP13 KO cells with or without ectopic expression of TRIP13 wt or p.Arg354X. Whole cell lysates of HCT116 wt and TRIP13 KO cells transduced with GFP-TRIP13 wt or GFP-TRIP13 p.Arg354X lentivirus, when indicated, were immunoblotted for TRIP13, GFP or tubulin. GFP-TRIP13 wt is indeed expressed, but GFP-TRIP13 p.Arg354X is not detected. Key: wt, wild-type; KO, knockout; GFP, green fluorescent protein; H3, Histone H3.

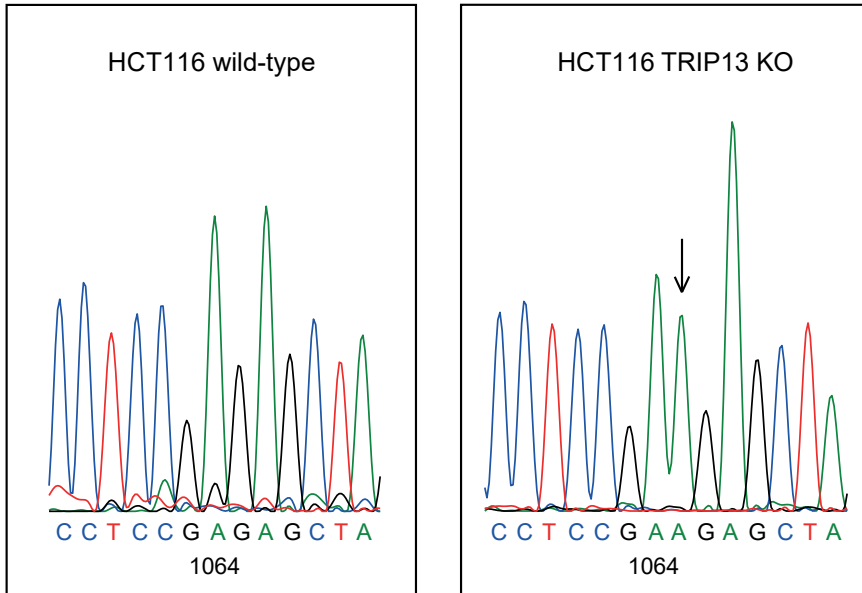


Figure S9. Sanger validation of homozygous alternate *TRIP13* c.1064dupA in the HCT116 *TRIP13* KO clone. Sanger sequencing reads of a PCR product amplified from the genomic DNA of HCT116 wt and *TRIP13* KO cells. The *TRIP13* KO cells have a single bp duplication in exon 11 causing a frameshift. Key: KO, knockout.

Table S1. Summary of samples from MVA families included in exome sequencing experiment.

Family ID	Individuals exome sequenced
ID_0641	Proband, Mother, Father
ID_0642	Proband
D_0648	Proband
ID_0658	Proband
ID_0660	Proband, Mother, Father, Unaffected_sib
ID_0664	Proband, Mother, Father
ID_0668	Proband, Mother, Father
ID_0671	Proband, Mother, Father
ID_1992	Proband, Mother, Father
ID_2129	Proband
ID_5823	Proband
ID_5827	Proband
ID_0319	Proband
ID_0639	Proband
ID_0640	Proband
ID_0644	Proband
ID_0661	Proband, Mother, Father
ID_5728	Proband, Mother, Father, Affected_sib, Unaffected_sib
ID_6246	Proband, Mother, Father
ID_7054	Proband, Mother, Father

Table S2. List of primers used.

Name	Forward	Reverse	Description
sgTRIP13	CACCGCAATCATCTCTAGCTCTCGG		sgRNA for HCT116 TRIP13 KO
cDNA	GCGCGGGATCCgacgaggccgtggg-cgaccctg	gcgcgactagttaaatgtaagctgcaagcttc	PCR TRIP13 cDNA
Mutagenesis 1	ctgccagcagctgctgaccctctaagagc-tagagatgattggcttc	GGCAGCAC TGCATAATTCT	Mutagenesis of TRIP13-WT to TRIP13-p.Arg354X
Mutagenesis 2	gaagccaatcatctctagctcttagagggt-cagcagctgctggcgag	AGAATTATGCAGTGCTGCC	Mutagenesis of TRIP13-WT to TRIP13-p.Arg354X
LAP-TRIP13-WT	atatggcgcgccagcttatggtgagcaag-ggc	atatgctagcttaaatgtaagctgcaagctcttcttc	Replacing H2B-mNeon with LAP-TRIP13-WT
H2B-mNeon 1	acctggtgcatgaccgcaaa	ggcgaccgttggcccatat	Replacing puromycin cassette with H2B-mNeon (pLV primers)
H2B-mNeon 2	atatgggataatagccacaacggtcgccatgccagagccagcgaagtc	ggcaccggccttgcgggtcatgcccaccaggtcgaccgggtagctagcctgtgac	Replacing puromycin cassette with H2B-mNeon (H2B primers)
pUB 1	cgtttagtgaccgtcagatcgc-3'	cggaaactccaagcttattcga-3'	Replacing CMV with ubiquitin promoter (pLV primers)
pUB 2	aaaatttattcgataagcttggagttccgcGAAAAAGTGCCACCTGACGTC-3'	gtctccaggcgtatcgaccgtcactaaacgAAGCTT-CGTCTAACAAAAAAGCCA-3'	Replacing CMV with ubiquitin promoter (pUB6 primers)
qPCR 1	CGTGTGATTGATGAGGTGG	ACGTGATCTTCTCGGTGAT	Quantitative real-time PCR: TRIP13
qPCR 2	5'-AATCCCATCACCATCTTCCA	TGGACTCCACGACGTACTCA	Quantitative real-time PCR: GAPDH

REFERENCES

1. Garcia-Castillo, H., Vasquez-Velasquez, A.I., Rivera, H. & Barros-Nunez, P. Clinical and genetic heterogeneity in patients with mosaic variegated aneuploidy: delineation of clinical subtypes. *Am J Med Genet A* 146a, 1687-95 (2008).
2. Warburton, D., Anyane-Yeboah, K., Taterka, P., Yu, C.Y. & Olsen, D. Mosaic variegated aneuploidy with microcephaly: a new human mitotic mutant? *Ann Genet* 34, 287-92 (1991).
3. Hanks, S. *et al.* Constitutional aneuploidy and cancer predisposition caused by biallelic mutations in BUB1B. *Nat Genet* 36, 1159-61 (2004).
4. Snape, K. *et al.* Mutations in CEP57 cause mosaic variegated aneuploidy syndrome. *Nat Genet* 43, 527-9 (2011).
5. Ricke, R.M. & van Deursen, J.M. Aneuploidy in health, disease, and aging. *J Cell Biol* 201, 11-21 (2013).
6. Holland, A.J. & Cleveland, D.W. Boveri revisited: chromosomal instability, aneuploidy and tumorigenesis. *Nat Rev Mol Cell Biol* 10, 478-87 (2009).
7. Torres, E.M., Williams, B.R. & Amon, A. Aneuploidy: cells losing their balance. *Genetics* 179, 737-46 (2008).
8. Thompson, S.L., Bakhoun, S.F. & Compton, D.A. Mechanisms of chromosomal instability. *Curr Biol* 20, R285-95 (2010).
9. Kajii, T. *et al.* Cancer-prone syndrome of mosaic variegated aneuploidy and total premature chromatid separation: report of five infants. *Am J Med Genet* 104, 57-64 (2001).
10. Jacquemont, S., Boceno, M., Rival, J.M., Mechinaud, F. & David, A. High risk of malignancy in mosaic variegated aneuploidy syndrome. *Am J Med Genet* 109, 17-21; discussion 16 (2002).
11. Ruark, E. *et al.* OpEx - a validated, automated pipeline optimised for clinical exome sequence analysis. *Sci Rep* 6, 31029 (2016).
12. Mahamdallie, S.S. *et al.* Mutations in the transcriptional repressor REST predispose to Wilms tumor. *Nat Genet*, 1471-1474 (2015).
13. Lek, M. *et al.* Analysis of protein-coding genetic variation in 60,706 humans. *Nature* 536, 285-91 (2016).
14. Ruark, E. *et al.* The ICR1000 UK exome series: a resource of gene variation in an outbred population. *F1000Res* 4, 883 (2015).
15. Vader, G. Pch2(TRIP13): controlling cell division through regulation of HORMA domains. *Chromosoma* 124, 333-9 (2015).
16. Eytan, E. *et al.* Disassembly of mitotic checkpoint complexes by the joint action of the AAA-ATPase TRIP13 and p31(comet). *Proc Natl Acad Sci U S A* 111, 12019-24 (2014).
17. Ye, Q. *et al.* TRIP13 is a protein-remodeling AAA+ ATPase that catalyzes MAD2 conformation switching. *Elife* 4(2015).
18. Wang, K. *et al.* Thyroid hormone receptor interacting protein 13 (TRIP13) AAA- ATPase is a novel mitotic checkpoint-silencing protein. *J Biol Chem* 289, 23928-37 (2014).
19. Nelson, C.R., Hwang, T., Chen, P.H. & Bhalla, N. TRIP13PCH-2 promotes Mad2 localization to unattached kinetochores in the spindle checkpoint response. *J Cell Biol* 211, 503-16 (2015).
20. Ma, H.T. & Poon, R.Y. TRIP13 Regulates Both the Activation and Inactivation of the Spindle-Assembly Checkpoint. *Cell Rep* 14, 1086-99 (2016).
21. Vleugel M, Hoogendoorn E, Snel B, Kops GJ. Evolution and function of the mitotic checkpoint. *Dev Cell* 23, 239-50 (2012).
22. Lunter, G. & Goodson, M. Stampy: a statistical algorithm for sensitive and fast mapping of Illumina sequence reads. *Genome Res* 21, 936-9 (2011).
23. Rimmer, A. *et al.* Integrating mapping-,

- assembly- and haplotype-based approaches for calling variants in clinical sequencing applications. *Nat Genet* 46, 912-8 (2014).
24. Munz, M. *et al.* CSN and CAVA: variant annotation tools for rapid, robust next-generation sequencing analysis in the clinical setting. *Genome Med* 7, 76 (2015).
 25. Abecasis, G.R. *et al.* An integrated map of genetic variation from 1,092 human genomes. *Nature* 491, 56-65 (2012).
 26. Gibson, D.G. *et al.* Enzymatic assembly of DNA molecules up to several hundred kilobases. *Nat Methods* 6, 343-5 (2009).
 27. Drost, J. *et al.* Sequential cancer mutations in cultured human intestinal stem cells. *Nature* 521, 43-7 (2015).
 28. Carpenter, A.E. *et al.* CellProfiler: image analysis software for identifying and quantifying cell phenotypes. *Genome Biol* 7, R100 (2006).



CHAPTER 4

CONSTITUTIONAL ANEUPLOIDY CAUSED BY DEFECTS IN SPLICING OF A RARE MINOR INTRON SUBTYPE

Bas de Wolf, Ali Oghabian*, Maureen V. Akinyi*, Sandra Hanks*, Eelco C. Tromer, Jolien J.E. van Hooff, Lisa van Voorthuijsen, Laura E van Rooijen, Jens Verbeeren, Esther C.H. Ujttewaal, Marijke P.A. Baltissen, Shawn Yost, Philippe Piloquet, Michiel Vermeulen, Berend Snel, Bertrand Isidor, Nazneen Rahman⁺, Mikko J. Frilander⁺, Geert J.P.L. Kops⁺

* Contributed equally

⁺ Joint senior authors

bioRxiv 2020.08.06.239418

ABSTRACT

Aneuploidy is the leading cause of miscarriage and congenital birth defects, and a hallmark of cancer. Despite this strong association with human disease, the genetic causes of aneuploidy remain largely unknown. Through exome sequencing of patients with constitutional mosaic aneuploidy, we identified biallelic truncating mutations in *CENATAC* (*CCDC84*). We show that CENATAC is a novel component of the minor (U12-dependent) spliceosome that promotes splicing of a specific, rare minor intron subtype. This subtype is characterized by AT-AN splice sites and relatively high basal levels of intron retention. CENATAC depletion or expression of disease mutants resulted in excessive retention of AT-AN minor introns in ~100 genes enriched for nucleocytoplasmic transport and cell cycle regulators, and caused chromosome segregation errors. Our findings reveal selectivity in minor intron splicing with a specific impact on the chromosome segregation process, and show how defects herein can cause constitutional aneuploidy.

INTRODUCTION

Chromosome segregation errors in mitosis or meiosis lead to aneuploidy, a karyotype that deviates from an exact multiple of the haploid set of chromosomes (**chapter 1.1**). Aneuploidy is the leading cause of congenital birth defects and associated with approximately 35% of all spontaneous human abortions (Nagaoka et al., 2012) (**chapter 1.3**). Furthermore, roughly 70% of human tumors are aneuploid, making it one of the most common genomic alterations in cancer (Duijf and Benezra, 2013; Knouse et al., 2017). Despite this common association of aneuploidy with human disease, little is known about its genetic causes. The study of aneuploidy-associated hereditary disorders can be instrumental in uncovering these causes.

Mosaic variegated aneuploidy (MVA; OMIM: 257300) is a rare autosomal recessive disorder characterized by mosaic aneuploidies in multiple tissues (**chapter 2.3.5, chapter 3**). Patients often present with microcephaly, developmental delay, various congenital abnormalities, and childhood cancers (**Addendum Table 1**) (García-Castillo et al., 2008). Pathogenic mutations in *BUB1B*, *CEP57*, or *TRIP13* have been identified in roughly half of all MVA patients (Hanks et al., 2004; Matsuura et al., 2006; Snape et al., 2011; Yost et al., 2017; **chapter 3**). These genes have well-documented roles in chromosome segregation (Sacristan and Kops, 2015; Suijkerbuijk et al., 2010; Vader, 2015; Zhou et al., 2016) (**chapter 2.3.5**). All three gene products (BUBR1, CEP57 and TRIP13) promote spindle assembly checkpoint (SAC) function (Alferi et al., 2018; Ma and Poon, 2016; Musacchio, 2015; Wang et al., 2014; Zhou et al., 2016), and BUBR1 and CEP57 additionally ensure correct kinetochore-microtubule attachment (Emanuele and Stukenberg, 2007; Sacristan and Kops, 2015) (see also **chapter 2.1**). As predicted, such mitotic processes are defective in cells from MVA patients carrying biallelic mutations in these genes, explaining the chromosomal instability (CIN) phenotype and resulting aneuploid karyotypes. CIN can also result from mutations in regulators of expression of mitotic genes. For example, mutations in the retinoblastoma gene (*RB1*) causes CIN by over expression of the SAC protein MAD2 (Hernando et al., 2004; Schwartzman et al., 2011; Sotillo et al., 2007). In this work, we show that chromosome segregation errors can be caused by a specific defect in minor intron splicing, another process governing correct gene expression.

While the conventional, major spliceosome targets most (>99.5%) human introns, the minor spliceosome recognizes and excises only a small subset (~700 introns) (Moyer et al., 2020; Turunen et al., 2013). These minor introns (also called U12-type introns) have highly conserved 5' splice site (5'ss) and branch point (BPS) sequences that are longer and differ at the sequence level from the respective sequences in major (U2-type) introns. Most minor introns have AT-AC or GT-AG terminal dinucleotides (24% and 69%, respectively) (Moyer et al., 2020; Sheth et al., 2006). In addition, the 3' terminal nucleotide can vary, thus giving rise to AT-AN and GT-AN classes of minor introns (Dietrich et al., 2005; Levine and Durbin, 2001). For simplicity, we refer these as A- and G-type introns, respectively. Thus far there has been no indication of mechanistic or functional differences between the minor intron subtypes.

Minor intron "host" genes, the position of the minor intron within the gene, and intron subtypes are all evolutionarily conserved (Abril et al., 2005; Alioto, 2007; Burge et al., 1998; Moyer et al., 2020; Sheth et al., 2006). Despite this high conservation, the functional significance of minor introns has remained elusive. Elevated levels of unspliced minor

introns in various cell types have been reported, giving rise to the hypothesis that these are rate-limiting controls for the expression of their host genes (Niemelä and Frilander, 2014; Niemelä et al., 2014; Patel et al., 2002; Younis et al., 2013). Nevertheless, the overall significance of the elevated intron retention levels has been questioned particularly at individual gene level (Singh and Padgett, 2009).

The overall architecture of the minor and major spliceosomes is highly similar. Both are composed of five small ribonucleoprotein (snRNP) complexes containing small nuclear RNA (snRNA) molecules and a large number of proteins components. One of the snRNAs (U5) is shared between the spliceosome, while U1, U2, U4 and U6 snRNAs are specific to major spliceosome and U11, U12, U4atac, and U6atac snRNAs to the minor spliceosome. Introns are initially recognized by the U1 and U2 snRNPs (major spliceosome) or by the U11/U12 di-snRNP (minor spliceosome), followed by the entry of the U4/U6.U5 snRNP or U4atac/U6atac.U5 tri-snRNP and subsequent architectural changes leading to catalytic activation of the spliceosome (Turunen et al., 2013). At the protein level, the main difference between the spliceosomes is in the composition of U11/U12 di-snRNP that contains seven unique protein components that are needed for recognition of the unique minor intron splice sequences (Will et al., 2004). In contrast, the protein composition between the minor and major tri-snRNPs appears similar, but rigorous comparative analyses have been difficult due to ~100-fold lower cellular abundance of the minor tri-snRNP (Schneider et al., 2002).

Here we report that germline mutations in a novel component of the minor spliceosome (*CENATAC/CCDC84*) cause chromosomal instability in MVA patients. We identify *CENATAC* as a minor spliceosome-specific tri-snRNP subunit that selectively promotes splicing of the A-type minor introns. *CENATAC* mutant patient cells show high levels of A-type intron retention in only a small set of genes including ones involved in chromosome segregation, suggesting a molecular explanation for MVA patient phenotype.

RESULTS

Biallelic truncating mutations in *CENATAC (CCDC84)* cause MVA

To search for additional causes of MVA, we performed exome sequencing and variant analyses on MVA patients and family members, as previously described (Yost et al., 2017) (**chapter 3**). We identified biallelic truncating mutations in coiled-coil domain-containing 84 (*CCDC84*, hereafter named *CENATAC*, for centrosomal AT-AC splicing factor, see below) in two affected siblings with 7.3% and 8.5% aneuploid blood cells, respectively (**Figures 1A, S1**). Both siblings were alive at 47 and 33 years of age and had microcephaly, mild developmental delay, and mild maculopathy (**Addendum Table 1**, patients 49 and 50). Neither individual had short stature, dysmorphism or cancer. Each parent was heterozygous for one of the mutations and the unaffected sibling had neither mutation. Moreover, the mutations were absent from the ExAC and ICR1000 series and we estimated the chance of an individual having two truncating *CENATAC* mutations to be 4.8×10^{-10} (Fitzgerald et al., 2015). We therefore consider it very likely that the *CENATAC* mutations are the cause of the siblings' phenotype. The paternal and maternal mutations (mutation 1 and mutation 2, respectively) both result in the creation of novel splice sites that lead to a frameshift and the loss of the C-terminal 64 amino acids of *CENATAC* (**Figures 1B, S2**). Although expression of

the mutant alleles was very low in the parental cells, expression of the maternal allele was elevated in the cells of patient 1 (hereafter called patient), and was responsible for the low expression of wild-type protein in these cells due to infrequent recognition of the original splice site (**Figures 1C, S2C**).

CENATAC is an essential gene whose product has previously been reported to interact with pre-mRNA splicing factors and to localize to centrosomes where it suppresses centriole over-duplication and spindle multipolarity (Hart et al., 2015; Wang et al., 2019). Analysis of *CENATAC* sequence conservation in metazoan species revealed the presence of two N-terminal C₂H₂ zinc-fingers and four well-conserved C-terminal sequence motifs, of which the two most C-terminal are lost as a result of the patient mutations (**Figures 1B, S3**).

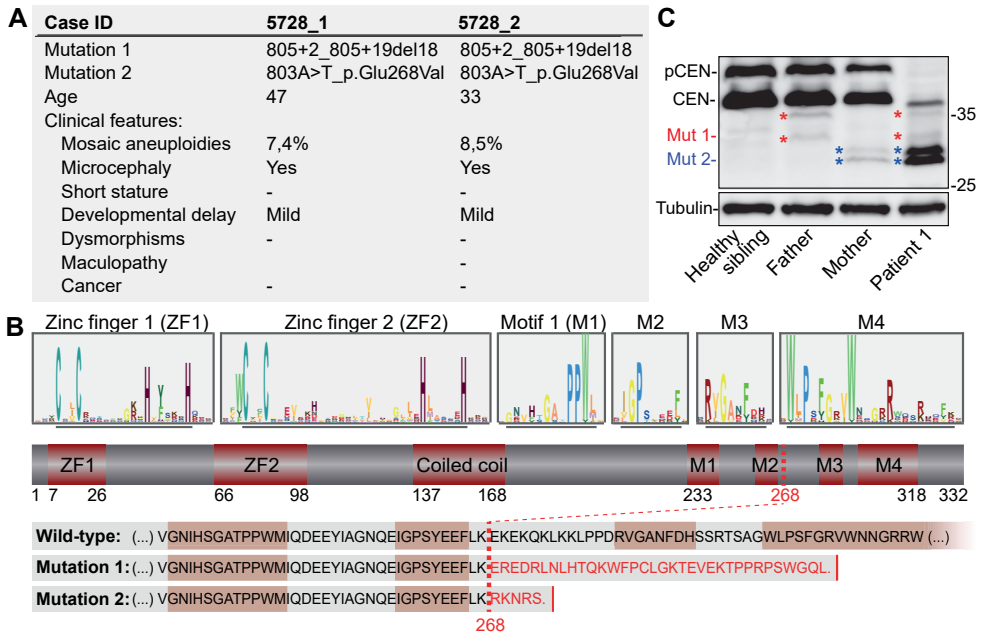


Figure 1. Biallelic truncating mutations in *CENATAC* (*CCDC84*) cause MVA.

A) Clinical phenotypes of *CENATAC* (*CCDC84*) mutant patients. See also **Figure S1**. **B)** Schematic representation of *CENATAC* annotated with zinc fingers (ZF1 and ZF2), predicted coiled coil, and conserved motifs 1-4 (M1-M4). Upper: sequence logos of both zinc fingers and the conserved residues defining motifs 1-4 (underlined). See **Figure S3** for the full-length logo. Lower: C-terminal protein sequences of wild-type and MVA mutant *CENATAC*. The MVA truncation site is indicated by the red dotted line; the four conserved motifs are outlined in red. **C)** *CENATAC* and tubulin immunoblots of lysates from lymphoblasts of patient 1 and relatives. Wild-type and truncated, mutant proteins are indicated. Wild-type *CENATAC* (CEN): 38 kDa. Mut1: 34.5 kDa (red asterisks), Mut2: 31.1 kDa (blue asterisks). pCEN indicates phosphorylated *CENATAC* (Wang et al., 2019).

CENATAC promotes error-free chromosome segregation

Live imaging of chromosome segregation in *CENATAC*-mutant patient lymphoblasts stably expressing H2B-mNeon (Yost et al., 2017) (**chapter 3**) revealed a mild chromosomal instability phenotype, consistent with the modest levels of aneuploidy in blood cells of these

patients (**Figures 1A, 2A**). To examine if *CENATAC* patient mutations cause chromosomal instability, we expressed mutant *CENATAC* alleles in HeLa cells in which the endogenous loci were modified to express AID-degron-tagged *CENATAC* (EGFP-AID-*CENATAC*, **Figure S4**) (Nishimura et al., 2009). Efficient depletion of *CENATAC* through a combination of siRNA treatment and auxin addition caused chromosome congression defects and a subsequent mitotic arrest (**Figures 2B-C, S4**). This phenotype was fully rescued upon re-expression of wild-type but not MVA-mutant *CENATAC* (**Figures 2C, S5 and S6**). Similarly, *CENATAC* alleles missing either of the two most C-terminal conserved motifs (**Figure 1B**, motifs 3 and 4) that are absent from MVA-mutant *CENATAC* did not rescue the mitotic defects. Instead, expression of the MVA or motif 3/4 mutants exacerbated the phenotype, suggesting that these proteins dominantly repressed the function of any residual wild-type protein (**Figure 2C**). Mutations in the zinc fingers or deletion of motifs 1 or 2 only partly compromised *CENATAC* function (**Figures 1B, 2C**).

Live imaging of EGFP-AID-*CENATAC* cells with fluorescently labelled chromatin and microtubules revealed that the chromosome congression defect upon *CENATAC* depletion preceded the previously described loss of spindle bipolarity (**Figures 2D-E and S7, Movies S1 and S2**) (Wang et al., 2019). In addition, we did not observe centriole over-duplication in *CENATAC*-depleted cells (**Figure S7C-D**). This is in contrast to what was recently reported for *CENATAC* knockout cells (Wang et al., 2019), raising the possibility that centriole over-duplication is a cumulative effect of prolonged *CENATAC* loss. Our attempts to examine this failed, as we were unable to create *CENATAC* knockout cells, consistent with it being an essential human gene (Blomen et al., 2015; Hart et al., 2015; Wang et al., 2015). Taken together, these data show that *CENATAC* has a function in promoting chromosome congression in mitosis, which is likely unrelated to its role in maintaining spindle bipolarity, and that MVA mutant *CENATAC* is defective for this function.

CENATAC is a novel component of the minor spliceosome

To investigate in which processes *CENATAC* plays a role, we performed a genome-wide, evolutionary co-occurrence analysis. Genes that function in the same biochemical process experience similar evolutionary pressures and therefore tend to co-evolve, i.e. they are lost or retained in a coherent fashion (Pellegrini et al., 1999). Genomes from a set of 90 informative eukaryotic species (**Table S1**) were mined for the presence or absence of *CENATAC* orthologs (Hooff et al., 2017). This provided a phylogenetic absence/presence profile that was used in an unbiased genome-wide query for genes with similar phylogenetic profiles (**Figure 3A**). The resulting list of genes most strongly co-occurring with *CENATAC* was significantly enriched for components of the minor (U12-dependent) spliceosome complex (**Figure 3B, Table S2**). We thus reasoned that *CENATAC* may play a role in splicing by the minor spliceosome.

As predicted by our co-evolution analysis and in agreement with a previous high-throughput screen (Hart et al., 2015; Hein et al., 2015; Huttlin et al., 2015, 2017), mass spectrometry analysis of proteins co-purifying with *CENATAC* identified several known spliceosome components that are shared by both the major and minor spliceosomes (**Figures 3C, S8**). Notably, the strongest *CENATAC* interactor (TXNL4B) was also the gene that showed the most significant co-occurrence with *CENATAC* in eukaryotic species (**Figure 3A**). To deter-

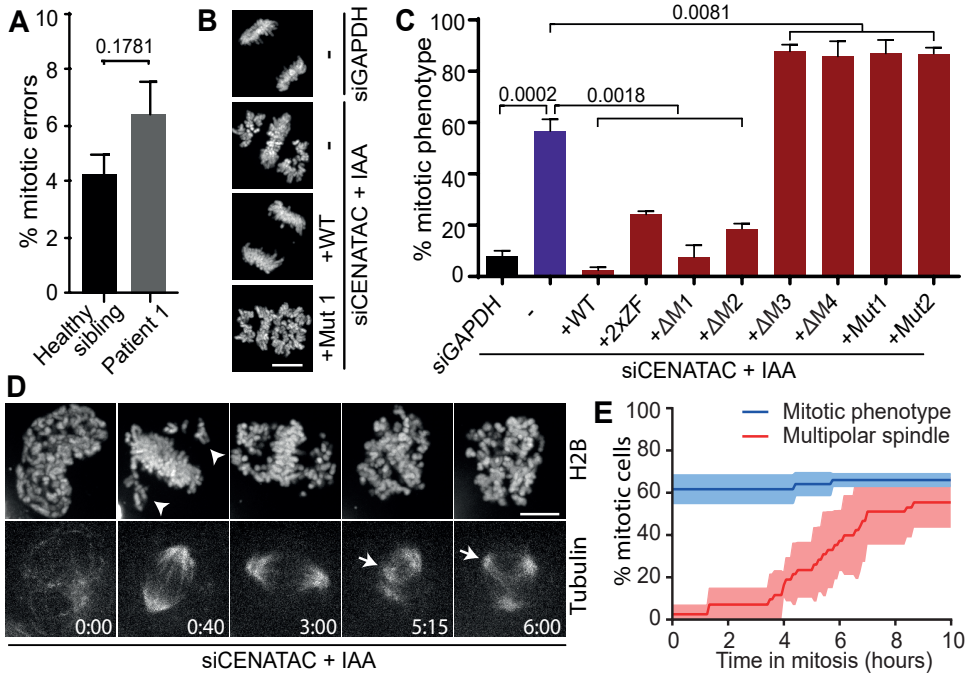


Figure 2. CENATAC promotes error-free chromosome segregation.

A) Quantification of chromosome segregation errors of patient and control lymphoblasts expressing H2B-mNeon. Each bar depicts the mean of four independent experiments \pm s.e.m., with >200 cells in total per condition. The P-value was calculated with a two-sided unpaired Student's t test. **B)** Representative images of H2B-mNeon-expressing EGFP-AID-CENATAC HeLa cells depleted of GAPDH (upper) or CENATAC (middle and lower) with or without re-expression of CENATAC variants as indicated. Scale bar, 10 μ m. **C)** Quantification of mitotic defects as in B) of cells treated as indicated. For 2xZF the four zinc-finger cysteines were mutated to alanines; for Δ 1-4 the corresponding motif was removed. Each bar depicts the mean of three or five independent experiments \pm s.e.m., with >85 cells in total per condition. P values were calculated with two-sided unpaired Student's t tests. **D)** Representative stills of EGFP-AID-CENATAC HeLa cells expressing H2B-mNeon and depleted of CENATAC. Microtubules were visualized with SiR-Tubulin. Arrowheads and arrows indicate non-congressed chromosomes and supernumerary spindle poles, respectively. Scale bar, 5 μ m. Time in hours. See **Figure S7** for the control condition. See also **Movies S1 and S2** **E)** Quantification of the mitotic phenotype and multipolar spindle formation in time in cells treated as in E). Each line depicts the mean of three experiments \pm s.e.m., with >44 cells in total per condition. See also **Figure S7**.

mine whether CENATAC preferentially associates with major or minor spliceosome components, we analyzed CENATAC co-immunoprecipitations by Northern blot analysis. This revealed a significant enrichment for the minor spliceosome-specific U4atac and U6atac snRNAs (**Figures 3D-E, S9**) CENATAC's association with the minor spliceosome was further supported by glycerol gradient analyses of HeLa nuclear extract preparations, which showed co-migration of CENATAC with U6atac snRNP, U4atac/U6atac di-snRNP and U4atac/U6atac.U5 tri-snRNP complexes (**Figure 3F**). Together, these data validate CENATAC as a bona fide functional component of the minor spliceosome and the first identified protein component that is specific to the U4atac/U6atac and U4atac/U6atac.U5 snRNP complexes (**Figure 3G**).

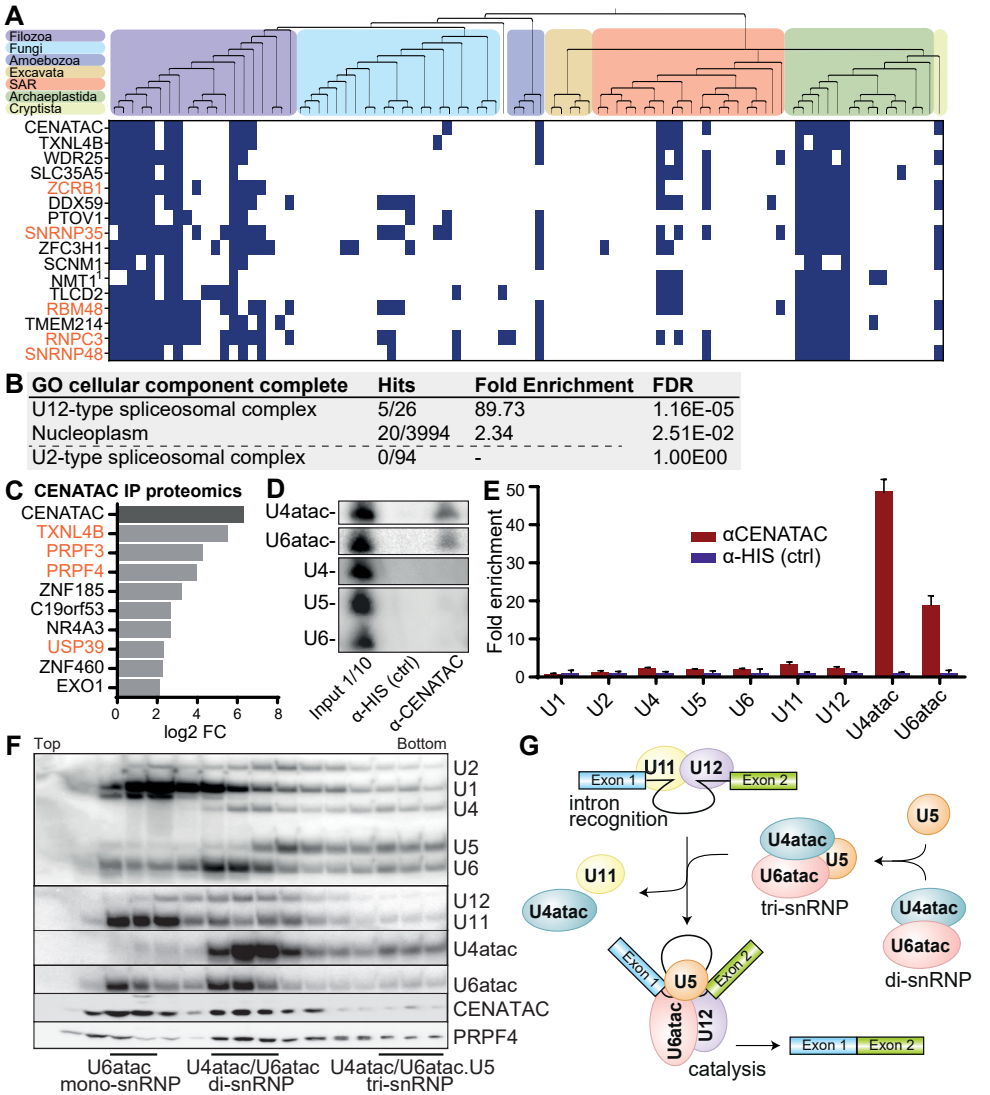


Figure 3. CENATAC is a novel component of the minor spliceosome.

A) Phylogenetic profiles (presences (blue) and absences (white)) of the top 15 genes co-occurring with *CENATAC* in go eukaryotic species. Top: phylogenetic tree of the eukaryotic species (see **Table S1**) with colored areas for the eukaryotic supergroups. ¹ for *NMT1* no human ortholog was found and instead the *Arabidopsis thaliana* ortholog is depicted. Genes associated with the minor (U12-dependent) spliceosome are depicted in orange. See also **Table S2**. **B)** GO term analysis of the genes co-occurring with *CENATAC* as in **A)** with a correlation score of >0.5 . **C)** Graph of fold-changes of proteins enriched (P-value < 0.05) in proteomics analysis of *CENATAC* vs. control co-immunoprecipitations. Each bar depicts the fold change of the mean log₂ transformed LFQ intensity of three independent experiments. Splicing factors are depicted in orange. See also **Figure S8**. **D-E)** Examples (**D**) and quantification (**E**) of Northern blot analyses of minor (U6atac, U4atac, U11, and U12) and major (U2, U1, U4, U5, and U6) spliceosome snRNAs. Each bar depicts the mean of 3 experiments normalized to the control \pm std. dev. See also **Figure S9**. **F)** Glycerol gradient analysis of HeLa nuclear extracts. snRNAs were detected by Northern blot analysis, proteins (*CENATAC* and *PRPF4*) by western blot. Locations of the U6atac mono-snRNP, U4atac/U6atac di-snRNP and U4atac/U6atac.U5 tri-snRNP are indicated. **G)** Schematics

showing key assembly stages in minor intron splicing and minor tri-snRNP assembly: intron recognition (A-complex) and the catalytic spliceosome (C-complex). For simplicity, several stages of spliceosome assembly are omitted, such as the pre-B-complex, which consists of the the intron recognition complex together with the tri-snRNP before architectural changes lead to the exclusion of U11 to give rise to the B complex, after which subsequent architectural changes lead to the exclusion of U4atac to give rise to the B^{ACT} complex, which is a precursor stage for the catalytically active C complex depicted in this figure (Turunen et al., 2013).

The role of *CENATAC* in minor spliceosome function was further supported by the presence of evolutionarily conserved competing U2-type and U12-type 5' splice sequences (5'ss) in animals that are predicted to generate productive and unproductive *CENATAC* mRNAs, respectively (**Figure S10**). This configuration is indicative of an autoregulatory circuit that is conceptually similar to the previously reported autoregulation of the minor spliceosome proteins 48K and 65K (Turunen et al., 2013; Verbeeren et al., 2010). In agreement with this, impaired minor spliceosome function, such as in Taybi-Linder syndrome (TALS/ MOPD1, OMIM: 210710) patients, leads to a significant increase in the use of U2-type 5'ss and upregulation of *CENATAC* mRNA levels (Cologne et al., 2019). Notably, evidence for a similar autoregulatory circuit is also present in plants (**Figure S10**), where retention or splicing of a U12-type intron results in productive or unproductive *CENATAC* mRNA, respectively.

Minor intron splicing defects in *CENATAC* mutant cells fully correlate with mitotic defects

In agreement with our finding that *CENATAC* is a novel minor spliceosome component, splicing of several minor (U12-type) introns was impaired upon depletion of *CENATAC*, whereas up- or downstream major (U2-type) introns were unaffected (**Figure 4A-B**). This was true also for *CENATAC*-mutant MVA patient cells (**Figure 4B**). Importantly, the splicing defect of U12-type introns in *CENATAC*-depleted cells was fully rescued by re-expression of wild-type but not MVA-mutant alleles (**Figure 4A**). Similar to the mitotic phenotype, expression of the disease alleles and mutants lacking motifs 3 and 4 exacerbated the splicing defect, whereas mutations in the zinc fingers and removal of motifs 1 and 2 partially rescued it (**Figure 4A**). Notably, the extent of the splicing defect strongly correlated with the extent of the mitotic phenotype for all mutations (**Figure 4C**), indicating that the chromosome congression phenotype is a secondary effect of impaired minor spliceosome function.

CENATAC selectively promotes splicing of A-type minor introns

Our discovery of reduced minor spliceosome function in a constitutional aneuploidy syndrome raised the question of which introns and transcripts were affected by *CENATAC* malfunction. To investigate this, we compared the transcriptomes of *CENATAC*-depleted HeLa cells to those of control-depleted and parental cell lines. The resulting RNAseq dataset was analyzed for changes in intron retention (IR) using IntEREst (Oghabian et al., 2018) and for alternative splicing (AS) using Whippet (Sterne-Weiler et al., 2018). In agreement with our RT-PCR-based observations (**Figure 4**), this analysis confirmed the significant retention of U12- but not U2-type introns after *CENATAC* depletion. Surprisingly, it also uncovered a remarkable enrichment for a specific subclass of U12-type introns: while only 24% of G-type introns (with GT-AG, GT-AT, GT-TG, GC-AG terminal dinucleotides) were affected by *CENATAC* depletion, virtually all (92%) of the A-type introns (with AT-AC¹, AT-AA, AT-AG, or AT-AT terminal dinucleotides) showed increased retention or activation of alternative U2-type splice sites (cryptic or annotated), or both (**Figures 5A-B and S11, Table S3**). For comparison, we carried out the same analysis on a previously published dataset

¹ *CENATAC* was named after AT-AC introns which make up 84% of U12 A-type introns

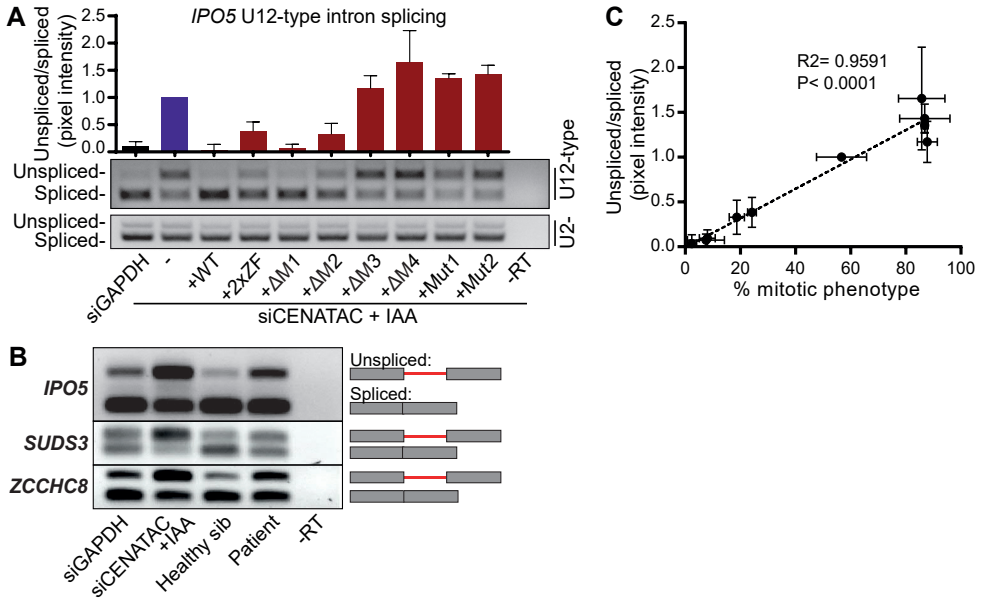


Figure 4. Minor intron splicing defects in *CENATAC* mutant cells fully correlate with mitotic defects.

A) RT-PCR (middle panel) and quantification (upper panel) of *IPO5* minor intron 21 (U12-type intron) splicing on RNA extracted from cells treated as in **Figure 2C**. Each bar depicts the mean of three independent experiments \pm s.e.m., normalized to siCENATAC + IAA. The bottom panel shows RT-PCR analysis of *IPO5* intron 19 (U2-type intron). **B)** RT-PCRs of *IPO5*, *SUDS3* and *ZCCHC8* minor introns on RNA extracted from patient lymphoblasts or EGFP-AID-*CENATAC* HeLa cells depleted of GAPDH or *CENATAC* as indicated. **C)** For each condition in A), U12-type intron splicing (**Figure 4A**) was plotted against the percentage of cells showing a mitotic phenotype (**Figure 2C**). R^2 and p-values are provided for the linear regression trendline (dotted line).

derived from myelodysplastic syndrome (MDS) patients carrying somatic mutations in the gene encoding for the U11/12-di-snRNP subunit *ZRSR2* (Madan et al., 2015). This dataset showed a nearly identical response for A- and G-type introns (**Figure 5B**, **Table S4**). Whereas depletion of *CENATAC* or mutations in *ZRSR2* led to an average increase of approx. 36% and 19% in retention of A-type introns, respectively (average $\Delta\Psi_{\text{CENATAC}} \sim -0.36$ and average $\Delta\Psi_{\text{ZRSR2}} \sim -0.19$), G-type introns were only strongly affected by *ZRSR2* mutations (average $\Delta\Psi_{\text{CENATAC}} \sim -0.07$ and average $\Delta\Psi_{\text{ZRSR2}} \sim -0.19$, **Figures 5C-D**, **S12**). Importantly, the effect on A-type introns was specific to U12-type introns as none of the 85 major AT-AC introns or related subtypes responded to *CENATAC* depletion (**Figure 5**, **Table S3**). The same subtype-specific effect on minor intron splicing was also observed in *CENATAC*-mutant MVA patient lymphoblasts (**Figures 5F and S13**, **Table S5**), in which the affected introns correlated strongly with those affected by *CENATAC* depletion (**Figures 5G**, **S13B**). Notably, the strongly affected transcripts did not include any of the genes known to cause MVA but did contain various mitotic regulators (**Figures S14 and S15**, **Table S3**). We were unable to rescue mitotic defects by restoring expression of individual candidate targets (*CEP170*, *SPC24*, *SMC3*, and *DIAPH2*, data not shown) in *CENATAC*-depleted cells, suggesting that correct splicing of multiple such transcripts may be required for promoting efficient chromosome congression.

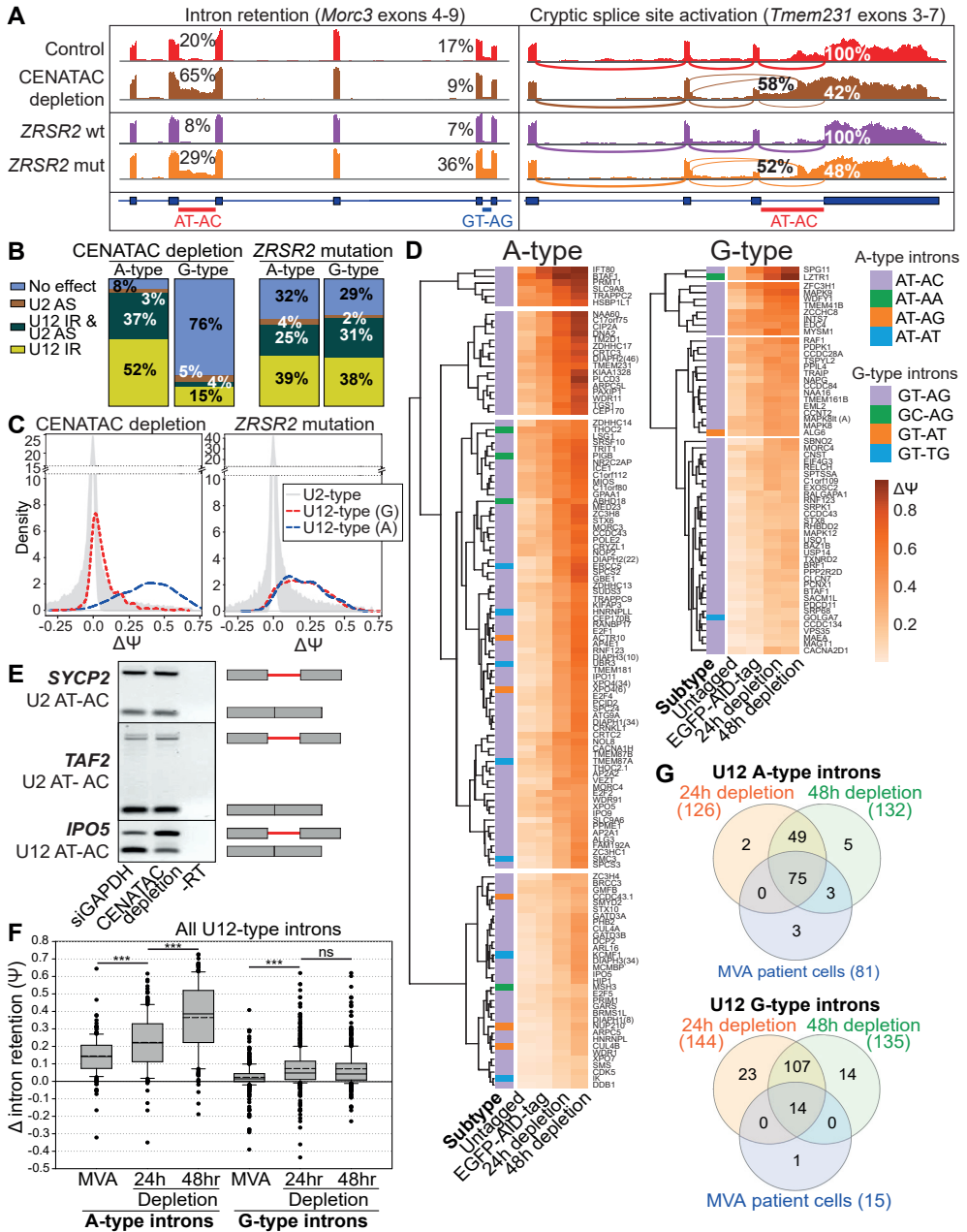


Figure 5. CENATAC selectively promotes splicing of A-type minor introns.

A) Sashimi plots showing the effect of CENATAC depletion (48hr) or *ZRSR2* mutations on AT-AC and GT-AG intron retention (*Morc3*, left panel), and AT-AC intron retention and cryptic splice site activation (*Tmem231*, right panel; percentages depict relative wild-type or parental unedited HeLa cell line usage). CENATAC control represents the parental unedited HeLa cell line. **B)** Transcriptome-wide statistics of CENATAC depletion (48hrs) and *ZRSR2* mutations on G- and A-type minor intron retention (U12 IR) and cryptic U2-type splice site activation (U2 AS). Only introns showing at least 5 exon-exon junctions reads were

included. For U12 IR, a statistical cutoff of $P_{\text{adj}} < 0.05$ was used. For U2 AS the probability cutoff of $P_r > 0.9$ was used. **C**) Density plots showing differences in intron retention (Δ) distribution after CENATAC depletion (48 hours) or in samples with *ZRSR2* mutations. **D**) Hierarchical clustering of A- and G-type intron retention in the unedited parental cell line treated with siGADPH for 48h or in the EGFP-AID-CENATAC cell line treated with siGADPH for 48h or auxin and siCENATAC for 24 or 48 hrs. Only introns showing a $P_{\text{adj}} < 0.05$ and $\Delta > 0.1$ in either the 24hr or 48hr depletion sample were included in the analysis. The A-type and G-type intron terminal dinucleotide subtypes are indicated with different colors in the first column. In case the gene contained multiple introns of the same type, the intron number is indicated in parentheses. **E**) RT-PCR of U2-type AT-AC introns in *SYCP2* (intron 5) and *TAF2* (intron 1), and U12-type AT-AC intron in *IPO5* (intron 21) on RNA extracted from cells depleted of GAPDH or CENATAC. Schematic representations of unspliced/spliced PCR products are depicted on the right. **F**) Δ intron retention values for the MVA patient dataset (compared to the healthy sibling) using all (significant and not significant) U12 A-type introns (n=179 for the depletion and n=177 for the MVA patient datasets) and U12 G-type introns (n=441 for the depletion and n=446 for the MVA patient datasets). Only introns with on average at least 5 intron-mapping reads were used in the analysis. The boundaries of the boxes indicate 25th and 75th percentiles. Whiskers indicate the 90th and 10th percentiles. Median is indicated with solid line, mean with dashed line inside the box. *** - $P < 0.001$, ns - $P > 0.05$ (Mann-Whitney Rank Sum Test). See also **Figure S13**. **G**) Venn-diagram analysis of the MVA and CENATAC depletion datasets. A- and G-type minor introns showing statistically significant intron retention in each dataset were used. See also **Table S6**.

A-type minor introns are spliced less efficiently

We next wished to understand the selectivity of CENATAC-dependent splicing for A-type minor introns. The observation that also some G-type introns were affected by CENATAC depletion (**Figure 5D**) argued against a direct interaction between CENATAC and intron-terminal nucleotides. Moreover, A- and G-type introns that were strongly affected by CENATAC depletion had higher basal levels of intron retention in control conditions compared to those unaffected by CENATAC depletion (**Figure 6A**). This suggested that CENATAC predominantly promotes splicing of U12-type introns that are normally spliced less efficiently, and that A-type introns as a group belong to this category. To test this hypothesis we engineered the widely-used P120 minigene (Hall and Padgett, 1996) to contain two tandem competing A- or G-type splice sites in all possible configurations (**Figure 6B**). Significantly, U12-type GT-AG splice sites were strongly preferred over AT-AC sites when in direct competition (**Figure 6B-C**), and they also outcompeted the unique GC-AG splice site that was significantly affected by CENATAC depletion (**Figures 5D, S16, LZTR1**). We thus conclude that CENATAC promotes splicing of minor introns that are recognized or spliced less efficiently, most prominently A-type minor introns.

DISCUSSION

In this work, we have uncovered a novel link between the minor spliceosome and defects in chromosome segregation in human cells. Using patient exome sequencing, evolutionary co-occurrence analysis and biochemistry, we identified CENATAC as a novel protein component of the U4atac/U6atac di-snRNP and U4atac/U6atac.U5 tri-snRNP that are necessary for the formation of the catalytically active U12-dependent spliceosome. Our RNAseq analysis of both patient cells and cells depleted of CENATAC revealed widespread defects in minor intron splicing, particularly intron retention, but also cryptic splice site activation, indicating that CENATAC is important for minor spliceosome function. Unexpectedly, intron retention in CENATAC depleted cells was strongly biased for A-type minor introns, which is a subtype that is defined by AT-AN dinucleotide splice sites. This in-

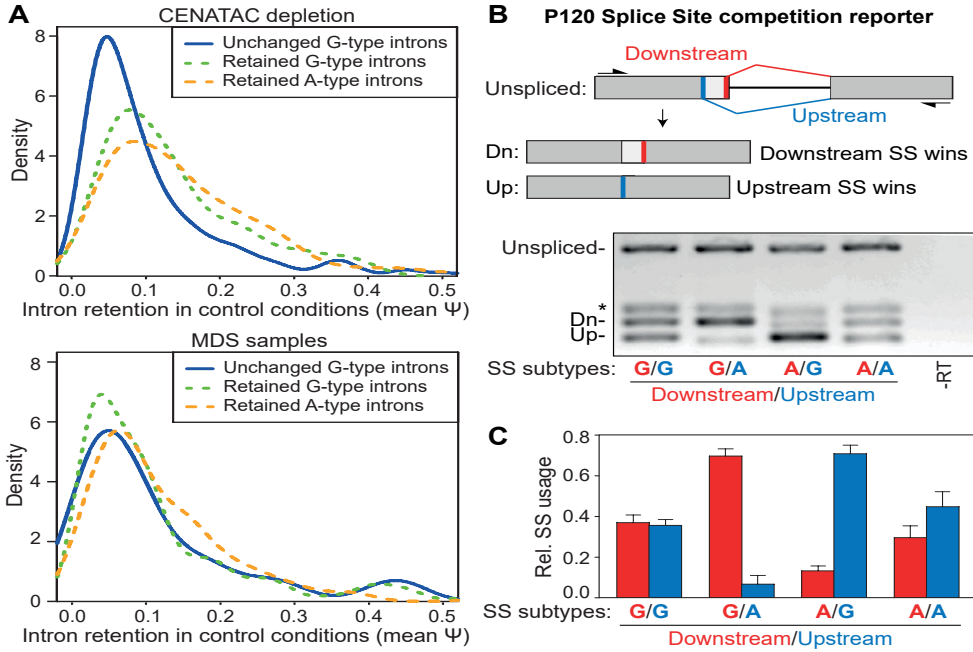


Figure 6. A-type minor introns are spliced less efficiently.

A) Density plots showing intron retention (Ψ) values in the unedited parental control cell line (depleted of GAPDH) of A- and G-type minor introns that were either unchanged or retained after or CENATAC depletion (top) or *ZRSR2* mutation (bottom). The median Ψ -values of the retained G- and A-type introns are significantly higher ($\Psi=0.130$ and $\Psi=0.115$, respectively; $P<0.01$, Mann-Whitney Rank Sum Test) compared to the unchanged introns ($\Psi=0.081$) in the CENATAC depletion dataset. **B)** RT-PCR P120 reporter assay (Hall and Padgett, 1996) to measure the relative usage of A-type (AT-AC) and G-type (GT-AG) 5' splice sites in direct competition. Upper: schematic diagram showing the overall architecture of the reporter construct with its down- and upstream splice site (thick red and blue bars, respectively) and the products created by splicing (Dn and Up, respectively). Lower: RT-PCRs of the reporter with A- or G-type splice sites in the down- or upstream positions as indicated below the gel. SS, splice site. *, PCR product after use of a cryptic U2-type splice site (not shown in the schematic). **C)** Quantification of relative splice site usage of A- and G-type splice sites in B). Cryptic splice site usage (*) in B) was omitted from this plot but included in the quantification.

intron subtype-specific function is unique among the minor spliceosome components and correlates tightly with mitotic fidelity. Minor intron subtype missplicing is therefore likely responsible, possibly in conjunction with centriolar defects, for the inefficient chromosome congression in CENATAC-mutant cells and for the aneuploidies observed in the two MVA siblings.

The minor spliceosome was originally thought to splice only introns with AT-AC termini (Hall and Padgett, 1994, 1996; Tarn and Steitz, 1996). Only later it was shown that there are also U2-type AT-AC introns and that most of the minor introns in fact have GT-AG termini (Dietrich et al., 1997; Sharp and Burge, 1997; Wu and Krainer, 1997) with infrequent variation in the 3' terminal nucleotide (Dietrich et al., 2005; Levine and Durbin, 2001), thus giving rise to AT-AN and GT-AN classes of minor introns that we here referred to as A- and G-type introns. However, none of the subsequent site studies, including several transcriptome-wide

investigations of minor spliceosome diseases, have been able to functionally differentiate the two types of minor introns. Rather, in all known minor spliceosome diseases for which comprehensive transcriptome data is available, splicing defects are roughly uniformly distributed between the A- and G-type introns (Argente et al., 2014; Cologne et al., 2019; Madan et al., 2015; Merico et al., 2015; **Figure 5B**). Thus, the selective A-type intron retention phenotype cannot be explained by a general loss of minor spliceosome functions but instead suggests that CENATAC has a unique, more defined function. Our observation that also a subset of G-type introns are sensitive to CENATAC depletion argues against a direct recognition of the intron 5' adenosine by CENATAC. Instead, our competition data and the observed elevated baseline activity of the affected introns suggest that a subset of minor introns with reduced intrinsic splicing activity may be particularly dependent upon CENATAC activity. This group includes nearly all A-type minor introns. Given that A-type minor intron host genes and the locations of these introns within the host gene are evolutionarily highly conserved among metazoan species, the selectivity of CENATAC in splicing raises the possibility that minor intron subtypes are part of a conserved but unexplored regulatory mechanism for gene expression. CENATAC undergoes reversible modifications (acetylation and phosphorylation) (Wang et al., 2019), which may provide the means to regulate its activity (also) in the minor spliceosome.

What could be the molecular function of CENATAC? Given its participation in di- and tri-snRNP complexes and sensitivity on 5'ss identity, CENATAC may function during or after the transition from initial intron recognition (A-complex) to pre-catalytic spliceosome (B-complex) (**Figure 3G**) and may for instance participate in 5'ss recognition analogous to U11-48K protein in the A-complex (Turunen et al., 2008). For a deep mechanistic understanding, high-resolution structures of relevant minor spliceosome complexes are required. Nevertheless, we note that TXNL4B, the main interactor of CENATAC (**Figures 3A, 3C and S8**), is a paralog of the major spliceosome protein TXNL4A/Dim1, both at sequence and structural level (Jin et al., 2013). High-resolution structures of both yeast and human spliceosomal B-complexes have placed TXNL4A/Dim1 in close proximity of the 5'ss and suggested a role in 5'ss recognition (Bertram et al., 2017; Wan et al., 2016). Assuming that the minor spliceosome B-complex shares the molecular architecture with its major spliceosome counterpart, this would place CENATAC with TXNL4B near the 5'ss to participate in the recognition event.

Presently all mutations associated with MVA have been mapped to genes that are known regulators of chromosome segregation (**chapters 2.3.5, chapter 3**). In contrast, while CENATAC has been reported to regulate centriole duplication (Wang et al., 2019), our data strongly argue that the chromosomal instability phenotype is a result of a primary defect in splicing of minor introns. Our attempts to rescue the congression defect by expressing individual genes for mitotic regulator with significant A-type intron retention (*CEP170*, *SPC24*, *SMC3*, and *DIAPH2*) failed, suggesting that the defect may be a result of a concerted action affecting multiple proteins simultaneously. This exemplifies that chromosomal instability and the resulting aneuploid karyotypes can result from a specific defect (retention of a rare intron subtype) in a general cellular process (pre-mRNA splicing). Similarly, among the human minor spliceosomal diseases, CENATAC-linked MVA represents a unique example where the disease leads to a discrete cellular defect, in this case in chromosome segregation.

Interestingly, the clinical phenotype of CENATAC-mutant MVA resembles that of MOPD1/

TALS, Roifman and Lowry-Wood syndromes, which are caused by mutations in the U4atac snRNA components of the minor spliceosome (see also **chapter 6.2.3**). Patients with these syndromes likewise present with microcephaly, developmental delay, and retinal abnormalities (Farach et al., 2018). No aneuploidies were found in some studies (Hallermayr et al., 2018; Wang et al., 2018), but karyotype analyses were not reported for the majority of patients. It will therefore be of interest to examine if aneuploidies occur in some of these patients, and if (and to what extent) affected transcripts and the extent of the splicing defect differ between MVA and these syndromes.

ACKNOWLEDGMENTS

We thank the family members for their participation in this study. We thank Anna Zachariou for assistance with recruitment, Emma Ramsay for performing the exome sequencing and Elise Ruark for discussions about the analyses. We thank the Kops, Frilander, Snel and Rahman labs for discussions and comments on the manuscript. We thank Benjamin Rowland and Andrew Holland for reagents. The Kops and Vermeulen labs are part of the Oncode Institute, which is partly funded by the Dutch Cancer Society. This study was further funded by the Cancer Genomics Center (CGC.nl), the Wellcome Trust (100210/Z/12/Z) to NR, Sigrid Jusélius Foundation (MF), Jane and Aatos Erkko Foundation (MF), Academy of Finland grant 1308657 (MF), and a Postdoctoral Research Fellowship by the Herchel Smith Fund at the University of Cambridge (ET).

Author Contributions

Conceptualization	BW, GK, MF, NR, ET
Investigation	BW, AO, MA, SH, JH, SY, ET, LV, MB, EU, JV, LR, PP
Formal analysis	BW, AO, MA, SH, JH, SY, ET, LV, MB, EU, JV, LR, PP
Methodology	BW, AO, MA, SH, JH, SY, ET, LV, MB, JV, PP, MF
Validation	BW, AO, MA, SH, JH, SY, ET, LV, MB, EU, JV, LR, PP
Visualization	BW, AO, MA, SH, ET, LV, JV, LR
Data Curation	BW, AO, MA, SH, SY, LV, JV, LR
Software	AO, JH
Writing – original draft preparation	BW, GK, MF, MA, NR
Writing – review and editing	BW, GK, MF, BS, MV, NR, BI, AO, MA, SH, JH, SY, ET, LV, EU, JV, LR
Project administration	GK, MF, BS, MV, NR, BI
Supervision	GK, MF, BS, MV, NR, BI
Resources	GK, MF, BS, MV, NR, BI
Funding acquisition	GK, MF, BS, MV, NR, BI

Declaration of Interests

Nazneen Rahman is a Non-Executive Director of AstraZeneca. The other authors declare no competing interests.

METHODS

Data availability

The authors declare that the data supporting the findings of this study are available within the paper and its supplementary information. The ICR1000 UK exome series data are available at the European Genome-phenome archive (EGA), reference number EGAS00001000971. Exome data for individual patients cannot be made publicly available for reasons of patient confidentiality. Qualified researchers may apply for access to these data, pending institutional review board approval.

HeLa cell RNAseq data is available at the NCBI Gene Expression Omnibus database, accession number GSE143392. RNAseq data from the patient and control subject cannot be made publicly available for reasons of patient confidentiality. Qualified researchers may apply for access to these data, pending institutional review board approval.

Samples

The MVA exome analyses were approved by the London Multicentre Research Ethics Committee (05/MRE02/17). DNA was extracted from whole blood using standard protocols. RNA was extracted from EBV-transformed lymphoblastoid cell lines (LCL) using the RNeasy Mini Kit protocol (QIAGEN).

For the functional experiments the following patient LCLs were used: ID_ 5728_1 (patient, biallelic CENATAC (CCDC84) mutations, ECACC ID: FACT5728DLB), ID_ 5728_3 (sibling, no CENATAC mutations, ECACC ID: FACT5728KC), ID_ 5728_4 (father, monoallelic CENATAC mutation, ECACC ID: FACT5728GLB), ID_ 5728_5 (mother, monoallelic CENATAC mutation, ECACC ID: FACT5728ALB).

LCLs were cultured in RPMI supplemented with 15% fetal bovine serum (FBS), 100 µg/ml penicillin/streptomycin and 2 mM alanyl-glutamine. Cells expressing H2B-mNeon were created by lentiviral transduction, using standard procedures. Imaging of LCLs was performed as previously described (Yost et al., 2017) (**chapter 3**).

Exome sequencing, alignment and variant calling, reference data sets, PTV prioritization method, recessive analysis, & sanger sequencing: as previously described (Yost et al., 2017) (chapter 3).

cDNA analysis of CENATAC (CCDC84) mutations

We synthesised cDNA using the ThermoScript RT-PCR System (Life Technologies) with random hexamers and 1 µg of total RNA. We amplified the mutation regions using cDNA-specific primers and sequenced the PCR products as described above. Primer sequences are available on request.

Conservation logos

Hidden Markov model (HMM) profiles were created from iterative jackhmmer searches (Potter

et al., 2018) (version: HMMER3/f [3.1b2 | January 2014]) with CENATAC's protein sequence against the sequences of all metazoan species within the uniprot database. In-between successive iterations, non-CENATAC sequences were manually removed. Logos were created using Skygln (Wheeler et al., 2014); letter height: information content above background.

Immunoblots

For the data in **Figures 1C, S4B-C, and S6**, cells were treated as indicated and lysed in Laemmli lysis buffer (4% SDS, 120 mM Tris pH 6.8 and 20% glycerol). Lysates were processed for SDS-polyacrylamide gel electrophoresis and transferred to nitrocellulose membranes. Immunoblotting was performed using standard protocols. Visualization of signals was performed on an Amersham Imager 600 scanner using enhanced chemiluminescence. Primary antibodies used were rabbit anti-CENATAC (CCDC84, Sigma, HPA071715) and mouse anti-Tubulin (Sigma, T5168). Secondary antibodies used were goat anti-mouse HRP (170-6516) and goat anti-rabbit HRP (170-6515), both obtained from Bio-Rad.

HeLa cell culture

HeLa T-REX Flp-In osTIR-gMyc::NEO cells (gift from Andrew Holland) were grown in DMEM high glucose supplemented with 10% Tetapproved FBS, 100 µg/ml penicillin/streptomycin, and 2 mM alanyl-glutamine. Stable expression of H2B-mNeon was done by lentiviral transduction using standard procedures.

Creation of HeLa EGFP-AID-CENATAC and EGFP-CENATAC cell lines

HeLa EGFP-AID-CENATAC and HeLa EGFP-CENATAC cell lines were derived from HeLa T-REX Flp-In osTIR-gMyc::NEO and HeLa T-REX Flp-In, respectively. Tagging of the endogenous locus of CENATAC was done according to the scCRISPR protocol (Arbab et al., 2015) using the Protospacer, HDR_insert, and HDR_ext primers in **Table S9**. pcDNA5-FRT-TO-EGFP-AID (Addgene, 80075) was used as template for both the EGFP-AID and EGFP tags. Cells were transfected with Lipofectamine LTX using standard procedures and subsequently FACS sorted (single cells) based on EGFP expression. Endogenous tagging was confirmed by PCR (using the Genomic primers, **Figure S4A**) and immunoblotting of CENATAC protein (**Figure S4B-C**).

Viral plasmids, cloning and virus production

For lentiviral re-expression of CENATAC variants, first pcDNA5 PURO FRT TO EGFP-AID-CENATAC was created by cloning CENATAC cDNA derived from HeLa cells into empty pcDNA5-FRT-TO-EGFP-AID (Addgene, 80075) using the cDNA PCR primers in **Table S9** and digestion of both the PCR product and the plasmid with NotI/ApaI. The CENATAC cDNA was subsequently cloned into pcDNA5 PURO FRT TO containing a LAP-tag to create pcDNA5 PURO FRT TO LAP-CENATAC by Gibson assembly (Gibson et al., 2009) with the PCR primers Gibson1 and Gibson2. Mutagenesis was then performed to make this construct resistant to CENATAC siRNA treatment (CCDC84, Dharmacon, J-027240-07) by Gibson assembly with PCR primers Gibson3. Next, in the siRNA resistant construct, CENATAC wild-type cDNA was mutated to: Mut1 (primers Gibson4), Mut2 (Gibson5), 2xZF (Gibson6; two

consecutive rounds of cloning), $\Delta 1$ (Gibson7), $\Delta 2$ (Gibson8), $\Delta 3$ (Gibson9), or $\Delta 4$ (Gibson10) by Gibson assembly. Lentiviral CENATAC iresRFP constructs were derived from a lentiviral construct encoding fluorescently tagged histone 2B (H2B) and a puromycin-resistance cassette (pLV-H2B-mNeon-ires-Puro) (Drost et al., 2015). First, the fluorescently tagged H2B was substituted by CENATAC derived from pcDNA5 PURO FRT TO LAP-CENATAC (see above) by Gibson assembly with PCR primers Gibson11 and digestion by *Ascl*/*NheI*. Next the puromycin-resistance cassette was substituted by tagRFP by Gibson assembly with PCR primers Gibson12. Finally, all siRNA resistant variants of CENATAC were cloned from their respective pcDNA5 PURO FRT TO LAP-CENATAC plasmids into pLV CENATAC ires-tagRFP by Gibson assembly with PCR primers Gibson13 and *PstI* digestion of the plasmid. Virions were generated by transient transfection of HEK 293T cells with the transfer vector and separate plasmids that express Gag-Pol, Rev, Tat and VSV-G. Supernatants were clarified by filtration.

Immunoprecipitation

For each sample a full 10 cm plate of HeLa EGFP-AID-CENATAC cells was used, treated as indicated (**Figure S4C**). The cells were lysed in ice-cold lysis buffer (50 mM Tris pH 7.5, 150 mM NaCl, 2% NP-40, 0.1% deoxycholate, proteasome inhibitors) and treated with benzonase for 15 minutes at 4°C. After centrifugation, the supernatant was incubated with beads (GFP-trap, ChromoTek) for 2.5 hours at 4°C and washed three times with ice-cold lysis buffer. The samples were finally eluted in Laemmli sample buffer.

Live cell imaging analysis of mitotic fidelity

LCLs were imaged as previously described (Yost et al., 2017) (**chapter 3**). HeLa cells were transfected (RNAiMAX, thermofisher) with 40 nM CENATAC siRNA (CCDC84, Dharmacon, J-027240-07) and 1mM 3-indoleacetic acid (IAA) in ethanol or 40 nM GAPDH siRNA (Dharmacon, D-001830-01-05) and ethanol (IAA vehicle) for 24 hours in a 24 well-plate before they were re-plate into 8-well Ibidi μ -slides with 2 mM thymidine (for early S-phase synchronization) and 100 μ l virus for CENATAC expression. After 18 hours the cells were released from thymidine for 6 hours and imaged in CO₂ independent medium in a heated chamber (37°C), while air-tight sealed in the well-plate. For the experiments in **Figure 2D-E**, the cells were incubated with 200 nM SiR-tubulin dye (Spirochrome) for 6 hours prior to imaging to facilitate visualization of the mitotic spindle. Images were acquired every 3 or 5 minutes at 1x1 binning in 7x 2.5 μ m z-stacks and projected to a single layer by maximum-intensity projection using NIS-Elements software 4.45. Imaging was performed with a Nikon Ti-Eclipse widefield microscope equipped with an Andor Zyla 4.2 sCMOS camera, 40x oil objective NA 1.3 WD 0.2 mm, and Lumencor SpectraX light engine. Analysis of these experiments was carried out with ImageJ software. When applicable, cells re-expressing CENATAC variants were identified through co-expression of cytosolic RFP (via ires-tagRFP); RFP-negative cells were omitted from the quantifications (see also **Figure S5**).

Immunofluorescence imaging

After treating the cells with siRNAs and IAA (see above) for 24 hours in a 24 well-plate, the cells were re-plated on round 12 mm coverslips and treated with 2 mM thymidine (for early S-phase synchronization) for 24 hours. 10 hours after release MG132 was added for 45 minutes after which the cells were pre-extracted with 0.1% Triton X-100 in PEM (100

mM PIPES pH 6.8, 1 mM MgCl₂ and 5 mM EGTA) for ±60 seconds. After 60 seconds 4% paraformaldehyde was added on top of the PEM in a 1:1 ratio (400 µl each) for 20 minutes to fixate the cells. The coverslips were subsequently washed twice with PBS and blocked with 3% BSA in PBS for 16 hours at 4°C, incubated with primary antibodies for 2 hours at room temperature, washed 3 times with PBS containing 0.1% Triton X-100, and incubated with secondary antibodies for 1 hour at room temperature. Coverslips were then washed 4 times with PBS/0.1% Triton X-100 and mounted using ProLong Gold Antifade with DAPI (Molecular Probes). All images were acquired on a deconvolution system (DeltaVision Elite; Applied Precision/GE Healthcare) equipped with a 100x/1.40 NA UPlanSApo objective (Olympus) using SoftWorx 6.0 software (Applied Precision/GE Healthcare). The images are maximum intensity projections of deconvoluted stacks. Random pro-metaphase and metaphase cells were selected and centrioles were counted by hand. Primary antibodies used were rabbit anti-Centrin1 (Abcam, ab101332, 1/500) and mouse anti-Tubulin (Sigma, T5168, 1/10.000). Secondary antibodies used were goat anti-mouse 647 (A21236) and goat anti-rabbit 568 (A11036), both obtained from ThermoFisher.

Co-evolution analysis

First, a phylogenetically diverse set of complete eukaryotic predicted proteomes was utilized. This set was previously compiled to contain the protein sequences of 90 eukaryotic species (Hooff et al., 2017; van Wijk and Snel, 2020). These species were selected based on their representation of eukaryotic diversity. If available, we selected two species per clade and model organisms were preferred over other species. If multiple proteomes or proteomes of different strains were available, the most complete proteome was selected. When multiple splicing variants of a single gene were annotated, the longest protein was chosen. A unique protein identifier was assigned to each protein, consisting of four letters and six numbers. The letters combine the first letter of the genus name with the first three letters of the species name. The versions and sources of the selected proteomes can be found in **Table S1**.

To define phylogenetic profiles for all human proteins, we determined automatic orthologous groups (OG) across the database using information from PANTHER 9.0 (Mi et al., 2016). PANTHER 9.0 contains 85 genomes with in total 1136213 genes. Of these genes, 759627 genes are in PANTHER families with phylogenetic trees, multiple sequence alignments and HMM profiles. In total there are 7180 PANTHER families and 52768 subfamilies. Families are groups of evolutionary related proteins and subfamilies are related proteins that are likely to have the same function. The division into subfamilies is done manually, by biological experts. Every subfamily of PANTHER is an OG at some taxonomic level in the tree of life. We used 'hmmScan' tool from the HMMER package (Potter et al., 2018) (HMMER 3.1b1) to find for each protein sequence in our database, the best matching profile of a mainfamily or subfamily in PANTHER9.0. The phylogenetic profile of panther main- or subfamily was subsequently defined by utilizing the hierarchical nature of the panther classification. Specifically the phylogenetic profile of a main- or subfamily also include all members of daughter families (and if relevant their daughter families etc.). Note that due to the automatic nature of orthology definition and the draft quality of a few genomes, phylogenetic profiles of the human proteins are not as accurate as those defined by manual analysis (van Hooff et al., 2019).

To determine the phylogenetic profile similarity, Pearson correlation (https://en.wikipedia.org/wiki/Phi_coefficient) was computed between the phylogenetic profile of the CENATAC panther (PTHR31198) and the phylogenetic profile of all other panther sub and main families using in-house scripts. To detect functional patterns in orthologous groups with similar phylogenetic profiles (correlation > 0.5), a GO Enrichment Analysis was performed (Ashburner et al., 2000; Carbon et al., 2019; Mi et al., 2019). GO cellular component overrepresentation (GO Ontology database: released 2020-01-03) was computed using PANTHER (test release 2019-07-11) with the human reference genome gene set as background. Statistical significance of overrepresented GO terms was computed using Fisher's exact test with FDR correction.

Nuclear extract and GFP pull down and mass spectrometry

Nuclear extract of wild-type and EGFP-CENATAC HeLa cells was prepared as described earlier (Kloet et al., 2016). In short, cells were harvested by trypsinization and resuspended in cold hypotonic buffer (10 mM Hepes KOH pH 7.9, 1.5 mM MgCl₂, 10 mM KCl). Afterwards, the cell pellet was homogenized using a Douncer with type B pestle (tight) to lyse the cell membrane. After centrifuging, the nuclei were washed with cold PBS and resuspended in cold buffer for lysis (420 mM NaCl, 20 mM Hepes KOH pH 7.9, 20% v/v glycerol, 2 mM MgCl₂, 0.2 mM EDTA) followed by rotation, centrifugation, and collection of the nuclear extract. 450 µl of nuclear extract was used for each GFP pull down using 15 µl slurry of GFP-Trap agarose beads (Chromotek), performed in triplicate. GFP pull-downs were done as described earlier (Smits et al., 2013), without the addition of EtBr during the incubation, and with an adapted buffer C (150 mM NaCl, 20 mM Hepes KOH pH 7.9, 20% v/v glycerol, 2 mM MgCl₂, 0.2 mM EDTA, complete protease inhibitors w/o EDTA, 0.5 mM DTT) for the incubation (+0.1% NP40) and washes (+0.5% NP40). Samples were digested using on-bead digestion with trypsin overnight (Hubner and Mann, 2011). The tryptic peptides were acidified with TFA and purified on C18 StageTips (Rappsilber et al., 2007).

After elution from the C18 StageTips, tryptic peptides were separated on an Easy-nLC 1000 (Thermo Scientific), connected online to a Q-Exactive HF-X Hybrid Quadrupole-Orbitrap Mass Spectrometer (Thermo Scientific), using an acetonitrile gradient of 7-30% for 48 min followed by washes of 50-90% acetonitrile, for 60 min of total data collection. Full scans were measured with a resolution of 120,000, the top twenty most intense precursor ions were selected for fragmentation with a resolution of 15,000 and dynamic exclusion set at 30 sec. Peptides were searched against the UniProt human proteome (downloaded June 2017) using MaxQuant (Cox and Mann, 2008) (version 1.6.0.1) with default settings, and iBAQ, LFQ, and match-between-runs enabled. Data analysis was done using Perseus (version 1.5.5.3), the volcano plot and stoichiometry calculations were done as described earlier (Smits et al., 2013) using in-house made scripts for R (version 3.6.1).

Nuclear Extract Preparations for Northern blots and glycerol gradients

Nuclear extract from HeLa cells were prepared according to the protocol described in Dignam et al., 1983 using buffer D containing 50 mM KCl in the final dialysis step.

Immunoprecipitation and Northern blots

100 μ l nuclear extract diluted in lysis buffer to a final volume of 200 μ l was incubated with 2 μ g of anti-CCDC84 antibody (SIGMA-HPA071715) overnight in the cold room with end-to-end rotation. The following day capture of antibody-antigen complexes was done using 50 μ l of resuspended Protein G Dynabeads prepared according to manufacturers instructions and incubated with the nuclear extract-antibody samples for 2 hr at 4°C. Beads were then washed four times with lysis buffer lacking protease and RNase inhibitors. RNA was eluted by proteinase K treatment, extracted once with phenol:chloroform:isoamyl alcohol (25:24:1; pH4.8) followed by ethanol precipitation. RNA dissolved to H₂O or 0.1X TE buffer.

Total volumes of 2 μ l (Input) and 5 μ l (IP) RNA samples were separated on a 6% polyacrylamide-Urea gel and analysed by Northern blotting essentially as described in (Tarn and Steitz, 1996). Individual snRNAs were detected using ³²P 5'-end labeled DNA or LNA oligonucleotides complementary to individual snRNAs. Northern blots were exposed to image plates and visualized using Typhoon FLA-9400 scanner (GE Healthcare, US) at 50 micron resolution. The data was quantified using AIDA software (Raytest, Germany).

Glycerol Gradient and ultracentrifugation

Nuclear extracts were preincubated for 0-20 min at +30 °C in a buffer containing 13 mM HEPES(pH 7.9), 2.4 mM MgCl₂, 20 mM creatine phosphate, 2 mM DTT, 40 mM KCl, 0.5 mM ATP. Aggregates were subsequently removed by a brief centrifugation (20 000 g, 1 min, +4°C) and the supernatant subsequently ultracentrifuged on a linear 10-30% gradient (20 mM HEPES, pH 7.9; 40 mM KCl, 2 mM DTT, 2.4 mM MgCl₂) for 18 hr at 29000 rpm, +4°C, Sorvall TH641 rotor. Following ultracentrifugation, the samples were fractionated. 20% of each fraction was deproteinized and used for RNA isolation and Northern blotting and the remaining 80% was subjected to TCA precipitation, separated on a 10% SDS-PAGE and analysed by Western blots. Each blot was probed for CENATAC (CCDC84-HPA071715, Sigma-Aldrich-Merck), PRPF4 (#HPA0221794, Sigma-Aldrich-Merck) and TXNL4B (E-AB-61535, Elabscience, US).

RT-PCRs

For **Figure 4A**: total cellular RNA was extracted using the RNeasy kit protocol (Qiagen) and treated with DNase I Amplification grade (Invitrogen) to remove potential genomic DNA contamination. cDNA synthesis was carried out using SuperScript™ II RT (Thermo Fisher Scientific) and Oligo(dT)18 primers. PCRs were performed with Phusion High-Fidelity DNA polymerase (Thermo Fisher Scientific) with the following cycling conditions: initial denaturation (98°C for 60 sec), followed by either 30 cycles of denaturing (98°C for 10 sec), annealing (gene-specific temp for 30 sec), extension (72°C for 30 sec) and a final extension (72°C for 1 min 30 sec). PCR primers and relevant annealing temperatures are listed in **Table S9**. PCR products were analyzed on 2% agarose gel run using 1X TBE buffer. For **Figures 4B and 5E** total RNA isolated was isolated from HeLa cells or patient/control subject lymphoblasts using Trizol extraction followed by an additional acidic phenol (pH 5.0) extraction. 1 μ g of RNA was converted to cDNA using Maxima H minus reverse transcriptase (Thermo Fisher) according the manufacturer protocol. PCRs were performed essentially as described above and gene specific primers and (annealing temperatures) are listed in **Table S9**.

RNA isolation and high-throughput sequencing

Total RNA isolated was isolated from EGFP-AID-CENATAC HeLa cells treated with siGAPDH (Dharmacon, D-001830-01-05) for 48 hours or with siCENATAC (CCDC84, Dharmacon, J-027240-07) and 1mM 3-indoleacetic acid (IAA) for 24 or 48 hours, or unedited HeLa parental cells treated with siGAPDH for 48 hours, or patient/control subject lymphoblasts using Trizol extraction followed by an additional acidic phenol (pH 5.0) extraction. RNAseq libraries were constructed using Illumina TruSeq Stranded Total RNA kit (Illumina) Human Ribo-Zero rRNA depletion kit (Illumina). Paired-end 150+150 bp sequencing was done with Illumina NextSeq 500 using NextSeq 500/550 High Output Kit v2.5 for HeLa samples and with Illumina NovaSeq 6000 using partial S4 flow cell lane for patient samples.

Mapping the reads to the genome

The STAR aligner (Dobin et al., 2013) was used for mapping the paired sequence reads to the genome (hg38/GRCh38). Transcript annotations were obtained from GENCODE (v29). The length of genomic sequence flanking the annotated junctions (sjdbOverhang parameter) was set to 161. The Illumina adapter sequences AGATCGGAAGAGCACACGTCTGAACTCCAGTCAC and AGATCGGAAGAGCGTCGTGTAGGGAAAGAGTGTAGATCTCGGTGGTCGCCGTATCATT were, respectively, clipped from the 3' of the first and the second pairs in the read libraries (using clip3pAdapterSeq parameter).

Differential alternative splicing analysis

Differential alternative splicing (AS) analysis was done using Whippet (v0.11) (Sterne-Weiler et al., 2018). Both merged aligned reads (bam files) and AS event annotations from GENCODE (v29) were used to build the index reference for AS events. To detect the significantly differential events, probability cutoff of $Pr > 0.9$ and Percentage Spliced In deviation cutoff of $|\Delta| > 0.1$ were used.

Differential intron retention analysis

For a comprehensive and sensitive intron retention (IR) analysis the IntERESt R/Bioconductor package was used (Oghabian et al., 2018). After reading binary alignment (.bam) files, IntERESt detects introns with significantly higher and lower number of mapped reads relative to the number of reads that span the introns. The DESeq2-based function of IntERESt, i.e. `deseqInterest()`, was used for the differential IR analysis. The Benjamini-Hochberg method was used for adjusting the p-values and a cutoff of $padj < 0.05$ was applied to extract the significantly differential IRs. The reference table was built from the NCBI RefSeq transcription annotations based on hg38/GRCh38 genome assembly.

Annotating U12-type introns

We used IntERESt R/Bioconductor package to annotate the U12-type introns as described previously (Oghabian et al., 2018) using threshold values of 0.07 and 0.14 for 5'ss and BPS scores, respectively. BPS sequence was identified by scanning intronic region from position -40 to position -3 upstream of the 3'ss and the highest scoring sequence was selected as the BPS. This list was manually appended with additional introns that did not fulfil our annotation criteria (typically because of poor BPS sequence), but have been previously identified as U12-type introns (Chang et al., 2007).

P120 minigene cloning, transfection and analysis of RNA

The double 5' splice site (5'ss) constructs were created by insertion mutagenesis PCR using the P120 minigene (Hall and Padgett, 1996) as a template, and further modifications of 5' splice sites were made by PCR using mutagenic primers (for a list of primers used see **Table S9**). The 3' splice site was modified to accommodate for GT-subtype splicing by insertion of a CAG trinucleotide sequence through insertion mutagenesis PCR. All mutations were confirmed by DNA sequencing. Chinese Hamster Ovary cells were transfected with the double 5'ss constructs (1600 ng per well of a 12-well plate) using Lipofectamine 2000 (ThermoFisher Scientific) and after 24h total RNA was isolated using TRIZOL reagent (ThermoFisher Scientific). Following DNase treatment, a pCB6 vector specific oligonucleotide (ACAGGGATGCCA) was used for reverse transcription of the RNA with Revertaid (ThermoFisher Scientific). RT-PCR was performed with primers binding exon 6 (GGATGAGGAACCATTTGTGC) and exon 7 (AGAACGAGACCGCCCTTC), and the resulting PCR products were analyzed on a 3 % MetaPhor™ (Lonza) agarose gel. The gel was imaged using Fuji LAS-3000 CCD camera and the band intensities were quantified using AIDA software (Raytest, Germany). Identities of the PCR products were confirmed by DNA sequencing.

SUPPLEMENTARY FIGURES

ID_5728. The patient was the first child of non-consanguineous healthy Caucasian parents. He had microcephaly, mild developmental delay and mild maculopathy. On last examination at 42 years, his head circumference was 52 cm (-3.5 s.d.). His youngest sister had the same clinical features. On last examination at 27 years, her head circumference was 48 cm (-6 s.d.). Neither individual had short stature, dysmorphism or cancer. Both were alive at 47 and 33 years of age, respectively. The siblings also have a healthy sister.

Cytogenetic studies were performed using standard R- and G-banding methods at the 550-band level of resolution. In the proband, five of 68 cells had an abnormal karyotype (47.XYY[1]/47.XY,-1,+4+18[1]/48.X-YY,+4[1]/47.XY,+21[1]/45.XY,-22[1]/46.XY[63]. In the proband's sister five of 59 cells had an abnormal karyotype [47.XX,+21[3]/47.XXX-1[1]/47.XXX,+18,-22[1]/46.XX[54].

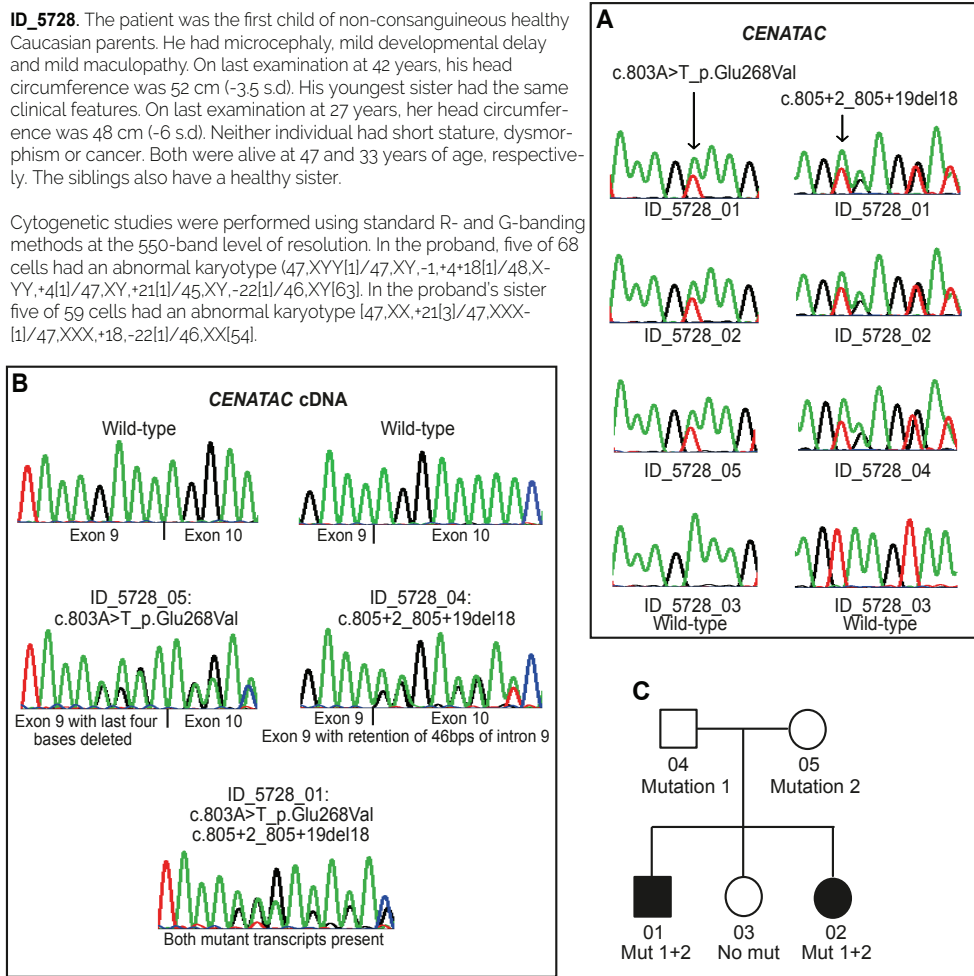


Figure S1. Case report and chromatograms of individuals with mutations in *CENATAC* (*CCDC84*).

A) Sequencing chromatograms showing mutations in blood DNA and corresponding wild-type sequence from a control. **B)** Sequencing chromatograms from Reverse Transcription-PCR analysis of RNA showing the effect of *CENATAC* mutations. Maternal cDNA sequencing (ID_5728_05) demonstrates that c.803A>T_p.Glu268Val leads to a translational frameshift as a result of deletion of the last four bases of exon 9. Paternal cDNA sequencing (ID_5728_04) shows that c.805+2_805+19del18 results in retention of 46 bps of intron 9. The affected child's cDNA sequencing (ID_5728_01) demonstrates both mutant transcripts are present. **C)** Pedigree of family ID_5728 showing *CENATAC* mutation status.

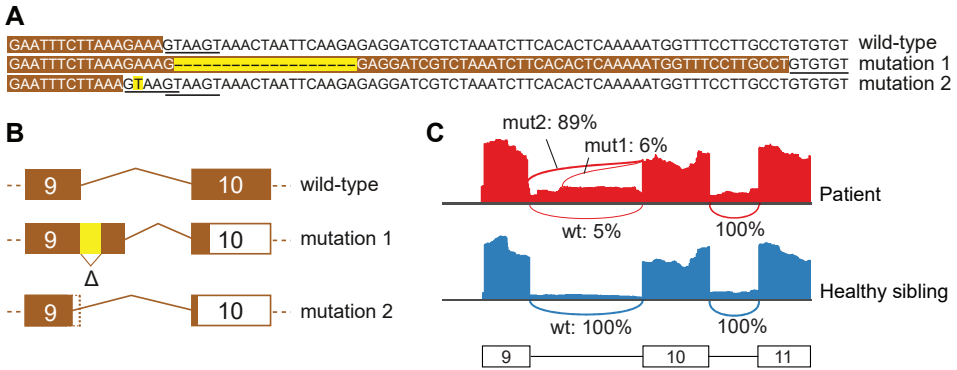


Figure S2. The effect of the MVA patient mutations on splicing of *CENATAC* intron 9. **A)** DNA sequences of exon 9 (white in brown boxes) and intron 9 (black) of wild-type and MVA mutated *CENATAC* alleles. The mutations (c.805+2_805+19del18, mut1; and c.803A>T, mut2) are indicated with yellow. Both the new and original 5' splice sites are underlined. **B)** Schematic showing the effect of the MVA patient mutations on splicing of *CENATAC* intron 9. Exons 9 and 10 are represented with rectangles; protein-coding regions within exons are indicated with fill, untranslated regions without fill. See also **Figure 1C**. **C)** Sashimi plots derived from patient and healthy sibling RNAseq data showing the effect of the MVA patient mutations on 5' splice site usage (percentages) of intron 9 in patient cells. The different splice sites are shown in A).

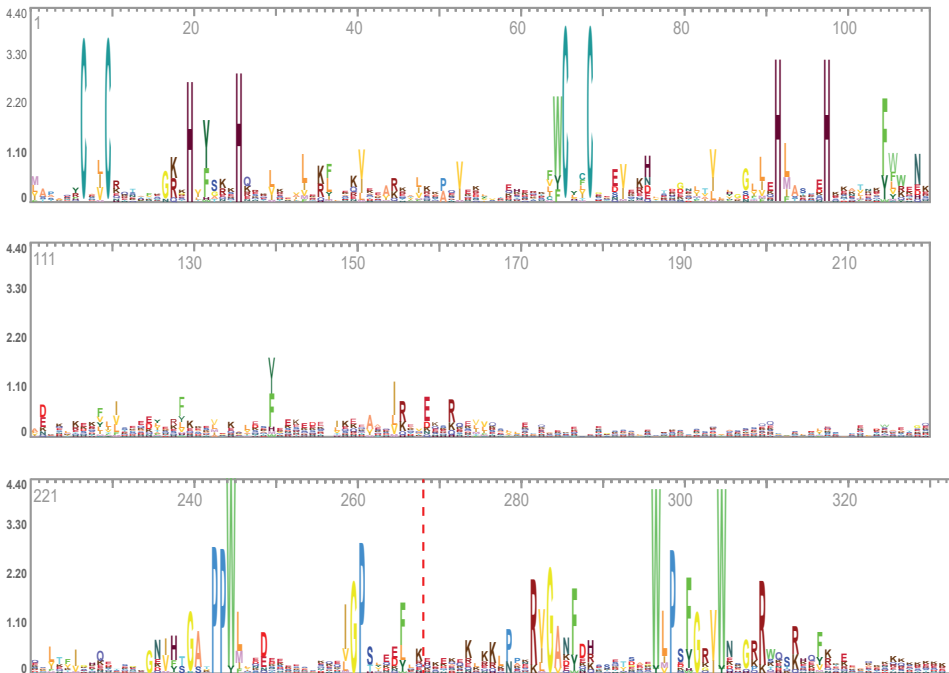


Figure S3. Full-length sequence logo of *CENATAC*'s conserved residues (in metazoan species) split in three. Amino acids are numbered. The location of the truncating MVA mutations is indicated with the red dotted line.

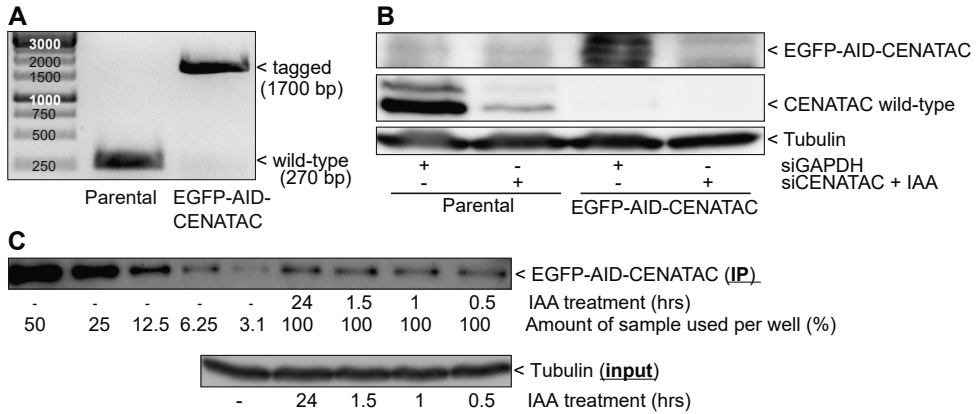


Figure S4. Endogenous EGFP-AID-CENATAC tag verification and CENATAC depletion. **A)** Genomic PCR of the *CENATAC* locus around the start codon. Left: parental cells; right: EGFP-AID-CENATAC cells. **B)** CENATAC (CENATAC) and tubulin (Tubulin) immunoblots of EGFP-AID-CENATAC and parental cells treated as indicated for 48 hours. **C)** CENATAC (CENATAC) immunoblot of EGFP-AID-CENATAC immunoprecipitated from cells treated with IAA for the indicated amounts of time (upper) and Tubulin (Tubulin) immunoblot of input samples (lower). The untreated IP sample (upper gel, 5 left-most wells) was divided into volumes of 50, 25, 12.5, 6.25 and 3.1% of the total volume, as indicated, for comparison with the IAA treated samples (4 right-most wells) of which 100% of the total volume was loaded.

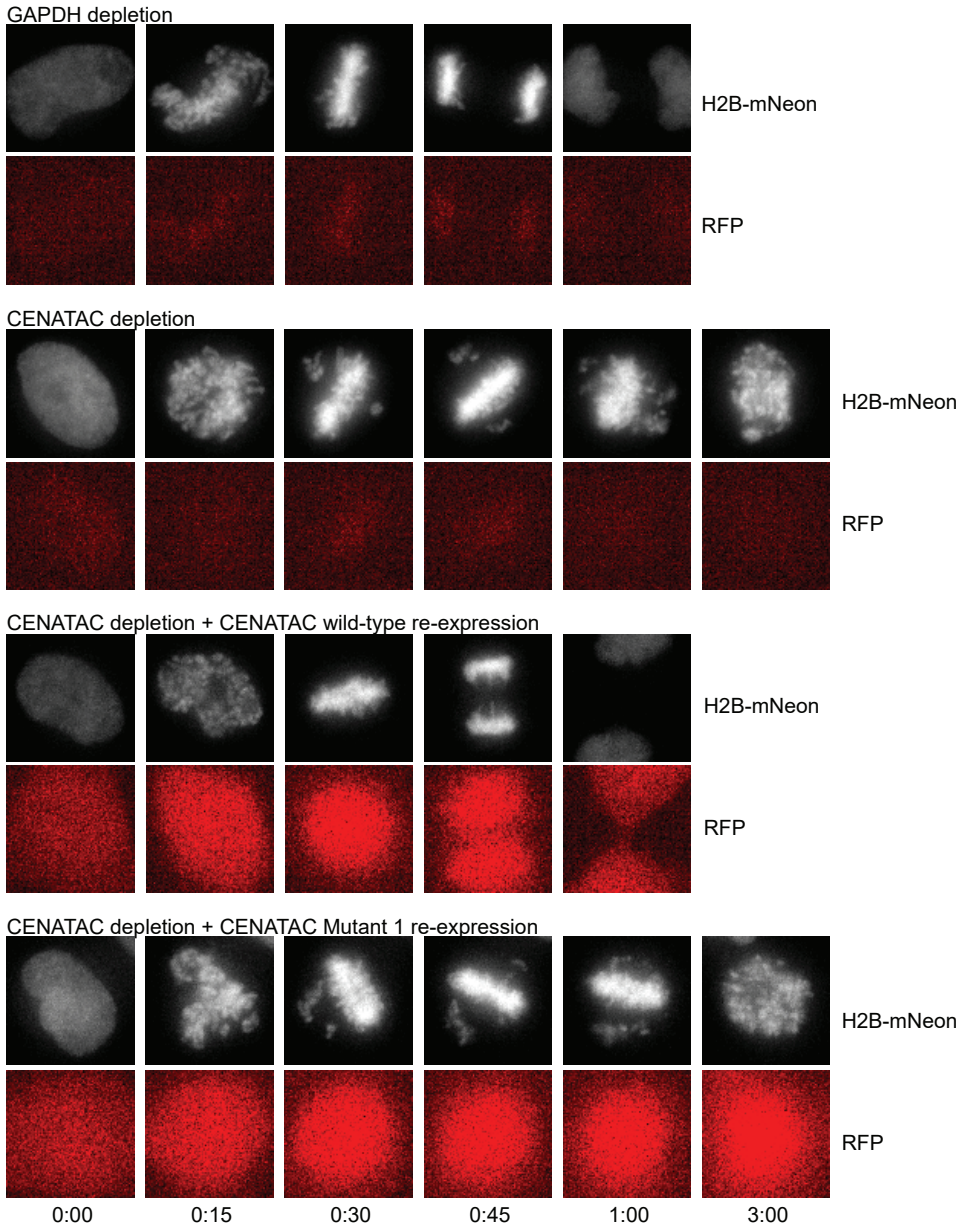


Figure S5. EGFP-AID-CENATAC cells expressing H2B-mNeon depleted of GAPDH or CENATAC, with or without re-expression of CENATAC variants as indicated. As in Figure 1F-G. Expression of cytosolic RFP was used as a marker to identify cells expressing CENATAC variants. Upper panels: H2B-mNeon; lower panels: RFP. Time in hours.

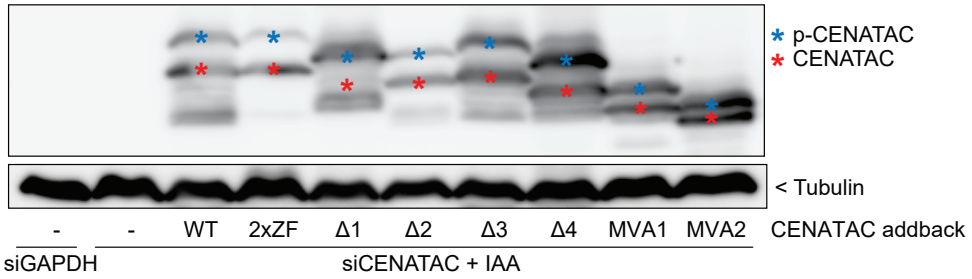


Figure S6. CENATAC (CENATAC) and tubulin (Tubulin) immunoblots of cells treated as in Figure 1G. p-CENATAC indicates phosphorylated CENATAC (blue asterisks).

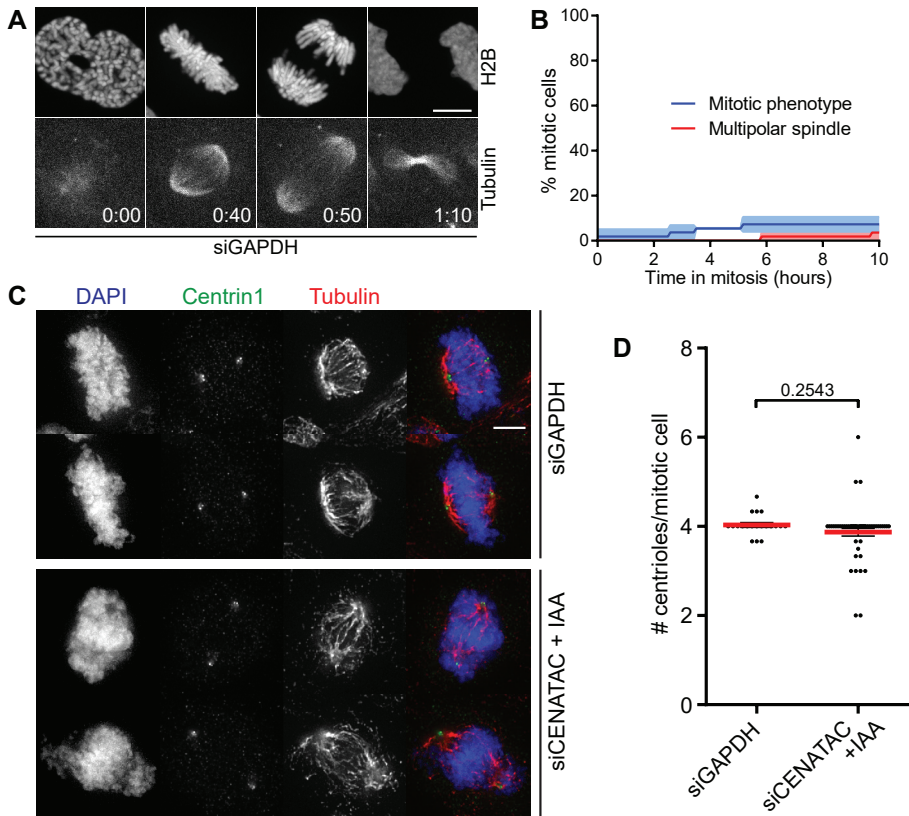


Figure S7. CENATAC's congression phenotype is not the result of a multipolar mitotic spindle. **A)** Representative stills of EGFP-AID-CENATAC HeLa cells expressing H2B-mNeon and depleted of GAPDH. Microtubules were visualized with SiR-Tubulin. Scale bar, 5 μm. Time in hours. See also **Movies S1 and S2**. **B)** Quantification of the mitotic phenotype and multipolar spindle formation in time in cells treated as in A). Each line depicts the mean of three experiments ± s.e.m., with >44 cells in total. **C)** Representative immunofluorescence images of EGFP-AID-CENATAC cells depleted of GAPDH or CENATAC and stained with antibodies against Centrin1 and Tubulin. Scale bar, 5 μm. **D)** Quantification of the amount of centrioles per mitotic cell treated as in C). Each line depicts the average of three experiments ± s.e.m., with >60 cells in total. The P value was calculated with a two-sided unpaired Student's t test.

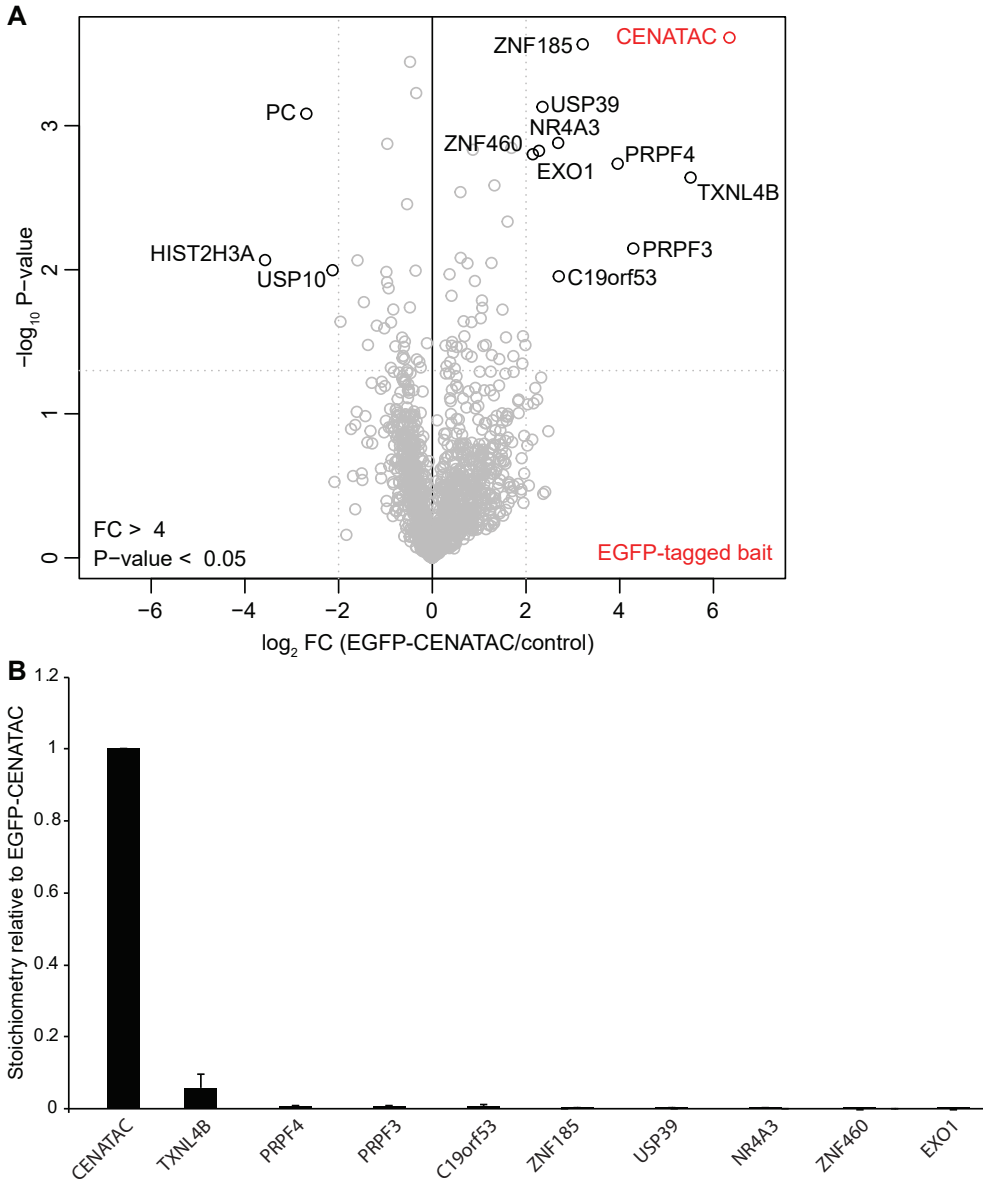


Figure S8. Volcano plot and stoichiometry of EGFP-CENATAC immunoprecipitations. A) Mass spec-based identification of interacting proteins with EGFP-CENATAC in HeLa cells. Statistically enriched proteins in the EGFP-CENATAC pull downs ($n = 3$), determined using a two tailed t-Test, are depicted on the right-hand side of the volcano plot. The fold change of the LFQ intensities, from the CENATAC over the wt pull-down, is depicted on the x-axis (\log_2). The y-axis shows the $-\log_{10}$ P-value. Cutoffs are shown with a dotted grey line, with a fold change of 4 and a P-value of 0.05. **B)** Stoichiometry of proteins interacting with EGFP-CENATAC. The iBAQ value of each protein is divided by the iBAQ value of CENATAC, and depicted with CENATAC set to 1. Data are shown as mean \pm s.d. ($n = 3$ pull-downs).

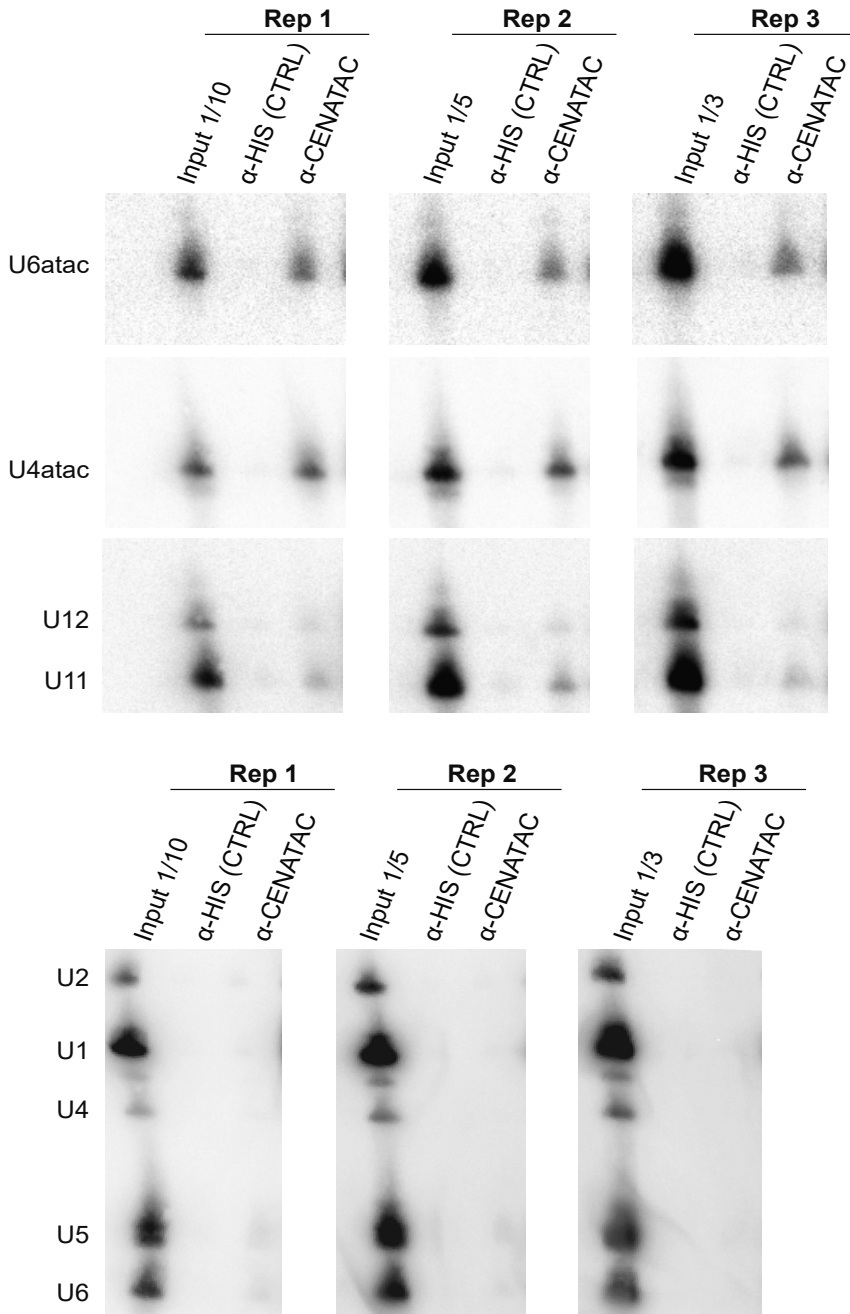


Figure S9. Northern blots of EGFP-CENATAC immunoprecipitations (N=3) used for the quantification in Figure 3E.

sequence logo construction using WebLogo (weblogo.berkeley.edu). **B**) In plants retention of a U12-type intron embedded in exon 3 leads to productive mRNA formation that includes the full-length *CENATAC* coding sequence. Splicing of the U12-type intron by the minor spliceosome leads to a nonproductive mRNA formation due to introduction of premature termination codon in exon 4. The sequence logo shows the conservation of the U12-type 5'ss, BPS and 3'ss elements within the retained intron. In both panels A) and B) the filled rectangles indicate protein-coding exons, open rectangles represent non-coding exons. Nucleotides showing at least 85% identity between the species are shaded.

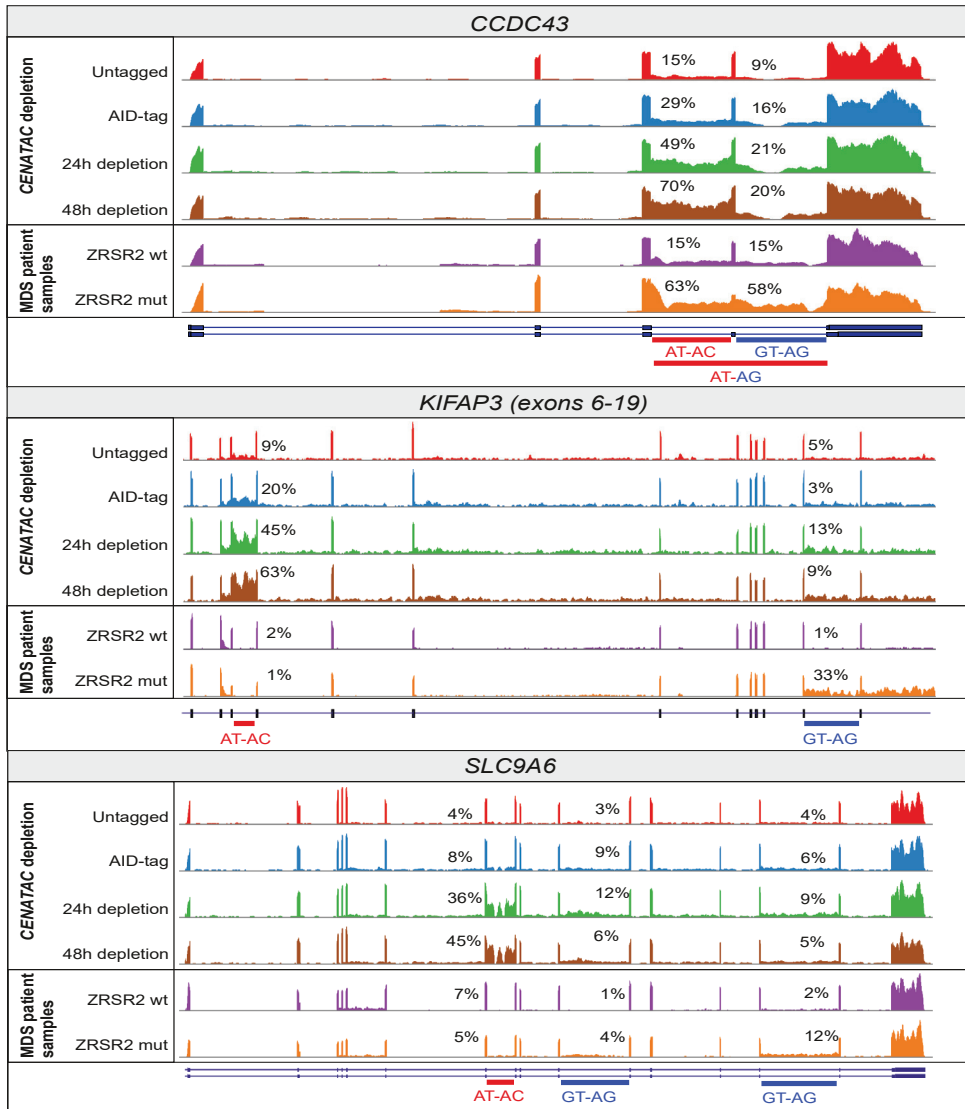


Figure S11. Sashimi plots showing the effect of CENATAC depletion (24 or 48 hours) in EGFP-AID-CENATAC HeLa cells or *ZRSR2* mutations in the MDS dataset on A- and G-type minor intron retention: AT-AC and GT-AG introns, respectively. Untagged represents the parental unedited HeLa cell line, AID-tag represents the EGFP-AID-CENATAC HeLa cell line; both were depleted of GAPDH for 48h. The AT-AG intron (*CCDC43*, in red and blue) is a hybrid intron that starts from 5' splice site of the AT-AC intron and ends with the 3' splice site of the GT-AG intron.

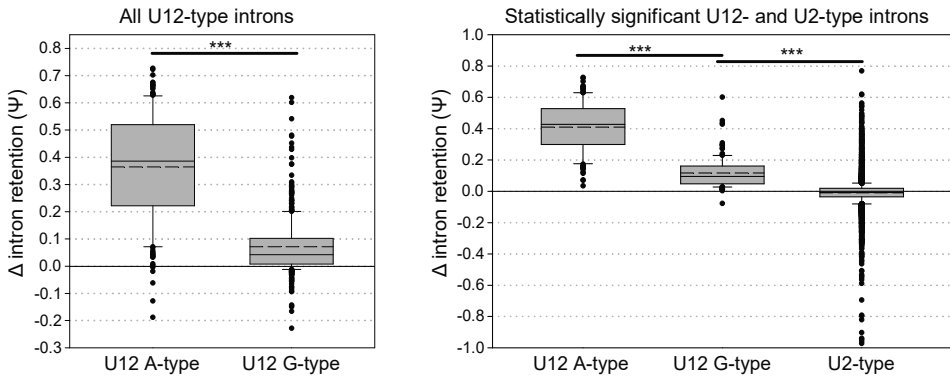


Figure S12. Comparison of the delta-psi values (EGFP-AID-CENATAC HeLa cells 48h CENATAC depletion vs. parental cell line 48h GAPDH depletion). A) Comparison of all (significant and not significant) U12 A-type (n=179) and U12 G-type (n=441) introns. **B)** comparison of statistically significant U12 A-type introns (n=133), U12 G-type introns (n=130), and U2-type introns (n=8818). Only introns with on average at least 5 intron-mapping reads were used in the analysis. The boundaries of the boxes indicate 25th and 75th percentiles. Whiskers indicate the 90th and 10th percentiles. Median is indicated with solid line, mean with dashed line inside the box. *** - $P < 0.001$, ns - $P > 0.05$ (Mann-Whitney Rank Sum Test).

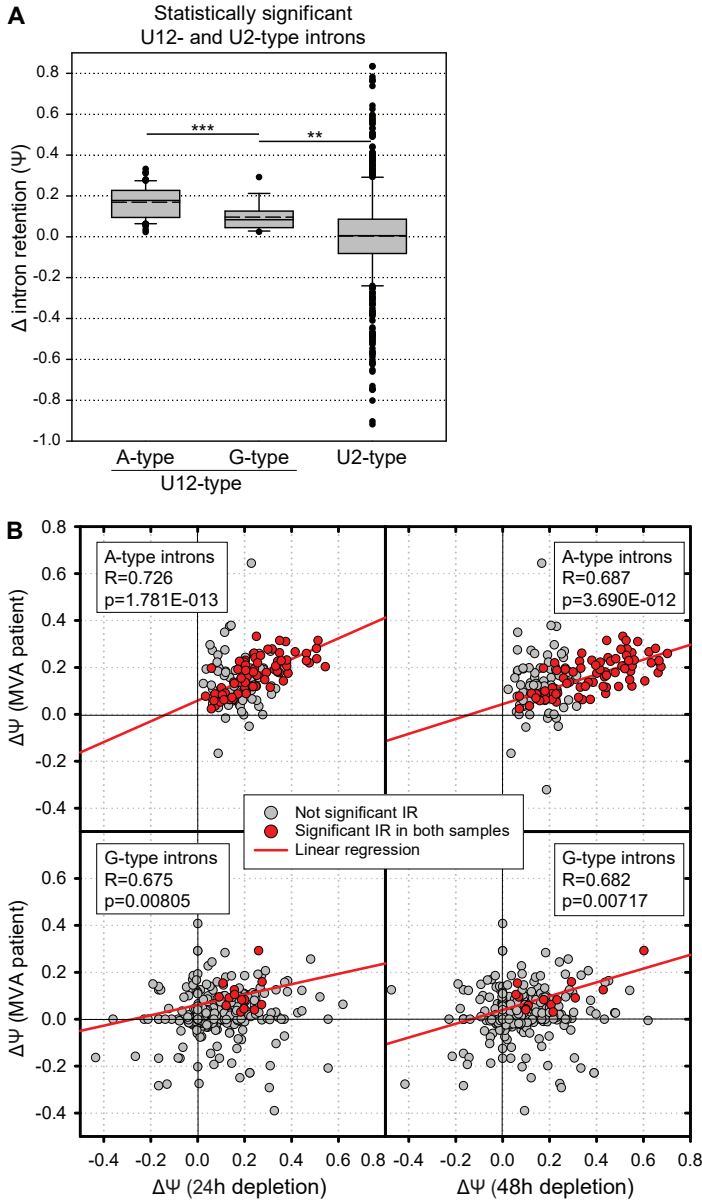


Figure S13. Analysis of the MVA patient intron retention dataset. A) Comparison of statistically significant U12 A-type introns ($n=81$), U12 G-type introns ($n=15$), and U2-type introns ($n=699$). Only introns with on average at least 5 intron-mapping reads were used in the analysis. The boundaries of the boxes indicate 25th and 75th percentiles. Whiskers indicate the 90th and 10th percentiles. Median is indicated with solid line, mean with dashed line inside the box. *** - $P<0.001$, ** - $P<0.01$, ns - $P>0.05$ (Mann-Whitney Rank Sum Test) **B)** Pairwise comparison of minor intron retention values (Δ) between the MVA dataset (y-axis) and the CENTAC depletion datasets (x-axis). Red circles indicate introns with statistically significant intron retention values, while with gray circles the retention values were not statistically significant. For the correlation coefficient calculations only the statistically significant intron retention values (red dots) were used.

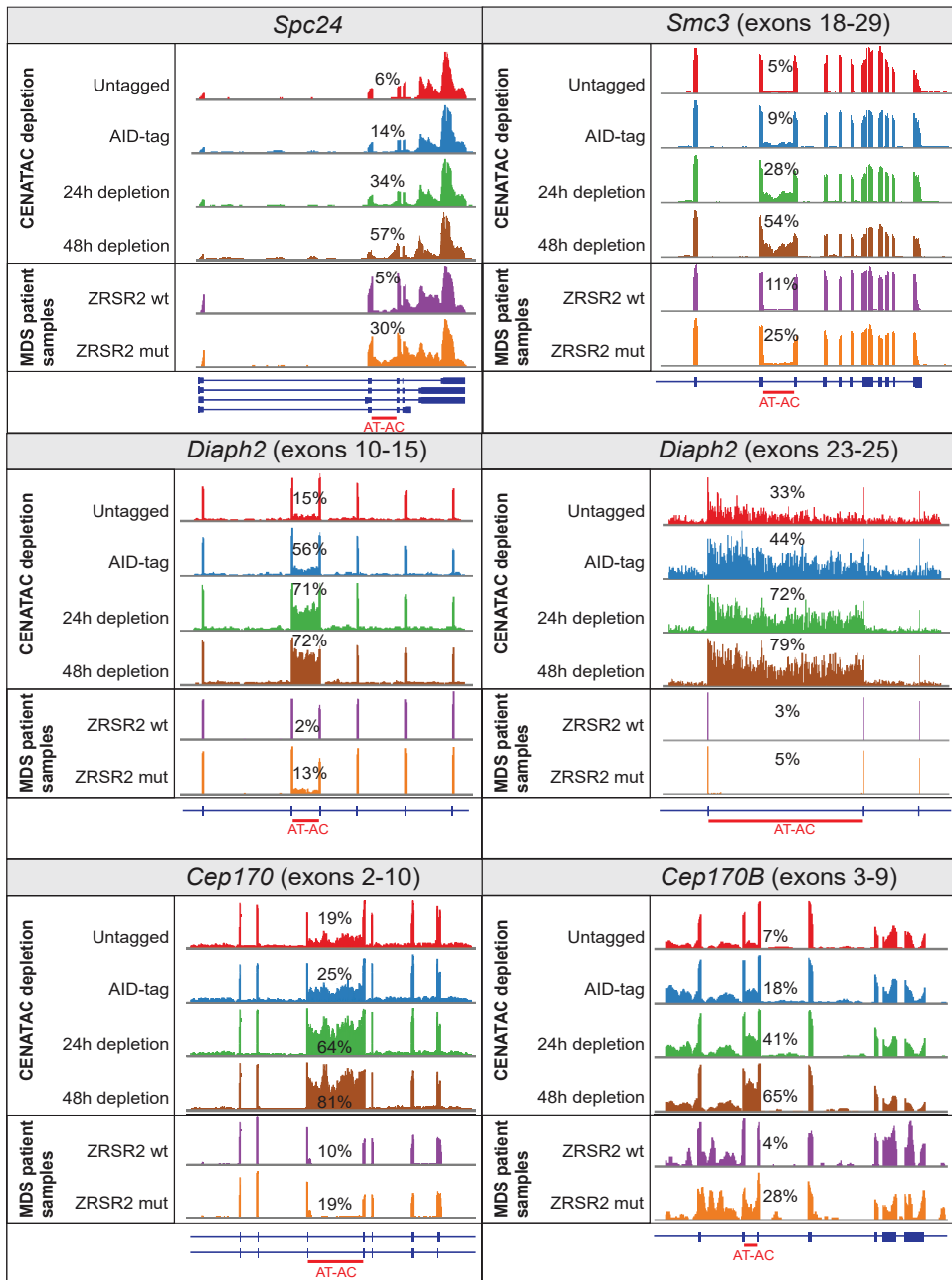


Figure S14. Sashimi plots of mitotic regulators showing the effect of CENATAC depletion in EGFP-AID-CENATAC HeLa cells (24 or 48 hours) or *ZRSR2* mutations in the MDS dataset on AT-AC intron retention (percentages). These genes were manually selected from the genes that were significantly affected by CENATAC depletion (Table S3) with the GO term kinetochore or mitotic spindle. Untagged represents the parental unedited HeLa cell line, AID-tag represents the EGFP-AID-CENATAC HeLa cell line; both were depleted of GAPDH for 48h.

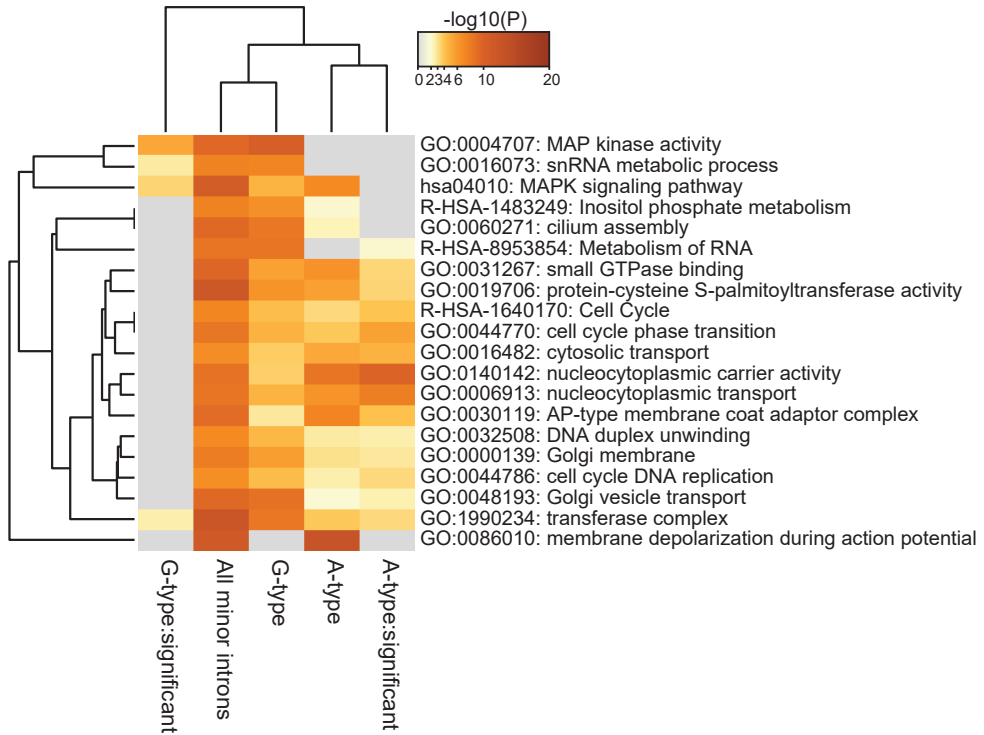


Figure S15. Metascape analysis (metascape.org) of genes containing significantly retained minor introns following 48h CENTAC depletion. Genes with significantly retained A- and G-type introns were analyzed separately (A-type:significant and G-type:significant, respectively) and compared to all genes containing A- or G-type introns (A-type and G-type, respectively) and to all genes containing minor introns. Default parameters were used in the analysis. The color scheme indicates the p-values. Top 20 categories are shown. **Table S7** includes the numeric p-values related to the figure. **Table S8** includes annotations at the gene level and details of the enriched clusters.

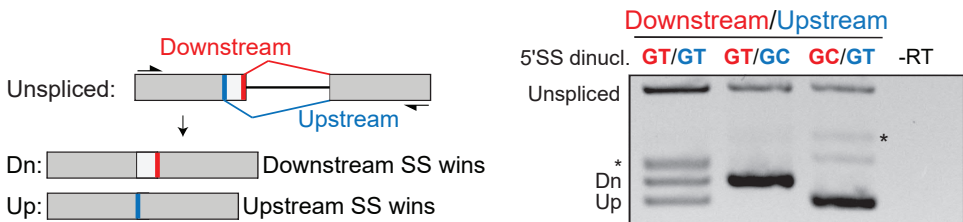


Figure S16. RT-PCR P120 reporter assay to measure the relative usage of GT-AG and GC-AG G-type U12 splice sites in direct competition. Left: schematic diagram showing the overall architecture of the reporter construct with its down- and upstream splice site (thick red and blue bars, respectively) and the products created by splicing (Dn and Up, respectively). Right: RT-PCRs of the reporter with GT-AG or GC-AG splice sites in the down- or upstream positions as indicated above the gel. SS, splice site. 5'SS dinucl., 5'SS dinucleotides. *, PCR product after use of a cryptic U2-type splice site (not shown in the schematic).

ONLINE FIGURES AND SUPPLEMENTARY DATA

OneDrive (link)



Google Drive (link)



Movie S1. GAPDH depletion EGFP-AID-CENATAC HeLa cells expressing H2B-mNeon (upper) and depleted of GAPDH. Microtubules were visualized with SiR-Tubulin (lower). Time in hours.

Movie S2. CENATAC depletion EGFP-AID-CENATAC HeLa cells expressing H2B-mNeon (upper) and depleted of CENATAC. Microtubules were visualized with SiR-Tubulin (lower). Time in hours.

Table S1. List of species used in the co-evolution analysis of Figure 3A with additional information and references.

Table S2. Co-evolution scores List of co-evolution correlation scores per Panther/Ensembl Gene ID.

Table S3. CENATAC depletion intron retention dataset CENATAC RNAseq data analyzed for intron retention using IntERESt and for alternative splicing using Whippet. Sequencing statistics and data for the subtypes of U2- and U12-type introns is shown in separate tabs.

Table S4. MDS intron retention dataset MDS RNAseq data (GEO GSE63816) analyzed for intron retention using IntERESt and for alternative splicing using Whippet. Sequencing statistics and data for the subtypes of U12-type introns is shown in separate tabs.

Table S5. MVA patient intron retention dataset CENATAC RNAseq data analyzed for intron retention using IntERESt. Sequencing statistics and data for the subtypes of U2- and U12-type introns is shown in separate tables.

Table S6. Venn diagram data related to Figure 5G.

Table S7. Go-term enrichment statistics related to Figure S15.

Table S8. Full metascape results table related to Figure S15.

Table S9. List of primers used.

REFERENCES

- Arbab, M., Srinivasan, S., Hashimoto, T., Geijsen, N., and Sherwood, R.I. (2015). Cloning-free CRISPR. *Stem Cell Reports* **5**, 908–917.
- Ashburner, M., Ball, C.A., Blake, J.A., Botstein, D., Butler, H., Cherry, J.M., Davis, A.P., Dolinski, K., Dwight, S.S., Eppig, J.T., et al. (2000). Gene ontology: Tool for the unification of biology. *Nat. Genet.* **25**, 25–29.
- Blomen, V.A., Májek, P., Jae, L.T., Bigenzahn, J.W., Nieuwenhuis, J., Staring, J., Sacco, R., Van Diemen, F.R., Olk, N., Stukalov, A., et al. (2015). Gene essentiality and synthetic lethality in haploid human cells. *Science* (80-.). **350**, 1092–1096.
- Carbon, S., Douglass, E., Dunn, N., Good, B., Harris, N.L., Lewis, S.E., Mungall, C.J., Basu, S., Chisholm, R.L., Dodson, R.J., et al. (2019). The Gene Ontology Resource: 20 years and still GOing strong. *Nucleic Acids Res.* **47**, D330–D338.
- Chang, W.C., Chen, Y.C., Lee, K.M., and Tarn, W.Y. (2007). Alternative splicing and bioinformatic analysis of human U12-type introns. *Nucleic Acids Res.* **35**, 1833–1841.
- Cologne, A., Benoit-Pilven, C., Besson, A., Putoux, A., Campan-Fournier, A., Bober, M.B., de Die-Smulders, C.E.M., Paulussen, A.D.C., Pinson, L., Toutain, A., et al. (2019). New insights into minor splicing—a transcriptomic analysis of cells derived from TALS patients. *RNA* **25**, 1130–1149.
- Cox, J., and Mann, M. (2008). MaxQuant enables high peptide identification rates, individualized p.p.b.-range mass accuracies and proteome-wide protein quantification. *Nat. Biotechnol.* **26**, 1367–1372.
- Dobin, A., Davis, C.A., Schlesinger, F., Drenkow, J., Zaleski, C., Jha, S., Batut, P., Chaisson, M., and Gingeras, T.R. (2013). STAR: Ultrafast universal RNA-seq aligner. *Bioinformatics* **29**, 15–21.
- Drost, J., van Jaarsveld, R.H., Ponsoien, B., Zimmerlin, C., van Boxtel, R., Buijs, A., Sachs, N., Overmeer, R.M., Offerhaus, G.J., Begthel, H., et al. (2015). Sequential cancer mutations in cultured human intestinal stem cells. *Nature* **521**, 43–47.
- Duijff, P.H.G.G., and Benezra, R. (2013). The cancer biology of whole-chromosome instability. *Oncogene* **32**, 4727–4736.
- Farach, L.S., Little, M.E., Duker, A.L., Logan, C. V., Jackson, A., Hecht, J.T., and Bober, M. (2018). The expanding phenotype of RNU4ATAC pathogenic variants to Lowry Wood syndrome. *Am. J. Med. Genet. Part A* **176**, 465–469.
- Fitzgerald, T.W., Gerety, S.S., Jones, W.D., Van Kogelenberg, M., King, D.A., McRae, J., Morley, K.I., Parthiban, V., Al-Turki, S., Ambridge, K., et al. (2015). Large-scale discovery of novel genetic causes of developmental disorders. *Nature* **519**, 223–228.
- García-Castillo, H., Vázquez-Velásquez, A.I., Rivera, H., and Barros-Núñez, P. (2008). Clinical and genetic heterogeneity in patients with mosaic variegated aneuploidy: delineation of clinical subtypes. *Am. J. Med. Genet. A* **146A**, 1687–1695.
- Gibson, D.G., Young, L., Chuang, R.Y., Venter, J.C., Hutchison, C.A., and Smith, H.O. (2009). Enzymatic assembly of DNA molecules up to several hundred kilobases. *Nat. Methods* **6**, 343–345.
- Hall, S.L., and Padgett, R.A. (1996). Requirement of U12 snRNA for in vivo splicing of a minor class of eukaryotic nuclear pre-mRNA introns. *Science* (80-.). **271**, 1716–1718.
- Hallermayr, A., Graf, J., Koehler, U., Laner, A., Schönfeld, B., Benet-Pagès, A., and Holinski-Feder, E. (2018). Extending the critical regions for mutations in the non-coding gene RNU4ATAC in another patient with Roifman Syndrome. *Clin. Case Reports* **6**, 2224–2228.
- Hanks, S., Coleman, K., Reid, S., Plaja, A., Firth, H., Fitzpatrick, D., Kidd, A., Méhes, K., Nash, R., Robin, N., et al. (2004). Constitutional aneuploidy and cancer predisposition caused by biallelic mutations in BUB1B. *Nat. Genet.* **36**, 1159–1161.

- Hart, T., Chandrashekar, M., Aregger, M., Durocher, D., Angers, S., Moffat, J., Crispr, H., Hart, T., Chandrashekar, M., Aregger, M., et al. (2015). High-Resolution CRISPR Screens Reveal Fitness Genes and Genotype-Specific Cancer Liabilities Screens Reveal Fitness Genes. *Cell* **163**, 1515–1526.
- Hein, M.Y., Hubner, N.C., Poser, I., Cox, J., Nagaraj, N., Toyoda, Y., Gak, I.A., Weisswange, I., Mansfeld, J., Buchholz, F., et al. (2015). A Human Interactome in Three Quantitative Dimensions Organized by Stoichiometries and Abundances. *Cell* **163**, 712–723.
- Hooff, J.J., Tromer, E., Wijk, L.M., Snel, B., and Kops, G.J. (2017). Evolutionary dynamics of the kinetochore network in eukaryotes as revealed by comparative genomics. *EMBO Rep.* **18**, 1559–1571.
- van Hooff, J.J.E., Tromer, E., van Dam, T.J.P., Kops, G.J.P.L., and Snel, B. (2019). Inferring the Evolutionary History of Your Favorite Protein: A Guide for Molecular Biologists. *BioEssays* **41**.
- Hubner, N.C., and Mann, M. (2011). Extracting gene function from protein-protein interactions using Quantitative BAC InteraCtomics (QUBIC). *Methods* **53**, 453–459.
- Huttlin, E.L., Ting, L., Bruckner, R.J., Gebreab, F., Gygi, M.P., Szpyt, J., Tam, S., Zarraga, G., Colby, G., Baltier, K., et al. (2015). The BioPlex Network: A Systematic Exploration of the Human Interactome. *Cell* **162**, 425–440.
- Huttlin, E.L., Bruckner, R.J., Paulo, J.A., Cannon, J.R., Ting, L., Baltier, K., Colby, G., Gebreab, F., Gygi, M.P., Parzen, H., et al. (2017). Architecture of the human interactome defines protein communities and disease networks. *Nature* **545**, 505–509.
- Kloet, S.L., Makowski, M.M., Baymaz, H.I., Van Voorthuisen, L., Karemaker, I.D., Santanach, A., Jansen, P.W.T.C., Di Croce, L., and Vermeulen, M. (2016). The dynamic interactome and genomic targets of Polycomb complexes during stem-cell differentiation. *Nat. Struct. Mol. Biol.* **23**, 682–690.
- Knouse, K.A., Davoli, T., Elledge, S.J., and Amon, A. (2017). Aneuploidy in Cancer: Seq-ing Answers to Old Questions. *Annu. Rev. Cancer Biol.* **1**, 335–354.
- Madan, V., Kanojia, D., Li, J., Okamoto, R., Sato-Otsubo, A., Kohlmann, A., Sanada, M., Grossmann, V., Sundaresan, J., Shiraishi, Y., et al. (2015). Aberrant splicing of U12-type introns is the hallmark of ZRSR2 mutant myelodysplastic syndrome. *Nat. Commun.* **6**, 6042–6042.
- Matsuura, S., Matsumoto, Y., Morishima, K.I., Izumi, H., Matsumoto, H., Ito, E., Tsutsui, K., Kobayashi, J., Tauchi, H., Kajiwara, Y., et al. (2006). Monoallelic BUB1B mutations and defective mitotic-spindle checkpoint in seven families with premature chromatid separation (PCS) syndrome. *Am. J. Med. Genet.* **140 A**, 358–367.
- Mi, H., Poudel, S., Muruganujan, A., Casagrande, J.T., and Thomas, P.D. (2016). PANTHER version 10: Expanded protein families and functions, and analysis tools. *Nucleic Acids Res.* **44**, D336–D342.
- Mi, H., Muruganujan, A., Ebert, D., Huang, X., and Thomas, P.D. (2019). PANTHER version 14: More genomes, a new PANTHER GO-slim and improvements in enrichment analysis tools. *Nucleic Acids Res.* **47**, D419–D426.
- Moyer, D.C., Larue, G.E., Hershberger, C.E., Roy, S.W., and Padgett, R.A. (2020). Comprehensive database and evolutionary dynamics of U12-type introns. *Nucleic Acids Res.*
- Nagaoka, S.I., Hassold, T.J., and Hunt, P.A. (2012). Human aneuploidy: Mechanisms and new insights into an age-old problem. *Nat. Rev. Genet.* **13**, 493–504.
- Nishimura, K., Fukagawa, T., Takisawa, H., Kakimoto, T., and Kanemaki, M. (2009). An auxin-based degron system for the rapid depletion of proteins in nonplant cells. *Nat. Methods* **6**, 917–922.
- Oghabian, A., Greco, D., and Frilander, M.J. (2018). IntERESt: Intron-exon retention estimator. *BMC Bioinformatics* **19**, 130.
- Pellegrini, M., Marcotte, E.M., Thompson, M.J., Eisenberg, D., and Yeates, T.O. (1999).

- Assigning protein functions by comparative genome analysis: Protein phylogenetic profiles. *Proc. Natl. Acad. Sci. U. S. A.* **96**, 4285–4288.
- Potter, S.C., Luciani, A., Eddy, S.R., Park, Y., Lopez, R., and Finn, R.D. (2018). HMMER web server: 2018 update. *Nucleic Acids Res.* **46**, W200–W204.
- Rappsilber, J., Mann, M., and Ishihama, Y. (2007). Protocol for micro-purification, enrichment, pre-fractionation and storage of peptides for proteomics using StageTips. *Nat. Protoc.* **2**, 1896–1906.
- Sacristan, C., and Kops, G.J.P.L.P.L. (2015). Joined at the hip: Kinetochores, microtubules, and spindle assembly checkpoint signaling. *Trends Cell Biol.* **25**, 21–28.
- Sheth, N., Roca, X., Hastings, M.L., Roeder, T., Krainer, A.R., and Sachidanandam, R. (2006). Comprehensive splice-site analysis using comparative genomics. *Nucleic Acids Res.* **34**, 3955–3967.
- Smits, A.H., Jansen, P.W.T.C., Poser, I., Hyman, A.A., and Vermeulen, M. (2013). Stoichiometry of chromatin-associated protein complexes revealed by label-free quantitative mass spectrometry-based proteomics. *Nucleic Acids Res.* **41**.
- Snape, K., Hanks, S., Ruark, E., Barros-Núñez, P., Elliott, A., Murray, A., Lane, A.H., Shannon, N., Callier, P., Chitayat, D., et al. (2011). Mutations in CEP57 cause mosaic variegated aneuploidy syndrome. *Nat. Genet.* **43**, 527–529.
- Sterne-Weiler, T., Weatheritt, R.J., Best, A.J., Ha, K.C.H., and Blencowe, B.J. (2018). Efficient and Accurate Quantitative Profiling of Alternative Splicing Patterns of Any Complexity on a Laptop. *Mol. Cell* **72**, 187–200.e6.
- Suijkerbuijk, S.J.E., Van Osch, M.H.J., Bos, F.L., Hanks, S., Rahman, N., and Kops, G.J.P.L. (2010). Molecular causes for BUBR1 dysfunction in the human cancer predisposition syndrome mosaic variegated aneuploidy. *Cancer Res.* **70**, 4891–4900.
- Tarn, W.Y., and Steitz, J.A. (1996). A novel spliceosome containing U11, U12, and U5 snRNPs excises a minor class (AT-AC) intron in vitro. *Cell* **84**, 801–811.
- Turunen, J.J., Verma, B., Nyman, T.A., and Frilander, M.J. (2013). HnRNPH1/H2, U1 snRNP, and U11 snRNP cooperate to regulate the stability of the U11-48K pre-mRNA. *RNA* **19**, 380–389.
- Vader, G. (2015). Pch2TRIP13: controlling cell division through regulation of HORMA domains. *Chromosoma* **124**, 333–339.
- Verbeeren, J., Niemelä, E.H., Turunen, J.J., Will, C.L., Ravantti, J.J., Lüthmann, R., and Frilander, M.J. (2010). An Ancient Mechanism for Splicing Control: U11 snRNP as an Activator of Alternative Splicing. *Mol. Cell* **37**, 821–833.
- Wang, T., Birsoy, K., Hughes, N.W., Krupczak, K.M., Post, Y., Wei, J.J., Lander, E.S., and Sabatini, D.M. (2015). Identification and characterization of essential genes in the human genome. *Science (80-.)*. **350**, 1096–1101.
- Wang, T., Zou, Y., Huang, N., Teng, J., and Chen, J. (2019). CCDC84 Acetylation Oscillation Regulates Centrosome Duplication by Modulating HsSAS-6 Degradation. *Cell Rep.* **29**, 2078–2091.e5.
- Wang, Y., Wu, X., Du, L., Zheng, J., Deng, S., Bi, X., Chen, Q., Xie, H., Férec, C., Cooper, D.N., et al. (2018). Identification of compound heterozygous variants in the noncoding RNU4ATAC gene in a Chinese family with two successive fetuses with severe microcephaly. *Hum. Genomics* **12**.
- Wheeler, T.J., Clements, J., and Finn, R.D. (2014). Skylign: A tool for creating informative, interactive logos representing sequence alignments and profile hidden Markov models. *BMC Bioinformatics* **15**.
- van Wijk, L.M., and Snel, B. (2020). The first eukaryotic kinome tree illuminates the dynamic history of present-day kinases. *bioRxiv* 2020.01.27.920793.

- Yost, S., de Wolf, B., Hanks, S., Zachariou, A., Marcozzi, C., Clarke, M., De Voer, R.M., Etemad, B., Ujttewaal, E., Ramsay, E., et al. (2017). Biallelic TRIP13 mutations predispose to Wilms tumor and chromosome missegregation. *Nat. Genet.* **49**, 1148–1151.
- Zhou, H., Wang, T., Zheng, T., Teng, J., and Chen, J. (2016). Cep57 is a Mis12-interacting kinetochore protein involved in kinetochore targeting of Mad1-Mad2. *Nat. Commun.* **7**, 10151.



CHAPTER 5

MUTATIONS IN KNL1 COMPLEX MEMBERS IN PATIENTS WITH MOSAIC VARIEGATED ANEUPLOIDY SYNDROME

Bas de Wolf, Sandra Hanks, Shawn Yost, Nazneen Rahman, Geert J.P.L. Kops

To be submitted for publication

ABSTRACT

Mosaic variegated aneuploidy (MVA) is a rare autosomal recessive disorder characterized by mosaic aneuploidies in different tissues and a broad spectrum of additional clinical features. Through exome sequencing, we identified monoallelic truncating mutations in *KNL1* or a biallelic truncating mutation in *ZWINT* in five patients diagnosed with MVA. *KNL1* and *ZWINT* together comprise the KNL1 complex, which is involved in kinetochore-microtubule attachment and spindle assembly checkpoint (SAC) signaling. The disease phenotype of the *KNL1*-mutant patients may involve a rare haplotype shared by all four patients, but we found no effect on *KNL1* transcript expression or splicing from that chromosome. Functional characterization of cells derived from *KNL1*-mutant MVA patients revealed that while most mitotic processes operated robustly, the SAC was weakened and kinetochore localization of key mitotic regulators was reduced. *KNL1* mutations have previously been associated with autosomal recessive primary microcephaly (MCPH4), a disorder with a clinical phenotype that closely resembles that of the *KNL1*-mutated MVA patients described in this study. This work highlights the clinical variability seen in patients harboring *KNL1* mutations and expands the list of mitotic regulators associated with MVA.

INTRODUCTION

Accurate chromosome segregation during mitotic or meiotic cell division is essential for maintaining the correct number of chromosomes in cells. Errors in chromosome segregation can lead to aneuploidy, a term that describes a karyotype that deviates from an exact multiple of the haploid set of chromosomes (**chapter 1.1**). Aneuploidies disturb the delicate balance of gene expression and are commonly associated with human diseases, including developmental disorders, spontaneous abortions, and cancer (1–3) (**chapter 1.3**).

Mosaic variegated aneuploidy (MVA; MIM 257300) is a rare autosomal recessive disorder characterized by mosaic aneuploidies involving multiple tissues and chromosomes (**chapter 2.3.5**). In conjunction with aneuploidies, a broad spectrum of additional clinical features is associated with MVA, including microcephaly, growth retardation, mental retardation, facial dysmorphisms, childhood cancers, and early mortality (**Addendum Table 1**) (4). Pathogenic mutations in *BUB1B*, *CEP57*, *TRIP13*, or *CENATAC* have been identified in roughly half of all MVA patients (**chapters 2.3.5, 3 and 4**) (5–7). The first three of these genes have well-documented functions in mitosis (**chapter 3**) (8–11), and in **chapter 4** we describe how *CENATAC* mutations impair chromosome segregation.

Flawless chromosome segregation requires the concerted activities of many molecular processes, including chromatid-spindle attachment and the spindle assembly checkpoint (SAC) (2, 11, 12). These processes take place at the kinetochore, a complex, multi-subunit structure that consist of more than a 100 different proteins in human cells. It is the structure that connect chromatids to spindle microtubules and is the platform upon which the SAC's anaphase-wait signal is generated. This signal, culminating in the anaphase inhibitory complex known as the mitotic checkpoint complex (MCC), arrests cells in mitosis until all kinetochores have achieved biorientation (stable attachment to spindle microtubules emanating from opposite spindle poles). When the last chromosome has achieved biorientation, the SAC is silenced and the cell is able to proceed to anaphase (11). See also **chapter 2.1**.

A central component of the kinetochore is the KNL1 complex, a heterodimer of KNL1 (formerly CASC5 or BLINKIN) and ZWINT. The KNL1 complex is part of the KMN-network (KNL1 complex, MIS12 complex, and NDC80 complex), which is the primary interface between the kinetochore and spindle microtubules (**chapter 2.1**) (11, 13). KNL1 is a large, multi-functional kinetochore scaffold protein (14). Its N-terminal region is involved in microtubule binding and SAC silencing (15), whereas a number of repeated motifs (hereafter referred to as MELT-motifs) throughout the protein form docking sites for BUB1 kinase upon phosphorylation by MPS1 (16) (**Figure 1A**). This MPS1-KNL1-BUB1 axis is responsible for recruiting a host of other proteins to the kinetochore, including those essential for SAC signaling (e.g. BUBR1, MAD1, MAD2, RZZ complex), and those required for chromosome biorientation (e.g. BUBR1) (**chapter 2.1**) (11). Depletion of KNL1 impairs chromosome biorientation and weakens the SAC, causing premature mitotic exit (17, 18). An important functional partner of KNL1 is its KNL1 complex member ZWINT, which interacts with a region in the C-terminal part of KNL1 to stabilize it (19, 20) (**Figure 1B**). Cells lacking ZWINT likewise have a weakened SAC, leading to aberrant, premature chromosome segregation (21).

Mutations in *KNL1* have been linked to autosomal recessive primary microcephaly (MCPH4, MIM 604321, **chapter 2.3.1**) (22–27), a condition in which infants are born with

an unusually small head circumference and mild to severe mental retardation, in some cases in combination with short stature and dysmorphic features (25). *KNL1* is upregulated in the ventricular zone of the human fetal brain, which could potentially explain why *KNL1* malfunction primarily affects cell proliferation in the brain (23, 28). No disease-associated mutations in *ZWINT* have been reported to date.

We here report the identification of mutations in *KNL1* and *ZWINT* in four families diagnosed with MVA syndrome. The patients had mosaic aneuploidies, microcephaly, developmental delay, and in some cases additional clinical features such as growth retardation, facial dysmorphisms, and congenital heart disease. We demonstrate that the *KNL1* patient mutations led to impaired SAC signaling and reduced kinetochore localization of key mitotic regulators.

RESULTS

Identification of mutations in *KNL1* and *ZWINT* in MVA patients

To identify genes responsible for causing MVA in patients of which disease-causing mutations were not known, we undertook exome sequencing in 43 individuals from 20 families, including 21 patients diagnosed with MVA. We generated exome data using the Illumina TruSeq exome capture assay and called variants using the OpEx pipeline as previously described (7, 29). We performed two analyses to prioritize variants for further evaluation: the full series of patients was analyzed with the protein-truncating variants (PTV) prioritization method to identify genes with truncating mutations in more than one patient, and we undertook an individual patient analysis to identify genes with two rare variants, as MVA is a recessively inherited condition (7).

We identified mutations in both members of the *KNL1* complex, *KNL1* and *ZWINT*. A homozygous truncating mutation in *ZWINT*, c.472delC, was found in DNA from a Greek fetus that had died preterm (**Figure 1C, Addendum Table 1**, patient 53a). Both parents were heterozygous for the mutation and a second child had also died in utero (**Figure 1D**), though no DNA was available for mutation analysis. The mutation was not present in ExAC or ICR1000 series. Chromosome analysis of the fetus revealed aneuploidies in 92% of cells involving different chromosomes (**Figure S1**). The mutation results in the loss of *ZWINT*'s C-terminal ZW10-interaction domain (**Figure 1B**) (30) and is expected to cause nonsense-mediated mRNA decay (NMD) (31). Although functional data are lacking due to the absence of viable patient cell lines, it is highly likely that the homozygous *ZWINT* mutation we identified is the cause of the severe phenotype in these siblings.

We furthermore identified three monoallelic truncating mutations in *KNL1* (c.1243delC, c.3654delA, and c.5028delG, **Figure 1C**) in four affected individuals from three Ashkenazi families (**Figures 1E and S1, Addendum Table 1**, patients 5 and 51-52b), none of which were present in ExAC or ICR1000 series. No plausible second mutation was identified in the *KNL1* coding sequence; only common variants were present. Parental samples were only available of family 0661 and showed that the mother carries the truncating mutation (**Figure 1E-F**, ID_0661_04). All four patients had microcephaly, developmental delay, and to a varying degree other symptoms such as growth retardation, facial dysmorphisms, and congenital heart disease (**Figures 1C, S1**). Chromosome analysis of different tissues revealed aneuploidies in 9-13% of cells involving many different chromosomes (**Figure**

S1). The patient ID_0639 was originally diagnosed with Seckel syndrome (MIM 210600), a rare autosomal recessive disorder characterized by intrauterine growth retardation, microcephaly with mental retardation, and characteristic facial dysmorphisms (32, 33).

All three truncating *KNL1* mutations lead to the loss of KNL1's MIS12-interaction domain, which is required for KNL1 kinetochore localization, and its ZWINT-interaction domain, which is required for the stabilization of KNL1 protein (**Figure 1A**) (20). In addition, all three mutations are expected to cause NMD. We therefore consider it very likely that these truncating mutations lead to a complete loss of KNL1 function from the affected allele. To examine the effect of these mutations on the expression level of *KNL1* transcript, we performed qPCR analysis on cDNA isolated from mitotic, immortalized fibroblasts derived from ID_0639 and ID_0640 (hereafter referred to as patient 1 and patient 2, respectively). As expected, *KNL1* transcript levels were reduced (to ~50% of controls, **Figure 1G**).

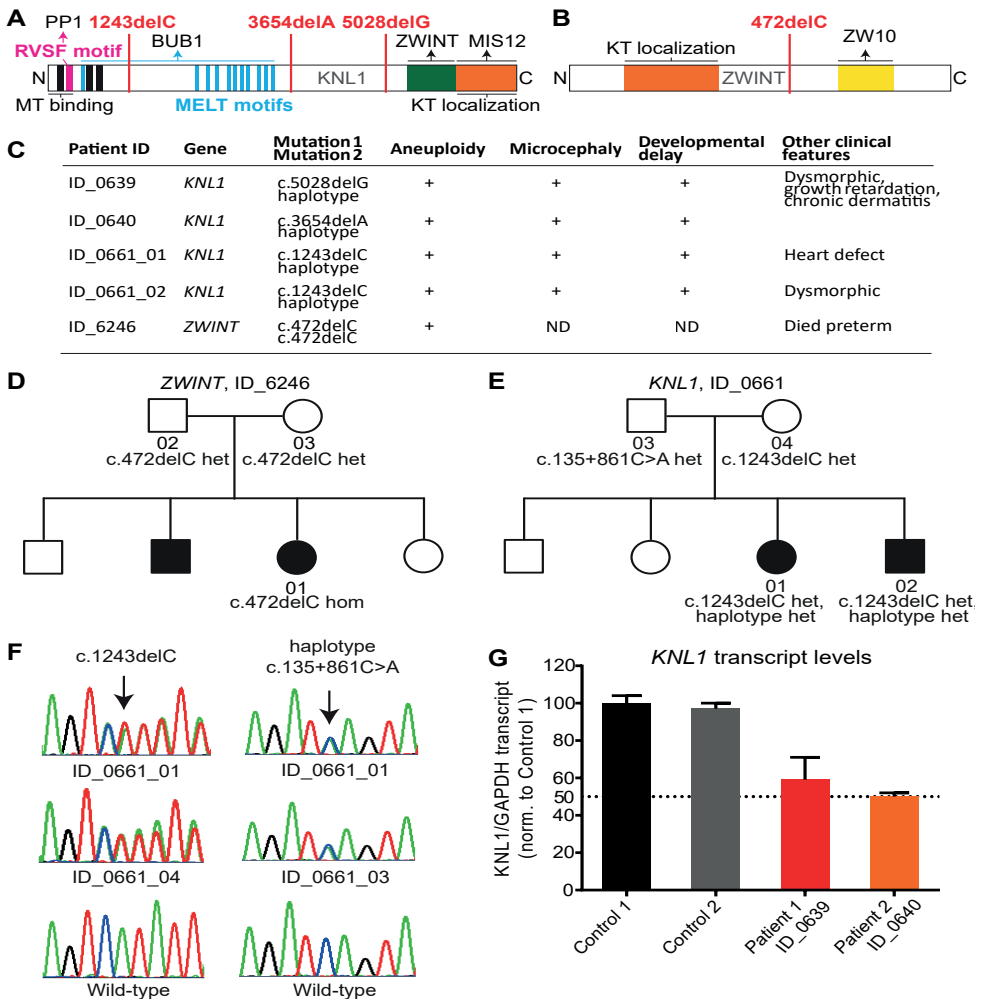


Figure 1. Identification of mutations in *KNL1* and *ZWINT* in MVA patients. A) Schematic of *KNL1*, including relevant domains and motifs. The locations of the truncating patient mutations are depicted with red lines. **B)** Schematic of *ZWINT*, including relevant domains and motifs. The location of the

truncating patient mutation is depicted with a red line. **C)** Molecular and clinical features of individuals with mutations in *KNL1* or *ZWINT*. ND: no data. **D)** Pedigree of family ID_6246 with indicated *ZWINT* mutations. Het: heterozygous, hom: homozygous. **E)** Pedigree of family ID_0661 with indicated *KNL1* mutations. Het: heterozygous. **F)** Chromatograms of individuals in E) depicting sequence flanking the indicated mutations. **G)** RT-qPCR quantification of *KNL1* mRNA in mitotic patient-derived fibroblast. Each bar depicts the mean of 3 technical replicates \pm SEM. Expression levels are normalized to GAPDH and are relative to control 1.

All *KNL1*-mutated MVA patients share a rare haplotype encompassing *KNL1*

Since no plausible second mutation was present in the *KNL1* coding sequence, we undertook whole genome sequencing in three affected individuals (patient 1, patient 2, and ID_0661_01) and the father of the 0661 siblings, which revealed a shared 3.4Mb haplotype on chromosome 15 encompassing *KNL1* (**Figure 2A-B**). This was the largest shared region, strongly suggesting that the second pathogenic mutational event was in the vicinity of *KNL1*. Within the shared haplotype, the intronic variant c.135+186C>A was the most plausible candidate mutation as it is the rarest variant and is absent from 1000 Genomes data. We genotyped 96 individuals of self-reported Ashkenazi Jewish origin for this and four flanking, rare variants on the shared haplotype (**Figure 2C-D**). None of the variants were present in 90 of the 96 individuals. Four individuals carried the full haplotype, whilst two individuals carried four of the five variants, but did not carry c.135+186C>A, adding further support that this is the most likely causal variant (**Figure 2D**).

Intronic mutations can have a major effect on pre-mRNA splicing, for instance by creating new splice sites, activating cryptic ones, or affecting the binding of splicing enhancers and silencers (34, 35). To investigate whether c.135+186C>A or any of the other four variants depicted in **Figure 2C** had an effect on splicing of *KNL1* pre-mRNA, we amplified the regions flanking each of the variants from cDNA isolated from cells derived from patients 1 and 2 (**Figure 2E-F**). However, no effect on splicing was observed in both patient-derived lymphoblasts and fibroblast (**Figures 2F, S2**). We thus find no evidence that these intronic variants affect *KNL1* pre-mRNA splicing. Nevertheless, given that the heterozygous parents are healthy and that this rare haplotype is shared by all patients, we deem it likely that these or other variants present in the haplotype somehow affected *KNL1* function, be it by affecting mRNA splicing or otherwise.

KNL1 patient mutations lead to a weakened SAC

All four *KNL1*-mutated MVA patients had aneuploidies in up to 13% of cells analyzed (**Figure S1**), which is indicative of increased rates of chromosome missegregation. Because *KNL1* has well-documented roles in chromosome biorientation, SAC signaling, and SAC silencing, we examined mitotic fidelity in cultured EBV-immortalized lymphoblasts derived from patient 1. As shown in **Figure 3A**, we did not detect appreciable levels of chromosome segregation errors, suggesting that all processes required for high fidelity chromosome segregation were working sufficiently, at least in immortalized lymphoblasts. Nor did we observe significant lengthening of prometaphase or metaphase, which would be indicative of inefficient chromosome biorientation or SAC silencing, respectively (**Figure 3B**). More detailed analysis, however, revealed that the cells of patients 1 and 2 had a weakened SAC.

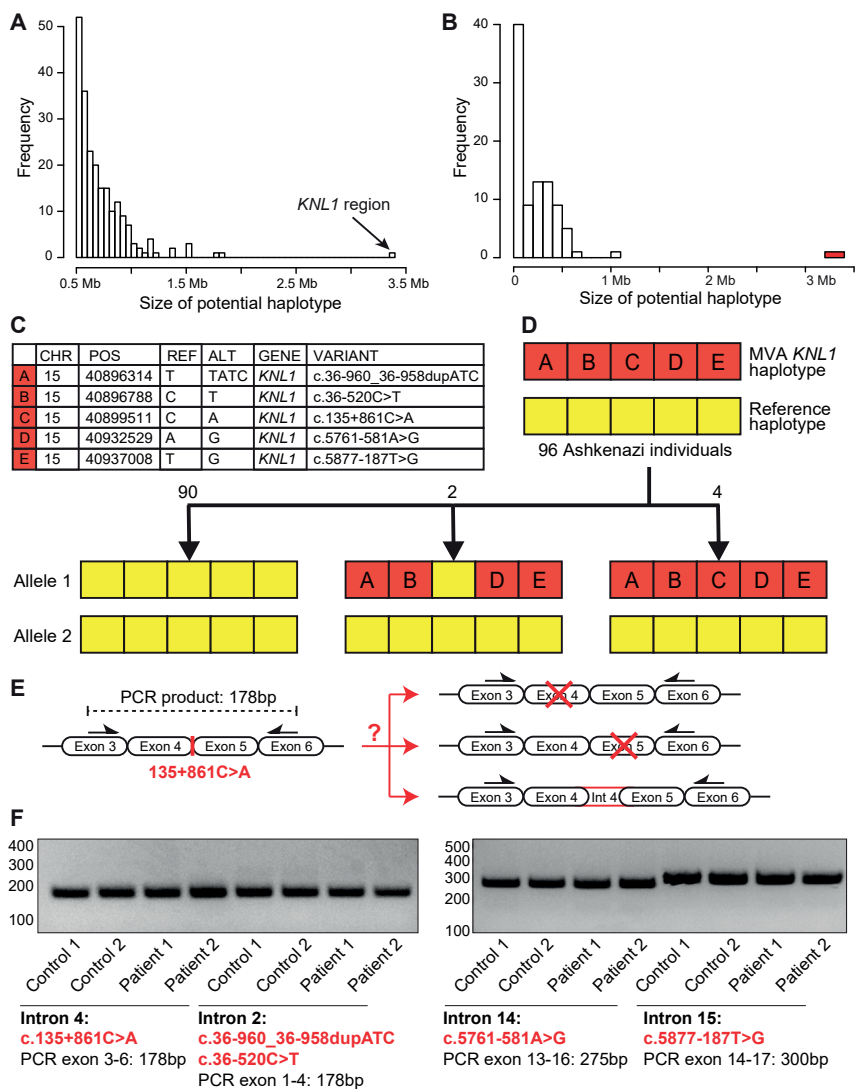


Figure 2. All *KNL1*-mutated MVA patients share a rare haplotype encompassing *KNL1*. **A)** Histogram of ≥ 0.5 Mb potential haplotypes shared between the three affected individuals with a *KNL1* protein-truncating variant (PTV). The 3.4Mb region around *KNL1* is the largest out of 217,379 potential haplotype regions. **B)** Histogram of potential haplotypes around *KNL1* for 100 random sets of three 1000 Genome Project individuals (white) and the three MVA cases with a *KNL1* PTV (red). The 3.4 Mb shared segment between the three MVA cases is more than 15 standard deviations away from the mean shared segment sizes of the 100 random sets of three. **C)** Locations of five intronic *KNL1* variants identified on the shared haplotype. **D)** *KNL1* haplotype analysis in 96 Ashkenazi individuals. Genotyping of the five intronic *KNL1* variants depicted in C) shows that Variant C, *KNL1* c.135+861C>A, is the rarest and most likely causal variant on the haplotype. **E)** Schematic of potential defects caused by the intronic variant c.135+861C>A in intron 4: skipping of exon 4 or 5, or inclusion of (part of) intron 4. Black arrows indicate primer locations for the RT-PCR analysis done in F). **F)** RT-PCRs of regions flanking the *KNL1* intronic variants in RNA extracted from patient- and control-derived fibroblasts (see **Figure S2** for the lymphoblast RT-PCRs).

When treated with nocodazole, a drug that causes microtubule depolymerization and thus arrests cells in mitosis with kinetochores not attached to microtubules, both control cells and cells derived from patient 1 were able to maintain a proper mitotic arrest for at least 5 hours (**Figure 3C**). To mimic a state with few unattached kinetochores, we next treated the cells with nocodazole and a low dose of Cpd5, which reduces SAC signaling and accelerates mitotic exit. As expected, whereas most controls cells were able to mount a SAC response that delayed mitotic exit for more than 3 hours, most patient cells exited from mitosis within 1-2 hours (**Figure 3D-E**). This reduction in SAC signaling was observed for both patient 1-derived lymphoblasts in low nocodazole and for patient 1- and patient 2-derived fibroblasts in low STLC (**Figure 3D-G**), implying that this is not a tissue-specific defect but likely present in all *KNL1*-mutated cells. We reasoned that if other functions of *KNL1* are likewise compromised only slightly, these defects might surface in sensitized assays such as treatment with low nocodazole, which reduces the formation of stable kinetochore-microtubule attachments and therefore reduces the efficiency of chromosome biorientation and SAC silencing. Unfortunately, this could not be conclusively examined, because the two control cell lines showed a substantially different response to low nocodazole (**Figure S3A-B**). In the absence of parental control lines or experimental introduction of the disease mutations in cells, it therefore remains unclear whether the *KNL1* mutations negatively affect chromosome biorientation and/or SAC silencing.

Kinetochore recruitment of key mitotic regulators is impaired in *KNL1*-mutated patient cells

To investigate how the *KNL1* patient mutations led to the observed reduction in SAC signaling, we measured the kinetochore localization of SAC proteins known to depend on *KNL1* for their kinetochore recruitment. As expected, kinetochore localization of *KNL1* and *ZWINT* was severely affected in patient-derived lymphoblasts, ~37% of controls (**Figure 4A-C**). This was a significantly stronger reduction than was observed for *KNL1* transcript expression, which was to ~50% of controls (**Figure 1G**). Although it is currently unclear what is responsible for this difference, it is tempting to speculate that the unique haplotype of the patients affects protein function by other means than reducing *KNL1* transcript expression. Kinetochore localization of the SAC proteins *BUB1*, *BUBR1*, *MAD1*, *MAD2*, and *ZWILCH* (*RZZ* complex member) was also significantly affected yet to a lesser extent than *KNL1* and *ZWINT* (to ~60-80% of controls; **Figure 4C**). Because the recruitment of these SAC proteins depends on the phosphorylation of *KNL1*'s MELT-motifs, we next measured MELT phosphorylation with an antibody that recognizes phospho-T943 and phospho-T1155 within two of *KNL1*'s MELT-motifs (36). As shown in **Figure 4C**, phosphorylation of these MELT-motifs was reduced to approximately 60% of the controls. Given that the kinetochore localization of *KNL1* was reduced to approximately 37% of controls, this means that per *KNL1* molecule T943 and T1155 were phosphorylated nearly twice as often in the patient cells. The relatively small reduction in kinetochore localization of the above SAC proteins may therefore be the result of an increase in the relative phosphorylation status of *KNL1*. Similar to the phosphorylation of its MELT-motifs, the phosphorylation of *KNL1*'s RVSF motif, which antagonizes the recruitment of PP1 phosphatase and SAC silencing (37), was also reduced to approximately 60% of controls (**Figure 4C**). Taken together, these results show that the *KNL1* patient mutations led to a reduction in kinetochore localization of *KNL1*, *ZWINT*, and of other downstream kinetochore proteins. This is consistent with and may explain the observed reduction in SAC signaling. Whether this reduction in kinetochore

localization likewise translated to a minor impairment of chromosome biorientation or SAC silencing remains unclear.

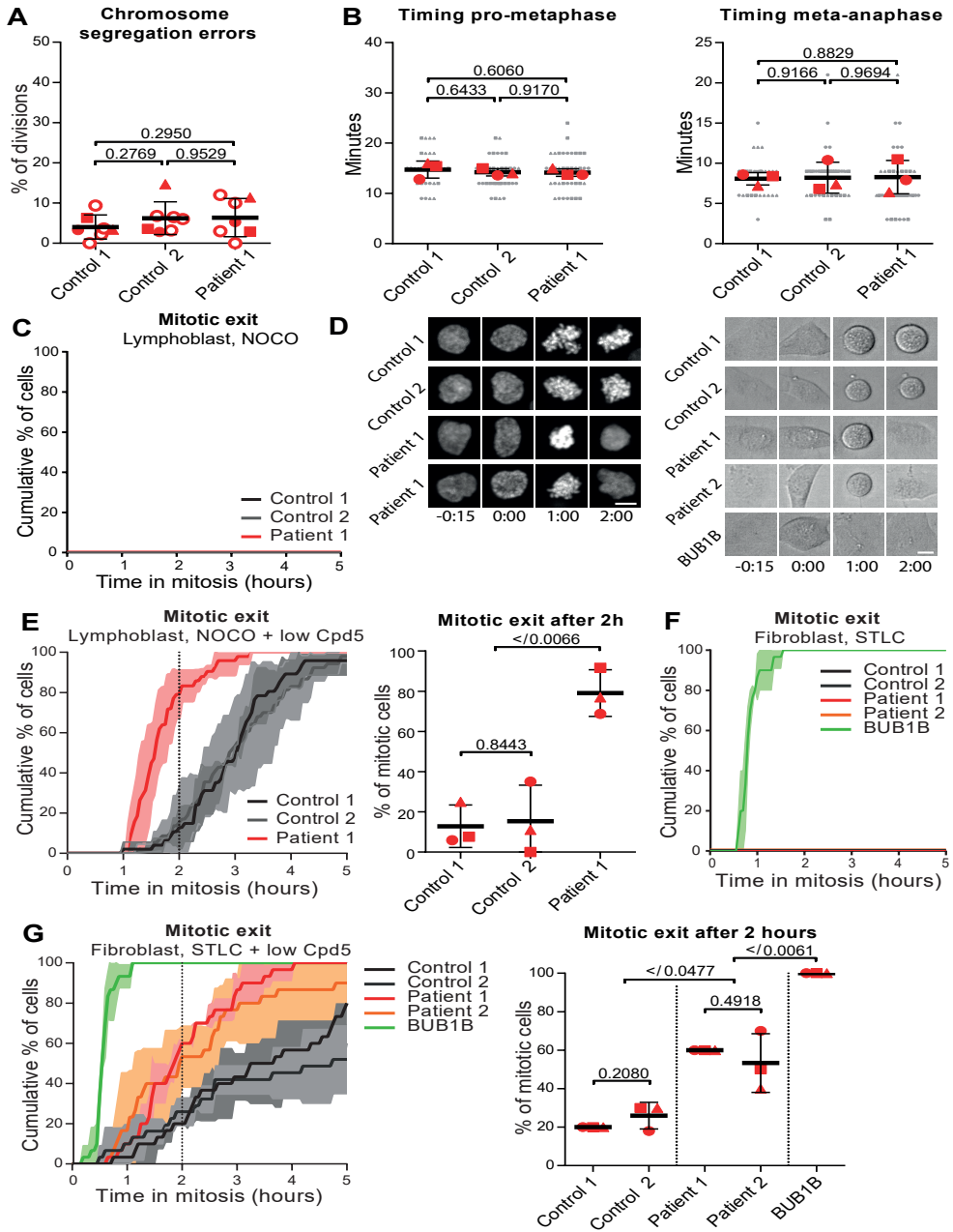


Figure 3. *KNL1* patient mutations lead to a weakened SAC. A) Quantification of chromosome segregation errors of patient and control lymphoblasts expressing H2B-mNeon to visualize the DNA. Each bar depicts the mean of seven independent experiments \pm SEM, with >25 cells per sample per experiment. Each separate experiment is depicted with a red symbol; of these, the filled circle, square,

and triangle correspond to the experiments that are similarly depicted in 2B). P-values were calculated with two-sided unpaired Student's t tests. **B)** Quantification of the timing of prophase to metaphase (left) and metaphase to anaphase (right) of cells in experiments depicted with full filled symbols in A). Each bar depicts the mean of three independent experiments \pm SEM, with >35 (left) and >28 (right) cells in total per condition. The average of each separate experiment is depicted with a red circle, square, or triangle; each individual cell is depicted with a gray small circle, square, or triangle, depending on the experiment. **C)** Quantification of cumulative mitotic exit in time of patient and control lymphoblasts in nocodazole. Each line depicts the mean of three independent experiments \pm SEM (shaded regions) with 10 cells per experiment per condition. **D)** Representative images of H2B-mNeon expressing patient and control lymphoblasts (left) and fibroblasts (right) going through mitosis in the presence of nocodazole (lymphoblasts) or STLC (fibroblasts) to activate the mitotic checkpoint and a low dose of the MPS1 inhibitor Cpd5 to accelerate mitotic exit. Time is in hours with mitotic entry at $t=0$. Scale bar, $5 \mu\text{m}$. **E)** Left: quantification of cumulative mitotic exit of patient and control lymphoblasts treated as in D). Each line depicts the mean of three independent experiments \pm SEM (shaded regions) with 15-20 cells per experiment per condition. The dotted line indicates the time point used in the graph on the right: the percentage of cells that had exited mitosis after 2 hours is plotted with each bar depicting the mean of the three experiments (red icons) \pm SEM. P-values were calculated with two-sided unpaired Student's t tests. **F)** Quantification of mitotic exit as in C) of patient and control fibroblasts treated with STLC. BUB1B refers to a patient-derived fibroblast cell line from a MVA patient with *BUB1B* mutations (MVA55, unpublished). Each line depicts the mean of three technical replicates \pm SEM (shaded regions) with 10 cells per experiment per condition. **G)** Left: quantification of mitotic exit of patient and control fibroblasts treated as in D). Each line depicts the mean of three independent experiments \pm SEM (shaded regions) with 10 cells per experiment per condition. The dotted line indicates the time point used in the graph on the right: the percentage of cells that had exited mitosis after 2 hours is plotted with each bar depicting the mean of the three experiments (red icons) \pm SEM. P-values were calculated with two-sided unpaired Student's t tests.

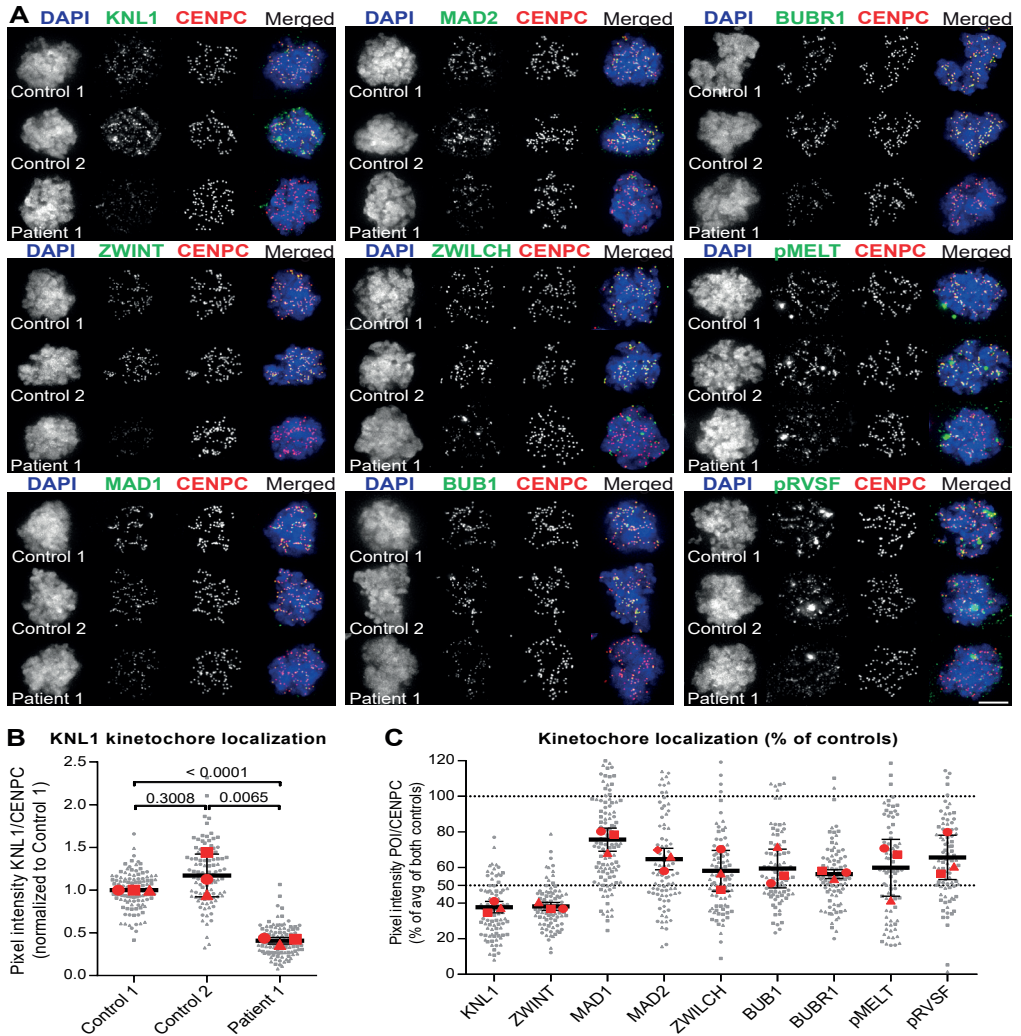


Figure 4. Kinetochore recruitment of key mitotic regulators is impaired in *KNL1*-mutated patient cells. A-C Immunofluorescence labeling (A) and quantification (B, C) of the indicated proteins in nocodazole-arrested control or patient lymphoblasts. Centrosome signals were omitted from the quantifications. In the plots, each bar depicts the mean of three independent experiments \pm SEM, with >25 cells per condition per experiment. The average of each separate experiment is depicted with a red circle, square, or triangle. Each individual cell is depicted with a gray small circle, square, or triangle, depending on the experiment. Average pixel intensities for each protein of interest (POI) per cell were normalized to the average pixel intensity of CENPC. In B) all values were normalized to the average of control 1. In C) the percentage of kinetochore localization compared to the average of both controls is depicted. P-values were calculated with two-sided unpaired Student's t tests. Scale bar, 5 μ m.

DISCUSSION

In this study, we identified pathogenic *KNL1* or *ZWINT* mutations in four families diagnosed with MVA. The *KNL1*-mutated MVA patients all had one of three different monoallelic truncating mutations that likely lead to NMD and a complete loss of KNL1 function. On the other chromosome, we found a rare a 3.4Mb haplotype encompassing *KNL1* that was shared by all four patients. Given that heterozygous carriers of the truncating mutation in *KNL1* are healthy (**Figures 1E, S1**) and that KNL1 kinetochore localization was reduced to below 50% of the controls, it is likely that this haplotype negatively affected KNL1 function and contributed to the disease phenotype.

If the haplotype is indeed involved, this pattern of *KNL1* mutations would be reminiscent of that of *BUB1B* (encoding BUBR1) in which patients with MVA typically have one truncating and one hypomorphic mutation (5). In a subset of MVA patients with a monoallelic truncating *BUB1B* mutation, a haplotype was found on the other chromosome that included an intergenic variant 44 kb upstream of the *BUB1B* transcription start site (38). This variant was later shown to be the causal mutation, though the mechanism of pathogenicity remains unclear (39). These data, together with the patterns of *KNL1* mutations observed in MCPH4 patients (see below), suggest that biallelic loss-of-function mutations in *KNL1* are not compatible with life, similar to mutations in the MVA genes *BUB1B* and *CENATAC* (8) (**chapter 4**).

The homozygous truncating mutation in *ZWINT* resulted in exceedingly high levels of mosaic aneuploidies (92% of analyzed cells, **Figure S1**) and caused preterm death. Functional data are lacking due to the absence of viable patient cell lines and it remains unclear what the effect of the mutation is. However, given that *ZWINT* is required for the stabilization of KNL1 protein (20) and that the KNL1-complex members are overrepresented on the short list of genes associated with MVA, it is likely that the pathogenicity of the *ZWINT* mutation is through a reduction in KNL1 function.

Characterization of patient-derived cells revealed that the *KNL1* mutations led to a weakened SAC and a reduction in kinetochore localization of KNL1, *ZWINT*, and of other downstream mitotic regulators. It is of note that mutations in the MVA genes *BUB1B* and *TRIP13* also resulted in a weakened SAC (**chapter 3**) (7, 8). In fact, we previously speculated that the severe SAC impairment associated with *BUB1B* and *TRIP13* mutations may be responsible for the frequent incidence of cancer in MVA patients with these mutations (**chapter 3**) (7). The SAC defect caused by the *KNL1* mutations, however, was significantly weaker (**Figure 3G**), which is in line with the lower levels of aneuploid cells and the milder, cancer-free clinical phenotypes of *KNL1*-mutated MVA patients (see also **chapter 6.4**). Whether KNL1's functions in chromosome biorientation and SAC silencing are similarly affected by the patient mutations remains unclear. Even though we did not observe appreciable chromosome segregation errors in patient-derived lymphoblasts, it is very likely that the weakened SAC, together with any potential minor effect on chromosome biorientation or SAC silencing, is responsible for the elevated levels of aneuploid cells in these patients. Cells in certain tissues and stem cell pools are likely more sensitive to minor disturbances in the processes governing chromosome segregation than cells cultured in optimal conditions.

Mutations in *KNL1* are associated with autosomal recessive primary microcephaly (MCPH), a neurogenic mitotic disorder that is characterized by decreased brain size and mental

retardation as a result of impaired neurodevelopment (**chapter 2.3.1**) (22–27, 40, 41). MCPH patients with mutations in *KNL1* (MCPH4, MIM 604321) exhibit mild to severe mental retardation, normal to short stature, and in some cases some dysmorphic features, but always without mosaic aneuploidies (22–27). This clinical phenotype closely resembles that of the MVA patients described in the present study. However, given that MCPH4 patients do not have mosaic aneuploidies and that they present with symptoms in tissues other than the brain less often than *KNL1*-mutated MVA patients do, it is possible that the mutations identified in MVA patients result in a significantly stronger impairment of *KNL1* function. MCPH4 *KNL1* mutations include homozygous splicing mutations that lead to exon skipping, a translational frameshift, and truncation of the protein (23, 24); heterozygous compound mutations consisting of one truncating mutation and one substitution mutation of unknown significance (26); and a homozygous in-frame deletion of unknown significance (27). An obvious difference between the MVA mutations and the MCPH4 splicing mutations is that the splicing mutations resulted in occasional skipping of exon 18 (23) or exon 25 (24) during *KNL1* pre-mRNA splicing, which translated to a reduction in transcript and protein levels to approximately 40–60% of controls depending on the cell-type (24). Furthermore, it was later confirmed that certain cell-types are more sensitive to *KNL1* splicing mutation than others (42). In contrast, the truncating *KNL1* mutations of MVA patients are expected to affect 100% of the transcripts derived from that allele in all cell-types. The MCPH4 heterozygous compound mutations (26), on the other hand, more closely resemble those found in the MVA patients: a truncating mutation in combination with a substitution mutation of unknown significance. Although we expect that also this truncating mutation results in a complete loss of *KNL1* function, no expression data is available for this patient and it is unclear if, and to what extent, the substitution mutation affects *KNL1* function. Given that no mosaic aneuploidies were found in this patient, and that its clinical phenotype is relatively mild (no developmental delay and no dysmorphic features (26)), we expect that the substitution mutation affects *KNL1* function to a lesser extent than the haplotype identified in MVA patients does. Alternatively, it is possible that the *KNL1* defect of the MCPH4 patient is somehow compensated for by other mechanisms.

ACKNOWLEDGEMENTS

We thank the families for their participation and the researchers that recruited them including K. Asakura-Hay, S. Bernardo de Sousa, P. Callier, D. Chitayat, J. Clayton-Smith, S. Fernandes, D. FitzPatrick, S. Jacquemont, R. Marin Iglesias, M. Micale, J. Tolmie. We thank Anthony Renwick, Shazia Mahamdallie and Chey Loveday for helpful discussions and Ann Strydom and Brittany Rex for assistance in preparing the manuscript. We acknowledge NHS funding to the Royal Marsden/ICR NIHR Biomedical Research Centre. The Kops lab is part of the OncoCode Institute, which is partly funded by the Dutch Cancer Society. This study was further funded by the Cancer Genomics Center (CGC.nl) (GK) and by the Wellcome Trust (100210/Z/12/Z) (NR). We thank the Kops and Rahman labs for discussions and Andrea Musacchio for reagents.

Nazneen Rahman is a Non-Executive Director of AstraZeneca. The other authors declare no competing interests.

Correspondence and material requests should be addressed to Geert Kops (g.kops@hubrecht.eu)

METHODS

Samples

The study was approved by the London Multicentre Research Ethics Committee (05/MRE02/17). Case DNA samples were obtained through our ongoing research and clinical studies of mosaic variegated aneuploidy syndrome and cancer predisposition genes, or from cell line repositories at the Coriell Institute for Medical Research, NJ, USA or the European Collection of Cell Cultures (ECACC), Salisbury, UK. Appropriate consent was obtained from patients and/or parents as applicable. DNA was extracted from whole blood or EBV-transformed lymphoblast cell lines using standard protocols. For the functional experiments the following patient lymphoblast cell line was used: ID_0639 (Coriell no. GM09703, *KNL1* mutations). Two control cell lines were also used: control 1 was from ID_5728_03 (ECACC no. FACT5728KC), control 2 was C0106 (ECACC no. g1071212). In addition, the following patient fibroblast cell lines were used: ID_0639 (Coriell no. GM09703, *KNL1* mutations), ID_0640 (*KNL1* mutations). Control 1: HDF-F, control 2: HDF-N.

LCLs were cultured in RPMI supplemented with 15% fetal bovine serum (FBS), 100 µg/ml penicillin/streptomycin and 2 mM alanyl-glutamine. Fibroblasts were cultured in DMEM supplemented with 10% fetal bovine serum (FBS), 100 µg/ml penicillin/streptomycin and 2 mM alanyl-glutamine. Cells expressing H2B-mNeon were created by lentiviral transduction, using standard procedures. Imaging of cells was performed as previously described (**chapter 3**) (43).

Exome sequencing, alignment and variant calling, reference datasets, PTV prioritization method, recessive analysis, Sanger sequencing, and multidimensional scaling analysis: performed as previously described (chapter 3, chapter 4) (43).

Whole genome sequencing

We generated whole genome sequencing data on ID_0639, ID_0640 and ID_0661_01 and the father of the 0661 siblings. The sequencing was performed by the High-Throughput Genomics Group at the Wellcome Trust Centre for Human Genetics, Oxford. Libraries were prepared from 1.5-5 µg genomic DNA using the NEBNext Ultra DNA Library Prep Kit for Illumina (New England BioLabs). For each sample, four PCRs were set up using custom indexes. Paired-end sequencing was performed on an Illumina HiSeq using v3 chemistry to reach approximately 25X coverage.

Haplotype analysis

We used the whole genome sequencing data to identify potential shared haplotypes across a set of three individuals. First, we took the union of all base substitutions called across the 18 given three individuals. Then for each chromosome, CHR, we started at the first variant site in which all three individuals shared at least one of two alleles. For example, if individual one had alleles BB then individual two and individual three had to be either AB or BB to be considered part of a haplotype. We then defined this variant site as the start of the possible haplotype, S. Next we extended the possible haplotype until we found a

variant site in which none of the alleles matched between at least two individuals. The end of the haplotype was defined as the last variant site that shared at least one allele between all three individuals, E. The possible shared haplotype was then defined as CHR:S-E. This process was repeated across the whole chromosome. Any possible shared haplotype overlapping or encompassing a centromere was removed (**Figure 2A**). In order to get a background rate for the possible shared haplotype we randomly selected three unrelated individuals from the 1000 Genomes Project 100 times. Each set of three was required to originate from the same subpopulation of the 1000 Genomes Project and we removed any duplicate sets of three. We downloaded the latest version of the variant data from the 1000 Genomes Project website (version 5). We then used PLINK to calculate the PL_HAT score or relatedness score for each pair of 1000 Genomes Project individuals. Next we removed any pair of individuals that were potentially related ($PL_HAT > 0$). Finally for each set of three 1000 Genome Project individuals, we applied the possible shared haplotype analysis described above (**Figure 2B**).

qRT-PCR

Fibroblasts were synchronized in early S-phase for 24 hours by addition of 2 mM thymidine and released the next morning in 0.83 μ M nocodazole. After 12 hours a mitotic shake-off was performed to harvest mitotic cells. Total mRNA was extracted using the RNeasy Mini kit (Qiagen). cDNA synthesis was carried out using SuperScript™ II RT (Thermo Fisher Scientific) and Oligo(dT)18 primers. Real-time quantification was performed with IQ SYBR Green Supermix (Bio-Rad) on a CFX Connect Real-Time system (Bio-Rad) using probes generated against KNL1 (CCAGATGCAACAGAAGGAGTTTT & TGGTGGACTTTTCACTTATGGG) and GAPDH (AATCCCATCACCATCTTCCA & TGGACTCCACGACGTAACA). The data were normalized to GAPDH expression and patient sample data were compared to the expression of control 1 to quantify relative expression levels of KNL1, using the $2^{-\Delta\Delta CT}$ method.

RT-PCR

Total cellular RNA was extracted using the RNeasy kit protocol (Qiagen) and treated with DNase I Amplification grade (Invitrogen) to remove potential genomic DNA contamination. cDNA synthesis was carried out using SuperScript™ II RT (Thermo Fisher Scientific) and Oligo(dT)18 primers. PCRs were performed with Phusion High-Fidelity DNA polymerase (Thermo Fisher Scientific). The following primer sets were used:

AGAGACCTGTTAGAAGACGGCA	Fw. 135+861C>A
TCATATGAGACTCCGTCTGGAA	Rev. 135+861C>A
AGAGCGTGTGGACCCCAAACA	Fw. 36-960_36-958dupATC and 36-520C>T
AGAGGACTCCTTGGGGTTTCA	Rev 36-960_36-958dupATC and 36-520C>T
TTGTGAAGAGAGCTTGAGGGAG	Fw. 5761-581A>G
CCAACAGCTTATCTTGGTTCGATGC	Rev 5761-581A>G
ACAGAGCAATCTCCAGGCA	Fw. 5877-187T>G
GAGTGAAGACTTTAGTCATCTTGGT	Rev 5877-187T>G

Live cell imaging and analysis of mitotic fidelity, timing and chromosome segregation errors

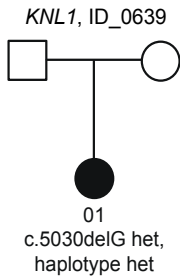
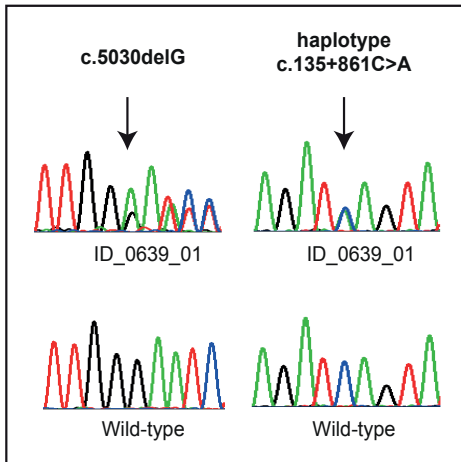
Was performed as previously described (**chapter 3**) (43). Fibroblast cells were plated without agar the day before the experiment, just before the addition of thymidine, and imaged with DIC instead of fluorescent light. Start of prophase: chromosome condensation, metaphase: full alignment, anaphase: chromosome separation. Nocodazole: 83 μM , STLC: 100 nM, low nocodazole: 40 nM, low Cpd5: 75 nM (lymphoblast), 20 nM (fibroblast).

Immunofluorescence imaging

Was performed as previously described (**chapter 3**) (43). Centrosome and filament structures were excluded from the quantifications, which were done using CellProfiler. Primary antibodies used were guinea pig anti CENP-C (MBL PD030), rabbit anti KNL1 (Abcam ab-70537), rabbit anti ZWINT (Abcam ab71982), mouse anti MAD1 (Merck Millipore MABE867), rabbit anti MAD2 (Custom B.O. 017), mouse anti Zwilch (gift by Andrea Musacchio, custom made, (44)), rabbit anti BUB1 (Bethyl A300-373A-1), rabbit anti BUBR1 (Bethyl A300-386A), rabbit anti pMELT (custom pKNL1 pT943/pT1155), rabbit anti pRVSF (custom). Secondary antibodies used were goat anti-rabbit 488 (A11036), goat anti-mouse 568 (A21236), and goat anti-guinea pig 647 (A21450), all three obtained from ThermoFisher.

SUPPLEMENTARY FIGURES

ID_0639. The proband was first reported by Warburton et al in 1991 and is of Ashkenazi origin. She had extreme microcephaly, growth retardation and severe intellectual disability. She also had a beaked nose, micrognathia, myopia, esotropia, limited elbow extension and chronic atopic dermatitis. Chromosome analyses were performed over several years in peripheral blood lymphocytes, fibroblast cultures from different biopsy sites, bone marrow and a lymphoblastoid cell line. At least 10% of cells in every tissue showed aneuploidies involving many different chromosomes and 1-3% had double trisomy. PCS was noted in a high number of metaphases examined. Parental samples were not available. The proband was alive at 17 years of age.



ID_0640. The proband is of Ashkenazi origin. She had severe microcephaly and developmental delay. Chromosome analysis revealed various aneuploidies in 13% of cells, including trisomy for chromosomes 7, 8 and 14 and monosomy for chromosomes 3, 17 and 22. Parental samples were not available. The proband was alive at 13 months of age.

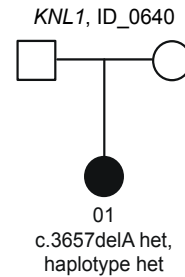
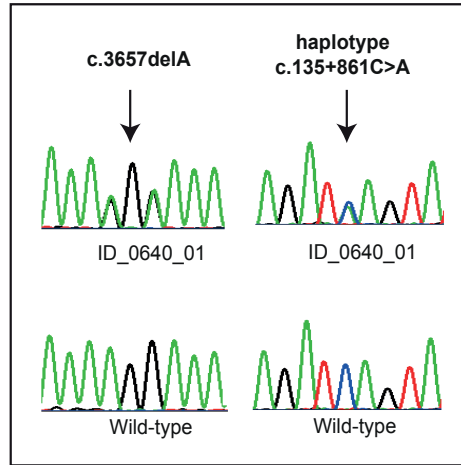


Figure S1. Case reports, pedigrees and chromatograms of individuals with mutations in *KNL1* or *ZWINT*. See also Figure 1D-E.

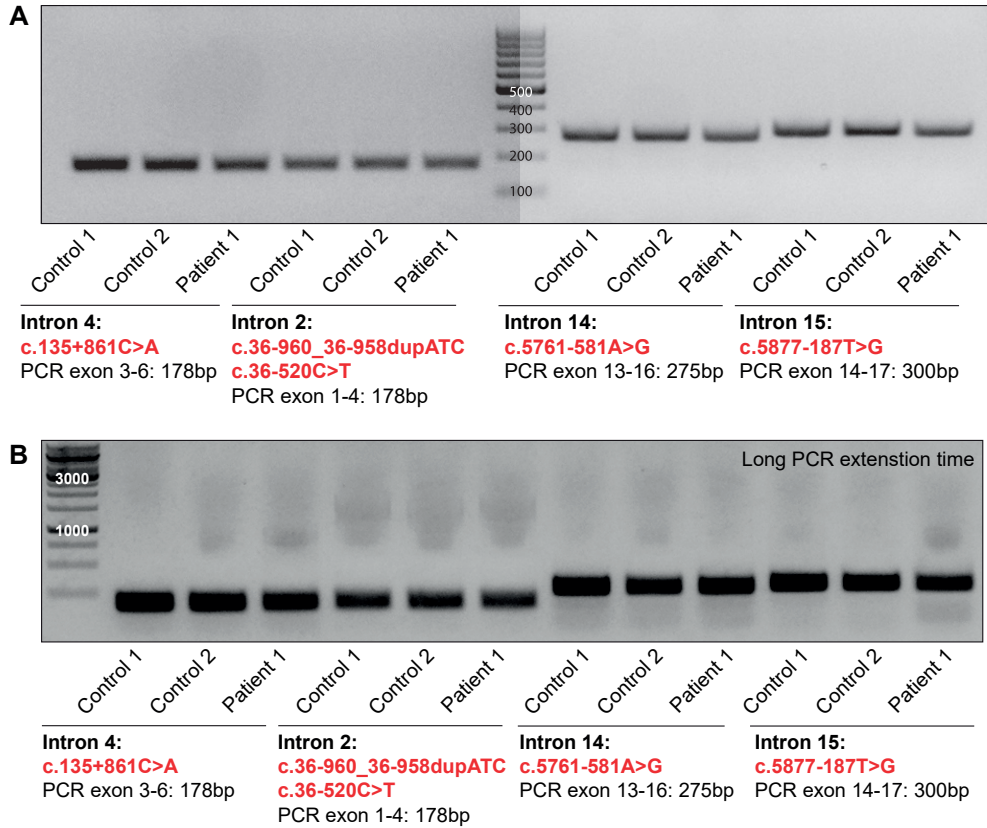


Figure S2. RT-PCRs of regions flanking the *KNL1* intronic variants in RNA extracted from patient and control lymphoblasts. The PCRs were performed with extension times calculated to allow for the detection of wild-type and exon skipping (**A**) and large intronic insertions (**B**).

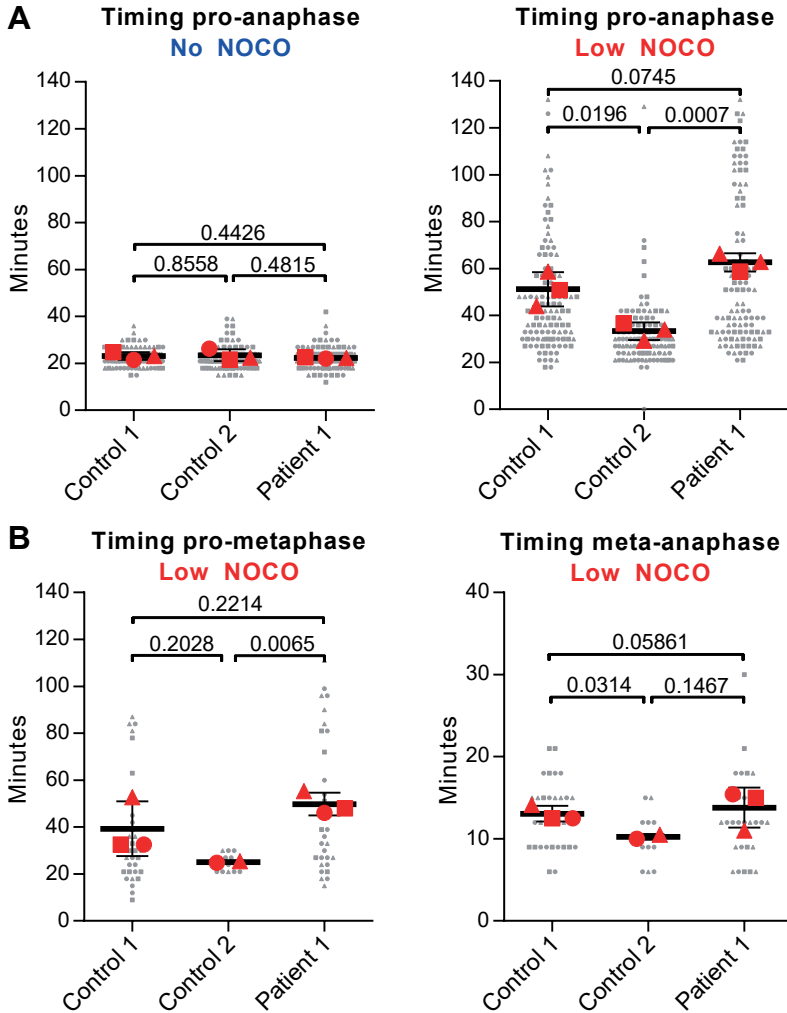


Figure S3. Mitotic timing of control- and patient-derived cells in the absence or presence of nocodazole. **A)** Quantification of the timing of prophase to anaphase of control- and patient-derived lymphoblasts expression H2B-mNeon in the absence (left) or presence (right) of a low dose of nocodazole (NOCO). Each bar depicts the mean of three independent experiments \pm SEM, with >88 (left) >96 (right) cells in total per condition. The average of each separate experiment is depicted with a red circle, square, or triangle; each individual cell is depicted with a gray small circle, square, or triangle, depending on the experiment. The experiments in the absence of nocodazole (left) correspond to those in **Figure 3A-B**; the experiments in the presence of low nocodazole (right) correspond to those with the same icons in B). **B)** Quantification of the timing of prophase to metaphase (left) and metaphase to anaphase (right) of cells in A) in low nocodazole (right). Each bar depicts the mean of three independent experiments \pm SEM, with >11 (left) >11 (right) cells in total per sample per experiment. The average of each separate experiment is depicted with a red circle, square, or triangle. Each individual cell is depicted with a gray small circle, square, or triangle, depending on the experiment.

REFERENCES

1. R. M. Ricke, J. M. van Deursen, Aneuploidy in health, disease, and aging. *J. Cell Biol.* 201, 11–21 (2013).
2. A. J. Holland, D. W. Cleveland, Boveri revisited: Chromosomal instability, aneuploidy and tumorigenesis. *Nat. Rev. Mol. Cell Biol.* 10, 478–487 (2009).
3. E. M. Torres, B. R. Williams, A. Amon, Aneuploidy: Cells losing their balance. *Genetics.* 179, 737–746 (2008).
4. H. Garcia-Castillo, A. I. Vásquez-Velásquez, H. Rivera, P. Barros-Núñez, Clinical and genetic heterogeneity in patients with mosaic variegated aneuploidy: delineation of clinical subtypes. *Am. J. Med. Genet. A.* 146A, 1687–95 (2008).
5. S. Hanks, K. Coleman, S. Reid, A. Plaja, H. Firth, D. Fitzpatrick, A. Kidd, K. Méhes, R. Nash, N. Robin, N. Shannon, J. Tolmie, J. Swansbury, A. Irrthum, J. Douglas, N. Rahman, Constitutional aneuploidy and cancer predisposition caused by biallelic mutations in BUB1B. *Nat. Genet.* 36, 1159–61 (2004).
6. K. Snape, S. Hanks, E. Ruark, P. Barros-Núñez, A. Elliott, A. Murray, A. H. Lane, N. Shannon, P. Callier, D. Chitayat, J. Clayton-Smith, D. R. Fitzpatrick, D. Gisselsson, S. Jacquemont, K. Asakura-Hay, M. a Micale, J. Tolmie, P. D. Turnpenny, M. Wright, J. Douglas, N. Rahman, Mutations in CEP57 cause mosaic variegated aneuploidy syndrome. *Nat. Genet.* 43, 527–529 (2011).
7. S. Yost, B. de Wolf, S. Hanks, A. Zachariou, C. Marcozzi, M. Clarke, R. M. de Voer, B. Etemad, E. Uijtewaal, E. Ramsay, H. Wylie, A. Elliott, S. Picton, A. Smith, S. Smithson, S. Seal, E. Ruark, G. Houge, J. Pines, G. J. P. L. Kops, N. Rahman, Supplementary: Biallelic TRIP13 mutations predispose to Wilms tumor and chromosome missegregation. *Nat. Genet.* (2017), doi:10.1038/ng.3883.
8. S. J. E. Suijkerbuijk, M. H. J. Van Osch, F. L. Bos, S. Hanks, N. Rahman, G. J. P. L. Kops, Molecular causes for BUBR1 dysfunction in the human cancer predisposition syndrome mosaic variegated aneuploidy. *Cancer Res.* 70, 4891–4900 (2010).
9. H. Zhou, T. Wang, T. Zheng, J. Teng, J. Chen, Cep57 is a Mis12-interacting kinetochore protein involved in kinetochore targeting of Mad1-Mad2. *Nat. Commun.* 7, 10151 (2016).
10. G. Vader, Pch2TRIP13: controlling cell division through regulation of HORMA domains. *Chromosoma.* 124, 333–339 (2015).
11. C. Sacristan, G. J. P. L. P. L. Kops, Joined at the hip: Kinetochores, microtubules, and spindle assembly checkpoint signaling. *Trends Cell Biol.* 25, 21–28 (2015).
12. S. L. Thompson, S. F. Bakhoun, D. A. Compton, Mechanisms of Chromosomal Instability. *Curr. Biol.* 20 (2010).
13. D. Varma, E. D. Salmon, The KMN protein network—chief conductors of the kinetochore orchestra. *J. Cell Sci.* 125, 5927–36 (2012).
14. G. V. Caldas, J. G. DeLuca, KNL1: Bringing order to the kinetochore. *Chromosoma.* 123, 169–181 (2014).
15. R. Bajaj, M. Bollen, W. Peti, R. Page, KNL1 Binding to PP1 and Microtubules Is Mutually Exclusive. *Structure.* 26, 1327–1336.e4 (2018).
16. N. London, S. Biggins, Signalling dynamics in the spindle checkpoint response. *Nat. Rev. Mol. Cell Biol.* 15, 736–47 (2014).
17. T. Kiyomitsu, C. Obuse, M. Yanagida, Human Blinkin/AF15q14 Is Required for Chromosome Alignment and the Mitotic Checkpoint through Direct Interaction with Bub1 and BubR1. *Dev. Cell.* 13, 663–676 (2007).
18. M. Vleugel, E. Tromer, M. Omerzu, V. Groenewold, W. Nijenhuis, B. Snel, G. J. P. L. Kops, Arrayed BUB recruitment modules in the kinetochore scaffold KNL1 promote accurate chromosome segregation. *J. Cell Biol.* 203, 943–955 (2013).

19. T. Kiyomitsu, H. Murakami, M. Yanagida, Protein Interaction Domain Mapping of Human Kinetochore Protein Blinkin Reveals a Consensus Motif for Binding of Spindle Assembly Checkpoint Proteins Bub1 and BubR1. *Mol. Cell. Biol.* 31, 998–1011 (2011).
20. G. Zhang, T. Lischetti, D. G. Hayward, J. Nilsson, Distinct domains in Bub1 localize RZZ and BubR1 to kinetochores to regulate the checkpoint. *Nat. Commun.* 6, 7162 (2015).
21. H. Wang, X. Hu, X. Ding, Z. Dou, Z. Yang, A. W. Shaw, M. Teng, D. W. Cleveland, M. L. Goldberg, L. Niu, X. Yao, Human Zwint-1 specifies localization of Zeste White 10 to kinetochores and is essential for mitotic checkpoint signaling. *J. Biol. Chem.* 279, 54590–54598 (2004).
22. C. R. Jamieson, C. Govaerts, M. J. Abramowicz, Primary autosomal recessive microcephaly: homozygosity mapping of MCPH4 to chromosome 15. *Am. J. Hum. Genet.* 65, 1465–9 (1999).
23. A. Genin, J. Desir, N. Lambert, M. Biervliet, N. Van der Aa, G. Pierquin, A. Killian, M. Tosi, M. Urbina, A. Lefort, F. Libert, I. Pirson, M. Abramowicz, Kinetochore KMN network gene CASC5 mutated in primary microcephaly. *Hum. Mol. Genet.* 21, 5306–5317 (2012).
24. S. Szczepanski et al., A novel homozygous splicing mutation of CASC5 causes primary microcephaly in a large Pakistani family. *Hum. Genet.* 135, 1–14 (2016).
25. A. Saadi, F. Verny, K. Siquier-Pernet, C. Bole-Feysot, P. Nitschke, A. Munnich, M. Abada-Dendib, M. Chaouch, M. Abramowicz, L. Colleaux, Refining the phenotype associated with CASC5 mutation. *Neurogenetics.* 17, 71–78 (2016).
26. Y. A. Zarate, J. A. Kaylor, K. Bosanko, S. Lau, J. Vargas, H. Gao, First clinical report of an infant with microcephaly and CASC5 mutations. *Am. J. Med. Genet. Part A.* 170, 2215–2218 (2016).
27. R. Wang, A. Khan, S. Han, X. Zhang, Molecular analysis of 23 Pakistani families with autosomal recessive primary microcephaly using targeted next-generation sequencing. *J. Hum. Genet.* 62, 299–304 (2017).
28. S. A. Fietz, R. Lachmann, H. Brandl, M. Kircher, N. Samusik, R. Schroder, N. Lakshmanaperumal, I. Henry, J. Vogt, A. Riehn, W. Distler, R. Nitsch, W. Enard, S. Paäbo, W. B. Huttner, Transcriptomes of germinal zones of human and mouse fetal neocortex suggest a role of extracellular matrix in progenitor self-renewal. *Proc. Natl. Acad. Sci. U. S. A.* 109, 11836–11841 (2012).
29. E. Ruark, M. Münz, M. Clarke, A. Renwick, E. Ramsay, A. Elliott, S. Seal, G. Lunter, N. Rahman, OpEx-a validated, automated pipeline optimised for clinical exome sequence analysis. *Sci. Rep.* 6, 31029 (2016).
30. L. J. Vos, J. K. Famulski, G. K. T. Chan, HZwint-1 bridges the inner and outer kinetochore: Identification of the kinetochore localization domain and the hZW10-interaction domain. *Biochem. J.* 436, 157–168 (2011).
31. E. Nagy, L. E. Maquat, A rule for termination-codon position within intron-containing genes: When nonsense affects RNA abundance. *Trends Biochem. Sci.* 23, 198–199 (1998).
32. D. Warburton, K. Anyane-Yeboah, P. Taterka, C. Y. Yu, D. Olsen, Mosaic variegated aneuploidy with microcephaly: a new human mitotic mutant? *Ann. Genet.* 34, 287–292 (1991).
33. A. Shanske, D. G. Caride, L. Menasse-Palmer, A. Bogdanow, R. W. Marion, Central nervous system anomalies in Seckel syndrome: Report of a new family and review of the literature. *Am. J. Med. Genet.* 70, 155–158 (1997).
34. A. Anna, G. Monika, Splicing mutations in human genetic disorders: examples, detection, and confirmation. *J. Appl. Genet.* 59, 253–268 (2018).
35. R. Vaz-Drago, N. Custódio, M. Carmo-Fonseca, Deep intronic mutations and

- human disease. *Hum. Genet.* 136, 1093–1111 (2017).
36. M. Vleugel, M. Omerzu, V. Groenewold, M. A. Hadders, S. M. A. Lens, G. J. P. L. Kops, Sequential Multisite Phospho-Regulation of KNL1-BUB3 Interfaces at Mitotic Kinetochores. *Mol. Cell.* 57, 824–835 (2015).
 37. D. Liu, M. Vleugel, C. B. Backer, T. Hori, T. Fukagawa, I. M. Cheeseman, M. A. Lampson, Regulated targeting of protein phosphatase 1 to the outer kinetochore by KNL1 opposes Aurora B kinase. *J. Cell Biol.* 188, 809–820 (2010).
 38. S. Matsuura, Y. Matsumoto, K. I. Morishima, H. Izumi, H. Matsumoto, E. Ito, K. Tsutsui, J. Kobayashi, H. Tauchi, Y. Kajiwara, S. Hama, K. Kurisu, H. Tahara, M. Oshimura, K. Komatsu, T. Ikeuchi, T. Kajii, Monoallelic BUB1B mutations and defective mitotic-spindle checkpoint in seven families with premature chromatid separation (PCS) syndrome. *Am. J. Med. Genet.* 140 A, 358–367 (2006).
 39. H. Ochiai, T. Miyamoto, A. Kanai, K. Hosoba, T. Sakuma, Y. Kudo, K. Asami, A. Ogawa, A. Watanabe, T. Kajii, T. Yamamoto, S. Matsuura, TALEN-mediated single-base-pair editing identification of an intergenic mutation upstream of BUB1B as causative of PCS (MVA) syndrome. *Proc. Natl. Acad. Sci. U. S. A.* 111, 1461–6 (2014).
 40. M. Naveed, S. K. Kazmi, M. Amin, Z. Asif, U. Islam, K. Shahid, S. Tehreem, Comprehensive review on the molecular genetics of autosomal recessive primary microcephaly (MCPH). *Genet. Res. (Camb)*. 100 (2018), doi:10.1017/S0016672318000046.
 41. X. Zhou, Y. Zhi, J. Yu, D. Xu, The yin and yang of autosomal recessive primary microcephaly genes: Insights from neurogenesis and carcinogenesis. *Int. J. Mol. Sci.* 21 (2020).
 42. A. Omer Javed, Y. Li, J. Muffat, K. C. Su, M. A. Cohen, T. Lungjangwa, P. Aubourg, I. M. Cheeseman, R. Jaenisch, Microcephaly Modeling of Kinetochore Mutation Reveals a Brain-Specific Phenotype. *Cell Rep.* 25, 368–382.e5 (2018).
 43. S. Yost, B. de Wolf, S. Hanks, A. Zachariou, C. Marcozzi, M. Clarke, R. M. De Voer, B. Etemad, E. Ujttewaal, E. Ramsay, H. Wylie, A. Elliott, S. Picton, A. Smith, S. Smithson, S. Seal, E. Ruark, G. Houge, J. Pines, G. J. P. L. Kops, N. Rahman, Biallelic TRIP13 mutations predispose to Wilms tumor and chromosome missegregation. *Nat. Genet.* 49, 1148–1151 (2017).
 44. G. Ciossani, K. Overlack, A. Petrovic, P. J. Huis In 't Veld, C. Koerner, S. Wohlgemuth, S. Maffini, A. Musacchio, The kinetochore proteins CENP-E and CENP-F directly and specifically interact with distinct BUB mitotic checkpoint Ser/Thr kinases. *J. Biol. Chem.* 293, 10084–10101 (2018).

CONTENTS

6.1 SUMMARY	138
6.2 WHAT IS THE PATHOGENIC MECHANISM UNDERLYING MVA?	138
6.3 CAUSES OF CIN IN MVA	142
6.4 MVA AND CANCER	143
6.5 PARTING THOUGHTS	144

CHAPTER 6

GENERAL DISCUSSION

6.1 Summary

Mosaic Variegated Aneuploidy (MVA) is a rare developmental disorder characterized by a clinically heterogeneous phenotype and the presence of mosaic aneuploidies (predominantly trisomies and monosomies of mostly random chromosomes). These aneuploid cells are most likely the result of chromosome segregation errors in mitosis, as disease-causing mutations were found in the mitotic genes *BUB1B* and *CEP57* (1, 2). Although several theories have been proposed (3–5), it is currently unclear what is the molecular mechanism of pathogenicity underlying MVA and whether the presence of aneuploid cells contributes to it. The aim of this thesis was to investigate the molecular causes of aneuploidy in MVA and to uncover MVA's underlying pathogenic mechanism. We first summarized the current knowledge about the processes governing mitosis and about the disorders that are associated with mutations in kinetochore genes (**chapter 2**). In the subsequent chapters, we presented clinical case studies of MVA patients in which we identified disease-causing mutations in mitotic regulators (*TRIP13*, *CENATAC*, *KNL1*, and *ZWINT*), and our findings concerning the molecular causes of CIN and aneuploidy in these patients (**chapters 3/4/5**). In **chapter 3**, we showed that patient mutations in both *BUB1B* and *TRIP13* led to a severe impairment of the spindle assembly checkpoint (SAC) and that there is a strikingly strong correlation between mutations in these two genes and the occurrence of specific childhood cancers in MVA patients. Moreover, all patients with mutations in *TRIP13* had developed Wilms tumors, and we subsequently identified non-MVA patients with Wilms tumors that also had germline *TRIP13* mutations. *TRIP13* may therefore be a Wilms tumor suppressor gene. In **chapter 4**, we identified *CENATAC* as a novel component of the minor spliceosome and showed that *CENATAC* depletion led to missplicing of a newly identified minor intron subtype, which in turn caused a chromosome congression defect in mitosis. In **chapter 5**, we showed that patient mutations in *KNL1* weakened the SAC and reduced the kinetochore localization of several key mitotic regulators. Based on these and other findings, I here discuss the different theories regarding the molecular mechanism of pathogenicity underlying MVA, and reveal that the current requirements for MVA's diagnosis are most likely incompatible with its disease-causing mechanism. In addition, I summarize cancer incidence in both MVA and MVA-like patients with mosaic aneuploidies, and I discuss the potential contribution of aneuploidy to the development of cancer in these patients. I conclude by comparing MVA to similar developmental disorders and discuss why it may be necessary to re-define MVA.

6.2 What is the Pathogenic Mechanism Underlying MVA?

Even though mosaic aneuploidies have been the defining feature of MVA since the 1980s, to date it is still unclear what is the mechanism of pathogenicity responsible for causing MVA, and whether aneuploidy plays a role in it. Alternative theories came from Miyamoto et al., who proposed that defective cilia may be responsible for the MVA phenotype (3), and Wijshake et al., who suggested that MVA may instead be caused by premature ageing (4). I here discuss these and other pathogenic mechanisms that could potentially underlie MVA.

6.2.1 Ciliary Defects

The idea that MVA may be a ciliopathy (a disorder caused by defective cilia) was based on the observation that cultured fibroblasts derived from two MVA patients with *BUB1B* mutations

did not grow primary cilia (antenna-like sensory organelles that protrude from the apical surface of most mammalian cells (6)) (3). Indeed, although heterogeneous, the phenotypes of ciliopathies include many symptoms associated with MVA, such as microcephaly, growth retardation, polycystic kidneys, cataracts, and congenital heart disease (7, 8). However, nearly complete deletion of *BubR1* from mice had no effect on the number, size or localization of primary cilia in the developing brain (9). Furthermore, although *CEP57* depletion was shown to result in the formation of morphologically abnormal, stunted cilia (10), none of the other genes associated with MVA (*TRIP13*, *KNL1*, *ZWINT*, *CENATAAC*) have been linked to either cilium formation or function. Although I cannot rule out the possibility that these genes have unknown functions in ciliogenesis, or that ciliary defects contribute to the development of certain symptoms, I therefore consider it unlikely that MVA is a ciliopathy.

6.2.2 Premature Ageing

The theory that MVA may instead be a progeroid syndrome (caused by premature ageing) comes from work done by Baker et al. and Wijshake et al., who demonstrated that increased levels of aneuploidy correlated with increased cellular senescence in mice with reduced expression of *Bub1b* (4, 11). This was accompanied by a variety of progeroid features that are also seen in MVA patients, such as growth retardation, facial dysmorphisms, and cataracts. Interestingly, selective removal of senescent cells by life-long or late-life elimination of cells that expressed p16^{Ink4a}, a biomarker for senescence, alleviated some of the progeroid features, implying that cellular senescence was indeed causally implicated in causing them (12). However, one of the most common MVA symptoms, microcephaly, was not part of the clinical phenotypes of the *Bub1b* mice (4, 11) and a mouse model that mimics a MVA mutation in *Cep57* did not undergo premature ageing (13). Furthermore, individuals with MVA do not have typical features of human premature aging syndromes such as thin and atrophic skin, loss of subcutaneous fat and alopecia (baldness) (14, 15). Therefore, although it is possible that cellular senescence and premature ageing may contribute to some of the MVA symptoms, I consider it unlikely that MVA is a progeroid syndrome.

6.2.3 Mosaic Aneuploidies

Although the defining feature of MVA is the presence of mosaic aneuploidies, and its diagnosis rests on their detection, there are several observations that argue against the presence of aneuploid cells being required for the development of MVA's clinical phenotype. *First*, the severity of the clinical phenotype of MVA does not correlate with the amount of aneuploid cells detected in a patient (Addendum Table 1), or with specific gains or losses (16). *Second*, whereas two of the Wilms tumor patients with mutations in *TRIP13* described in chapter 3 had clinical phenotypes typical of MVA (microcephaly, growth retardation, developmental delay, seizures, abnormal skin pigmentation), mosaic aneuploidies were not detected in their tissue samples (Addendum Table 1, patients 54 and 55). Likewise, although the clinical phenotypes of *KNL1*-mutant MVA and MCPH4 (chapters 5 and 2.3.1, respectively) are virtually identical (microcephaly, normal to short stature, developmental delay and in some cases some dysmorphic features), mosaic aneuploidies were only detected in the MVA patients (Addendum Table 1, patients 5, 51, 52a-b, and 56a-d). Although it is possible that mosaic aneuploidies were only present in some non-examined tissues, or that the MCPH4 mutations affected brain stem cells in ways unrelated to mitosis, these observations suggest that the clinical phenotype of MVA is not always associated with the presence of mosaic

aneuploidies. *Third*, whereas four colorectal cancer (CRC) patients with either a homozygous mutation in *BUB1B* (17) or a heterozygous mutation in *BUB1* or *BUB3* (18) had high levels of mosaic aneuploidies in different tissues, they did not have a clinical phenotype typical of MVA. In fact, only 2/4 patients had some symptoms associated with MVA (below average head circumference, although not severe enough to be termed microcephaly, and some mild dysmorphic features) (**Addendum Table 1**, patients 57-59) (18). In line with this, most aneuploid mouse models did not exhibit any of the symptoms associated with MVA apart from a predisposition to develop cancer (19-21). Taken together, this suggests that a high amount of aneuploid cells is not sufficient to cause the clinical phenotype of MVA. *Fourth*, whereas the clinical phenotype of MVA closely resembles that of other developmental disorders, such as some DNA repair disorders, cohesinopathies and minor spliceosome disorders (**Table 1**), the presence of mosaic aneuploidies is rarely detected in patients affected by these disorders (22-24). In fact, some of these disorders are so alike that one MVA patient with mutations in *KNL1* was initially diagnosed with Seckel syndrome (**chapter 5**, (25)), and for two other individuals their initial diagnosis of MVA was later reverted after mutations were identified in *CENPF* (linked to Strømme Syndrome (**Table 1, chapter 2.3.2**)) and *ATRX* (linked to ATR-X Syndrome (**Table 1**)). Taken together, these observations suggest that the clinical phenotype of MVA does not rely on the presence of aneuploid cells and that the requirement of detecting mosaic aneuploidies for the diagnosis of MVA may be wrongfully excluding patients.

6.2.4 Apoptosis

When a cell becomes aneuploid, it either becomes senescent, continues proliferating, or undergoes apoptosis (**chapter 1.3**). Given that MVA's clinical phenotype does not seem to rely on the presence of aneuploid cells (**chapter 6.2.3**), the molecular mechanism of pathogenicity underlying MVA may instead be apoptotic cell death. Importantly, given that mitotic errors can also lead to a mitotic arrest and apoptosis without cell division, this does not necessarily require the production of aneuploid cells and will be referred to as CIN-induced apoptosis.

This theory is supported by the following observations. *First*, CIN induced in the brains of mice and *Drosophila* caused aneuploidy and apoptosis of brain stem cells, which impaired brain development and ultimately caused microcephaly (one of the most frequently recurring symptoms of MVA, see also (**Addendum Table 1**) (31, 32)). In line with this, conditional deletion of the MVA genes *Knl1* and *Bub1b* from mouse brain cells caused aneuploidy, DNA damage and p53-dependent apoptosis, ultimately leading to severe microcephaly (9, 33). *Second*, as mentioned above (**chapter 6.2.3**), two of the Wilms tumor patients with mutations in *TRIP13* described in **chapter 3** had clinical phenotypes typical of MVA yet without the presence of mosaic aneuploidies. A possible explanation for this is that CIN-induced apoptosis is responsible for both the observed phenotype and for the lack of aneuploid cells in these patients. The amount of aneuploid cells present at any given moment in a tissue depends on the balance between the rate of aneuploidization and the rate of death. Factors that could push this balance towards more death include a stronger apoptosis response (either because of more efficient activation of apoptosis or more severe aneuploidy per cell) and more efficient clearance of aneuploid cells by the immune system (**chapter 1.3**). Likewise, a stronger apoptosis response could explain why no aneuploid cells were detected in the MCPH4 patients with mutations in *KNL1*, even though they were clinically indistinguishable

Table 1. Examples of developmental disorders with clinical phenotypes that closely resemble that of MVA.

Disease	Seckel	Nijmegen breakage	Roberts	ATRX	Strømme	MOPD1	Roifman	
Category	DNA repair		Cohesinopathy				Minor spliceosome	
MIM #	210600	210900	268300	301040	243605	210710	616651	
Mosaic aneuploidies	Yes (22)	No	Yes (26)	No	No	No	No	
Microcephaly	Yes	Yes	Yes	Yes	Yes	Yes	Yes	
Growth retardation	Yes	Yes	Yes	Yes	No	Yes	Yes	
Mental retardation	Yes	Yes	Yes	Yes	Yes	Yes	Yes	
Facial dysmorphisms	Yes	Yes	Yes	Yes	Yes	Yes	Yes	
Cancer predisposition	No	Yes	No	No	No	No	No	
Other characteristics		Immunodeficiency	Limb abnormalities	Muscle weakness, genital abnormalities	Intestinal obstructions, ocular abnormalities	Skeletal abnormalities	Skeletal abnormalities, Immunological defects	
References	(27)	(24)	(28)	(28)	(29)	(30)	(30)	

from MVA patients with similar mutations in *KNL1* (**chapters 5 and 6.2.3**). *Third*, as mentioned above (**chapter 6.2.3**), whereas high levels of mosaic aneuploidies were detected in different tissues of CRC patients with mutations in *BUB1B*, *BUB1*, or *BUB3*, their clinical phenotypes did not resemble that of MVA. In line with this, most aneuploid mouse models did not exhibit any of the symptoms associated with MVA apart from a predisposition to developing cancer (19–21). Although it is currently unclear why these patients and mice are less vulnerable to aneuploidy, it is possible that whereas the apoptosis response may be strong in the above-mentioned patients with mutations in *TRIP13* and *KNL1*, the apoptosis response may instead be weak in these backgrounds. It is worth emphasizing that high levels of mosaic aneuploidies are compatible with the relatively long and healthy lives of these CRC patients (compare to those of MVA patients). This not only suggests that aneuploidy-induced apoptosis may be more detrimental to a patient than the presence of live aneuploid cells, it also implies that it may be beneficial to inhibit apoptosis in MVA patients as a form of therapy. In line with this, inhibition of apoptosis in microcephalic mouse brains partially restored brain size (31, 33). *Fourth*, as mentioned above (**chapter 6.2.3**), although the clinical phenotypes of several other developmental disorders closely resemble that of MVA (**Table 1**), mosaic aneuploidies were rarely detected in the affected patients. Importantly, all of these disorders are characterized by CIN and/or increased apoptosis (24, 34–36). This increase in apoptosis is not always related to CIN and aneuploidy, however, as for instance DNA damage in the DNA repair disorders can cause apoptosis in other phases of the cell cycle. For the minor spliceosome disorders it is currently unclear what exactly is causing apoptosis, although it is known that impaired minor intron splicing predominantly affects the growth of proliferating tissues (35) and is associated with defects in various phases of the cell-cycle, including S-phase and mitosis (36, 37). The common denominator here is that in both the above disorders and MVA, predominantly proliferating cells are affected. Taken together, these observations suggest that the clinical phenotype of MVA does not rely on the presence of a population of aneuploid cells and is instead most likely caused by CIN-induced apoptosis.

How exactly CIN-induced apoptosis may lead to the development of the different MVA symptoms remains to be investigated. One possibility is the depletion of stem cell pools as was the cause for microcephaly in aneuploid mouse and *Drosophila* models (9, 31–33). Although the presence of mosaic aneuploidies may therefore not be a reliable requirement for the diagnosis of MVA, it could be an indication of what mechanism is responsible for causing the CIN that ultimately leads to the clinical phenotype of the affected patients.

6.3 Causes of CIN in MVA

As mentioned in **chapter 1.2**, both mitotic and non-mitotic defects can lead to CIN, for instance through a SAC defect or defective DNA repair. We showed in **chapter 3** that of several patient-derived cell lines, only those with mutations in *BUB1B* and *TRIP13* had a severely weakened SAC. Although mutations in *KNL1* also weakened the SAC (**chapter 5**), the fact that this was only a mild effect suggests that other mitotic defects related to the function of *KNL1* (see below) may contribute to causing CIN in these patients. Other mitotic defects associated with the MVA genes are unstable kinetochore-microtubules attachments (*BUB1B* (**chapter 2.3.5**), *CEP57* (**chapter 2.3.5**), *KNL1* (**chapter 5**), *ZWINT* (**chapter 5**), and *CENATAC* (data not shown)), supernumerary spindle poles (*CEP57* (**chapter 2.3.5**), *CENATAC* (**chapter 4**)), and defective DNA repair (*TRIP13* (40)). Although further investigation will be

required to pinpoint the exact mechanisms responsible for causing CIN in each of the different patients, given the heterogeneity in mitotic functions of the MVA genes, it is likely that MVA can be caused by various mitotic defects that have in common that they lead to both the presence of mosaic aneuploidies and apoptosis.

6.4 MVA and Cancer

Aneuploidy is a hallmark of cancer: approximately 90% of solid tumors and 35-60% of haematopoietic cancers are aneuploid (41–43). Although aneuploidy is thought to be detrimental in general, it can also confer a fitness advantage and drive tumorigenesis under specific circumstances. Whether this happens depends on many factors such as cell type, genetic make-up, tumor stage, tumor microenvironment, and immune system interactions (41). The existence of characteristic aneuploidy patterns within a given cancer type, for instance, suggests that specific aneuploidies may drive tumorigenesis in certain tissues (44).

Given this strong association, it is not surprising that cancer is a common occurrence in MVA (**Addendum Table 1**). The relationship between aneuploidy and cancer in MVA patients, however, is not straightforward. Almost all patients that developed cancer had mutations in either *BUB1B* or *TRIP13* and either developed Wilms tumor (WT, *BUB1B*: 6/20² patients, *TRIP13*: 3/3 patients), Rhabdomyosarcoma (RMS, *BUB1B*: 4/20), or both (*BUB1B*: 2/10). Five other patients also developed cancer, three of which had WT (one also had RMS) and two of which had leukemia (the cause of MVA remains unknown for all six cases) (45, 46). Strikingly, none of the patients with mutations in *CEP57*, *CENATAC*, *KNL1*, or *ZWINT* developed cancer. The absence of cancer in these patients, even though most outlived the age at which patients with mutations in *BUB1B* or *TRIP13* developed cancer (the age of 4), suggests that aneuploidy by itself may not be sufficient to cause these types of cancer. On the other hand, these cancers are often associated with specific aneuploidies (47). Trisomy 8, for instance, is associated with RMS (48–51), WT (51, 52), and leukemia (51, 53), and was often found in the karyotypes of MVA patients (16). The same is true for trisomy 18, which is associated with both RMS and WT (16, 54–56). In addition, monosomy 7 is associated with leukemia (57) and was found in 35% of bone marrow cells of a MVA patient that had developed leukemia (45). Although only present in *BUB1B* and *TRIP13* mutant patients, these observations suggest that the gain or loss of specific chromosomes has likely led or contributed to the development of these cancers. This raises the question why none of the patients with mutations in *CEP57*, *CENATAC*, or *KNL1* developed these cancers. One possibility is that the severe SAC defect associated with mutations in *BUB1B* or *TRIP13* (**chapter 3**) may lead to significantly higher levels of CIN and thus a significantly larger chance of creating that specific karyotype required for tumorigenesis. This would be in line with the relatively high levels of mosaic aneuploidies observed in these patients (**Addendum Table 1**). Alternatively, *BUB1B* and *TRIP13* insufficiency may somehow affect these tissues more severely, be it through a mitotic or non-mitotic function. Another possible explanation is that, instead of a *BUB1B*- or *TRIP13*-specific contribution to tumorigenesis, mutations in *CEP57*, *CENATAC*, and *KNL1* somehow suppress the development of cancer. In mice, *Bub1b* insufficiency does not increase the rate of spontaneous tumor development, whereas insufficiency of *Cep57* does (4, 13). However, given this obvious discrepancy with the pattern of cancer occurrence in MVA patients, it is questionable whether these mice are a valid model to study the effects

² This is excluding patient 32 of Addendum Table 1, which presented with CRC and mosaic aneuploidies, yet without other MVA-associated symptoms (see also chapter 6.2.3).

of MVA mutations and aneuploidy on the development of cancer in humans.

Interestingly, whereas high levels of mosaic aneuploidies were detected in the previously mentioned CRC patients with a mutation in *BUB1B*, *BUB1*, or *BUB3* (**chapter 6.2.3**), these patients, like most of the MVA patients, did not develop any of the childhood cancers associated with MVA mutations in *BUB1B* and *TRIP13* (**Addendum Table 1**, patients 32, 57-59). Instead, they developed gastrointestinal cancers at the ages of 29-37 (**17, 18**). Why these cases are phenotypically similar to each other yet very different from the MVA patients is currently unclear. However, given that these patients developed cancer later in life, and that MVA patients rarely survive until that age (**Addendum Table 1**), it is possible that CIN and/or aneuploidy predispose to the development of gastrointestinal cancers later in life. The main difference between the *BUB1B* mutation of the CRC patient and those of the MVA patients is that it leads to a significantly stronger reduction in the expression of BUBR1 protein (**17**). Interestingly, in heterozygous *Apc^{min}* mice (**58**) and cultured human colorectal cancer cells (**59**), *BUB1B* insufficiency led to a reduction in the formation of intestinal polyps and cell death, respectively. It is therefore possible that whereas reduced BUBR1 expression can contribute to tumor development, a too strong reduction is instead detrimental for certain types of cancer cells. This tumor suppressive effect has also been observed for other mitotic genes such as *MAD2* (**59, 60**), *CENPE* (**60, 61**) and *MPS1* (**62**), and likely exploits a vulnerability of cancer cells for increased CIN (**63, 64**). Whether CIN caused by mutations in any of the MVA genes likewise contributes to reduced tumorigenesis in MVA patients is unclear.

6.5 Parting Thoughts

Although the mosaic aneuploidies that define MVA are the result of CIN, it is likely that a different consequence of CIN, namely increased apoptosis, is the culprit responsible for the pathogenicity underlying MVA (**chapter 6.2**). However, whereas CIN-induced apoptosis does not require the presence of a detectable population of aneuploid cells, the diagnosis of MVA does. As discussed in **chapter 6.2.3**, this likely explains why some patients with a typical MVA-phenotype, and with the same patient mutations as MVA patients, did not present with mosaic aneuploidies. Given that these and likely additional cases are not recognized as MVA patients, it may be appropriate to remove the requirement of detecting mosaic aneuploidies for the diagnosis of MVA. Instead, it may be possible to determine whether the cells of these patients are predisposed to gaining whole-chromosome aneuploidies when CIN-induced apoptosis is prevented by treatment with apoptosis inhibitors. Detection of such a predisposition in cultured cells would be an indication of mitotic defects and thus of MVA. The relevance for patients of such a minor change in the diagnosis of MVA may be limited, especially since there is no known treatment. However, if apoptosis is indeed more detrimental to a patient than the presence of aneuploid cells (**chapter 6.2.4**), it may one day guide new therapy options (such as inhibiting apoptosis in CIN patients). In such a scenario, the efficacy of inhibiting apoptosis could depend on whether patient cells are predisposed to gain whole-chromosome or structural aneuploidies, with MVA patients potentially benefitting the most.

REFERENCES

1. S. Hanks, K. Coleman, S. Reid, A. Plaja, H. Firth, D. Fitzpatrick, A. Kidd, K. Méhes, R. Nash, N. Robin, N. Shannon, J. Tolmie, J. Swansbury, A. Irrthum, J. Douglas, N. Rahman, Constitutional aneuploidy and cancer predisposition caused by biallelic mutations in BUB1B. *Nat. Genet.* 36, 1159–61 (2004).
2. K. Snape, S. Hanks, E. Ruark, P. Barros-Núñez, A. Elliott, A. Murray, A. H. Lane, N. Shannon, P. Callier, D. Chitayat, J. Clayton-Smith, D. R. Fitzpatrick, D. Gisselsson, S. Jacquemont, K. Asakura-Hay, M. a Micalé, J. Tolmie, P. D. Turnpenny, M. Wright, J. Douglas, N. Rahman, Mutations in CEP57 cause mosaic variegated aneuploidy syndrome. *Nat. Genet.* 43, 527–529 (2011).
3. T. Miyamoto, S. Porazinski, H. Wang, A. Borovina, B. Ciruna, A. Shimizu, T. Kajii, A. Kikuchi, M. Furutani-Seiki, S. Matsuura, Insufficiency of BUBR1, a mitotic spindle checkpoint regulator, causes impaired ciliogenesis in vertebrates. *Hum. Mol. Genet.* 20, 2058–2070 (2011).
4. T. Wijshake, L. A. Malureanu, D. J. Baker, K. B. Jeganathan, B. van de Sluis, J. M. van Deursen, Reduced Life- and Healthspan in Mice Carrying a Mono-Allelic BubR1 MVA Mutation. *PLoS Genet.* 8, e1003138 (2012).
5. J. L. Tolmie, E. Boyd, P. Batstone, M. E. Ferguson-Smith, L. al Roomi, J. M. Connor, Siblings with chromosome mosaicism, microcephaly, and growth retardation: the phenotypic expression of a human mitotic mutant? *Hum. Genet.* 80, 197–200 (1988).
6. C. Kempeneers, M. A. Chilvers, To beat, or not to beat, that is question! The spectrum of ciliopathies. *Pediatr. Pulmonol.* 53, 1122–1129 (2018).
7. R. Shaheen, K. Szymanska, B. Basu, N. Patel, N. Ewida, E. Faqeih, A. Al Hashem, N. Derar, H. Alsharif, M. A. Aldahmesh, A. M. Alazami, M. Hashem, N. Ibrahim, F. M. Abdulwahab, R. Sonbul, H. Alkuraya, M. Alnemer, S. Al Tala, M. Al-Husain, H. Morsy, M. Z. Seidahmed, N. Meriki, M. Al-Owain, S. AlShahwan, B. Tabarki, M. A. Salih, T. Faquih, M. El-Kalioby, M. Ueffing, K. Boldt, C. V. Logan, D. A. Parry, N. Al Tassan, D. Monies, A. Megarbane, M. Abouelhoda, A. Halees, C. A. Johnson, F. S. Alkuraya, Characterizing the morbid genome of ciliopathies. *Genome Biol.* 17 (2016), doi:10.1186/s13059-016-1099-5.
8. A. M. Waters, P. L. Beales, Ciliopathies: An expanding disease spectrum. *Pediatr. Nephrol.* 26, 1039–1056 (2011).
9. A. J. Simmons, R. Park, N. A. Sterling, M. H. Jang, J. M. A. Van Deursen, T. J. Yen, S. H. Cho, S. Kim, Nearly complete deletion of BubR1 causes microcephaly through shortened mitosis and massive cell death. *Hum. Mol. Genet.* 28, 1822–1836 (2019).
10. S. Graser, Y.-D. Stierhof, S. B. Lavoie, O. S. Gassner, S. Lamla, M. Le Clech, E. a Nigg, Cep164, a novel centriole appendage protein required for primary cilium formation. *J. Cell Biol.* 179, 321–30 (2007).
11. D. J. Baker, K. B. Jeganathan, J. D. Cameron, M. Thompson, S. Juneja, A. Kopecka, R. Kumar, R. B. Jenkins, P. C. de Groen, P. Roche, J. M. van Deursen, BubR1 insufficiency causes early onset of aging-associated phenotypes and infertility in mice. *Nat. Genet.* 36, 744–9 (2004).
12. J. M. van Deursen, N. K. LeBrasseur, D. J. Baker, B. G. Childs, T. Tchkonja, B. van de Sluis, T. Wijshake, J. L. Kirkland, T. Tchkonja, N. K. LeBrasseur, B. G. Childs, B. van de Sluis, J. L. Kirkland, J. M. van Deursen, Clearance of p16Ink4a-positive senescent cells delays ageing-associated disorders. *Nature.* 479, 232–6 (2011).
13. K. Aziz, C. J. Sieben, K. B. Jeganathan, M. Hamada, B. A. Davies, R. O. Fierro Velasco, N. Rahman, D. J. Katzmman, J. M. Van Deursen, Mosaic-variegated aneuploidy syndrome mutation or haploinsufficiency in Cep57 impairs tumor suppression. *J. Clin. Invest.* 128, 3517–3534 (2018).
14. D. Lessel, C. Kubisch, Hereditary syndromes

- with signs of premature aging. *Dtsch. Arzteblatt Online* (2019), doi:10.3238/arztebl.2019.0489.
15. M. X. R. Foo, P. F. Ong, O. Dreesen, Premature aging syndromes: From patients to mechanism. *J. Dermatol. Sci.* 96, 58–65 (2019).
 16. H. Garcia-Castillo, A. I. Vásquez-Velásquez, H. Rivera, P. Barros-Núñez, Clinical and genetic heterogeneity in patients with mosaic variegated aneuploidy: delineation of clinical subtypes. *Am. J. Med. Genet. A.* 146A, 1687–95 (2008).
 17. T. R. Frio, J. Lavoie, N. Hamel, T. Rio Frio, J. Lavoie, N. Hamel, F. Geyer, Y. Kushner, D. Novak, L. Wark, C. Capelli, J. Reis-Filho, S. Mai, T. Pastinen, M. Tischkowitz, V. Marcus, W. D. Foulkes, Homozygous BUB1B mutation and susceptibility to gastrointestinal neoplasia. *N. Engl. J. Med.* 363, 2628–2637 (2010).
 18. R. M. De Voer, A. Geurts van Kessel, R. D. A. Weren, M. J. L. Ligtenberg, D. Smeets, L. Fu, L. Vreede, E. J. Kamping, E. T. P. Verwiel, M.-M. M. Hahn, M. Ariaans, L. Spruijt, T. van Essen, G. Houge, H. K. Schackert, J. Q. Sheng, H. Venselaar, C. M. a van Ravenswaaij-Arts, J. H. J. M. Van Krieken, N. Hoogerbrugge, R. P. Kuiper, Germline mutations in the spindle assembly checkpoint genes BUB1 and BUB3 are risk factors for colorectal cancer. *Gastroenterology.* 145, 544–547 (2013).
 19. S. J. Pfau, A. Amon, Chromosomal instability and aneuploidy in cancer: From yeast to man. *EMBO Rep.* 13, 515–527 (2012).
 20. R. M. Ricke, J. H. van Ree, J. M. van Deursen, Whole chromosome instability and cancer: a complex relationship. *Trends Genet.* 24, 457–466 (2008).
 21. C. J. Sieben, K. B. Jeganathan, G. G. Nelson, I. Sturmlechner, C. Zhang, W. H. Van Deursen, B. Bakker, F. Fojjer, H. Li, D. J. Baker, J. M. Van Deursen, BubR1 allelic effects drive phenotypic heterogeneity in mosaic-variegated aneuploidy progeria syndrome. *J. Clin. Invest.* 130, 171–188 (2020).
 22. H. Potter, H. J. Chial, J. Caneus, M. Elos, N. Elder, S. Borysov, A. Granic, Chromosome Instability and Mosaic Aneuploidy in Neurodegenerative and Neurodevelopmental Disorders. *Front. Genet.* 10 (2019), doi:10.3389/fgene.2019.01092.
 23. Z. H. Wu, Phenotypes and genotypes of the chromosomal instability syndromes. *Transl. Pediatr.* 5, 79–83 (2016).
 24. A. M. R. Taylor, C. Rothblum-Oviatt, N. A. Ellis, I. D. Hickson, S. Meyer, T. O. Crawford, A. Smogorzewska, B. Pietrucha, C. Weemaes, G. S. Stewart, Chromosome instability syndromes. *Nat. Rev. Dis. Prim.* 5 (2019), doi:10.1038/s41572-019-0113-0.
 25. D. Warburton, K. Anyane-Yeboah, P. Taterka, C. Y. Yu, D. Olsen, Mosaic variegated aneuploidy with microcephaly: a new human mitotic mutant? *Ann. Genet.* 34, 287–292 (1991).
 26. E. W. Jabs, C. M. Tuck-Muller, R. Cusano, J. B. Rattner, Studies of mitotic and centromeric abnormalities in Roberts syndrome: Implications for a defect in the mitotic mechanism. *Chromosoma.* 100, 251–261 (1991).
 27. M. K. Zeman, K. A. Cimprich, Causes and consequences of replication stress. *Nat. Cell Biol.* 16, 2–9 (2014).
 28. J. Piché, P. P. Van Vliet, M. Pucéat, G. Andelfinger, The expanding phenotypes of cohesinopathies: one ring to rule them all! *Cell Cycle.* 18, 2828–2848 (2019).
 29. M. Alghamdi, W. H. Alkhamis, F. A. Bashiri, D. Jamjoom, G. Al-Nafisah, A. Tahir, M. Abdouelhoda, Expanding the phenotype and the genotype of Stromme syndrome: A novel variant of the CENPF gene and literature review. *Eur. J. Med. Genet.* 63, 103844 (2020).
 30. B. Verma, M. V. Akinyi, A. J. Norppa, M. J. Frilander, Minor spliceosome and disease. *Semin. Cell Dev. Biol.* 79, 103–112 (2018).
 31. V. Marthiens, M. a Rujano, C. Pennetier, S. Tessier, P. Paul-Gilloteaux, R. Basto,

- Centrosome amplification causes microcephaly. *Nat. Cell Biol.* 15, 731–40 (2013).
32. J. S. Poulton, J. C. Cuningham, M. Peifer, Centrosome and spindle assembly checkpoint loss leads to neural apoptosis and reduced brain size. *J. Cell Biol.* 216, 1255–1265 (2017).
 33. L. Shi, A. Qalieh, M. M. Lam, J. M. Keil, K. Y. Kwan, Robust elimination of genome-damaged cells safeguards against brain somatic aneuploidy following Knl1 deletion. *Nat. Commun.* 10 (2019), doi:10.1038/s41467-019-10411-w.
 34. M. Zakari, K. Yuen, J. L. Gerton, Etiology and pathogenesis of the cohesinopathies. *Wiley Interdiscip. Rev. Dev. Biol.* 4, 489–504 (2015).
 35. H. König, N. Matter, R. Bader, W. Thiele, F. Müller, Splicing Segregation: The Minor Spliceosome Acts outside the Nucleus and Controls Cell Proliferation. *Cell.* 131, 718–729 (2007).
 36. K. D. Drake, C. Lemoine, G. S. Aquino, A. M. Vaeth, R. N. Kanadia, *bioRxiv*, in press, doi:10.1101/2020.03.16.994384.
 37. M. Baumgartner, A. M. Olthof, G. S. Aquino, K. C. Hyatt, C. Lemoine, K. Drake, N. Sturrock, N. Nguyen, S. al Seesi, R. N. Kanadia, Minor spliceosome inactivation causes microcephaly, owing to cell cycle defects and death of self-amplifying radial glial cells. *Dev.* 145 (2018), doi:10.1242/dev.166322.
 38. H. Wang, X. Hu, X. Ding, Z. Dou, Z. Yang, A. W. Shaw, M. Teng, D. W. Cleveland, M. L. Goldberg, L. Niu, X. Yao, Human Zwint-1 specifies localization of Zeste White 10 to kinetochores and is essential for mitotic checkpoint signaling. *J. Biol. Chem.* 279, 54590–54598 (2004).
 39. H. Zhou, T. Wang, T. Zheng, J. Teng, J. Chen, Cep57 is a Mis12-interacting kinetochore protein involved in kinetochore targeting of Mad1–Mad2. *Nat. Commun.* 7, 10151 (2016).
 40. C. S. Clairmont, P. Sarangi, K. Ponnieselvan, L. D. Galli, I. Csete, L. Moreau, G. Adelmant, D. Chowdhury, J. A. Marto, A. D. D'Andrea, TRIP13 regulates DNA repair pathway choice through REV7 conformational change. *Nat. Cell Biol.* 22, 87–96 (2020).
 41. U. Ben-David, A. Amon, Context is everything: aneuploidy in cancer. *Nat. Rev. Genet.* 21, 44–62 (2020).
 42. N. K. Chunduri, Z. Storchová, The diverse consequences of aneuploidy. *Nat. Cell Biol.* 21, 54–62 (2019).
 43. P. H. G. G. Duijf, R. Benezra, The cancer biology of whole-chromosome instability. *Oncogene.* 32, 4727–36 (2013).
 44. A. M. Taylor, et al., Genomic and Functional Approaches to Understanding Cancer Aneuploidy. *Cancer Cell.* 33, 676–689.e3 (2018).
 45. S. Jacquemont, M. Bocéno, J. M. Rival, F. Méchinaud, A. David, High risk of malignancy in mosaic variegated aneuploidy syndrome. *Am. J. Med. Genet.* 109, 17–21 (2002).
 46. J. Scheres, T. Hustinx, K. Madan, J. Beltman, D. Lindhout, in *7th International Congress of Human Genetics* (Berlin, 1986), p. 163.
 47. I. Ganmore, G. Smootha, S. Izraeli, Constitutional aneuploidy and cancer predisposition. *Hum. Mol. Genet.* 18, R84–93 (2009).
 48. E. Manor, L. Bodner, P. Kachko, J. Kapelushnik, Trisomy 8 as a sole aberration in embryonal rhabdomyosarcoma (sarcoma botryoides) of the vagina. *Cancer Genet. Cytogenet.* 195, 172–174 (2009).
 49. C. U. Dietrich, B. B. Jacobsen, H. Starklint, S. Heim, Clonal karyotypic evolution in an embryonal rhabdomyosarcoma with trisomy 8 as the primary chromosomal abnormality. *Genes, Chromosom. Cancer.* 7, 240–244 (1993).
 50. A. Afify, H. F. L. Mark, Trisomy 8 in embryonal rhabdomyosarcoma detected by fluorescence in situ hybridization. *Cancer Genet. Cytogenet.* 108, 127–132 (1999).
 51. V. M. Riccardi, B. F. Crandall, Karyotype-phenotype correlation: Mosaic trisomy 8

- and partial trisomies of different segments of chromosome 8. *Hum. Genet.* 41, 363–367 (1978).
52. A. Valind, N. Pal, J. Asmundsson, D. Gisselsson, L. Holmquist Mengelbier, Confined trisomy 8 mosaicism of meiotic origin: A rare cause of aneuploidy in childhood cancer. *Genes Chromosom. Cancer.* 53, 634–638 (2014).
 53. A. L. Hemsing, R. Hovland, G. Tsykunova, H. Reikvam, Trisomy 8 in acute myeloid leukemia. *Expert Rev. Hematol.* 12, 947–958 (2019).
 54. S. Weber-Hall, J. Anderson, A. McManus, S. Abe, T. Nojima, R. Pinkerton, K. Pritchard-Jones, J. Shipley, Gains, losses, and amplification of genomic material in rhabdomyosarcoma analyzed by comparative genomic hybridization. *Cancer Res.* 56, 3220–3224 (1996).
 55. C. E. Anderson, H. H. Punnett, V. Huff, J. P. De Chadarevian, Characterization of a Wilms tumor in a 9-year-old girl with trisomy 18. *Am. J. Med. Genet.* 121 A, 52–55 (2003).
 56. J. M. Olson, A. Hamilton, N. E. Breslow, Non11p Constitutional Chromosome Abnormalities in Wilms' Tumor Patients. *Med. Pediatr. Oncol.* 24, 305–309 (1995).
 57. D. Aktas, E. Tuncbilek, Myelodysplastic syndrome associated with monosomy 7 in childhood: a retrospective study. *Cancer Genet. Cytogenet.* 171, 72–75 (2006).
 58. W. Dai, Q. Wang, T. Liu, M. Swamy, Y. Fang, S. Xie, R. Mahmood, Y. M. Yang, M. Xu, C. V. Rao, Slippage of Mitotic Arrest and Enhanced Tumor Development in Mice with BubR1 Haploinsufficiency. *Cancer Res.* 64, 440–445 (2004).
 59. G. J. P. L. Kops, D. R. Foltz, D. W. Cleveland, Lethality to human cancer cells through massive chromosome loss by inhibition of the mitotic checkpoint. *Proc. Natl. Acad. Sci. U. S. A.* 101, 8699–704 (2004).
 60. A. D. Silk, L. M. Zasadil, A. J. Holland, B. Vitre, D. W. Cleveland, B. a Weaver, Chromosome missegregation rate predicts whether aneuploidy will promote or suppress tumors. *Proc. Natl. Acad. Sci. U. S. A.* 110, E4134–41 (2013).
 61. L. M. Zasadil, E. M. C. Britigan, S. D. Ryan, C. Kaur, D. J. Guckenberger, D. J. Beebe, A. R. Moser, B. A. Weaver, High rates of chromosome missegregation suppress tumor progression, but do not inhibit tumor initiation. *Mol. Biol. Cell.* 27, 1981–1989 (2016).
 62. W. H. M. Hoevenaar, A. Janssen, A. I. Quirindongo, H. Ma, S. J. Klaasen, A. Teixeira, B. van Gerwen, N. Lansu, F. H. M. Morsink, G. J. A. Offerhaus, R. H. Medema, G. J. P. L. Kops, N. Jelluma, Degree and site of chromosomal instability define its oncogenic potential. *Nat. Commun.* 11 (2020), doi:10.1038/s41467-020-15279-9.
 63. G. Simonetti, S. Bruno, A. Padella, E. Tenti, G. Martinelli, Aneuploidy: Cancer strength or vulnerability? *Int. J. Cancer.* 144, 8–25 (2019).
 64. S. F. Bakhoum, L. C. Cantley, The Multifaceted Role of Chromosomal Instability in Cancer and Its Microenvironment. *Cell.* 174, 1347–1360 (2018).



CHAPTER 7

ADDENDUM

TABLE 1. OVERVIEW OF CLINICAL AND CYTOGENETIC FINDINGS IN MVA PATIENTS

Patient	Sex	Age	Gene	Mutations	Aneuploidy	PCS	Cancer	Clinical phenotype	References
1	F	Died 42y	?		15%	60%	AML (<42y)	Microcephaly, growth & mental retardation, eye abnormalities	(22, 23)
2	F	Alive 7y	?		38-84%	-	-	Microcephaly, growth & severe mental retardation, seizures	(1, 23-25)
2	M	Died 3y	?		0-22%	-	-	Microcephaly, growth & mental retardation	(1, 23-25)
3	M	Alive 32y	?		17-20%	-	-	Microcephaly, growth & mental retardation, juvenile onset limb-girdle muscular dystrophy	(23, 26)
3	F	Alive 23y	?		17-20%	-	-	Microcephaly, growth & mental retardation, juvenile onset limb-girdle muscular dystrophy	(23, 26)
4	M	Alive 8m	?		78%	39-51%	-	Microcephaly, growth & mental retardation, flat broad nasal bridge, low-set ears, nystagmus, hemangiomas, seizures, ambiguous genitalia	(22, 27)

Patient	Sex	Age	Gene	Mutations	Aneuploidy	PCS	Cancer	Clinical phenotype	References
5	F	Alive 17y	<i>KNL1</i>	c.5028delG, unknown	6-20%	Yes	-	Extreme microcephaly, growth & mental retardation, beaked nose, micrognathia, myopia, esotropia and limited elbow extension	(22, 23, 28)
6	F	Died 1.5y	<i>BUB1B</i>	c.1833delT, ss802470619 G>A	14.5-20%	67-86%	WT (1.5m)	Microcephaly, growth & mental retardation, cataracts, dandy-walker malformation, cleft palate	(22, 23, 25, 29-31)
7	M	Died <2y	?		7-15%	84-87.5%	-	Microcephaly, growth & mental retardation, cataracts	(22, 23, 29)
8	F	Alive 5y	?		8%	-	-	Mild microcephaly, growth retardation, and mild errors of morphogenesis	(23, 32)
8	F	Alive 2y	?		19%	-	-	Mild microcephaly, growth retardation, and mild errors of morphogenesis	(23, 32)
9	M	Alive 14y	<i>BUB1B</i>	c.580C>T, c.2530C>T + c.2763G>C	22 + 33%	Yes	RMS (prenatal)	Microcephaly, growth retardation, mild malar hypoplasia, upturned nasal tip, smooth filtrum, cryptorchidism, rhabdomyosarcoma, clinodactyly	(1, 22, 23, 25, 33)

Patient	Sex	Age	Gene	Mutations	Aneuploidy	PCS	Cancer	Clinical phenotype	References
10	M	Died 3y	<i>BUB1B</i>	c.1833delT, ss802470619 G>A	17 + 24%	82%	WT (7m)	Microcephaly, growth & mental retardation, hypertelorism, exophthalmos, corneal opacities, cataracts, broad nasal bridge, upturned nasal tip, short neck, Dan-dy-walker malformation, seizures	(23, 25, 30, 31, 34, 35)
11	M	Alive adult	?		ND	-	ND	ND (journal is discontinued, paper cannot be found)	(23)
12	M	Died 5m	?		yes	<48%	WT (9w)	Microcephaly, growth & mental retardation, dan-dy-walker malformation	(22, 23, 36)
13a	F	Died 1.5y	<i>BUB1B</i>	c.1VS10-1G>T, c.1649G>A (R550Q)	12%	46%	RMS (5m)	Microcephaly, growth & mental retardation, convergent strabismus, thin upper lip, square shaped ears Hemangioma, thumb adduction, cyst in posterior fossa	(1, 22, 23, 25, 35)
13b	?	Died prenatal	<i>BUB1B</i>	c.1VS10-1G>T, c.1649G>A (R550Q)	51%	43%	-	ND	(1, 23, 25)

Patient	Sex	Age	Gene	Mutations	Aneuploidy	PCS	Cancer	Clinical phenotype	References
14	F	Alive 7y	<i>BUB1B</i>	c.2726T>C (I909T), unknown	28%	81%	-	Microcephaly, growth & mental retardation, horizontal nystagmus, vermiform hypoplasia, ventriculomegaly, colpocephaly	(1, 22, 23, 25, 35)
15	M	ND	?		40%	<25%	-	Microcephaly, growth retardation	(22, 23)
16	M	Died 0.4y	<i>BUB1B</i>	c.IVS10-5A>G, ss802470619 G>A	9%	48 + 73%	WT (8w)	Growth retardation	(23, 25, 30, 31, 35)
17	F	Alive 8y	<i>BUB1B</i>	c.107G>A (R36Q), ss802470619 G>A	25%	68 + 83%	WT (10m)	Microcephaly, growth & mental retardation, cataracts, dandy-walker malformation	(23, 25, 30, 31, 35)
18a	M	Died 1.1y	<i>BUB1B</i>	c.1833delT, ss802470619 G>A	18%	36%	WT + RMS (3m)	Microcephaly, growth & mental retardation, cataracts, dandy-walker malformation	(23, 25, 30, 31, 35)
18b	M	Died 0.6y	<i>BUB1B</i>	c.1833delT, ss802470619 G>A	32%	yes	WT (4m)	Microcephaly, growth & mental retardation, cataracts, dandy-walker malformation	(23, 25, 30, 31, 35)
19	F	Died 16m	?		20%	10.50%	WT (7m)	Microcephaly, growth & mental retardation	(23, 35)
20	M	Died 3y	?		8-10%	-	ALL (3y)	Microcephaly, growth & mental retardation	(23, 37)

Patient	Sex	Age	Gene	Mutations	Aneuploidy	PCS	Cancer	Clinical phenotype	References
21	M	Died 15y	<i>CEP57</i>	hom. c.915_925dup11	24%	-	-	Microcephaly, growth & mild mental retardation, mildly dysmorphic facial features	(21, 23, 38)
22	M	Died 3w	<i>CEP57</i>	hom. C.241C>T (R81X)	17%-18%	-	-	Growth retardation, developmental delay, mild dysmorphic features, several congenital defects	(1, 21, 25)
23	M	Alive 2y	<i>BUB1B</i>	c.2211-2insGTTA , c.2441G>A (R814H)	30%	ND	-	Microcephaly, growth retardation, eye abnormality, multicystic kidney, lissencephaly, bilateral hip dysplasia, clinodactyly	(1, 25)
24	?	Alive 6y	?		17%	-	-	Microcephaly, growth & mental retardation, mild facial dysmorphisms, seizures	(1, 25)
25	F	Died 4m	<i>BUB1B</i>	c.2211-2insGTTA, c.3035T>C (L1012P)	83%	-	-	Microcephaly, growth retardation, corneal opacities, glaucoma, micrognathia, pulmonary stenosis, anemia, clinodactyly, hypothyroidism	(1, 25)
26	ND	Died prenatal	?		44%	yes	-	Microcephaly growth retardation, oligohydramnios	(23, 39)

Patient	Sex	Age	Gene	Mutations	Aneuploidy	PCS	Cancer	Clinical phenotype	References
27	M	Alive 19m	?		3-54%	-	-	Growth & mental retardation, dysmorphic face	(23)
28	F	Alive 0.3y	<i>BUB1B</i>	c.670C>T (R224X), ss802470619 G>A	12%	17%	-	Growth retardation, annular pancreas	(25, 30, 31)
29	F	Died 0.8y	<i>BUB1B</i>	c.1833delT, ss802470619 G>A	10%	66.50%	WT + RMS (<9m)	Microcephaly, growth & mental retardation, cataracts, dandy-walker malformation	(25, 30)
30	F	Alive 3.5y	?		13%	ND	-	Mental retardation, obesity, mild epicanthal folds, tapering fingers, relatively small hands and feet, alternating exotropia, nasal speech limited to short phrases, generalized hypotonia	(25, 40)
31a	M	alive 8.4y	<i>CEP57</i>	520_521delGA + 915_925dup11	53%	-	-	Growth retardation, cranofacial dysmorphism, a cafe-au-lait spot, clinodactyly, transient hypothyroidism	(21, 25)
31b	F	alive 4.5y	<i>CEP57</i>	520_521delGA + 915_925dup11	48%	14%	-	Growth retardation, craniofacial dysmorphism	(21, 25)

Patient	Sex	Age	Gene	Mutations	Aneuploidy	PCS	Cancer	Clinical phenotype	References
32	M	Alive 68y	<i>BUB1B</i>	hom. c.2386-11A>G	60-78%	57%+ 84%	AC (34y), CRC (61y), SC (64+65y), - SC (66y), CRC (66y)	Growth retardation with relative sparing of the head, mildly delayed development, rhizomelic shortening of the upper limbs, craniosynostosis with premature fusion of the sagittal and metopic sutures	(41)
33	F	Alive 4y	<i>CEP57</i>	hom. c.915-925dup11	32%	-	-	Microcephaly, severe developmental delay, hypotonia, seizures, Dandy-Walker malformation	(42)
34	M	Died 4y	?		yes	59.50%	WT + RMS* (22m)	No microcephaly or Dandy-Walker anomalies or cataracts or polycystic kidneys but still has uncontrollable clonic seizures and does not speak meaningful words	(43)
35	M	Alive 8y	<i>BUB1B</i>	hom. ss802470619 G>A	17%	67.00%	RMS (2m)		(31)

Patient	Sex	Age	Gene	Mutations	Aneuploidy	PCS	Cancer	Clinical phenotype	References
36	M	Alive prenatal	?		35-62%	63,00%	-	Prenatal ultrasound: microcephaly, Dandy-walker malformation	(44)
37	F	Alive 27y	?		20-30%	ND	-	Short neck without microcephaly, growth retardation, menarche, chronic menstrual irregularities, secondary amenorrhea, facial dysmorphism temporal bossing, triangular face, hypertelorism and micrognathia	(45)
38	M	Alive 0y	<i>BUB1B</i>	Alu insertion mutation intron 8, ss802470619 G>A	Yes	27,20%	-	Extreme microcephaly, growth retardation, congenital cataracts, a prominent nasal bridge, a low-set ear, micrognathia and ambiguous genitalia	(46, 47)
39	M	Alive 43y	<i>TRIP13</i>	hom for c.1060C>T, p.R354X	46%	yes	WT (4y)	Growth retardation	(48)
40	F	Alive 5y	<i>TRIP13</i>	hom for c.1060C>T, p.R354X	10%	yes	WT (2y)	Multiple café au lait patches. He did not have microcephaly or developmental delay	(48)

Patient	Sex	Age	Gene	Mutations	Aneuploidy	PCS	Cancer	Clinical phenotype	References
41	M	Alive 6y	<i>TRIP13</i>	hom for c.1060C>T, p.R354X	Yes	ND	WT (2y)	Microcephaly, severe developmental delay, multiple cerebral cysts, dysmorphic features included large, low-set ears, a beaked nose and cleft palate. He also had severe cone-rod dystrophy and nystagmus and horseshoe kidney	(48)
42	F	Alive 2y	<i>BUB1B</i>	Alu insertion mutation intron 8, ss802470619 G>A	yes	ND	WT (6m)	Extreme microcephaly, growth retardation	(49)
43	M	Alive 5y	<i>CEP57</i>	hom. c.915-925dup-CAATGTTTCAGC	20%	ND	-	Growth retardation, craniofacial dysmorphisms, narrow chest, bilateral cryptorchidism, rhizome-lyc shortening in both the upper and lower limbs, abnormal palmar creases, clinodactyly	(50)

Patient	Sex	Age	Gene	Mutations	Aneuploidy	PCS	Cancer	Clinical phenotype	References
44	F	Alive 11.5y	<i>CEP57</i>	hom. 697delA, p.Ly- s235Argfs*31	23%	ND	-	Growth & mild mental retardation, developmental delay, acanthosis nigricans, and precocious puberty, prominent forehead and nose, frontal bossing, triangular face, and mild rhizomelic shortening of upper limbs	(51)
45	F	Alive 1.9y	<i>BUB1B</i>	c.826delG, c.2441G>A	55%	ND	-	Microcephaly, severe growth retardation, feeding difficulty, short stature, facial anomalies, scoliosis, visual impairment, hypotonia, chylothorax, and renal lesions	(52)
46	F	Alive 11m	<i>BUB1B</i>	1833delT, ss802470619 G>A	27%	37%	RMS (8m)	Microcephaly, growth retardation, hypoplasia of the cerebellar hemispheres and cerebellar vermis, a small gyrus volume, and enlargement of the post-cerebellar space, congenital bilateral cataracts, microphthalmia	(53)

Patient	Sex	Age	Gene	Mutations	Aneuploidy	PCS	Cancer	Clinical phenotype	References
47	M	Alive 11y	<i>BUB1B</i>	c.498_505delAAACT-TTA, c.1288+5G>A	50%	ND	-	Microcephaly, growth & mental retardation, facial anomalies (frontal bossing, a triangular face, and micrognathia), multiple areas of skin café au lait hyperpigmentation, alopecia, Dandy-walker malformation	(54)
48	M	Died 6m	<i>CEP57</i>	hom. c.915_925dup11	28%	ND	-	Macrocephaly, wide anterior fontanel, high forehead with frontal bossing, hypertelorism, short neck, rhizomelic shortening of the limbs, mostly the upper ones, brachydactyly of hands and feet	(55)
49	M	Alive 46y	<i>CENATA</i>	c.803A>T_p.Glu-268Val, c.805+2_805+19del18	7.3%	ND	-	Microcephaly, mild developmental delay and mild maculopathy	Chapter 4
50	F	Alive 33y	<i>CENATA</i>	c.803A>T_p.Glu-268Val, c.805+2_805+19del18	8.5%	ND	-	Microcephaly, mild developmental delay and mild maculopathy	Chapter 4
51	F	Alive 13m	<i>KNL1</i>	c.3654delA, unknown	13%	ND	-	Severe microcephaly and developmental delay	Chapter 5

Patient	Sex	Age	Gene	Mutations	Aneuploidy	PCS	Cancer	Clinical phenotype	References
52a	F	Alive 11y	<i>KNL1</i>	c.1243delC, unknown	9%	-	-	Microcephaly, developmental delay, congenital heart disease	Chapter 5
52b	M	Alive 10y	<i>KNL1</i>	c.1243delC, unknown	ND	-	-	Microcephaly up-slanting palpebral fissures	Chapter 5
53a	F	Died prenatal	<i>ZW/INT1</i>	hom. c.472delC	92%	ND	-	Died prenatal	Chapter 5
53b	M	Died prenatal	<i>ZW/INT1</i>	hom. c.472delC	92%	ND	-	Died prenatal	Chapter 5

ND: no data, hom.: homozygous, AML & ALL: leukemia, WT: Wilms tumor, RM: rhabdomyosarcoma, AC: ampullary carcinoma, CRC: colorectal cancer, SC: stomach cancer

Non-MVA cases with mutations in *TRIP13* or *KNL1*

Patient	Sex	Age	Gene	Mutations	Aneuploidy	PCS	Cancer	Clinical phenotype	References
54	F	Died 10y	<i>TRIP13</i>	hom. c.1060C>T (R354X)	-	50%	WT (2y)	Microcephaly, growth retardation, seizures, abnormal skin pigmentation on her trunk	(48)
55	F	Alive 2.5y	<i>TRIP13</i>	hom. c.673-1G>C	-	ND	WT (15m)	Microcephaly, developmental delay, congenital ventricular septal defect, treatment-resistant and progressive multifocal epilepsy at 13 months	(48)
56a	M	Alive 27y	<i>KNL1</i>	hom. c.6125G>A	-	ND	-	Microcephaly, growth retardation, intellectual disability, developmental delay, dysmorphic features including a sloping forehead, thick eyebrows, synophris, low columella	(56)
56b	F	Alive 24y	<i>KNL1</i>	hom. c.6125G>A	-	ND	-		
56c	M	Alive 23y	<i>KNL1</i>	hom. c.6125G>A	-	ND	-		
56d	M	Alive 21y	<i>KNL1</i>	hom. c.6125G>A	-	ND	-		

ND: no data; hom.: homozygous; WT: Wilms tumor

Non-MVA cases with mosaic aneuploidies

Patient	Sex	Age	Gene	Mutations	Aneuploidy	PCS	Cancer	Clinical phenotype	References
57	F	Alive 37y	BUB1	1.7 Mb deletion	35-37.5%	ND	CRC (37y)	Head circumference of 52.5 cm (20.7 in., -1.7SD), which is below the 10th percentile after correction for height, mild dysmorphic features, including an asymmetrical face and hairline and a prominent forehead	(57)
58	F	Alive 29y	BUB3	c. 790T>C (Phe264Leu)	27-40%	ND	CRC (29y), LC (44y)	Head circumference of 53.5 cm (21.1 in., -1SD), which is below the 25th centile after correction for height, mild dysmorphic features, including an asymmetrical face, a crooked nose and a short philtrum	(57)
59	M	Alive 32	BUB3	c. 63G>C (Lys21Asn)	6.6-23%	ND	CRC (32y)		(57)

ND: no data, CRC: colorectal cancer, LC: lung cancer

NEDERLANDSE SAMENVATTING

Het onderzoek dat in dit proefschrift staat beschreven is gedaan naar de zeldzame ontwikkelingsstoornis Mozaïek Gevarieerde Aneuploidie (MVA). Deze ziekte wordt gekenmerkt door een breed scala aan symptomen en mozaïek-aneuploidie: de aanwezigheid van cellen die van willekeurige chromosomen (DNA) te veel of te weinig kopieën hebben. Deze zogenaamde aneuploïde cellen zijn hoogstwaarschijnlijk te wijten aan chromosoom-segregatiefouten tijdens de mitose (celdeling), aangezien ziekteverwekkende mutaties zijn gevonden in de mitotische genen *BUB1B* en *CEP57*. Hoewel mozaïek-aneuploidie het bepalende kenmerk is van MVA, is het momenteel onduidelijk wat het pathogene mechanisme is dat ten grondslag ligt aan deze ziekte en of de aanwezigheid van aneuploïde cellen hieraan bijdraagt. Het onderzoek beschreven in dit proefschrift is dan ook gericht op het ontdekken van de moleculaire oorzaken van aneuploidie in MVA-patiënten, en op het achterhalen hoe deze defecten bijdragen aan het pathogene mechanisme van MVA.

In **hoofdstuk 2** geef ik eerst een samenvatting van de huidige kennis over de processen die een belangrijke rol spelen in de mitose, en een overzicht van de aandoeningen die momenteel geassocieerd zijn met mutaties in mitotische genen.

De volgende hoofdstukken (**3, 4 en 5**) bevatten de experimenten die hebben geleid tot de identificatie van ziekteverwekkende mutaties in de mitotische regulatoren *TRIP13*, *CENATAC*, *KNL1* en *ZWINT*. Daarnaast bevatten deze hoofdstukken casusrapporten van de betreffende patiënten, en de resultaten van ons onderzoek naar hoe een defect in deze genen kan leiden tot chromosoom-segregatiefouten en aneuploidie.

In **hoofdstuk 3** laten we zien dat patiëntmutaties in zowel *BUB1B* als *TRIP13* leidden tot een ernstige verzwakking van het mitotische checkpoint (een belangrijk proces in de celdeling) en dat er een opvallend sterke correlatie bestaat tussen mutaties in deze twee genen en het ontstaan van bepaalde typen kinderkanker in MVA-patiënten. Bovendien hadden alle patiënten met mutaties in *TRIP13* Wilms-tumoren (een vorm van nierkanker) en hebben we *TRIP13*-mutaties geïdentificeerd in niet-MVA-patiënten met Wilms-tumoren. Het is daarom mogelijk dat *TRIP13* een Wilms-tumorsuppressor is.

In **hoofdstuk 4** identificeren we ziekteverwekkende mutaties in *CCDC84* (dat we hernoemen naar *CENATAC*), een gen waarvan de functie onbekend was. Gedreven door de wetenschap dat een defect in *CENATAC* de ziekte MVA kan veroorzaken, en dat zijn functie daarom van groot belang moet zijn, gingen we op zoek naar zijn rol in de mitose. We laten zien dat het een tot op heden onbekend onderdeel is van de minor spliceosome, een eiwit/RNA complex dat een belangrijke rol speelt in de genexpressie door atypische intronen te verwijderen uit RNA. Daarnaast laten we zien dat de depletie van *CENATAC* resulteerde in een defect in dit proces, wat vervolgens chromosoom-segregatiefouten veroorzaakte in de mitose. Dit leidde bovendien tot de ontdekking dat de minor spliceosome onderscheid maakt tussen verschillende soorten van deze atypische intronen.

In **hoofdstuk 5** laten we zien dat het mitotische checkpoint was verzwakt in de cellen van MVA-patiënten met *KNL1*-mutaties (zij het in mindere mate dan bij mutaties in *BUB1B* en *TRIP13*). Bovendien ontdekken we een intrigerende inconsistentie tussen de klinische fenotypen van patiënten met MVA en MCPH4: beide ziektes zijn het gevolg van een

defect in *KNL1* en geassocieerd met dezelfde symptomen, maar aneuploidie werd alleen gedetecteerd in de weefsels van MVA-patiënten.

Ten slotte bespreek ik in **hoofdstuk 6** de verschillende theorieën over welk ziekteverwekkend mechanisme ten grondslag ligt aan MVA, en concludeer ik dat dit waarschijnlijk niet de aanwezigheid van aneuploïde cellen is (een van de lopende hypothesen), maar celdood. Wanneer een chromosoom mis-segregeert in de mitose (wat twee aneuploïde dochtercellen tot gevolg heeft) wordt meestal een proces gestart dat leidt tot celdood. Aneuploïde cellen zijn immers niet gezond en kunnen in het ergste geval kanker veroorzaken. In MVA-patiënten worden echter veel levende aneuploïde cellen gedetecteerd, wat betekent dat zij dit proces hebben ontlopen. Het feit dat deze aneuploïde cellen werden waargenomen in meerdere patiënten heeft in het verleden geleid tot het definiëren van de ziekte MVA, met als bepalende kenmerk deze aneuploïde cellen. Echter, mijn onderzoek suggereert nu dat het niet de aanwezigheid van aneuploïde cellen is dat verantwoordelijk is voor het ziektebeeld van MVA, maar celdood. Dit verklaart hoogstwaarschijnlijk waarom er geen aneuploïde cellen werden waargenomen in een aantal patiënten met mutaties in de MVA-genen *TRIP13* en *KNL1*, en met een ziektebeeld dat klinisch verder niet te onderscheiden was van MVA-patiënten. Ik besluit met de suggestie om de vereiste van het detecteren van aneuploidie voor de diagnose van MVA te laten vallen, aangezien dit waarschijnlijk leidt tot het foutief uitsluiten van patiënten. Als alternatief stel ik voor om te testen of de cellen van mogelijke MVA-patiënten de aanleg hebben om aneuploïd te worden in de aanwezigheid van apoptose (celdood)-remmers. Het detecteren van een dergelijke aanleg zou een indicatie zijn van fouten in de mitose en dus van MVA.

Ελληνική σύνοψη | GREEK SUMMARY

Η έρευνα που περιγράφεται σε αυτήν τη διατριβή διεξήχθη για τη σπάνια αναπτυξιακή διαταραχή με το όνομα «μωσαϊκή ποικίλη ανευπλοειδία» (MVA). Η ασθένεια αυτή χαρακτηρίζεται από μια πληθώρα συμπτωμάτων, καθώς και από ανευπλοειδία, δηλαδή την παρουσία κυττάρων που έχουν περισσότερα ή λιγότερα αντίγραφα χρωμοσωμάτων (DNA) σε σχέση με τα φυσιολογικά κύτταρα. Αυτά τα ανευπλοειδή κύτταρα πιθανότατα προκύπτουν λόγω σφαλμάτων στο διαχωρισμό των χρωμοσωμάτων κατά τη διάρκεια της μίτωσης (κυτταρικής διαίρεσης), μιας και στα συγκεκριμένα κύτταρα τα γονίδια *BUB1B* και *CEP57* που ελέγχουν τη μίτωση βρέθηκαν να περιέχουν μεταλλάξεις. Παρόλο που η ανευπλοειδία είναι το καθοριστικό χαρακτηριστικό της MVA, προς το παρόν δεν είναι σαφές ποιος είναι ο παθογόνος μηχανισμός που διέπει την ασθένεια και αν η παρουσία των ανευπλοειδών κυττάρων συμβάλλει σε αυτόν. Ως εκ τούτου, η έρευνα που περιγράφεται σε αυτή τη διατριβή στοχεύει στον προσδιορισμό των μοριακών αιτιών της ανευπλοειδίας σε ασθενείς με MVA και στη διερεύνηση του τρόπου με τον οποίο γενετικά «ελαττώματα» συμβάλλουν στον παθογόνο μηχανισμό της ασθένειας.

Στο **κεφάλαιο 2**, παρέχεται μια σύνοψη της τρέχουσας γνώσης σχετικά με τις διαδικασίες που διαδραματίζουν σημαντικό ρόλο στη μίτωση, και μια επισκόπηση των παθήσεων που σχετίζονται με μεταλλάξεις στα μιτωτικά γονίδια.

Τα ακόλουθα κεφάλαια (**3, 4 και 5**) περιέχουν τα πειράματα που οδήγησαν στον εντοπισμό παθογόνων μεταλλάξεων στα γονίδια *TRIP13*, *CENATAC*, *KNL1* και *ZWINT*, τα οποία ρυθμίζουν τη μίτωση. Επιπλέον, αυτά τα κεφάλαια περιέχουν αναφορές περιπτώσεων ασθενών με MVA, καθώς επίσης και τα αποτελέσματα της έρευνάς μας σχετικά με το πώς ένα ελάττωμα στα παραπάνω γονίδια μπορεί να οδηγήσει σε σφάλματα διαχωρισμού χρωμοσωμάτων και ανευπλοειδία.

Στο **κεφάλαιο 3**, δείξαμε ότι οι μεταλλάξεις τόσο στο γονίδιο *BUB1B* όσο και στο *TRIP13* οδηγούν σε σοβαρή εξασθένηση του μιτωτικού σημείου ελέγχου (μια σημαντική διαδικασία κατά την κυτταρική διαίρεση) και ότι υπάρχει μια εντυπωσιακά ισχυρή συσχέτιση μεταξύ των μεταλλάξεων σε αυτά τα δύο γονίδια και της ανάπτυξης ορισμένων τύπων παιδικού καρκίνου σε ασθενείς με MVA. Όλοι οι ασθενείς με μεταλλάξεις στο γονίδιο *TRIP13* είχαν όγκους Wilms (νεφροβλάστωμα), ενώ αντίστοιχες μεταλλάξεις εντοπίστηκαν σε ασθενείς με όγκους Wilms που δεν είχαν MVA. Είναι επομένως πιθανό το γονίδιο *TRIP13* να είναι υπό φυσιολογικές συνθήκες ένα γονίδιο καταστολής του όγκου Wilms.

Στο **κεφάλαιο 4**, εντοπίσαμε παθογόνες μεταλλάξεις στο γονίδιο *CCDC84* (το οποίο μετονομάσαμε σε *CENATAC*), ένα γονίδιο του οποίου η λειτουργία ήταν πρότινος άγνωστη. Με γνώμονα το γεγονός ότι ένα ελάττωμα στο γονίδιο *CENATAC* μπορεί να προκαλέσει MVA και ότι επομένως η λειτουργία του πρέπει να είναι πολύ σημαντική, ξεκινήσαμε τη διερεύνηση του ρόλου του στη μίτωση. Δείξαμε ότι αποτελεί ένα μέρος του δευτερεύοντος

σωματίου συναρμογής, ενός συμπλέγματος πρωτεΐνης / RNA που παίζει σημαντικό ρόλο στην έκφραση γονιδίων. Επιπλέον, δείχνουμε ότι η αφαίρεση του γονιδίου *CENATAC* οδηγεί στη δυσλειτουργία αυτής της διαδικασίας, κάτι που στη συνέχεια προκαλεί σφάλματα διαχωρισμού χρωμοσωμάτων κατά τη μίτωση.

Στο **κεφάλαιο 5**, δείξαμε ότι το μιτωτικό σημείο ελέγχου υπολειπουργεί στα κύτταρα ασθενών με MVA που περιέχουν μεταλλάξεις στο γονίδιο *KNL1* (αν και σε μικρότερο βαθμό όταν οι μεταλλάξεις βρίσκονται στα γονίδια *BUB1B* και *TRIP13*). Επιπλέον, ανακαλύψαμε μια ενδιαφέρουσα ασυνέπεια μεταξύ των κλινικών φαινοτύπων των ασθενών με MVA και αυτών με την ασθένεια MCRH4: ενώ και οι δύο ασθένειες οφείλονται σε ένα ελάττωμα στο γονίδιο *KNL1* και χαρακτηρίζονται από τα ίδια συμπτώματα, ανευπλοειδία εντοπίστηκε μόνο στους ιστούς των ασθενών με MVA.

Τέλος, στο **Κεφάλαιο 6**, συζητώ τις διαφορετικές θεωρίες σχετικά με το ποιος παθογόνος μηχανισμός χαρακτηρίζει την ασθένεια MVA και καταλήγω στο συμπέρασμα ότι δεν είναι η παρουσία ανευπλοειδών κυττάρων (το καθοριστικό χαρακτηριστικό της ασθένειας), αλλά μάλλον ο κυτταρικός θάνατος που προκαλείται από σφάλματα στη μίτωση. Δεδομένου ότι τα νεκρά κύτταρα δεν ανιχνεύονται, αυτό πιθανότατα εξηγεί γιατί δεν βρέθηκε ανευπλοειδία σε όλους τους ασθενείς με μεταλλάξεις στα γονίδια *TRIP13* και *KNL1*, παρόλο που η κλινική εικόνα αυτών των ασθενών δεν διέφερε από αυτήν των ασθενών με MVA. Αυτό θα σήμαινε ότι η παρουσία ανευπλοειδών κυττάρων δεν είναι απαραίτητη για να αναπτύξει κάποιος MVA. Καταλήγω με την πρόταση να εγκαταλείψουμε την ιδέα ότι απαιτείται ανίχνευση ανευπλοειδών κυττάρων για τη διάγνωση της MVA, καθώς είναι πιθανό να οδηγήσει σε εσφαλμένο αποκλεισμό ασθενών. Ως εναλλακτική λύση, προτείνω να εξεταστεί εάν τα κύτταρα πιθανών ασθενών με MVA έχουν την προδιάθεση να γίνουν ανευπλοειδή παρουσία αναστολέων απόπτωσης (κυτταρικού θανάτου). Η ανίχνευση μιας τέτοιας προδιάθεσης θα υποδείκνυε σφάλματα στη μίτωση και κατά συνέπεια την ασθένεια MVA.

LIST OF PUBLICATIONS

de Wolf, B. and Kops, G.J.P.L. (2017). Kinetochore Malfunction in Human Pathologies. *Advances in Experimental Medicine and Biology* 1002, 69-91.

Yost, S.* , **de Wolf, B.***, Hanks, S.* , et al. (2017). Biallelic TRIP13 mutations predispose to Wilms tumor and chromosome missegregation. *Nature Genetics* 49(7), 1148-1151. *Co-first authors.

de Wolf, B., et al. (2020). Constitutional aneuploidy caused by defects in splicing of a rare minor intron subtype. *bioRxiv* 2020.08.06.239418

CURRICULUM VITAE

Bas de Wolf was born on June 6, 1989 in Amsterdam. In 2007, he obtained his VWO high school diploma at the RSG Tromp Meesters in Steenwijk. after which he immediately enrolled in the BSc program Biology at Utrecht University. After completing this in 2011 with a Minor in Geographical Information Systems, Bas continued his education at Utrecht University with the MSc program Molecular and Cellular Life Sciences. He undertook his major research project at Utrecht University in the group of Dr. P.M.P. van Bergen and Henegouwen under the supervision of Dr. S. Oliveira. During this internship, he conducted research into the optimal production of anti-EGFR nanobodies coupled to fluorescent dyes. Subsequently, he did his minor research project at the UMC Utrecht in the group of Prof. Dr. G.J.P.L. Kops, under the supervision of Dr. N. Jelluma. During this internship, he studied the role of metabolic pathways in the mitotic progression of tumor and non-tumor cells. Bas also wrote a literature study on the pathogenic mechanism underlying the disorder Mosaic Variegated Aneuploidy. After obtaining his Master's degree in 2014, which also includes a Minor in the Fundamentals of Business and Economics, he immediately started his doctoral studies in the group of Prof. Dr. G.J.P.L. Kops in the UMC Utrecht. The results of his studies are described in this thesis.

DANKWOORD | ACKNOWLEDGEMENTS

After 6 years and a bit of a sprint at the end to write this thesis (apologies Geert and Litha, I know you would have preferred a little less risky deadlines) here we are! Some of you may have wondered whether I was ever going to finish my PhD, but why rush through something that you enjoy? Because I can honestly say that I really enjoyed the whole journey: my colleagues, my new friends, my projects. I feel like I have grown a lot on both a professional and personal level and am grateful for the whole experience.

Geert, first of all: thanks for having me! It feels strange to move on after having spent so many years and different chapters of my career in your group, starting with my Master's thesis, an internship, my PhD, and by then even a bit as a postdoc. But I cannot imagine a better group for any of it and I feel lucky to have been a part of it. I admire how you manage to create a working environment that is both very pleasant to work in and stimulating at the same time. Your input and guidance are always very valuable, and your genuine care for the people in your lab makes you an amazing boss. Thank you for everything!

To the PhD committee members, **Paul Coffer** and **Rachel Giles**, and the other members of the assessment committee, **Susanne Lens**, **Richarda de Voer**, **René Medema**, and **Michiel Vermeulen**: thank you for your time and interest in assessing this thesis. **Paul** and **Rachel**, your guidance was always much appreciated!

Litha, thank you for making this whole process happen smoothly! I may have been pushing it at the end so I am glad that you were there to back me up and that you had everything well under control.

A lot of work in this thesis would not have been possible without my collaborators. From the Frilander lab: **Mikko**, **Maureen**, **Ali**, and **Jens**; from the Rahman lab: **Nazneen**, **Sandra** and **Shawn**; from the Vermeulen lab: **Michiel**, **Lisa**, and **Marijke**; and from the Snel lab: **Berend** and **Laura**. It was a pleasure working with you these past few years, thank you so much!

Spiros, my partner in crime in PhD-land, and **Freek**, my best friend, thank you for being my paranymphs! **Spiros**, you and I did our PhDs together nearly from start to finish and I wouldn't have wanted it any other way. You're a great friend and having you around made my PhD so much more enjoyable. Although I will be breaking the second rule: I miss our fightclubs! These long evenings with unhealthy food, good company, and maybe some work, really added a lot to the whole experience. I'm still not sure how we came up with that name though. **Freek**, since the moment we met as students and flat mates it immediately clicked between us. Since then, we experienced many adventures together and I am looking forward to those yet to come!

To my student **Esther**: thanks a lot for all the help! Without you, I would probably still be trying to PCR CENATAC cDNA right now. I really enjoyed working with you, good luck with your own PhD!

My fellow **Kopsies**, thanks for the amazing time I had with you! You are a great group of people, and the many retreats, dinners, board game sessions, and boat rides, really made these years unforgettable. **Banafsheh** aka the lab therapist (and man-cave infiltrator), always looking out for everyone's feelings. You finally thought you got the best of me when

naming me a T-Rex, but I think we all know that a T-Rex is much much cooler than a monkey. I wish you and Willem all the best! **Richard**, my squash partner, I really enjoyed our matches and winning those broodjes kroket! **Ajit**, always jumping around and in for a laugh. What a shame that you had to leave the lab because of your allergies, but on the positive side: all the more time to enjoy your nice little family! I will never forget the Ardennes trips that you helped organize, those were amazing! **Timo**, the microscope hulk, I almost wish I had some of your temper. Thanks for fixing the microscopes countless of times and for keeping the title of longest PhD away from me. **Ana**, your ability to do 100 different things at the same time always baffled me, maybe all those different colors really worked. You were one of the driving forces behind the SKAvonden, thanks for that! All the best to you, Pablo and Pablito! **Carlos & Eelco**: two of the smartest and most driven people I know and at the same time you have hearts of gold. Eelco, thanks for all the help with my projects, you really helped push them to the next level. Your motivation and dedication is a great inspiration. The same goes for you Carlos! I don't think I know anyone that works as hard and is as capable as you. I have no doubt you will push it very far as a group leader. **Jolien**, you and Eelco opened up the CENATAC project for me, thanks for that! We didn't see you around as often as we'd have liked but it was great having you. **Wilma**, the badass biker of the lab, all the best to you and Huub in Scotland! **Nannette**, thanks for showing me the ropes all those years ago. I could always count on you to point out the missing controls. **Jingchao**, my ML1 buddy. Sometimes it felt like you lived there for days on end. Always sneaking around the lab trying to scare me, maybe one day you'll even succeed. **Kim**, you joined the lab not that long ago but you immediately became the heart of the party. I loved editing the lab movies with you, your creativity brought them to a whole new level. I'm sure we'll be playing board games for many years to come! **Pim**, the squash beast, I'm glad I was able to beat you at least a few times at the end. Your open and loud personality brings a lot of energy to the lab, keep that up! **Bastiaan**, another late addition to the lab but you and I clicked immediately. You're a great addition to the man-cave and I can't wait to beat you in Hearthstone again. **Nico**, it really is nice to have a crazy person around in the lab. I'm looking forward to our future fishing sessions! **Maike**, finally someone that can appreciate Pokémon! I am amazed by how you are able to bring so much style to a laboratory. It has been great seeing you grow into a confident scientist. **Joana**, another driving force behind the SKAvonden, thanks for that! I'm glad that you're back as my squat competitor, bring it on! **Sjoerd**, the baby giraffe who is not that young anymore. I have enjoyed seeing you grow from the lab junior that you were to the lab junior that you still are. I hope your investments pay out in the long run! **Tetrahemine**: cry cry. I promise I'll try not to scare you anymore, maybe. **Dani**, another new lab member that fit in immediately. I enjoyed our spikeball and board game sessions and I am sure that many more will follow. **Anko**, thanks a lot for all the microscope help! **Simona** and **Thomas**, I haven't been around much since you joined but it was immediately clear that you'll be great additions to the group.

To all other ex-lab members: **Richarda**, **Antoinette**, **Joris**, **Claudia**, **Debora**, **Vincent**, **Manja**, **Xiaorong**, **Alexandra**, **Desiree**, **Camilla**, **Sonja**, **Marek**, **Debbie**, **Oskar**, **Matthijs**, **Wilco** and **Tale**, thanks for everything. **Richarda**, although it was short-lived, it was great having you in the lab. I wish you all the best as a group leader and am looking forward to seeing you across the table on the 15th! **Antoinette**, we may not have always seen eye-to-eye but I appreciate all you did for the lab & wish you all the best in the future.

To all members of the other labs that I have been in close contact with over the years:

Lens, Medema, Saurin, Wolthuis, and **Rowland:** thanks for the great discussions and the memorable retreats!

And thanks to all other Hubrecht and UMC colleagues and friends that made my time in these institutes unforgettable. **Corina**, what a shame that the coronavirus outbreak threw soot in the water and forced us to cancel our shared defenses and celebrations. It was great though to experience our PhDs and the writing phase together, and of course our shared garden! Good luck on the 15th! **Gaby** and **Andrea**, more board games nerds, I loved having you around and am sure we will continue to play for many years to come. **Anne, Bas, Marta, Maya, Brian, Hesther**, thanks for making the ML1 a fun place to be! To the other members of the **van Rooij, Kind, Galli,** and **Tanenbaum** groups, and everyone else on the second floor: thanks for everything!

Opa de Wolf, ik heb altijd gezegd dat jij en oma de meest lieve en goedaardige mensen zijn die ik ooit heb mogen kennen, een beter voorbeeld voor mijn eigen leven kan ik me niet voorstellen. Bedankt daarvoor! Het is jammer dat oma er niet meer is, maar in gedachten zal ze altijd bij ons zijn. **Oma Schou**, net als opa en oma de Wolf heb jij een grote rol in mijn leven gespeeld, bedankt voor alle goed zorgen!

Papa, mama, thanks for being the best parents! You gave me all the freedom in the world to do whatever I wanted and to become whoever I wanted to be. Dad, you gave me my rationality/practicality that got me where I am today; mom, your empathy made me a better person. Your support has allowed me to live my life to the fullest. I appreciate all you ever did for me. To my little pot bellied pigs brothers, **Tim** and **Arno**, I just want to say that I expect to be called *Dr. Bas* from now on.

Στην ελληνική μου οικογένεια, σας ευχαριστώ που με δεχτήκατε και με αγκαλιάσατε! Παρ'όλο που μιλάμε διαφορετικές γλώσσες, με κάνατε να νιώσω σαν στο σπίτι μου από την πρώτη στιγμή που σας γνώρισα. Είστε μια τόσο ζεστή και χαρούμενη οικογένεια, είμαι πραγματικά ευγνώμων που είμαι μέρος της. Τώρα που ολοκλήρωσα το διδακτορικό μου, σας υπόσχομαι ότι θα μάθω να μιλάω ελληνικά!

And last but not least, **Sofia:** thanks for putting up with me these last few months. I know it is an understatement to say that I wasn't the most social person to be around: only focused on writing, eating, and sleeping (maybe I should have started writing a little bit earlier?). And to make matters worse I was growing my hair during the corona lockdown so you were basically stuck with a non-responsive hobo. Nonetheless, you did your best to support me and provided me with an avalanche of (Greek) culinary treats that kept me going strong. Thanks for that! Without you, the whole process wouldn't have gone nearly as smoothly. You are the Greek fire that lights up my life and I can't wait to spend the rest of it with you!

